Resting state fMRI as a marker for progression from mild cognitive impairment to Alzheimer's disease

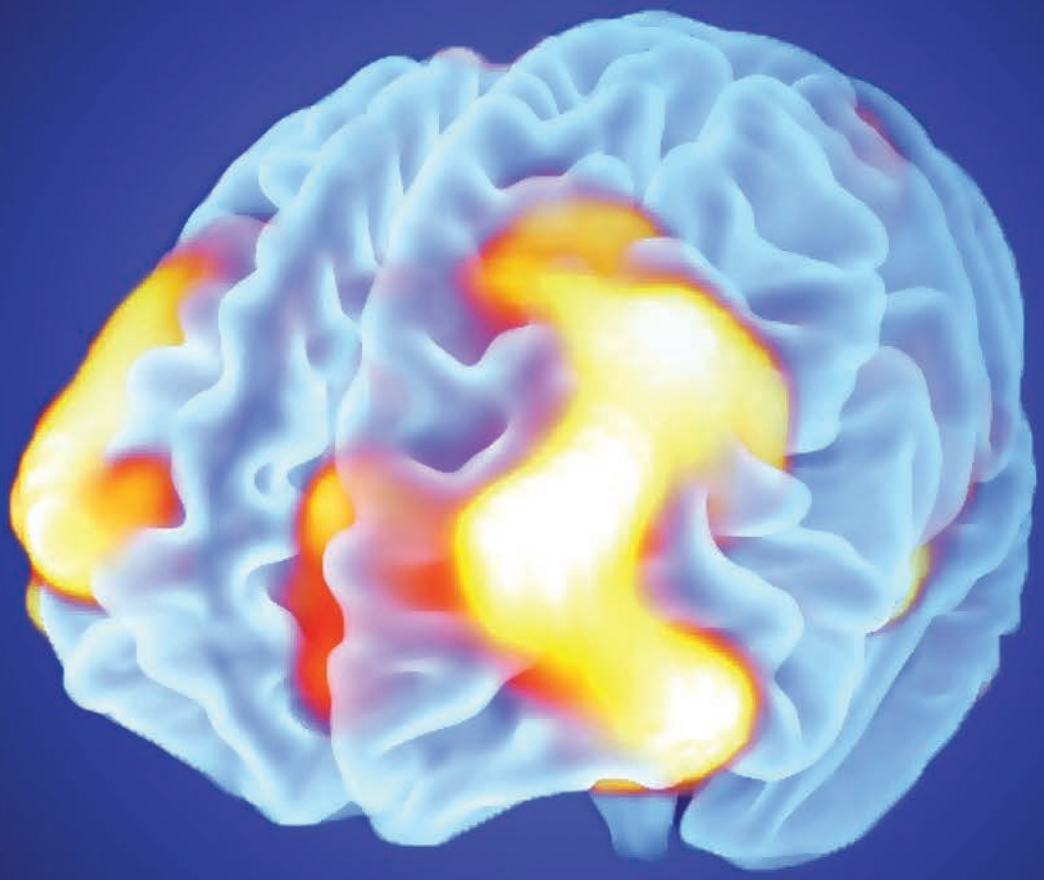

Tor Olof Strandberg,
Supervisor: Peter Mannfolk,
Medical Radiation Physics,
Lund University, 2013

Resting state fmri as a marker for progression from Mild Cognitive Impairment to Alzheimer's disease

Tor Olof Strandberg,
Supervisor: Peter Mannfolk,
Medical Radiation Physics,
Lund University, 2013.

Abstract

The arc of progression in the most common neurological affliction known as Alzheimer's Disease (AD), is characterized by a prodromal stage of Mild Cognitive Impairment (MCI). MCI subjects have traditionally been diagnosed with a battery of cognitive tests, but in recent times two good biomarker predictors of incipient AD have been identified. The cerebrospinal fluid levels of the protein residues amyloid-beta and phosphorylated tau can be quantified and directly relate to the imprint of associated pathologies in the brain. This work aims to elucidate the impact of tau- and amyloid-related pathologies on the functional networks of the brain, as gauged by a resting-state fMRI connectivity analysis. In this context, we aim to identify optimal model parameters that yield maximal contrast between subspecies of MCI and healthy controls, such as the most sensitive frequency interval for the Blood Oxygenation Level Dependent (BOLD) time-series and the resolution of whole-brain parcellation schemes. The connectivity analysis exposes the impact of biomarker pathology and outlines a tentative progression pattern, relating the decline of functional connectivity to increasingly pathological levels of biomarkers. A progression hypothesisis proposed, reviewing pattern progression in the light of neuronal communication breakdown and phase-lag. Furthermore, failure of key hubs are identified using graph theoretical centrality measures and the relative group separations with connectivity pattern is evaluated by means of support-vector machines.

Relative healthy controls, MCI with non-pathological CSF levels of biomarkers exhibit a widespread pattern of reduced connectivity, likely due to a mix many dementia subtypes. MCI subjects with pathological amyloid CSF levels but normal values of tau, has a large set of failing links converging on crucial network hubs: thalamus, caudate nucleus and putamen, and are additionally affected in key regions such as hippocampus. This finding supports the view of Alzheimer's progression in terms of global disconnection syndrome by failing hub regions. Furthermore, these patterns are manifested in relevant graph theoretical centrality measures. MCI with pathological levels of both CSF biomarkers produce the strongest contrast relative healthy controls, involving reduced connectivity beteween parietal and frontal areas, but also implicating areas linked with cognitive decline, such as hippocampus and posterior cingulate cortex. The similarity of this contrast to that of controls vs. Alzheimer's subjects, indicates the presence of a functional progression pattern with two biomarker levels. Our findings merit further investigation of the biomarker progression line using larger cohorts further stratified with cognitive test scores.

Contents

1 Introduction **5**

2 Pathology **5**
2.1 Alzheimer's disease and other dementias . . . 5
2.2 Cerebrospinal fluid biomarkers . . . 5
2.3 Biomarker cohorts for fMRI . . . 7

3 The resting state and default mode network **9**

4 fMRI **11**
4.1 BOLD signal and acquisition parameters . . . 11
4.2 Preprocessing and quality assurance . . . 12

5 Functional connectivity extraction **13**
5.1 Parcellation strategies . . . 13
5.2 Connectivity measures . . . 15
5.3 Statistical analysis and multiple comparison error control . . . 17
5.3.1 False Discovery Rate . . . 17
5.3.2 Network-Based Statistic (NBS) . . . 18

6 Optimization of connectivity parameters **19**
6.1 Frequency dependence . . . 19
6.2 ROI resolution dependence . . . 23

7 Connectivity **28**
7.1 Distance dependence . . . 28
7.2 Strength . . . 33
7.3 General features . . . 34
7.4 HC versus MCI with non-pathological CSF . . . 36
7.5 HC versus MCI with pathological $a\beta$-levels . . . 42
7.6 HC versus MCI with pathological $a\beta$- and $p\tau$-levels . . . 51
7.7 MCI with low vs high $a\beta$-levels . . . 59
7.8 MCI with low vs high $p\tau$-levels . . . 64
7.9 Controls versus AD . . . 66

8 Summary of connectivity in biomarker space **69**

9 Progression **70**

10 Graph theoretical measures **85**
10.1 Nodal strength . . . 87
10.2 Eigenvector centrality . . . 89
10.3 Betweenness centrality . . . 90

11 SVM separation of groups **93**

12 Comparison with literature **101**

13 How I learned to stop worrying and love resting-state fMRI **106**

Resting-state fMRI som markör för progression från mild kognitiv störning till Alzheimers sjukdom

Alzheimers är den vanligaste neurologiska sjukdomen som år 2006 uppskattades påverka 27 miljoner av världspopulationen. Sannolikt kommer mer än var hundrade person att vara drabbad år 2050. Både EU och USA har nyligen initierat forskningsprogram där stora resurser satsas på hjärnforskning. Kartläggning av 'the human connectome' (samlingsnamn för olika sätt att karakterisera hjärnans strukturella och funktionella arkitektur) har likställts med the human genome project. I satsningen ingår en central del som syftar till att förstå och behandla neurologiska åkommor som Parkinsons och Alzheimers sjukdom.

En nyckelroll i connectomeforskningen spelas av funktionell MR, med dess förmåga att avbilda hjärnans funktionella arkitektur, dvs den regionala, neuronala aktiviteten och funktionella kopplingar mellan dessa regioner. De mönster av syresättning och tillflöde av oxygenerat blod som mäts med MR-kameran, är direkt relaterade till neurologisk aktivitet och kan användas för att kartlägga hjärnans funktioner. Dessa kartor ger ovärdelig information om hur specialiserade funktioner samspelar och integreras, men kan även användas för att lokalisera dysfunktionella epicentra associerade med olika neuropatologier.

För att förstå mönstrens betydelse, är det nödvändigt att dela in patientmaterialet i grupper som reflekterar sjukdomsgraden. I sammanhanget har två biomarkörer i form av proteinrester som manifesteras i cerebrospinalvätskan visat sig användbara. Grovt förenklat, kan sjukdomsförloppet karakteriseras som att CSF-nivån av den ena biomarkören nivå stiger under en längre tid, medan den andra i ett senare skede stiger i rask takt med allt sämre kognition. CSF-nivåerna av dessa biomarkörer är därför mycket användbara för att stratifiera patientmaterial med målet att karakterisera tillhörande patologi.

Resting-state fMRI syftar på att mätningen görs i frånvaro av ett klassiskt fMRI paradigm. Paradigmet består i vanliga fall av att patienten i kameran utför någon uppgift som syftar till att aktivera specifika hjärnregioner. I resting-state avbildning är instruktionerna till patienten betydligt enklare: Ligg still, slut ögonen, tänk inte på något speciellt, försök att inte somna. För patienter med kognitiv nedsättning kan frånvaron av klassiskt paradigm vara en stor fördel. I detta vilotillstånd är hjärnan långt ifrån inaktiv och i frånvaron av yttre stimuli stiger vi in i en introspektiv fas. fMRI visar att denna fas domineras av ett nätverk som via viktiga nav integrerar minnen och intryck med planerande och exekutiva funktioner. Här ingår simuleringar av potentiella framtider och handlingsförlopp som fokuserar alla våra intryck och minnen i jakten på deras logiska slutsats. Den mönsterjonglerande hjärnan och dess remarkabla komplexitet har vuxit fram på en evolutionär tidsskala och ger oss en unik förmåga att förutsäga framtiden.

Under kontinuerlig mätning av den spontana syresättningen i resting-state, aktiveras områden som är helt centrala för kognition. Resting-state fMRI har därmed en unik förmåga att karakterisera kognitiv dysfunktion och ger oss en ovärderlig inblick i sjukdomsförloppet.

För närvarande existerar ingen behandling mot Alzheimers sjukdom och sk bromsmediciner (denna nomenklatur kan ifrågasättas) behandlar symptom, inte den bakomliggande patologin. Deep brain stimulation, dvs svaga elektriska pulser i nyckelområden, har visat sig användbar i behandlingen av Parkinsons. Liknande metoder kan komma att användas i kampen mot Alzheimers och kräver detaljerad kunskap om funktionella kopplingar och hur dessa påverkas, så att rätt måltavla väljs för behandlingen.

För att en behandling ska bli framgångsrik, krävs även att sjukdomen upptäcks i sitt prodromala stadie. Detta förstadie till Alzheimers, vilket karakteriseras av en mild kognitiv nedsättning, är fokus för vår studie. Vi undersöker hur olika nivåer av cerebrospinala biomarkörer relaterar till skillnader mellan patienter med kognitiva svårigheter och friska, åldersmatchde individer. Förhoppningen är att hitta mönster som kan stärka diagnoser och behandlingsval, att särskilja individer som kommer att utveckla Alzheimers sjukdom från de som förblir stabila, men även att erhålla en djupare förståelse för hur hjärnans funktionella arkitektur rubbas av sjukdomen.

1 Introduction

2 Pathology

2.1 Alzheimer's disease and other dementias

Alzheimer's disease (AD) is the single most common neurological disorder affecting some 27 million people world-wide (2006) and is estimated to affect approximately 1.2% of the world population by 2050 [1]. In developed countries, the prevalence is estimated to 1.5% at 65, increasing to 30% at 80 years of age [2]. There is presently no known cure or effective treatment of the neurodegenerative disorder, which ultimately leads to death, as the autonomous nervous system fails to maintain vital functions. From the time of diagnosis, the average survival period is 8 years [3].

The primary risk factor of AD is age, with the vast majority of subjects diagnosed above 65, although exits an early onset subgroup with a genetic component, providing clues to the origins of the disease. Aside from age, a family member with AD and specifically genetic predisposition in the presence of the $APOE * E4$ allele are among the few confirmed other risk factors [2]. The association of AD with pathological levels of certain biomarkers manifested in the cerebrospinal fluid, is much stronger than with any of the identified risk factors [4]. These biomarkers will be used to define our patient cohorts.

The prodromal stage of AD known as Mild Cognitive Impairment (MCI) is most often characterized with a battery of cognitive tests. These subjects suffer a 4-6 times higher risk of developing AD (15% within a year) [5].

There are many forms of dementia, with different neuropathological origins: Alzheimer's disease, dementia with Lewy bodies, frontotemporal dementia, and dementia following other diseases (e.g. AIDS) [2]. These dementias may be mixed with some neuropathological overlap, greatly complicating the task of identifying AD pathways. One of our subgroups contains subjects with an MCI diagnosis[1], but with non-pathological levels of known AD biomarkers in the cerebrospinal fluid. This often loosely defined group likely contains several different dementias in addition to those with an AD endpoint.

Vascular dementia (10-50%, estimates vary greatly depending on markers employed) is the second most frequent form of dementia, caused by impaired blood flow and oxygenation [2]. Frequently associated with several small strokes, vascular dementia can be identified by visual inspection of anatomical images, meaning that this subgroup could be partially eliminated by QA protocols. However, about 10% of all dementias are mixed, predominantly thought to be a juxtaposition of vascular dementia and AD.

Lewy body dementia [7] is the third most common major form of dementia and is defined by a set of distinctive symptoms, e.g. vivid hallucinations. The so-called Lewy bodies refers to deposits of the protein alpha-synuclein, which can be found in both Alzheimer's and Parkinson's subjects, thus complicating their diagnosis with multiple pathways. In the early stages of Lewy body dementia, symptoms are often Parkinson's-like with disrupted movement, but also overlaps with AD symptom's in the form of memory problems.

The MCI group with non-pathological AD biomarker levels will contain a plethora of different dementias, making this group particularly difficult to interpret. The MCI group with pathological levels should be screened from the aforementioned afflictions by virtue of appropriate biomarker limits, but we cannot completely exclude mixed dementias contaminating our primary target group - the MCIs at high risk of AD.

2.2 Cerebrospinal fluid biomarkers

In terms of neuropathology, two biomarkers are primarily used in gauging progression [8]:

1. Extracellular plaques composed of residues of the protein amyloid beta ($a\beta 42$).
2. Intracellular neurofibrillary tangles (NFT) composed of hyperphosphorylated tau-protein ($p\tau$).

Both $a\beta$ and $p\tau$ can be measured in the CSF. Although these biomarkers have proven to be quite good predictors of incipient AD [4], the neural health degeneration likely precedes their manifestation by some time. Here, Resting-State (RS) fMRI could provide auxiliary power by imaging early changes in the brain's functional architecture.

The so-called senile-plaques form when amyloid-β protein aggregates in extracellular space [8]. The amyloid protein itself originates in sequential cleaving of a precursor protein by the two proteolytic

[1] The diagnosis based on complaints of memory loss and cognitive decline, then verified by a neurologist who makes use of cognitive tests, such as ADAS [6].

enzymes β- and γ-secretase, involving precursors of different length, $a\beta 40 - 43$. The precise function of amyloid-β is unknown, it likely has a multifunctional role making its activity difficult to map out [9]. The presence of amyloid plaques leads to oxidative stress and it has been shown that amyloid peptides can induce ion flux through holes in the lipid membranes, allowing calcium ions to enter [10] and disrupt the ion balance. As the level of amyloid plaques increase in the brain, the CSF-levels of $a\beta 42$ decrease. The genetic component of early-onset AD is linked with enzyme deficiencies, which has fueled the notion of an amyloid pathway being central to AD. Senile-plaques increase naturally with age - a phenomenon not necessarily accompanied by cognitive decline. The normally aging group forms a reasonably discernible constellation of lower amyloid levels as gauged by PET[2], which we make use of in the definition of our biomarker cohorts below.

Whereas the amyloid protein is extracellular, the tau protein is manufactured inside the neuronal cell in order to assemble microtubules and promote their structural stability [8, 11]. Amyloid- and oligomer-induced toxicity cause a chain-reaction of tau hyperphosphorylization, whereby the proteins release from the microtubuli and polymerize into helical filaments, leaving a destabilized microtubule assembly, Formation of so-called NeuroFibrillary Tangles (NFTs) ultimately lead to neuronal cell death, with a severe impact on gray matter integrity and functional connectivity.

There situation of identifying early onset of AD is complicated by the potential existence of several pathways, with some debate regarding the importance of the amyloid levels. The appearance of high levels of NFTs in neurons with correspondingly high $p\tau$ CSF-levels is at least partly caused by the amyloid pathology. This is consistent with increased $p\tau$ as hallmark of a relatively late disease stage.

The amyloid has been hypothesized to be the main pathway leading to AD, a theory supported by the presence of the gene for the amyloid precursor protein in chromosome 21 combined with the fact that Down's syndrome almost invariably leads to AD in later midlife [12]. In addition, one of the identified risk factors involves the coding of apolipoprotein 4 (APOE4), which is a very poor enhancer of the amyloid breakdown compared to other protein varieties of similar function [13].

Tau pathology is thought to be related to amyloid pathology, but leads to more direct neural cell damage in formation of NFTs. This is hypothesized to occur in cascades, where $p\tau$ releases and then pairs with other τ, effectively disintegrating the microtubuli structure and the cell's vital transport system [14].

Amyloid burden can be more accurately measured using PET amyloid tracers (i.e. Pittsburgh compound B), exhibiting a spatial pattern overlapping with the nodes of the Default Mode Network (DMN - the network of the brain which dominates resting-state activity) [15], in particular the Posterior Cingulate Cortex (PCC). This overlap has added fuel to the hypothesis of an dominant amyloid pathway, causing many studies to focus on DMN dysfunction as gauged by independent component analysis. Because amyloid deposits occur normally with age, there are individuals with high amyloid burden, but no detectable cognitive deficits. Tau pathology on the other hand, more indicative of cognitive impairment, seems to accumulate more in the limbic system [16]. Therefore, we would expect significant differences in hippocampus, parahippocampal complex, amygdala, thalamic nuclei and cingulate gyrus.

The chances of a successful treatment critically hinge on early detection of prodromal AD and even though these biomarkers are useful in categorizing subjects, their CSF manifestation is most likely preceded by an earlier phase of degeneration [8, 17]. RS fMRI has the potential to image early onset changes to functional networks of the brain and could form an important part of the diagnostic toolbox. Additionally, the spatial resolution of fMRI allows mapping epicenters of functional degeneration and how these evolve with disease progression.

Ideally, a biomarker should be specific, identify the present progression stage and the following time-course of degradation (allowing the physician to choose treatment strategy), and should also be useful in assessment of any treatment (for a short list of various markers see Ref. [8]). Besides its spatial resolution and ability to image functional networks, fMRI methods meet the latter criterion, as it can be used to gauge the neural health at any instant. More ambitiously, if a functional connectivity degradation evolution could be mapped out, a useful scale for assessing disease progression would be within reach. Furthermore, CSF biomarkers require a spinal tap, whereas fMRI has the added advantage of being non-invasive.

[2]Of course, the normal group may contain very early AD subjects - perhaps it is more precise to speak of a potentially very slowly progressing group and a latter stage group in faster decline.

2.3 Biomarker cohorts for fMRI

The groups defined here follow the perceived progression pattern in terms of CSF-biomarker levels, ultimately reflecting incipient AD. Somewhat oversimplified, the current working hypothesis is that a longer period of decreasing $a\beta 42$-levels in the CSF (with correspondingly increased senile plaque levels and oxidative stress) eventually leads to NFT-formation and increased $p\tau$-levels.

One may attempt to create cohorts for fMRI studies using CSF-levels of τ-protein rather than its hyperphosphorylated state. Similarly, the levels of total τ (i.e. $t\tau = \tau + p\tau$) can be used as a predictive biomarker (see Fig. 1 (d-f)).

$p\tau$ and τ are closely related (see Fig. 1 (c)) and respective cohorts result in similar fMRI difference patterns. Indeed, $p\tau$ and τ appear to be in an almost one-to-one correspondence, albeit with increasing spread for greater concentrations. In what follows, we therefore choose to focus on Functional Connectivity (FC) as a function of $p\tau$, rather than related quantities. From a neurophysiological point of view, it also makes more sense to focus on $p\tau$, as this is the form of the protein most directly related to NFTs and neuronal dysfunction.

We use two biomarker space partitions that are particularly illuminating with regard to FC as a function of biomarker space (see Fig. 1 (a,b)), designed to elucidate the relative impact on FC of $a\beta$/senile plaques and $p\tau$/NFT, respectively. Beyond the scope of the present study, one may additionally combine biomarker data with various cognitive test scores.

For the purposes of mapping changes in functional connectivity with disease progression, we define the following groups:

HC Healthy age-matched Controls (HC). At the time of writing, biomarker data for this group is in the process of being collected. This means that some subjects with pathological levels of biomarkers is likely to be present (better classified as $M_{a\beta}$ or $M_{p\tau}$ below).[3]

M_0 Patients diagnosed with MCI, who have non-pathological levels of biomarkers in their CSF:

$$a\beta > 550\ ng/l\ and\ p\tau < 80\ ng/l.$$

These subjects have a lower risk of progressing to AD, or are in very early stages of the disease. This group likely contains a broader spectrum of MCI, as caused by e.g. incipient vascular or Lewy body dementia.

$M_{a\beta}$ Patients diagnosed with MCI, who have pathologically low levels of amyloid-β residues in their CSF:

$$a\beta < 550\ ng/l\ and\ p\tau < 80\ ng/l.$$

These subjects have high levels of senile plaques and suffer a high risk of progressing to AD.

$M_{p\tau}$ Patients diagnosed with MCI, who have pathologically low levels $a\beta$ as well as high levels of $p\tau$ in their CSF:

$$a\beta < 550\ ng/l\ and\ p\tau > 80\ ng/l.$$

These subjects have high levels of plaques/NFT and suffer a very high risk of progressing to AD. They are presumably in the latter stages of disease progression.

AD Patients with confirmed Alzheimer's Disease.

The exact M_0 group composition is unknown and contain broad spectrum of MCI subjects. Although AD is the statistically dominant dementia, M_0 is potentially populated by several varieties (see 2.1). However, the common occurrence (50-70%) of AD dementia implies that most of the M_0 subjects are likely to progress along this path.

The exact limits on biomarkers are somewhat arbitrary and in scrutinizing Fig. 1 (with clustering of data in mind), it appears likely that a lower level of $p\tau < 70\ ng/l$ would in fact capture $p\tau$-pathology equally well with better statistics in the high-$p\tau$ range, although emerging patterns would certainly be very similar.

Refinements of biomarkers predictive power have been made [4] by means of the quota $q = \alpha\beta/\tau$, which gives the slope of the dividing line that somewhat arbitrarily cuts through a densely populated

[3] Less likely and disruptive, some contamination by undiagnosed MCI subjects remains possible (better classified as group M_0)

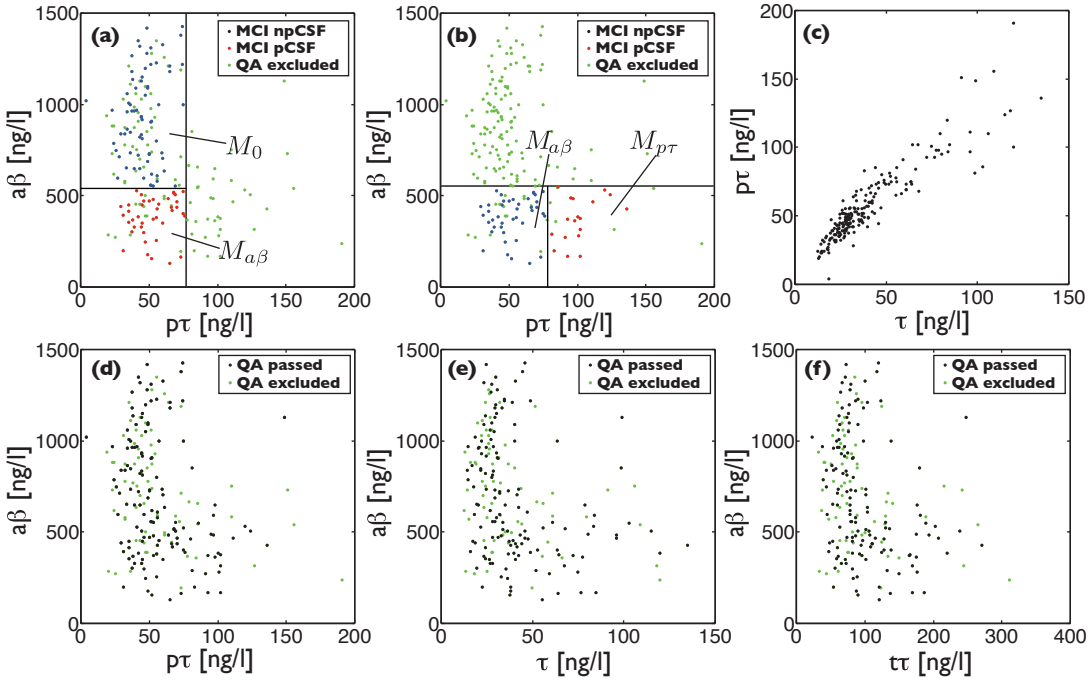

Figure 1: CSF biomarker space ($a\beta 42-$ and τ-levels) for MCI subjects. The MCI groups are defined according to relative disease progression in terms of their CSF biomarker levels (a, b). The choice of NFT-measure is not critical as $p\tau$ and τ are closely related (c). The three different measures of neuronal dysfunction caused by NFT: (d) $p\tau$, (e) τ and (f) total $t\tau = p\tau + \tau$.

region of low $a\beta$/high $p\tau$-subjects. Although quotas cutting diagonally in $a\beta - p\tau$ space may have added predictive power in terms of incipient AD, they do not add greatly to the understanding of qualitative FC-pattern trends and will therefore not be used in this work.

At the time of writing[4], there are 126 HC, 135 MCI and 8 AD[5] subjects, after applying QA protocols (see Subsec. 4.2). The partitions of biomarker space in Fig. 1 (a) and (b), result in 70 M_0, 42 $M_{a\beta}$ and 18 $M_{p\tau}$. These groups will we compared amongst each other as indicated in Fig. 2.

Tab. 1 summarizes the groups examined in this paper. The groups do not differ from HC in terms of age or gender (with the exception of the small AD group), and their main defining characteristic is the CSF biomarker configuration. The common general cognitive test Mini-Mental Examination Score (MMSE) does not differentiate the groups very well, but follows the same trend as the simpler ADAS 3 word recollection score with worse test scores as $a\beta$ drops, but no detectable change with increasing $p\tau$.

[4]These numbers will increase to approximately 500 MCI and HC when acquisition period ends.

[5]Due to the very low number of AD subjects, any associated results should be interpreted with great caution. AD will only be compared with HC.

Table 1: Characterization of the groups studied in terms of mean values (standard deviations). With the exception of AD, the groups do not differ significantly in age or gender. The two columns following CSF levels refer to a general cognitive test (MMSE, range 0-30, low is bad), and a word recollection score (ADAS 3, range 0-10, low is good). Note that CSFs of HC have not been analyzed yet and that ADAS 3 was not performed for the 8 AD subjects.

Group	Subjects	Age [y]	Sex (% female)	$p\tau$ [ng/l]	$a\beta 42$ [ng/l]	MMSE	ADAS 3
HC	126	71.1 (4.1)	0.55	-	-	29.2 (0.9)	1.7 (1.7)
M_0	70	70.3 (5.6)	0.52	45.8 (12.0)	729.1 (171.4)	28.1 (1.6)	4.1 (2.5)
$M_{a\beta}$	42	71.4 (4.8)	0.45	54.7 (16.0)	417.8 (165.2)	27.6 (1.8)	5.6 (2.7)
$M_{p\tau}$	18	71.8 (5.3)	0.56	97.2 (18.6)	365.6 (76.5)	27.9 (1.4)	5.4 (2.6)
AD	8	75.9 (6.7)	0.75	101.6 (25.7)	321.0 (57.1)	19.0 (3.7)	-

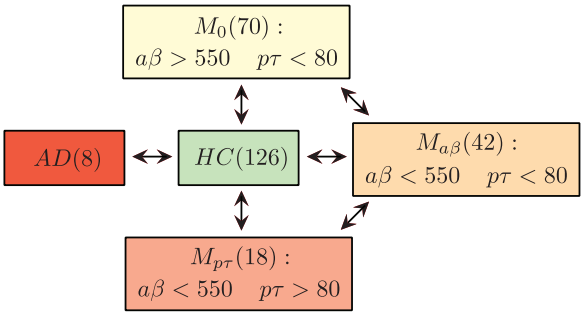

Figure 2: Statistical testing scheme. Double arrows indicate group-wise comparisons.

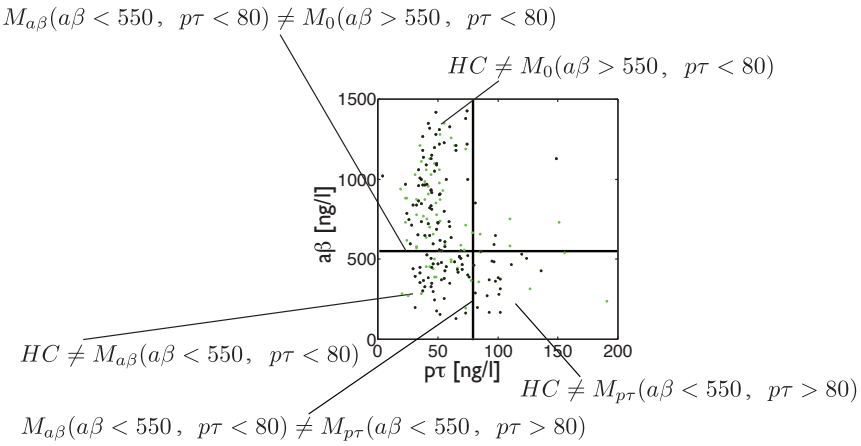

Figure 3: Biomarker cohort and HC comparison graphical map that will be used in data presentation.

Whereas all MCI groups have significantly worse test scores compared to HC ($p < 0.01$, one-tailed t-test), there is only a trend-level reduction for M_0 relative $M_{p\tau}$ and $M_{a\beta}$, but M_0 has significantly better ADAS 3 than the other MCI.

Note that there is no reason to expect a natural partition in functional connectivity corresponding to a given biomarker partition. Functional changes may manifest themselves uniquely in any given subject, as may senile plaque distribution and NFT formation. Therefore our comparisons yield significant group-level differences and should not be mistaken for an average individual, rather the combined contribution of several individuals who may not even be optimally bundled by the biomarker dividing lines.

A useful map labeling the various tests for significant differences between biomarker-defined cohorts and HC is shown in Fig. 3. Whenever a HC-biomarker cohort comparison is made, the corresponding area of biomarker space will be indicated. When two biomarker cohorts are compared, the border between the adjoining areas will be indicated.

3 The resting state and default mode network

Our networks represent functional connectivity maps of the human brain, calculated from the spontaneous oxygenation oscillations that occur during the so-called Resting-State (RS). These patterns are not random, rather they represent a specific phase of brain activity that takes place in the absence of external stimuli and tasks. The RS approach contrasts the customary fMRI experimental design [18], in which a paradigm is defined and task execution is required to activate regions of interest relevant to the hypothesis. Naturally, not requiring a patient with cognitive impairment to perform a specific task is advantageous. It greatly simplifies the experimental design, reduces the risk of spurious effects, minimizes the hazards of a bias introduced by paradigm design or even its experimental implementation.

On the other hand, we will always face difficulties related to individual RS variations, and some steps

must be taken to maximize the probability of true RS imaging. Motion artifacts can become a severe problem as a continuous signal is recorded. Clearly, external stimuli in terms of auditory, visual and sensory input should be kept to an absolute minimum. The setup is exceedingly simple compared to task-based imaging and we simply instruct patient to relax with eyes closed and not to think of anything in particular during a six minute fMRI scan, recording the spontaneous BOLD signal.

What does the brain do during this mysterious resting-state period? The most consistent network that forms the major component in an Independent Component Analysis (ICA), is the so-called Default Mode Network (DMN) [19]. The DMN signal is remarkably consistent across subject during RS imaging - a fundamental feature our minds, in which the absence of sensory input triggers important high-level processing.

Areas involved in DMN are deactivated during task execution and are therefore often referred to as task-negative. The current hypothesis around which consensus has crystallized, is that DMN represents an introspective phase of sorting, combining and processing past experiences in an attempt form an apex of logical conclusions. Therefore, the DMN processing generates a plan for the future, a best guess of things to come, based on past experiences.

Fundamentally holistic by nature, the brain forms a new whole out of scattered parts, i.e. impressions and experiences. Evolution has shaped the brain and its functional and structural architecture into a remarkable machinery acutely tuned to predicting future events, providing us with better chances of survival.

Functional connectivity analysis [19] indicates that DMN consists of several interacting subsystems. For example, the medial temporal lobe provides memories for the medial prefrontal lobe to access in simulations involving the self. Particularly important in the DMN function are integrating parts such as the posterior cingulate cortex, which acts as a hub and coordinator between the subsystems. Failure to integrate autobiographical memories with frontal executive control, leads to a catastrophic cognitive decline and vulnerable hub regions has therefore the potential to cause a global disconnection syndrome.

Various neuropathological afflictions such as AD, MCI, Parkinson's, fronto-temporal dementia has been linked to a deficient DMN. Given improved imaging techniques of the future, one may conjecture that RS patterns hold promise as a potentially universal neural health gauge.

As mentioned, the DMN has been identified by ICA methods. Let us say we are tasked with the objective of analyzing the various sources of voices in a room full of people, given that a number of microphones have been placed. The precursor of ICA, so-called Principal Component Analysis, will then provide us with archetypes of voices that represent the largest variation in the data. Orthogonalizing these, we can then extract independent components, that form orthogonal base vectors spanning the data-space. Now, equate the voices in the room with neurons firing to produce voices in the head (recorded in the form of oxygenation patterns) and equate the microphones with fMRI voxels, and the analogy is complete.

ICA extracts independent components of the spontaneous resting-state signal, which, in a normal person, should yield the DMN. ICA would therefore seem ideal as tool to analyze DMN deficiencies, but the method several drawbacks that makes it ill suited for our problem.

Firstly, ICA tends to smear and smooth out group differences, reducing contrast and power[20]. Secondly, the method does not order the components found in a consistent way across subjects, meaning that manual inspection is usually required to identify DMN. Such an approach is not feasible with hundreds of subjects in the cohort. Furthermore, the limited set of DMN regions are far from the only active regions during resting-state and functional connectivity breakdown in other regions would therefore be missed.

It is also very tempting to perform a dimensionality reduction via PCA. Unfortunately, even though the DMN is a fairly consistent signal, there is substantial variation in the resting-state activation across subjects in the same cohort. Indeed, we can never be quite sure what goes on in a patients brain when instructed to lie down, relax and thing of nothing in particular. Despite this individual variation, it is possible to identify consistent group differences at a statistically significant level. It does however mean that the pathological contrast generally does not lodge in the principal components.

In the context of our analysis, we use high-resolution ROIs with multiple anatomical tags derived from an anatomical atlas [21]. To condense notation we let sup=superior, inf=inferior, med=medial, post=posterior, ant=anterior and mid=middle. The anatomical labels corresponding to the task-negative or DMN network [22] contain or are in close proximity to the following anatomical atlas labels [21]: frontal sup L/R, frontal sup med L/R, cingulum ant L/R, cingulum post L/R, parahippocampal gyrus L/R, angular L/R, temporal mid R and temporal inf L [23]. These labels are of special interest because many studies have chosen to focus on DMN dysfunction associated with cognitive decline. We have instead

chosen to focus on a whole-brain analysis of which the DMN forms a part.

4 fMRI

In this section we will give a cursory description to the steps leading up to the functional connectivity analysis, from imaging of the Blood Oxygenation Level Dependent (BOLD) signal and the associated MR sequences, through the numerous preprocessing steps leading up to the gray matter signal used in connectivity analysis. Finally, we describe the implemented quality assurance protocols used to purge the material of artifactual data.

Since these techniques are fairly standard and not the focus of this paper, the depth of information will be limited. For a more in-depth description, the reader is referred to Ref. [18], the book on which the review in this section is based.

4.1 BOLD signal and acquisition parameters

In essence, heightened regional neuronal activity triggers an increased flux of oxygenated blood through the area, which in turn alters the local magnetic properties, increasing homogeneity of magnetic susceptibility. This mechanism produces more oxygen than the neuronal cells are consuming, producing a relative surplus which can be measured. The measured BOLD signal itself, originates not only in oxygenation, but susceptibility is also altered by interplay with blood flow and volume. Naturally, the changes in blood flow are not on the same time-scale as the ionic currents measured in EEG, and the BOLD signal is both blurred and delayed. Neuronal activity occurs on the scale of milliseconds, whereas the resulting oxygenation dynamics is three orders of magnitude slower.

The hemodynamic response is an ideal function that comes into play whenever the neuronal activity occurs in an idealized delta-spike fashion. Within 4-6 seconds, the response reaches a maximal peak height, directly related to the amount of neuronal activity. The signal then decays back to baseline within 12-20 seconds, with some undershoot.

There is variability across both brain regions and individuals of the hemodynamic response - something which complicates the functional connectivity analysis. This effect can potentially be mitigated by using measures that are less sensitive to noise (see Sec. 5.2).

In activation based experiments, one would typically use a template hemodynamic response function and deconvolute the BOLD signal in order to reveal neuronal activity blocks. In this context, the (approximate) linear time invariant property of BOLD is very important. Linearity simply means that the BOLD response scales linearly with neuronal activity, which implies the imaging of a summed response. Time-invariance refers a BOLD signal that follows any time-shift in neuronal activity perfectly. This last property is very important in our functional connectivity analysis, which relies on the correlation between time-series, ultimately reflecting correlations between neuronal activity.

The Generalized Linear Model [18] approach (see below) to extracting the neuronal signal relies on the linearity property, which can be broken by two distinct sources. Firstly, there may exist an intrinsic non-linearity between BOLD and neuronal signal. Secondly, and perhaps less important in resting-state imaging, there can be a non-linearity between stimulus and BOLD signal. This could for example occur in repeated stimulation, where the subject adapts, producing a reduced neuronal response due to the repetitive nature of the sensory input. Imaging resting state, we would perhaps be more vulnerable to other variables, e.g. the time-of-day during which imaging is done.

In resting-state imaging, the continuous oxygenation signal is recorded and modeling the hemodynamic response is less meaningful. Our GLM includes nuisance regressors for translation/rotation, estimated physiological noise and the white matter/CSF signal, leaving us with the gray matter oxygenation oscillations.

Since we are interested in imaging changes in local susceptibility, we choose T2* sequence gradient Echo Planar Imaging (EPI). It is necessary to include the static dephasing of spins in order to pinpoint the BOLD signal as local susceptibility changes.

6 minutes of spontaneous BOLD signal is recorded using the gradient EPI with TR/TE=2000/30 ms in 3x3x3 mm^3 voxels covering the whole brain in 33 slices (on a Siemens Trio 3T). The first ten seconds of the time-series are dumped in anticipation of a steady state. Other resting state set-ups exist, such as asking the subject to focus on an image of cross hairs. This procedure is designed to prevent the patient

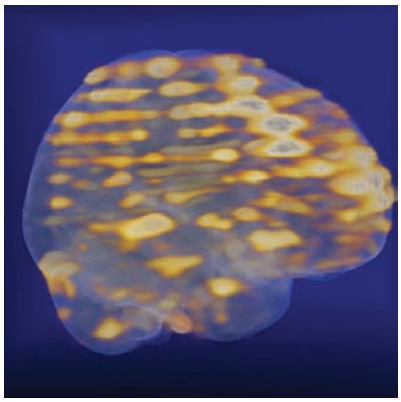

Figure 4: Banding artifact caused by motion between acquisition of interleaved slice sets.

from falling asleep, which disrupts the resting-state signal. The brain is geared to detect motion, and focusing on a stationary object for a long time causes most of the field of vision to vanish. Studies have shown that the two approaches lead to very similar results [24].

The fast EPI sequence is necessary to achieve a good time-resolution. The chosen sequence grants a repetition time of 2 seconds, which could be pushed further down to a few hundred milliseconds with greatly accelerated techniques such as multi-band EPI [25].

For the purposes of segmentation and registration, we also record a high-resolution MPRAGE anatomical image (TR/TE=1950/3.4 ms, 1x1x1 mm^3, 178 slices). The anatomical image can also be used to quantify atrophy in selected regions and assess anomalies such as white matter damage and stroke effects.

4.2 Preprocessing and quality assurance

Preprocessing of fMRI data generally involves a large number of steps. These include distortion correction, motion correction, slice timing correction, spatial smoothing of noise, and normalization to standard space, regression of white matter/CSF/motion and temporal band-pass filtering to further block unwanted signals. It is also necessary to perform brain extraction and segmentation to obtain gray matter/white matter/CSF masks. At the end of all this, we are left with a gray matter activity signal, where unwanted signals have been removed or regressed out.

Because we use gradient EPI, there is a large amount of *distortion* at air-tissue interfaces (e.g. sinuses and ear canal), where main field homogeneity is disrupted. Here, signal drop-out can also occur, something which can only be reduced by selecting an appropriate sequence. Distortion occurs because the gradients used to encode location is scrambled by the inhomogeneity, disrupting in the phase-encoding direction. Shimming has limited ability to reduce complex gradients from susceptibility differences. In so-called z-shimming a shimming pulse precedes each image acquisition, counteracting the effect of the susceptibility gradients [26]. Inferior and frontal/temporal lobes are most affected by distortion, owing to their proximity to air cavities. Distortion can be corrected for using a field-map technique, where the phase difference between two EPI with difference TE can be used to compute the field inhomogeneity, that is then used to displace voxels to their real position.

We do not perform a distortion correction, but the effect is counteracted in the non-rigid registration step and spatial smoothing. In addition, voxel time-series are averaged over regions of interest. It is not clear that a distortion correction would lead to better results - a procedure such as the z-shimming pulse will invariably lead to degradation of the signal in other parts of the image.

Slice timing correction is necessary because each acquisition has a certain duration. In our case, we use interleaved slices, first even and then odd slices (for example), causing a mismatch in time between acquisitions. This acquisition mode can also lead to an artifact called banding. If the subject moves between the two interleaved acquisitions, the signals overlap an sum, causing bands to appear across the image (see Fig. 4)

Motion is one of the major problems of fMRI, and must be dealt with accordingly. In bulk motion, the whole head moves, which can be compensated by registration against a reference image. The reference image is in turn aligned with the anatomical MPRAGE, in turn normalized to a standard space image, which provides a template for locating group differences, We use the commonly employed Montreal Neurological Institute (MNI) normalized space, based on hundreds of normal brains[27]

Motion can lead to artifactual activation near the edges of the gray matter area that is imaged, due to the sudden intensity increase caused by overlapping shifted voxels. The MRI signal can also be disrupted by protons moved into a voxel from a neighboring slice. This so-called spin-history effect can cause large intensity shifts a slice or set of slices (also giving rise to the banding artifact in Fig. 4).

Bulk motion is corrected for using a rigid transform with six degrees of freedom corresponding to rotation and translation. Here we have an important quality assurance checkpoint and we apply a relatively strict exclusion threshold for a maximum translation/rotation of 1 mm/1 degree.

Before functional connectivity analysis is performed, a spatial *smoothing* with a Gaussian of FWHM of 6 mm is performed. This is mainly done to reduce noise, but some statistical analyses such as Gaussian random field theory, require a certain degree of smoothness to be valid.

The high-resolution anatomical image is segmented and combined with tissue prior probability maps, to obtain masks for white/gray matter and CSF. These are needed to extract the the gray matter signal which best reflects neuronal activity. Severely atrophied brains with structural deviations cannot always be included in the functional connectivity analysis, because their geometries deviate to the degree that the segmentation algorithm fails (for this purpose we use SPM 8). These subjects have therefore been excluded.

After discrimination against excessive motion and mask size deviations, 70 MCIs are removed and we are left with MCI 130 subjects. Similarly, after QA, we have 126 healthy controls.

Equipped with motion correction data and the various masks, we are ready to extract the gray matter signal. For this purpose, we use the CONN toolbox [28]. The voxel-wise gray matter time-courses are obtained by solving a GLM, that includes regressors for gray/white matter, CSF and the motion parameters, assuming that the primary contribution to the signal comes from linear composition of a distinct set of sources. In order to proceed with the functional connectivity extraction, me must now define our regions of interest, which is the subject of the next section.

5 Functional connectivity extraction

5.1 Parcellation strategies

A network consists of N nodes or ROIs with $N(N-1)/2$ connections. The connections themselves represent correlation between the average voxel time-series of each region. The simple question: "Why not use voxel data?", has an equally simple answer: "Because we cannot.". Firstly, the calculation of the network would simply take to long to be feasible when dealing with hundreds of subjects. Secondly, using a relatively low resolution of a quarter million voxels, the network size requires a few hundred megabytes and the size of the data cache would be enormous with prohibitively large transport times. Thirdly, results are more susceptible to noise effects, although these could be adequately dealt with by clustering algorithms. In fact, deriving ROI sets from resting state voxel data is to be preferred to coarse anatomical schemes. In our analysis, we make use of a set of functionally homogeneous ROIs derived by Craddock et al (see below) [20].

For many years, most FC analysis were based on a low-resolution anatomically derived set of ROIs. A common choice was the atlas created by Tzourio-Mazoyer et al. [21]. This ROI-set is created by means of an Automated Anatomical Labeling (AAL) procedure, wherein anatomical parcellation of a single-subject, normalized, high-resolution T1 image from the Montreal Neurological Institute (MNI) was performed. By delineating sulci to define landmarks, 45 ROIs in each hemisphere were then defined by manual drawing.

The anatomical atlas has several severe limitations, making it ill suited for use with RS fMRI. Firstly, the resolution is far too low to detect pathological changes between normal controls and MCI subjects. This limitation means that a very well defined and strong contrast has to be present in order to detect differences. Secondly, it is anatomically derived rather than functionally. Any ROI-set aimed at pinpointing differences in RS fMRI patterns should delineate functional subunits, which are hardly captured by the coarse AAL partitions. One is left with two main choices: 1) subdivide the AAL atlas (or similar) into a given number of subunits which hopefully contain the sought functional subunits, or 2) use real voxel-resolution RS data from healthy brains with normal function to derive a set that on average will capture the functional subunits.

Such a method has been devised by Craddock et al. [20] and since our analysis crucially depend the chosen ROI sets, we give a brief description of their construction here.

Craddock et al. motivate their approach by listing several key observations. Clearly, functionally homogeneous regions are extremely advantageous in whole-brain FC analyses and this objective is clouded by: the experimental bias of manually drawn ROIs (or even the selection of a small subset), the mismatch between the brains anatomical macro-structure and its functional architecture, and the smoothing of detail that comes with clustering methods that look for functional networks such as Independent Component Analysis (ICA).

Construction of functionally homogeneous ROIs proceeds by spatially constrained spectral clustering of whole-brain RS fMRI 4x4x4 voxel data from 41 healthy subjects with mean age 29. In other respects the RS FC extraction is very similar to ours, e.g. the regressing out of motion, white matter and CSF signals, and bandpass filtering below 0.08 Hz[6].

The model is based on the very effective so-called NCUT spectral clustering algorithm, which is particularly robust against outliers and can easily incorporate constraints [29]. The voxel data can considered as similarity graph, where weights connecting the nodes (voxels) represent some measure of similarity. Each voxel constitutes one node in the network and spatial coherence is maintained by restricting connections for each voxel to a local neighborhood. The graph is cut into a given number of clusters while seeking to maximize intra- and minimize intercluster similarity, adding a normalization to balance cluster size. This is the problem of graph cuts. Every time the graph is cut, a cost is incurred equal to the sum of cut connection weights. Cutting a given graph G defined by a connection matrix with similarities w_{ij} connecting node i and j, into subgraphs A and B is given by

$$cut(A, B) = \sum_{i \in A, j \in B} w_{ij}. \tag{1}$$

To avoid catastrophic shrinkage to a single voxel, a normalization factor is introduced,

$$N_{cut}(A, B) = \frac{cut(A, B)}{\sum_{i \in A, n \in G} w_{in} + \sum_{i \in B, n \in G} w_{jn}}, \tag{2}$$

where n runs over all nodes in the graph. Now we do not only minimize the cutting cost, but also maximize the within-cluster similarity. The normalization inflates the clusters by simultaneously increasing the within-cluster w_{ij}, but may introduce some bias toward equal sizes.

Two measures of similarity are evaluated in Ref. [20]: a suprathreshold applied to Pearson correlation between voxel time-series $r_t > 0.5$, and the same threshold applied to FC maps (themselves consisting of correlation) belonging to a node $r_s > 0.5$[7].

Reproducibility is then evaluated by comparing the results for a single subject to that of the result of the whole group with that particular individual excluded (this can be done for example with a measure such as the variation of information or the Dice coefficient). In addition the resulting homogeneity of the clusters is evaluated and the accuracy of reproducing default mode networks between various anatomical atlases and the functionally derived ROI-sets.

Each individual is clustered, where after corresponding binary affinity networks (weights are either one or zero) are averaged and clustering is reapplied to the resulting matrix.

The conclusions of the work can be summarized as: r_t produces the best reproducibility, cluster homogeneity improves as the number of clusters increase at the expense of reproducibility. Comparing with the atlases, the clustering method gives superior representation of voxel data for more than one-hundred ROIs. This behavior is consistent with resolution being the crucial factor and one may indeed obtain good results with random, equally sized partitions [30]. In general, anatomical atlases perform better for motor and visual networks than for DMN.

In this work we evaluate the AAL atlas with 90 ROIs and ROI-sets optimized for functional homogeneity of various sizes, generated by Craddock et al. prioritizing reproducibility with r_t.

What is the downside of this seemingly ideal approach to ROI-selection? Apart from the increased noise level, a large number of functionally derived ROIs reduces tractability and labeling becomes increasingly problematic. Technically, we mitigate this problem by assigning each ROI a label composed of the largest overlapping anatomical AAL regions and their associated volume percentage. Simplifying further still, in figures with labels to follow below, the AAL regions are computed and overlaid using a labeling algorithm taking the given imaging viewpoint into account [31].

[6] We could also have derived ROI sets ourselves for our healthy age-matched subjects, but since biomarker data is currently not available for these, we have instead chosen a ROIs set derived from halt young subjects.

[7] We may imagine sitting on each voxel and seeing a certain distribution of intensities generated by other voxels within our range of vision. The algorithm works by grouping voxels with similar viewpoints within a common radius.

5.2 Connectivity measures

The choice of functional connection strength lies at the very core of the FC analysis, completely defining the network and its properties. It is generally unclear what the optimal choice is and the answer depends on the hypothesis to be tested and its related contrast.

Pearson correlation is the most common choice for connectivity measure, perhaps due to the strong contrasts it produces. In addition, there is only so much you can do with the poor time-resolution of most RS fMRI data. Using a state-of-the-art multiband EPI sequence the time-resolution can be pressed down to an impressive few hundred milliseconds. The high frequency information contains potentially valuable information[32], but can only be accessed by recording physiological data during acquisition, for subsequent regression of the unwanted signal[33].

Other measures are mutual information (representation independent similarity measure based on relative occurrence), coherency[34] (coupling of the signals frequency spectra), partial correlation (correlation between two regions residues after linear regression with controlling variables), mean phase coherence (see below) and synchronization likelihood (see below).

In this work, we have chosen a basic, simple and powerful measure of connection strength, correlation, reflecting linear dependencies between regions. This power to detect weak contrasts is not without its price. Correlation comes with some major drawbacks, many of which have become apparent during the course of this work. Correlation analysis is however perfectly doable, as long as you are aware of these pitfalls, This situation is precarious when attempting to identify progression patterns.

The pitfalls will be outlined in great detail below, but consists mainly of the following two points. Firstly, the presence of negative coupling strength (negative correlation) causes breakdown of the graph theoretical formalism used to characterize of network topology. Common practice is to cut negative values (which are in minority) or binarize the connection matrix by a more or less arbitrary threshold. However, the negative correlations appear to play an important role, signaling a reduced connectivity in the form of an increased lag between regions. This effect becomes apparent in the latter stages of disease progression.

In addition, correlation has a worrisome blind spot. The measure erroneously equates the following two situations: two periodic time-series of identical shape but a relative shift of a quarter period, and two completely random signals. Both situations result in correlation zero. There is a subset of links in a normally functioning brain, that come with an intrinsic approximate phase shift of a quarter period[8]. Complete functional breakdown of these links, can therefore not be directly detected,

There are other connectivity measures which do not suffer from the maladies of correlation. A subvariety of generalized synchronization, called synchronization likelihood (SL), is by construction a probability in the interval $[0, 1]$. SL reconstructs the dynamical attractors phase space via time-embedding vectors and Takens' theorem [35, 36, 37]. Time-embedding simply means that we cut out segments (or vectors) of the complete time-series. For region k at the discrete time-step i, the vector is

$$X_{k,i} = (x_{k,i}, x_{k,i+1}, ..., x_{k,i+m-1}) \tag{3}$$

where m is the so-called embedding dimension, defining the length of our time-series cut-outs. These segments are then compared *within* the same time-series using some similarity metric, for example the Euclidean distance. When *two different time-series* have internal recurrence at the *same two time-points*, likelihood of synchronization increases.

SL starts by considering the approximation to the correlation integral in chaos theory, which measures the mean probability that two states at different times (i.e. our vectors) are the same, and is used to extract a critical distance for each region. This critical distance is chosen to ensure that a specified fraction p of the time-embedded vectors (time-series cut-outs) are considered as recurrences.

$$p = \frac{1}{(N-w+1)(N-w)/2} \sum_{i,j=1}^{N} \Theta(j-(i+w-1))\Theta(\epsilon_k - |X_{k,i} - X_{k,j}|), \tag{4}$$

where we have N time-embedding vectors, w is a time-window reducing autocorrelation effects, Θ is the Heaviside function and ϵ_k is the critical distance for region k that produces (say) $p = 0.05$. Equipped with the various ϵ, we can now define the synchronization likelihood between two regions k and l as simultaneous recurrences within the two series, as specified by the associated critical distance,

$$S_{kl} = \frac{1}{p} \frac{1}{(N-w+1)(N-w)/2} \sum_{i,j=1}^{N} \Theta(j-(i+w-1))\Theta(\epsilon_k - |X_{k,i} - X_{k,j}|)\Theta(\epsilon_l - |X_{l,i} - X_{l,j}|). \tag{5}$$

[8]The natural phase-shift is related to the physical distance between regions, but this may not be the whole truth and it would be best to consider it as a more abstract functional distance.

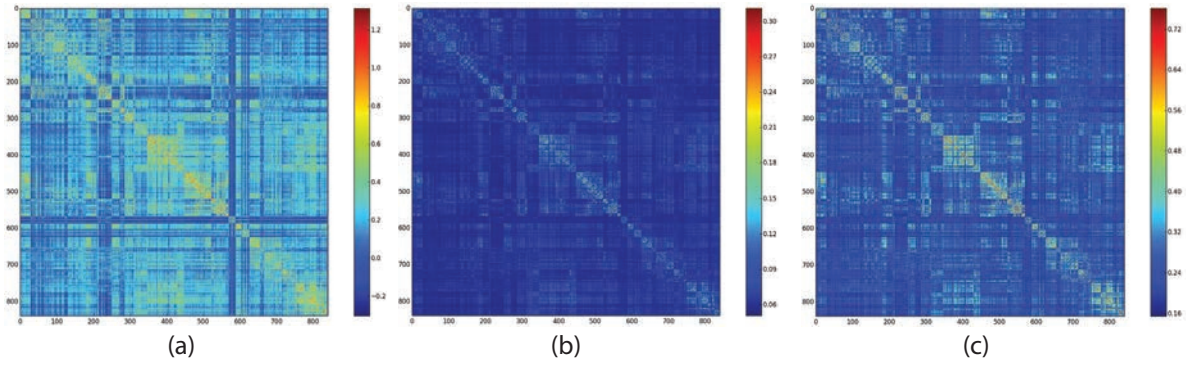

Figure 5: Different measures of functional connectivity. The panels show the 840x840 mean subject connectivity matrix for healthy controls: (a) correlation (Fisher-Z transformed), (b) synchronization likelihood, and (c) mean phase coherence.

Therefore, the measure can detect non-linear relationships, i.e. the two different regions do not have to execute the exact same sequence, as long as they repeat their region-specific patterns at same points in time. [9]

Another measure of great interest in this context is based on the phenomenon of phase-locking. Phase locking is a fundamental property of many dynamic, non-linear systems, frequently occurring in nature, for example in the synchronization of firefly flashes.

The abysmally poor time-resolution of RS fMRI is made even worse by further bandpass filtering away physiological noise. In addition, there can be individual variations in hemodynamic response, making comparison even more susceptible to this intrinsic noise. However, the relative phase could still remain relatively robust across individuals.

The instantaneous phase of a signal is elegantly calculated by first rendering the signal in its so-called analytic representation. This is conveniently done via a Hilbert transform, where after the instantaneous phase angle can be easily extracted [38],

$$\phi_{k,i} = \arctan(\frac{\mathcal{H}(x_{k,i})}{x_{k,i}}), \tag{6}$$

where $\mathcal{H}$ is the Hilbert transformation acting on time-series x_k of region k with discrete time index i[10]. An index characterizing phase-locking probability between regions k and l can now be computed as:

$$\Phi_{kl} = \sqrt{\langle \cos(\Delta\phi) \rangle^2 + \langle \sin(\Delta\phi) \rangle^2} \tag{7}$$

where $\Delta\phi = \phi_k - \phi_l$ and the brackets indicate temporal average.

Both phase index and SL originate in EEG analysis, where the time-resolution is in milliseconds, but the spatial resolution is limited. EEG and fMRI can be used in conjunction in attempts to amend their respective shortcomings.

Although beyond the scope of the present paper, synchronization likelihood and phase coherency are important candidates for measures that could allow pinpointing progression patterns. A comparative plot of the 840x840 mean connection matrix (for 840 regional time-series of spontaneous gray matter oxygenation) for healthy controls is shown in Fig. 5. The measures of phase coherence and synchronization likelihood are more conservative than correlation and give a smaller amount significant differences, but are on the other hand perhaps less sensitive to the noise present in our RS fMRI data.

Furthermore, it is important to note that the presence of high correlation or indeed phase coherence does not necessarily imply a direct functional link between the two areas. In this sense, synchronization likelihood is a better measure of functional connection, with its ability to capture non-linear relations. As such, it measures probability of connectivity, regardless of the local shape or representation of the neuronal/BOLD signal.

[9] The value of non-linearity is perhaps greater when analyzing EEG with a superior time-resolution, than RS fMRI data.
[10] Note that we should extend the arctan function to the range $[-\pi, \pi]$ by respecting the complex plane quadrant.

5.3 Statistical analysis and multiple comparison error control

There are many ways elucidate hypothesized group differences by means of statistical analysis. Perhaps the simplest approach is to perform Students' t-test on all connection weights (correlations) in the network and then some form of generic multiple comparison correction such as the Benjamini-Hochberg method [39].

The multiple comparison problem can easily get out of hand when mass-univariate testing of some 350 000 links, reducing the number of corrected significant links to zero. Using the most conservative correction methods (such as Bonferroni where one simply multiplies the p-values by the number of tests) this is almost certainly the case. T-tests are only valid for normal distributions when in general we have a mixed set of distributions.

There are then non-parametric tests, such as the Mann-Whitney U-test, but these are of a more conservative nature and not always suitable for weak group contrasts. A convenient solution is the non-parametric permutation tests, in which one generates the empirical null distribution by creating random groups (of the same sizes as the original groups) [40, 41]. In terms of how conservative the results are, permutation tests generally fall somewhere between t-tests and Mann-Whitney U tests.

Permutation testing can be computationally expensive and a simple t-test serves as a good indicator of what to expect after permutation convergence (somewhat overestimated). In this paper, we present permutation tests of two kinds: 1) testing for individual links, and 2) search for connected components comprising links above a given significance threshold. The two methods are described in the subsections to follow.

Due to the computationally demanding nature of permutation testing and the resources at hand during the course of this work, link-testing was limited to 10000 permutations. Although the number of permutations needed varies with group, calculations since then has shown this is in general not enough to ensure convergence. However, the component search converges quickly and is in very good correspondence with the link tests. It is however important to underline that the individual link tests in some cases correspond to a higher type I error than reported below. The component search method has been constructed precisely to fill the need of a less conservative method.

5.3.1 False Discovery Rate

The permutation testing at individual link level is performed by first pooling the data for the two groups under consideration, and then create two new, random groups of the same sizes as the original groups [40]. The null hypothesis asserts that the group labels are exchangeable under the constraints this randomization scheme (i.e. given group sizes). The test statistic (for example in our case the difference in mean value) is then stored in a null distribution, specific to each link. Two new groups are then generated and the procedure repeated until the null distribution has stabilized along with any p-values derived from it. The two-tailed p-value of the link in question is computed as the fraction of the absolute of the null distribution that is greater than the test-statistic for the originally postulated groups. This is the reason why permutation testing is so expensive. Generating completely random groups in a Monte Carlo fashion, it takes a long time to calculate the crucial tail of the distributions.

The problem of performing several hundred thousands of tests is that you will get a number of false positives by virtue of the sheer number of tests. This False Discovery Rate (FDR) has to be controlled, for which a number of methods exist. We use a popular method of intermediate conservativeness known as the Benjamini-Hochberg control of FDR [39] It is also possible to perform the multiple comparison correction at once in the permutation testing scheme. One would then pool all link distributions, and create a maximal test-statistic distribution against which all link differences in the postulated groups are gauged [40]. This scheme is not suitable for the RS fMRI data and is far too conservative to be of any use. It gives strong control over experiment-wise type I error [42].

The Benjamini-Hochberg procedure controls FDR and the family-wise error rate in the weak sense. We use a step-up procedure that controls the FDR at level α. The procedure begins by sorting all the uncorrected p-values in ascending order, creating an array p_i where i refers to the link number $i = 1, ..., N_l$. We then locate the largest element in the sorted array that satisfies

$$p_i = \frac{i}{N_l}\alpha, \tag{8}$$

Call this index i_{max}. Significance is now declared for all $i = 1, ..., i_{max}$. What we are in fact doing, is to divide all uncorrected p-values by a constant i_{max}/N_l that becomes large when the relative proportion of low-lying p-values grows.

The point of this procedure is to adjust the type I/II error balance in accordance with the distribution of significances found. For instance, if all p-values are already close to unity, except for a handful of them, then a false positive is disastrous. If we find tens of thousands of low, uncorrected p-values, a false discovery is less disastrous.

The procedure considers all linktests to be independent, which is not really the case. A better way to handle the multiple comparison problem is to look for connected components of highly significant links and gauge their significance against a null-distribution of component sizes. This procedure is covered in the next subsection.

5.3.2 Network-Based Statistic (NBS)

Controlling the FDR and family-wise error rate in the weak sense, as outlined in the last subsection, is often too conservative. This situation is the starting point for Zalesky et al, who designed a less conservative method called Network Based Statistic (NBS) [41]. The procedure can be summarized in the following points:

- Select a suprathreshold t-statistic t_{sup} (in our case a the t-value from a t-test)
- Evaluate test statistic t for all links across our two postulated groups.
- Retain the set of links which satisfies $t > t_{sup}$ and seek connected components of links.
- Store the size of these components.
- Generate a null distribution of maximal component sizes by pooling the two groups and randomly assign new group labels, matching the original group sizes.
- Seek the largest component with $t > t_{sup}$ between the randomized groups and log its size in the null distribution.
- The p-value of the component found to differ between the original groups is the fraction of randomized null distribution sizes greater than the original component size.

Because we select only the largest components in the null distribution, multiple comparison has been controlled. The procedure generally converges p-values to three decimals within 10000 permutations. This number is generally much smaller than that required for link-testing convergence, although the algorithm seeking components increase the computational burden and memory requirements.

There are both advantages and drawbacks to this method. It comes with a greater power to detect weak contrasts and multiple comparison control is enforced within a generally low number of permutations. With the ability to identify failing network components, comes the failure in locating individual links. In fact, we cannot point finger at a given link in the significantly different component. We have by construction asked the question "What is the probability of finding a significantly different component this big for random groups of given sizes?". Generally this question leads to interesting answers.

There are two useful measures of component size: 1) the number of links (extent) 2) sum of the links' t-values (intensity). Intensity is suitable for stronger contrasts, whereas the extent has some added power. In this work, we only use intensity as a measure of component size.

Zalesky et al are careful to characterize the method as a complement to mass univariate link testing, as outlined in the previous subsection. One can also speculate that many neurological disorders lead to disrupted subnetworks and parts of these would be clearly visible as failing components. Note that all components presented in this paper constitute a connected set of links where healthy controls have higher correlation than MCI or AD. The method implicitly assigns significance to particular nodes with a large number of failing links, which on their own constitute a weak contrast. One node and many failing links is hardly a random pattern.

It is also necessary to select a suprathreshold, a procedure for which there is no rule. This is also a strength of the model, because exploring different values of supratheshold exposes the relative weakness of contrasts and the spatial spread of highly significant regions into weaker ones, hinting at common epicenters for dysfunction. This is a very useful feature when attempting to gauge relative contrast strength for different group comparisons.

6 Optimization of connectivity parameters

In the sections to follow, we will characterize differences in functional connectivity between biomarker cohorts and how these patterns evolve with disease progression. Summarizing the procedure leading up to this point, we quantify functional connectivity using correlations between BOLD time series of gray matter ROIs during resting state activity of the brain. We then form a functional network consisting of $N(N-1)/2$ links (correlation values) connecting the N specified ROIs. Significant group differences are determined by performing Student's t-test on each of the $N(N-1)/2$ network links across subjects, and subsequently apply a multiple comparison correction (FDR) with permutation testing [41, 43], which finally yields a corrected type-I error used to declare significance. The remaining set of links is the subject of below analysis, where we will also analyze the connected network components emerging from the NBS approach.

To begin with, we examine how differences between subgroups in biomarker space depend on the temporal and spatial scales chosen for the FC analysis. The temporal scale is set by the frequency band of the GM spontaneous oxygenation signal, a choice in theory limited by TR, but in practice by physiological noise and scanner drift. The spatial scale is set by the number, size and position of ROIs used in the analysis, i.e. essentially the resolution underlying the FC calculation. In theory, this choice is limited by the noise level, but in practice by computational resources.

The results of the frequency and ROI analysis will motivate our choice of parameters used in the calculation of significant differences between MCI subgroups, HC and AD. Although many patterns of significant FC differences will be shown in the subsections treating parameter optimization, these patterns and trends will not be fully addressed until subsection 7. We will, however, comment on FC frequency dependence and offer an interpretation in the light of disease progression.

Unfortunately, calculating the functional connectivity in all different frequency intervals and for many subjects was beyond the capability of available resources. At the time of writing, functional connectivity data in all frequency intervals was therefore only available for the MCI group and for a relatively low resolution ROI-set of 392 regions. This resolution is likely good enough, but crucial data in the form of connectivity for all frequencies for healthy controls was not available. The results below represent the best choice of frequency, based on the available data. Since then, examination of high-res data for $HC-MCI$ has shown that a highly sensitive interval is the all-encompassing interval $f = 0.01-0.1Hz$. [11]. However, the majority of significant differences encountered in 0.01-0.1 Hz are in fact coming from 0.03-0.06 Hz. In addition, the encompassing interval contains more noise, such as physiological and motion signal, and is probably more susceptible to artifacts.

6.1 Frequency dependence

Albeit an active area of research, consensus is currently that the spontaneous oxygenation signal measured in RS fMRI is related to neuronal activity. One might therefore conjecture that EEG studies of the frequency dependency in neuronal activity may have some bearing on the oxygenation oscillations. In this context, neuronal activity as measured by EEG reveals clusters of neurons in close proximity correlating at higher frequencies, whereas long distance correlations occur at lower frequencies [44].

There are various strategies for selecting the frequency interval of the spontaneous BOLD timeseries used for FC analysis. The simplest approach is to select a frequency interval that remains reasonably unaffected by physiological interference from breathing and heart beat [45]. In the same way, low frequency scanner drift can be eliminated by imposing a lower bound. This line of reasoning typically leads to selection of an interval $f = 0.01 - 0.1$ Hz.

Although this choice will likely reduce physiological noise, the higher frequencies could be accessed by recording the physiological data during image acquisition and subsequently regressing them out of signal [46, 45]. However, this procedure would require a short repetition time and a high time resolution [46], necessitating state-of-the-art optimized sequences, such as multiband-EPI [25]. Since our sequence has $TR = 2000$ ms, the highest frequency available is 0.5 Hz - not likely to be sufficient even if physiological data were available.

In addition, band pass filtering induces some correlations, but CONN accounts for this effect by correcting the number of degrees of freedom [47].

The pragmatic approach is to select the interval most sensitive to the pathology of interest [48, 30, 49]. Focusing on the lower frequencies below 0.1 Hz in order to avoid physiological noise, we may further band

[11] The new data represent a larger set of subjects with different QA protocols and segmentation routines - results cannot be combined with the data of this thesis.

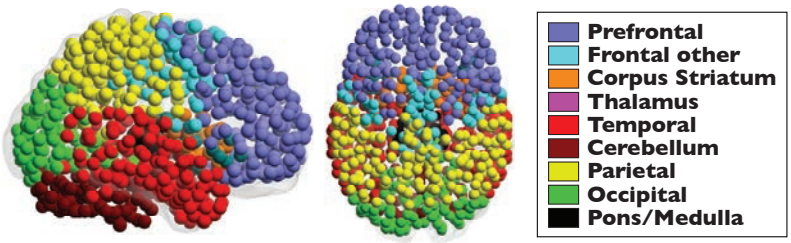

Figure 6: Coloring scheme by lobe. Illustration is of 840 node ROI-set.

pass filter the signal and look for an optimal subinterval, with regard to some distinguishing feature in the resulting FC or graph theoretical measure.

Supekar et al. select the interval that corresponds to the greatest clustering coefficients[12] in binarized FC matrices, for both HC and AD: $f = 0.01 - 0.05$ Hz [48]. Wang et al. chose the frequency interval that produced significantly lower mean wavelet correlation and higher proportion of short-range connections (< 45 mm) in amnestic MCI relative HC: $f = 0.031 - 0.063$ Hz [30]. The most sensitive frequency interval may vary with neurological affliction. Schizophrenia, for example, appears to contrast HC in a relatively high frequency interval compared to MCI and AD: $f = 0.06 - 0.125$ Hz [49, 50].

Given the hypothesis of correspondence between EEG and RS fMRI frequencies, the interval most sensitive to differences between say MCI and HC, becomes a reflection of the most salient spatial range of communication breakdown (we will explore this dependence further in subsection 7).

In order to assess frequency dependence we calculate FC in the ranges 0.01-0.1, 0.01-0.03, 0.03-0.06 and 0.06-0.10 Hz. For the purposes of identifying the most optimal interval, we select a reasonably high resolution set of 392 ROIs[13], extracted by spectral clustering and optimized for functional homogeneity [20] (see subsection 5.1 for details). We seek the interval which maximizes the number of significant differences between important MCI groups, where in general the contrasts are relatively weak. The two MCI partitions employed in the analysis of frequency-dependent differences are (see Fig. 1 (a) and (b)):

1. Effect of $a\beta$-pathology (group M_0 vs. $M_{a\beta}$):
   (a) $a\beta > 550$, $p\tau < 80$ ng/l (70 subjects),
   (b) $a\beta < 550$, $p\tau < 80$ ng/l (42 subjects),
2. Effect of τ-pathology, (group $M_{a\beta}$ vs. $M_{p\tau}$)
   (a) $a\beta < 550$, $p\tau < 80$ ng/l (42 subjects),
   (b) $a\beta < 550$, $p\tau > 80$ ng/l (18 subjects),

referred to as the $a\beta$- and $p\tau$-partition, respectively.

The FDR-corrected type I error is set to $\alpha = 0.01$ and we seek significant differences between the partition subgroups. The number of significantly different FC-links (a.k.a. edges) and number of linked-up ROIs (a.k.a. nodes), as well as their relative numbers, will be used in gauging the relevance of intervals. In addition, we look at the mean FC of groups and the total FC of significantly different sets of links. Each node is colored by lobe according to color coding scheme displayed in Fig. 6.

Fig. 7 (a) and (b-c) show emerging FC differences as a function of frequency interval for the $p\tau$- and $a\beta$-partition, respectively. In these figures, the size of the spheres (centered on a given ROI and colored by lobe) corresponds to what is known as nodal degree in graph theoretical parlance: the number of links connecting to a given node[14].

Using a familiar train of thought from statistical threshold mapping, having a large number of links with small number of nodes would amount to highly significant patterns. We may therefore naively seek a large quota $Edges/Nodes$, i.e. the number of significantly different links over the number of ROIs involved.

[12]The clustering coefficient is higher in optimally organized networks which exhibit modularized processing. These modules is then further connected on a global scale.

[13]As is shown below, high resolution ROI parcellations is essential to successful identification of biomarker phenotype by FC pattern. However, 392 ROIs is sufficient for the purposes of identifying the frequency intervals of interest.

[14]Note that the sphere size is scaled according each graphs data. If the graph is considered without inspecting the link density, the sphere size may be misleading when comparing different graphs.

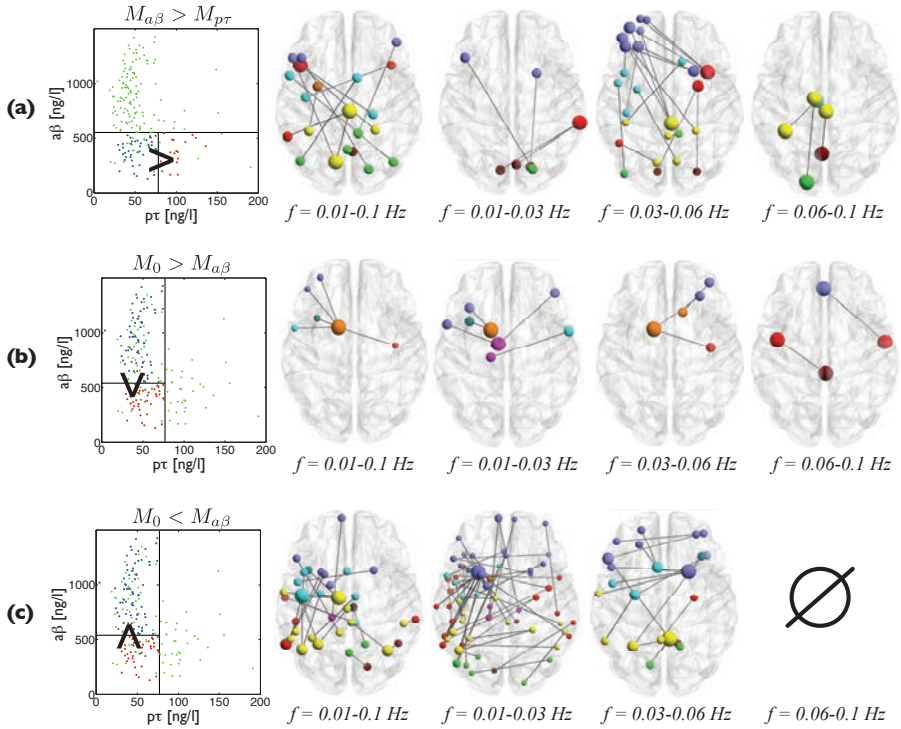

Figure 7: FC frequency dependence for $p\tau$- and $a\beta$-partition in (a) and (b-c) respectively. The connectivity graphs show links that are significantly greater or smaller (sign is indicated by $>$ or $<$ placed on interface between compared areas in biomarker space). For the $p\tau$-partition only $M_{a\beta} > M_{p\tau}$ FC is present.

Table 2: $M_{a\beta} > M_{p\tau}$ edges and nodes.

Frequency band [Hz]	Edges	Nodes	Edges/Nodes
0.01-0.10	12	21	0.57
0.01-0.03	4	7	0.57
0.03-0.06	18	26	0.69
0.06-0.10	3	6	0.50

Table 3: $M_0 < M_{a\beta}$ edges and nodes.

Frequency band [Hz]	Edges	Nodes	Edges/Nodes
0.01-0.10	23	38	0.61
0.01-0.03	49	64	0.77
0.03-0.06	15	22	0.68
0.06-0.10	∅	∅	∅

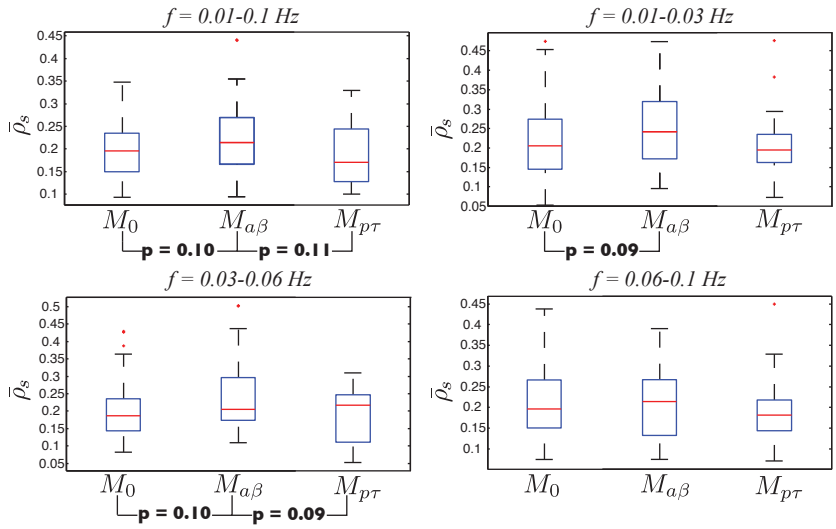

Figure 8: Box-plots of subjects mean FC for the biomarker subgroups. Despite poor significance, a trend towards reduced FC with $p\tau$ and increased FC with $a\beta$ is visible across the MCI groups. P-values result from a two tailed t-test.

For the $p\tau$-partition, the emerging interval of interest from this procedure is $f = 0.03 - 0.06$ Hz. Visually, the cluster of nodes in the left frontal lobe adds to this conclusion (see 7 (a)).

Turning to the $a\beta$-partition (see Fig. 7 (b)), we see that as $a\beta$ drops, FC decreases in a very small group of nodes connected to the same central node in corpus striatum. The group is so small however, that the quota loses meaning, and the intervals $f = 0.01 - 0.1$ Hz and $f = 0.03 - 0.06$ Hz basically perform equally well, whereas $f = 0.06 - 0.10$ Hz yields only two links.

As seen in Fig. 7 (c), the major effect of lower $a\beta$ appears to be an increased connectivity with many significant differences for $M_0 < M_{a\beta}$. Even though $f = 0.03 - 0.06$ Hz performs well, $f = 0.01 - 0.03$ Hz yields a larger number of significant differences while maintaining a low number of nodes, and we note a trend towards cluster formation in the left hemisphere. Increased FC also appears in $f = 0.03 - 0.06$ Hz implying either 1) compensatory effect in response to the oxidative stress caused by increased amyloid burden, 2) a reflection of the multitude of MCIs in M_0 relative $M_{a\beta}$.

The trends across $a\beta-$ and $p\tau$-partitions hints at a potential FC progression pattern involving a slowing down of oscillations (shift to lower frequencies) and a compensatory mechanism in response high amyloid burden. The compensatory effect may really stem from an inhomogeneous M_0.

Fig. 8 shows box-plots of the subjects mean FC (Fisher transformed correlation between regional time series),

$$\overline{\rho}_s = \frac{1}{N(N-1)/2} \sum_{i=1}^{N(N-1)/2} \rho_{si} \tag{9}$$

where subject s belongs to group $s = M_0, M_{a\beta}, M_{p\tau}$ and the mean is over all links in the $N = 392$ node network.

With a caveat for very poor significance (as can be expected when forming mean of all network links), the aforementioned trends are surprisingly discernible given the relatively crude measure employed; the mean values reflect the set of the significantly different links in Fig. 7. We note in passing, that the mid-range ($f = 0.03 - 0.06$ Hz) and encompassing ($f = 0.01 - 0.1$ Hz) intervals have the lowest p-values, performing roughly equally well.

Discarding the vast majority of links, we now inspect total FC of subject s on the differing set of links for group g_1 and g_2,

$$\widetilde{\rho}_{g_1>g_2,s} = \sum_{i \in S_{g_1>g_2}} \rho_{si} \tag{10}$$

as is shown in Figs. 9. $S_{g_1>g_2}$ denotes the set of links where the FC of g_1 is significantly greater than g_2. In Fig. 9 all total FC between displayed subgroups are significantly different ($p < 0.001$), hinting at a crude classification parameter.

Referring to Fig. 9 (a), it can be seen that $f = 0.03 - 0.06$ Hz is performing very well, with an almost clean separation of $p\tau$-subgroups. Fig. 9 seems to indicate that all intervals except the highest one, do

roughly equally well in separating the $a\beta$-subgroups. However, the lowest interval results in by far the greatest difference between subgroup means, although this effect is accompanied by an increased spread.

In summary, it appears that the encompassing interval $f = 0.1 - 0.01$ Hz is able to pick up some differences seen more clearly in the subintervals, but the power to detect these contrasts is reduced. In addition, the main effects of $a\beta$- and $p\tau$-pathology appear to lodge in different intervals, implying a potential benefit of monitoring more than one interval.

Focusing on the subintervals, $f = 0.03 - 0.06$ Hz is the most sensitive to pathology overall, reflecting both reduction and enhancement of FC. This finding is consistent with previous results [48, 30].

We conclude that $f = 0.03 - 0.06$ Hz is a good choice of interval for detecting biomarker related differences in FC, with a an excellent separation of $p\tau$- and a good separation of $a\beta$- partition subgroups. It appears however, that the lowest subinterval $f = 0.01 - 0.03$ Hz is sensitive to the increase of FC with $a\beta$-level, and we keep an eye on this interval when analyzing the $a\beta$-partition.

6.2 ROI resolution dependence

In this subsection we analyze how significant FC differences depend on the choice of ROIs and the spatial resolution underlying the FC calculation. For this purpose, we select the appropriate frequency interval identified in the previous subsection, i.e. $f = 0.03 - 0.06$ Hz.

Resolution is the parameter expected to have the greatest influence on the FC analysis. Intuitively, it is not hard to understand why. Choosing large ROIs gives poor resolution, such as in the commonly applied AAL parcellation[21] based on anatomical landmarks. This will average the constituent time-series from several, functionally distinct volumes encompassed by the larger ROI, reducing power when testing for differences in correlation. On the other hand, choosing too small ROIs and high resolution can cause problems with noise.

Clearly, a desirable strategy would be to perform the FC analysis on a voxel-to-voxel basis for each subject. In a secondary stage, one could then proceed to identify functional centers and significant differences via statistical mapping. Such a procedure would be prohibitively computationally demanding when dealing with hundreds of subjects. To illustrate the problem, consider the preprocessed GM signal, comprising approximately 240000 voxel timeseries in our approach. The resulting single subject connectivity matrix would contain a staggering 29 billion links and require 115 Gb of storage in single precision floating point numbers.

A more feasible strategy along the same lines was proposed by Craddock et al. in Ref. [20], who used spectral clustering to extract a user-specified number of ROIs optimized for functional homogeneity (see subsection 5.1 for details). It should be noted that for a sufficiently large number of ROIs one can achieve good results even with randomly chosen, equal volume ROIs [20, 30], indicating that resolution is the crucial component. However, the functional parcellation algorithm should be capable of picking up more subtle nuances in the delineation of functional centers, providing a clear advantage, even though these centers are then averaged across many subjects to produce a functional atlas.

Here, we look at how FC differences evolve starting from the low resolution anatomical parcellation AAL [21] ($N = 90$), to functional parcellations of increasing resolution ($N = 180, 392, 840$) [20] (see Fig. 10), using the same two biomarker partitions as in the previous subsection. Since the contrast between the MCI groups is relatively weak, we will augment this study with ROI-dependent trends in MCI-HC differences.

Figs. 11 (a,b) and (c,d) show how the connectivity differences in the $p\tau$- and $a\beta$-partitions develop with increasing resolution. Not until $N = 392$ does a pattern of reduced FC emerge for $p\tau > 80$ relative $p\tau < 80$ [$M_{a\beta} > M_{p\tau}$, see Fig. 11 (a)]. This pattern is greatly reinforced and expanded when N is doubled.

Only for the highest resolution does a structure of enhanced FC ($M_{a\beta} > M_{p\tau}$) appear with links between MTL and corpus striatum [see Fig. 11 (b)]. The compensatory effect that did not appear for the $p\tau$-partition in the frequency analysis of the previous subsection, does in fact appear here at the highest resolution level, highlighting the relative weakness of $p\tau$-compensatory effects.

Similarly, for the $a\beta$-partition [see Fig. 11 (d)], the enhanced FC pattern begins to appear for $N = 392$ and is further developed at $N = 840$. In Fig. 11 (c)), we see hints of reduced connectivity starting at $N = 180$, but only at $N = 840$ does the pattern extend from the left Corpus Striatum.

The frequently used AAL parcellation yields only a single link for the $p\tau$- and none at all for the $a\beta$-partition. Such an overwhelmingly poor performance is a clear indicator that the coarse anatomical parcellation is unsuitable to detect weak contrast and can easily produce misleading results.

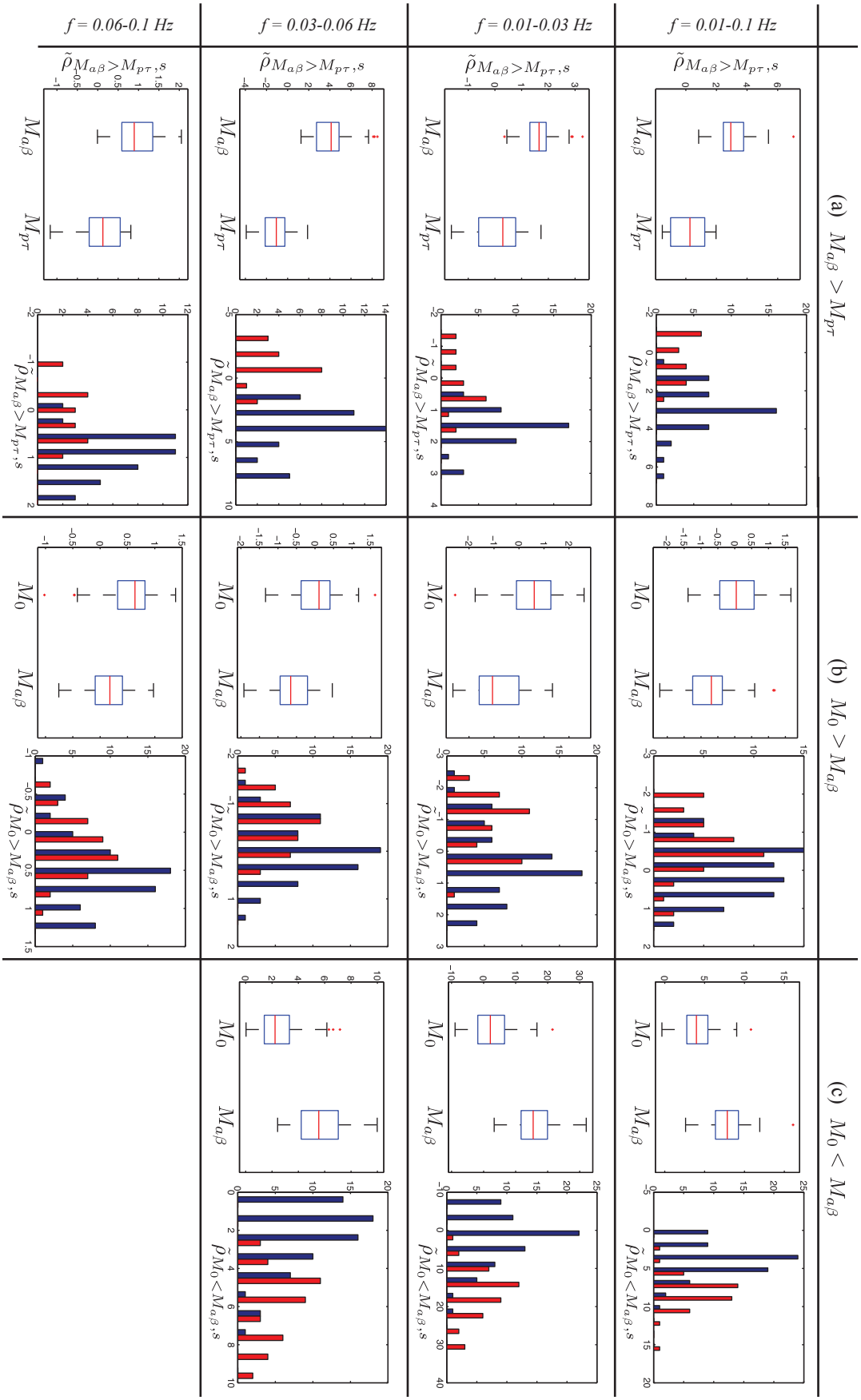

Figure 9: Total FC of $p\tau$ and $a\beta$-partition set of significantly different links corresponding to Fig. 7 (a-c).

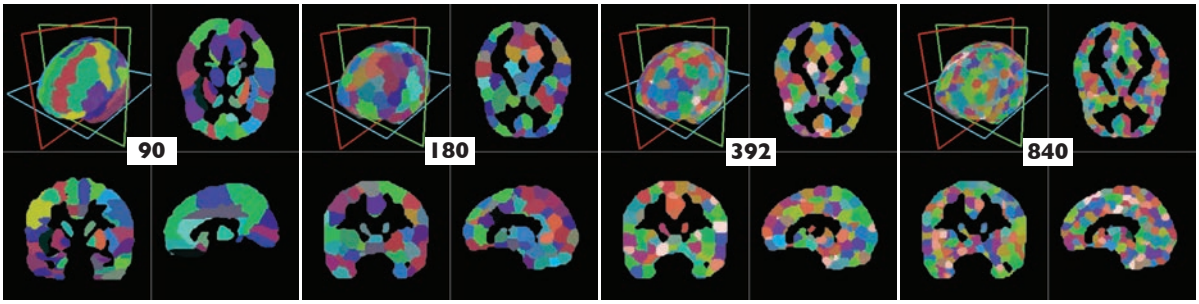

Figure 10: The four sets of ROIs evaluated: AAL [21] with $N = 90$ (excluding cerebellum for this anatomical set only) three ROI sets optimized for functionally homogeneity [20] with $N = 180, 392, 840$.

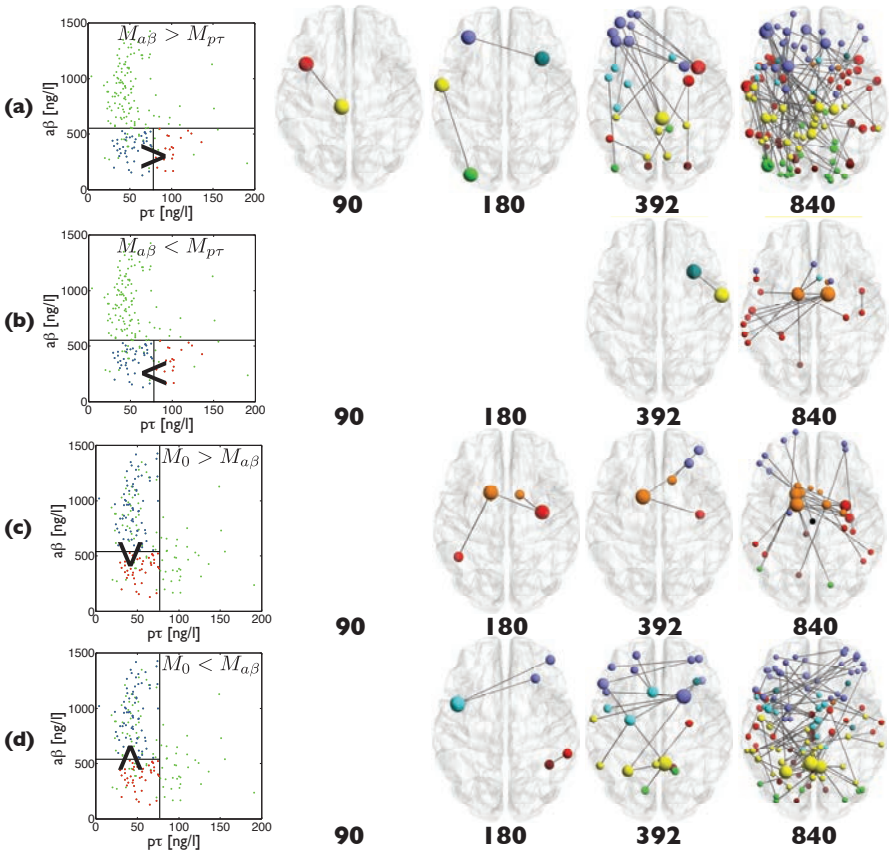

Figure 11: Significant FC differences as a function of ROI set for $p\tau$-partition (a-b) and $a\beta$-partition (c-d).

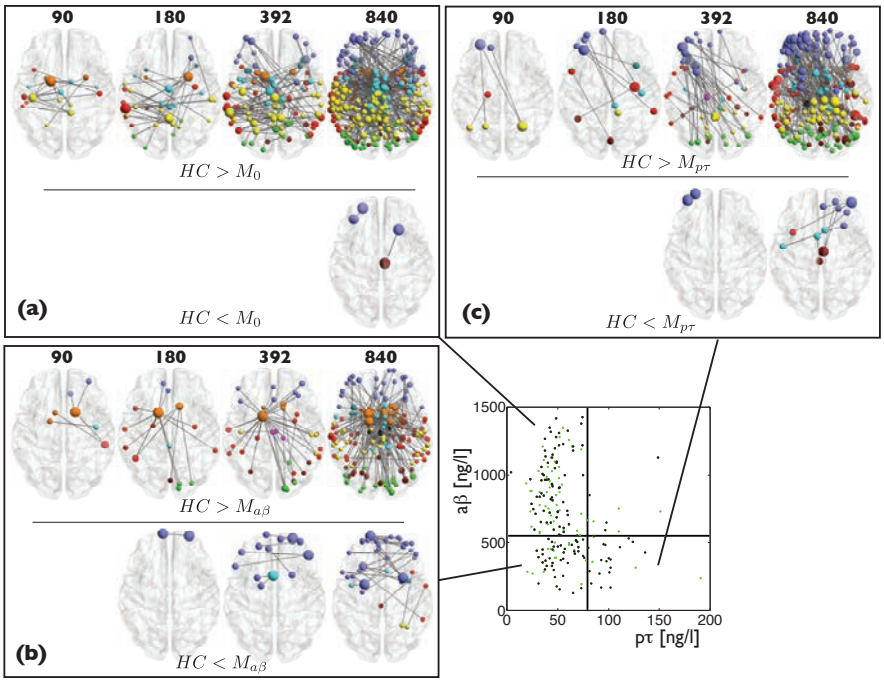

Figure 12: Significant HC-MCI FC differences as a function of ROI set.

With caveat for contamination in the HC group, the HC-MCI contrast should be greater than MCI-MCI and therefore we expect already the low resolution ROI sets to pick up differences. Fig. 12 shows the results of comparing HC to the MCI subgroups. Indeed, the low resolution ROI sets show traces of the patterns that grow stronger with N. Still, the highest resolution proves superior, and clearly does a better job at finding weaker contrasts [MCI > HC Fig. 12 (b,c)] . Relative MCI-MCI, HC-MCI develops more gradually, such that stronger contrasts can be accessed with low resolution ROI sets. This is a useful insight that allows us to also make use of the lower resolutions in providing a simplified overview, when needed.

As before, we can quantify the performance of the ROI-set by the number of significantly different edges, associated nodes, and *edges/nodes* (see Fig. 13), demonstrating the greater performance of the high resolution ROI-set. The figure also hints at the relative scale of group differences; comparing panels (b, d) to (a, c, e) in Fig. 13 and focusing on $N = 840$ we see that the HC-MCI contrast is indeed stronger than MCI-MCI.

Fig. 13 (a) and Fig. 12 (a) show a massive number links with reduced FC in M_0 relative HC. This pattern is fairly consistent at all resolutions, but peaks with some 400 edges and $edges/nodes = 1.31$ for $N = 840$, still corresponding to a small fraction of all possible connections: $\frac{400}{840(840-1)/2} \approx 0.1\%$. Such a large number of links in a supposedly early stage of dementia may seem surprising, but it should be remembered that M_0 is a fairly inhomogeneous group of MCI subjects. In addition, just looking at the number of links is misleading in this case, as it does not reflect the total FC reduction[15].

In Fig. 13 (b) the $M_0 > M_{a\beta}$ dominates (red curve); this is the strong compensatory effect previously noted. Moving on to panel (c) the $M_{a\beta} > M_{p\tau}$ is stronger, but the trend in (a) has been lessened by the compensatory effect visible in (b). In this context, we note some similarity between the corresponding patterns in Fig. 12 (b) and Fig. 11 (c), hinting that M_0 is closer to HC than $M_{a\beta}$.

As $p\tau$ increases (Fig. 13 (d)), FC again drops further with only a small compensatory effect. We note the similarity between Fig. 11 (a) and Fig. 12 (c) - the latter qualitatively similar but stronger than the former, hinting that $M_{a\beta}$ is closer to HC than $M_{p\tau}$.

All these observations points to a progression pattern related to biomarker levels involving different regions at different times. We will return to this progression pattern later on.

The NBS method looks for whole components and has the potential to find weaker contrasts with a greater number of connected links below a user-specified significance suprathreshold (see subsection 5.3). This procedure only works when there are connected components differing between groups, restricting results to HC-MCI.

[15] I.e. we have many, but small differences. This pattern will be further addressed below.

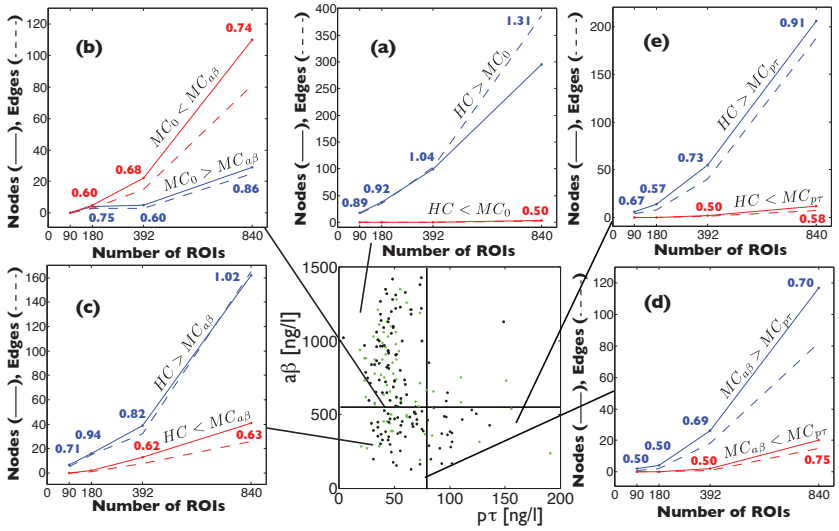

Figure 13: Nodes and edges as a function of ROI set. The dashed curves represent the number of significantly different edges and the associated nodes. Inset numbers by data points show *edges/nodes*. Note the inverted order of the curves in panel b, marking the compensatory effect.

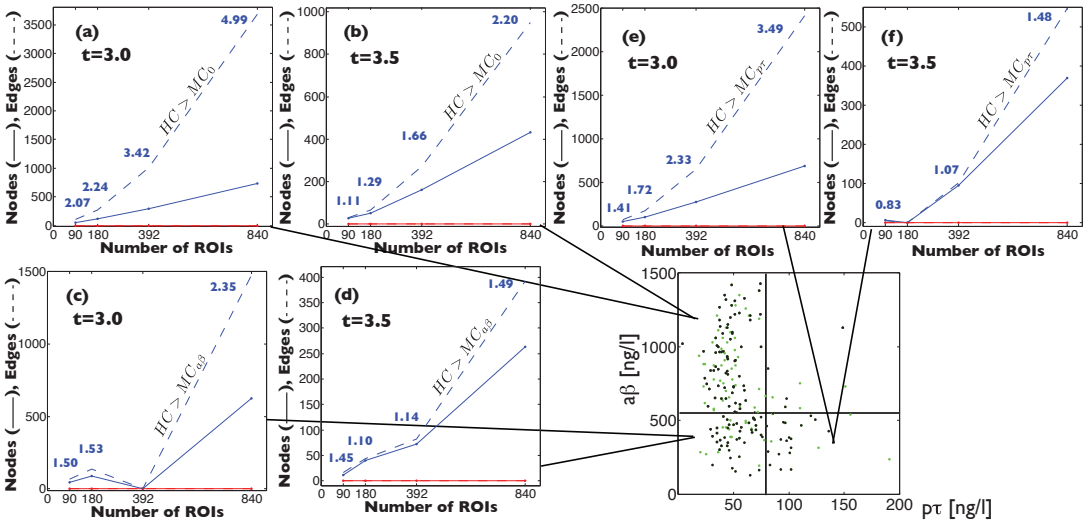

Figure 14: Nodes and edges of NBS components representing group differences between HC-MCI for suprathreshold values of $t = 3.0$ and $t = 3.5$. Only values with an associated inset *edges/nodes* value converged to a significant component.

Fig. 14 shows the nodes and edges as a function of N for the NBS components from HC-MCI testing. Qualitatively, the curves are similar to the ones in 13 but involving many more links. In addition the edge-to-node ratio is much greater, as expected from a clustering approach such as NBS. Note the absence of any compensatory components, which makes sense given that increased FC with disease progression probably represents isolated and sporadic attempts at restoring communication.

These network components are hard to visualize even though they constitute a small fraction of the total number of possible links (350000 for $N = 840$). However, the components can be useful in examining topological properties and graph theoretical measures that require richer statistics. Although our initial approach is to set the suprathreshold as high as possible in order to identify the most significant components, this threshold can be lowered further in order to facilitate comparisons and generate larger components.

Summarizing this subsection, high resolution is paramount to identifying contrasts between our cohorts, in particular for the weaker MCI-MCI contrast.

7 Connectivity

We are now in a position to fully address the differences in FC patterns that emerge when selecting temporal and spatial scales optimized to differentiate MCI groups, i.e. a frequency interval of $f = 0.03 - 0.06$ Hz and the highest spatial resolution with 840 ROIs optimized for functional homogeneity. In addition, we study the effect of lowered $a\beta$ in $f = 0.01 - 0.03$ Hz. HC-AD comparisons will only be included as parenthetical data, due to the small group size and poor statistics.

Fig. 15 shows how the MCI-MCI and HC-MCI significant FC differences vary across biomarker space. This figure will serve as a road-map along the progression that naively starts with a reduction in $a\beta$ and ends with an increase in $p\tau$. Although there appears to be a progression trend, consistent across MCI-MCI and HC-MCI patterns, we again underline the two important caveats: 1) it is important to remember that M_0 ($a\beta > 550$, $p\tau < 80$) is an inhomogeneous group of MCI, whose exact composition is unknown and 2) since biomarker data for HC is currently missing, some contamination from subjects with pathological biomarker levels cannot be excluded.

We begin by looking at the distribution of FC values and link-length dependence, and then proceed to analyze link patterns in more detail employing an important graph measure known as strength. At the end of this section, we will summarize our findings and compare with available literature.

7.1 Distance dependence

There are various definitions of the length of the links that connect the network nodes. The continuous connectivity value opens up for definitions of functional distance, but in this subsection we address the dependence of FC on physical Euclidean distance between ROI centeroids (nodes).

Fig. 16 shows some plots relevant to the distance dependence analysis, exemplified by properties of the 840×840 mean connectivity matrices of HC and M_0. In (a) the number of links binned by distance and FC are shown, and in the last column the M_0 histogram has been subtracted from that of controls (this operation is valid when the same binning is used in both plots).

We first note the general characteristics of FC-distance distributions: a sharp tail of short-distance, high-FC links, spreading into a majority pool centered around $FC \approx 0.2$ and $d \approx 8$ cm. Very long links cross over into negative correlations, hypothesized to represent long-range integration of distributed, modularized processing [51]. An increased shift towards negative correlations can also be interpreted as a pathological effect, representing a time-lag, possibly the effect of signal rewiring.

An area where HC has many more links than M_0 emerges close to the distribution centers at $d \approx 8$ cm in the upper range of connectivities. This area is accompanied by a corresponding increase in low-FC M_0-links, indicating the presence of a general downshift in connectivity. There appears to be no marked specific length scale of this downshift in M_0 connectivity; the affected links form a subset uniformly sampled from the full distribution of links. This is hardly surprising, given the inhomogeneous character of M_0.

Fig. 16 (b) shows the distribution of link-lengths for $N = 840$ and panel (c) the distribution of link-lengths in the $HC \neq M_0$ subset. Comparing them, we see reduced FC in M_0 at all length scales. This is consistent with the widespread pattern in Fig. 15 (a), likely representing several pathologies at once. As

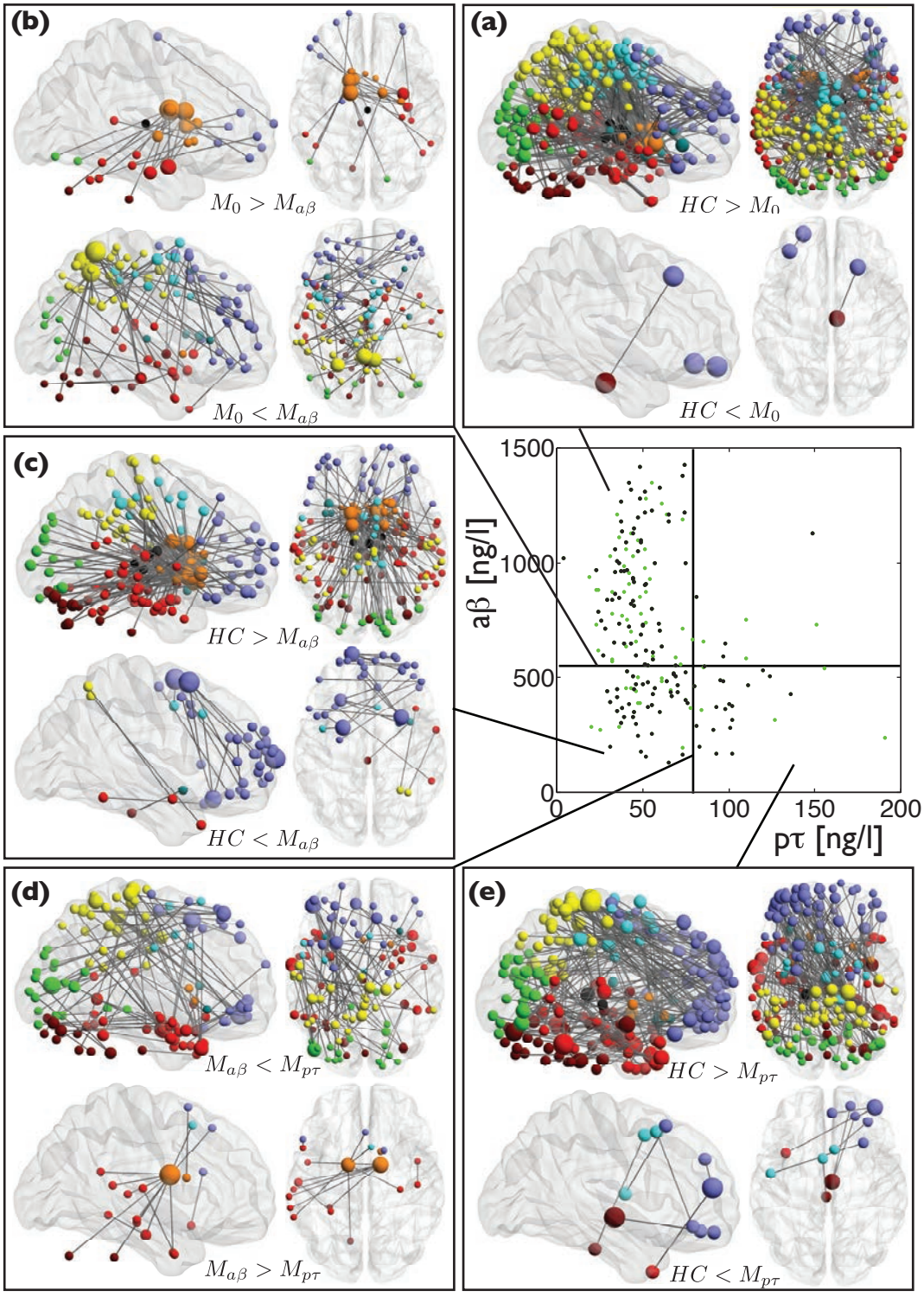

Figure 15: Significant FC differences between HC-MCI and MCI-MCI for $N = 840$ and $f = 0.03 - 0.06$ Hz. The same map for $N = 340$ can be found in appendix A.

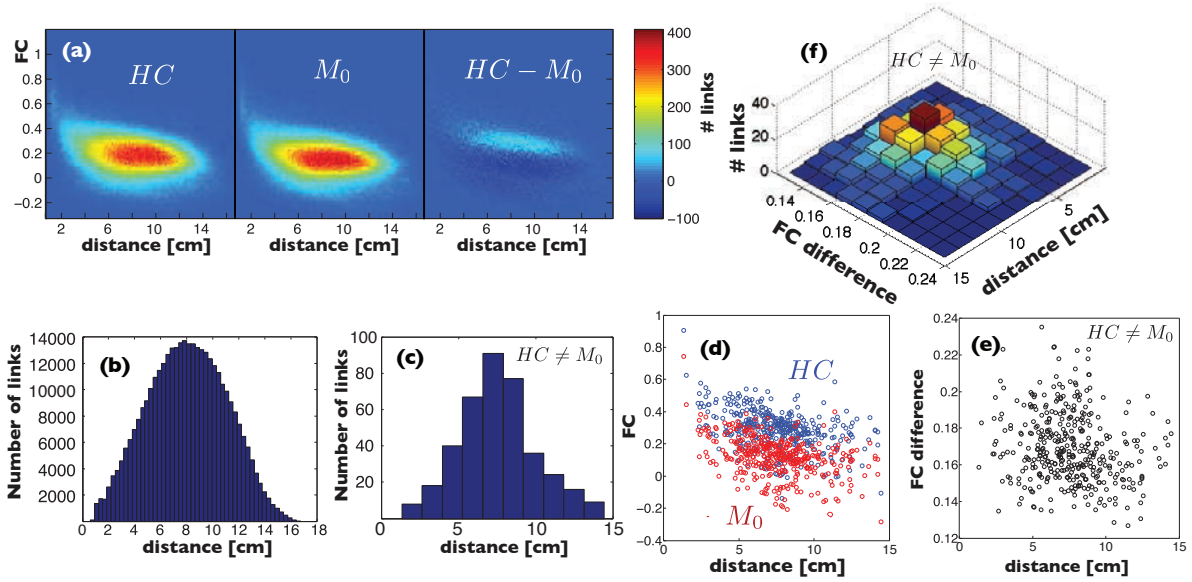

Figure 16: FC-distance plots. (a) shows histograms with links binned by FC and distance for the HC group mean (left) and M_0 (center) connectivity matrix, and finally the difference between these (right). In (b) and (c), the $N = 840$ and $HC \neq M_0$ link-length distributions are shown, respectively. (d) and (e) show corresponding FC-distance scatter-plots, and (f) the histogram of (e).

we will see below, despite a large number of widespread links, the pattern is associated with a relatively low reduction in M_0 subjects' mean FC.

Fig. 16 (d) shows scatter-plots of FC versus distance for HC and M_0 on the set of significantly different links, and panel (e) their FC difference versus distance. The latter is shown as a histogram in (f), where the majority FC reduction is seen to be centered on approximately $FC = 0.17$ and $d = 8$ cm. This distance coincides with the majority link length (see Fig. 16 b), consistent with a FC reduction on a subset of links roughly uniformly sampled from the full link set.

Similarly, we can examine distance dependence in the set of links separating MCI-MCI and HC-MCI groups for all biomarker partitions. Fig. 17 shows FC histograms and scatter-plots of significantly differing links (see Fig. 15), and Fig. 18 the physical length distribution of these links.

Turning to the $M_0 \to M_{a\beta}$ transition, there are similarities between $M_0 \neq M_{a\beta}$ and $HC \neq M_{a\beta}$ [cf. Fig. 17 (b,c) and (d,e) with FC patterns in Fig. 15], but also crucial differences. Comparing $M_0 > M_{a\beta}$ and $HC > M_{a\beta}$ we see that the pattern of reduced MCI-MCI indeed overlaps HC-MCI [Fig. 15 (b) and (c)], albeit with a weaker contrast, and the link distributions in Fig. 17 (b) form a subset of those in (d).

In the same way, the enhanced, compensatory FC patterns (i.e. $HC < M_0$ and $M_0 < M_{a\beta}$) have similarities, but now the MCI-MCI contrast that is stronger and more widespread. Enhanced FC ($M_0 < M_{a\beta}$) is found in interhemispherical frontal connections and for some temporal/frontal areas converging on the superior parietal lobe. Arguably easier to interpret (owing to the complex, heterogeneous character of M_0), $HC < M_{a\beta}$ has a small number of left-right links in the frontal area, albeit with much stronger presence in the anterior-most parts. This handful of short-ranged (< 5 cm) and unusually strong MCI connections stick out in Fig. 17. There are two reasons to be very careful with results from the front-most parts: 1) these are susceptible to motion artifacts due to large distance from pivot point, 2) susceptibility artifacts are strong in this region. Having said all that, the left right pattern seems to persist towards anterior parts.

According to amyloid levels, M_0 subjects are in an earlier stage than $M_{a\beta}$ subjects, hence the relative functional proximity to controls, resulting in $HC \neq M_{a\beta}$ patterns similar to $M_0 \neq M_{a\beta}$. As such, the M_0 subjects have a subjective diagnosis of MCI, but are unlikely to progress to AD within the foreseeable future.

One could also argue that the $M_0 < M_{a\beta}$ compensatory FC contrast is stronger than $HC < M_{a\beta}$ due to control contamination. However, if HC was greatly contaminated with low $a\beta$ subjects, then the $HC > M_{a\beta}$ pattern should also weaken, and not expand and strengthen as it clearly does. Rather, it is possible that the differences in contrast stem from the comparison of different MCI groups (e.g. vascular or Lewy body dementia) to MCI with low $a\beta$ (marking incipient AD). However, it is interesting to

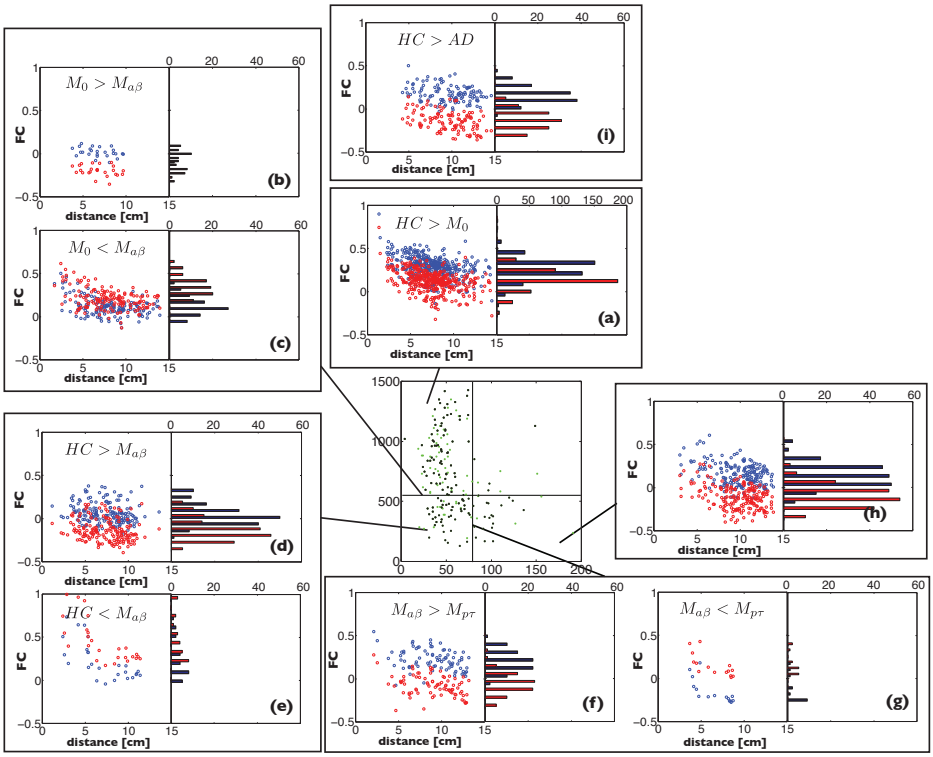

Figure 17: Distribution of FC values on the significantly different set of links (see Fig. 15).

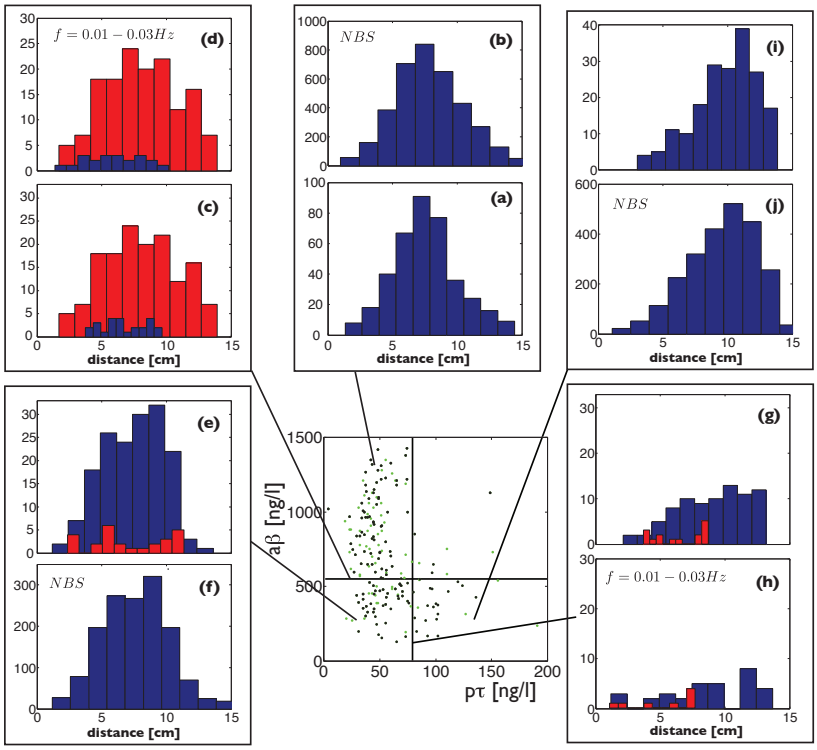

Figure 18: Distribution of physical link length for significantly different FC (see Fig. 15).

link set	*number of links*	$\overline{d} \pm \sigma_d$ [cm]	*skewness*
$HC > M_0$	386	7.6 ± 2.5	0.25
$M_0 > M_{a\beta}$	25	6.8 ± 1.7	0.00
$M_0 < M_{a\beta}$	81	7.0 ± 2.8	0.20
$HC > M_{a\beta}$	165	7.4 ± 2.3	-0.14
$HC < M_{a\beta}$	26	7.0 ± 2.9	0.00
$M_{a\beta} > M_{p\tau}$	82	9.0 ± 2.7	-0.43
$M_{a\beta} < M_{p\tau}$	15	6.5 ± 2.0	-0.14
$HC > M_{p\tau}$	188	9.8 ± 2.4	-0.73

Table 4: Mean link distance, standard deviation and skewness for the differing sets of links resulting from univariate testing with controlled FDR.

note that vital parts of entorhinal cortex and corpus striatum appear with reduced connectivity already for $M_0 > M_{a\beta}$, and it is tempting, however speculative, to attribute this to early $a\beta$-pathology. The inhomogeneous character of M_0 makes it difficult to draw strong conclusions. Another possibility is that a larger number of HCs (126) relative M_0 (70) gives a different statistically prevailing pattern. Increased subject numbers and biomarker data for HC will help in answering these questions. Subdividing the MCI groups with cognitive test scores can also provide valuable information.

In Fig. 18 red bars indicate the number of links where $M_0 < M_{a\beta}$, $HC < M_0$ and $M_{a\beta} < M_{p\tau}$ whereas blue bars indicate inverted relations. In each subpanel, an extra histogram referring to NBS is included for HC-MCI comparisons, and an extra panel for univariate difference testing in $f = 0.01 - 0.03$ Hz is included for MCI-MCI.

Comparing Fig. 18 (a) and (b), we see that the NBS-based component contains a lot more links and the distance distribution has widened - now more similar to the full distribution of link lengths [Fig. 16 (b)]. This is to be expected from the connected component search, which incorporates links with lower significance. Overall, NBS produces many more links than FDR, but in spite of this, the distance distribution remains very similar [see Figs. 18 (b,f,j)], only widening slightly.

Figs. 18 (c) and (e) clearly show that the number of compensatory FC links is much greater for $M_0 < M_{a\beta}$ than $HC < M_{a\beta}$ (red bars), and that the number of links with reduced FC is much greater in $HC > M_{a\beta}$ relative $M_0 > M_{a\beta}$ (blue bars). As discussed above, this paradoxal effect occurs despite some qualitative similarities between the HC-MCI and MCI-MCI patterns. The difference in link numbers carry through to the mean FC of subjects.

The compensatory distribution of $M_0 < M_{a\beta}$ in 18 (c) is relatively wide, containing a subset of longer interlobular links [see Fig. 15 (b)]. Likewise, $HC > M_{a\beta}$ has a wide distribution, containing short links within corpus striatum, and longer links between cortex and this hub region [see Fig. 15 (c)]. We interpret deviations from the all-link distribution in Fig. 16 (b) as manifestations of symptomatic changes in regional connectivity, rather than a random, uniform sampling of all possible links.

$f = 0.01 - 0.03$ Hz is of interest mainly in association with the compensatory effect of $M_0 < M_{a\beta}$, possibly representing a slowing down of oscillations in early stages of disease progression. This slowing-down effect appears to be related to that of increasing time-lag between oscillations, which leads to reduced FC and is related to interregional connectivity failure. Looking at Figs. 18 (d) and (c) the distance distribution in the two frequency intervals are remarkably similar, reflecting a common origin involving the same patterns and regions (although exact ROIs connected in encompassing region may vary).

Figs. 18 (g) and (h) witness of a much smaller spillover-effect into $f = 0.01 - 0.03$ Hz going from $M_{a\beta}$ to $M_{p\tau}$, and the effect seems to be associated with pathological $a\beta$, leaving a mark earlier on in the progression [16].

The scatter-plots of (f) and (h) (representing $M_{a\beta} > M_{p\tau}$ and $HC > M_{p\tau}$) reveal similar distributions that belong to similar patterns with long, interlobular links [see Fig. 15 (d) and (e)]. Interestingly, panel (g) shows a strong shift to positive values in a small group of nodes in the posterior left temporal lobe connecting to corpus striatum [see Fig. 15 (d)].

The mean distance, standard deviation and skewness of the distribution of links resulting from univariate testing with controlled FDR is shown in table 4, and the corresponding values for NBS components

[16] It is also possible that it is not a slow-down effect at all, rather the set of links in $M_0 \neq M_{a\beta}$ operate in a broader band relative $M_{a\beta} \neq M_{p\tau}$. However, given the similarities between $M_0 < M_{a\beta}$ in the two bands, the hypothesis seems plausible. Calculating the lower band FC for controls could help in answering this question.

link set	*number of links*	$\overline{d} \pm \sigma_d$ [cm]	*skewness*
$HC > M_0$	3680	7.8 ± 2.6	0.22
$HC > M_{a\beta}$	1475	7.6 ± 2.5	0.09
$HC > M_{p\tau}$	2417	9.5 ± 2.7	-0.50

Table 5: Mean link distance, standard deviation and skewness for the NBS components.

are listed in table 5. These values should be compared with that of the full distance distribution of links with mean distance (8.0 ± 3.0) cm and zero skewness.

The NBS components have a smoothing effect on the distributions, causing a reduction in skewness magnitude, without affecting mean values. NBS components generally contain one permille of the total number of links, and the univariate link testing yields 0.1 permille.

There is no great reduction in mean link length for reduced FC sets when $a\beta$ drops, but a substantial increase when $p\tau$ increases. The mean values is not always very characteristic, but we see a stronger trend in skewness, which reduces with lower $a\beta$, and then further as $p\tau$ increases.

For the enhanced FC, we generally have to few links to draw conclusions regarding distributions, with the exception of $M_0 > M_{a\beta}$, which appears to be biased towards shorter links, as one might expect from a compensatory effect.

An important general conclusion from Fig. 17 is that the differences appear to be general shifts in FC distributions, with a very similar FC difference for all links after controlling the FDR. It is also clear from Figs. 17 (f-h), that the separation in FC between $M_{a\beta} \neq M_{p\tau}$ and $HC \neq M_{p\tau}$ is the greatest overall. In fact, the FC-distance profile of AD [see Fig. 17 (i)] is very similar with regard to both FC difference magnitude and long-distance bias. Clearly, in the latter stages of disease progression, distributions are skewed towards longer link length [see Figs. 17 (f-h) and 18 (g-h)]. The distribution now peaks around 10 cm signaling the breakdown of long distance communication, affecting global process integration. This observation fits well with the description of AD as a disconnection syndrome hypothesized in the literature. The detailed analysis of these disconnection patterns will be presented in the subsections to follow.

7.2 Strength

We will now analyze the difference in FC patterns in greater detail, relying on various graphing techniques as well as an auxiliary graph measure known as strength. To provide background for the detailed analysis of group differences, it is instructive to inspect properties of the group mean connectivity matrices. Fig. 19 shows the group mean matrices of HC and M_0.

Strength is a very important and fundamental graph theoretical measure that greatly facilitates identification of FC trends. The strength s_i of node i is defined as

$$s_i = \sum_{j=1}^{N} \phi_{ij} \tag{11}$$

where ϕ_{ij} is the FC between node i and j, which in our case amounts to correlation between ROI time-series. In other words, we sum all the connections to a given node in Fig. 15. Strength is a generalization of the degree measure introduced above (representing sphere size in Fig. 15) to a weighted formalism that deals with continuous connection values rather than binary links. Although s_i is defined for each subject with connectivity set $\{\phi_{ij}\}$, it is more useful to restrict the use of Eq. 11 to group mean matrices, and work with group g mean strength s_i^g of node i corresponding to the group mean set of connectivities $\{\phi_{ij}^g\}$, i.e.

$$s_i^g = \sum_{j=1}^{N} \phi_{ij}^g \tag{12}$$

Fig. 19 (a) illustrates Eq. (12) for the two group mean FC matrices of HC and M_0. We note the presence of negative correlations, strong and widespread enough to completely dominate the strength of certain regions, most notably the caudate nuclei in corpus striatum and parts of thalamus [Fig. 19 (a)], but also several subsets in the frontal lobe.

The price of reducing the number of features under scrutiny via Eq. (11) from a massive $N(N-1)/2 = 840 \times (840-1)/2 = 352\,380$ to $N = 840$, is clearly a heavy reduction in power. If we restrict the sum

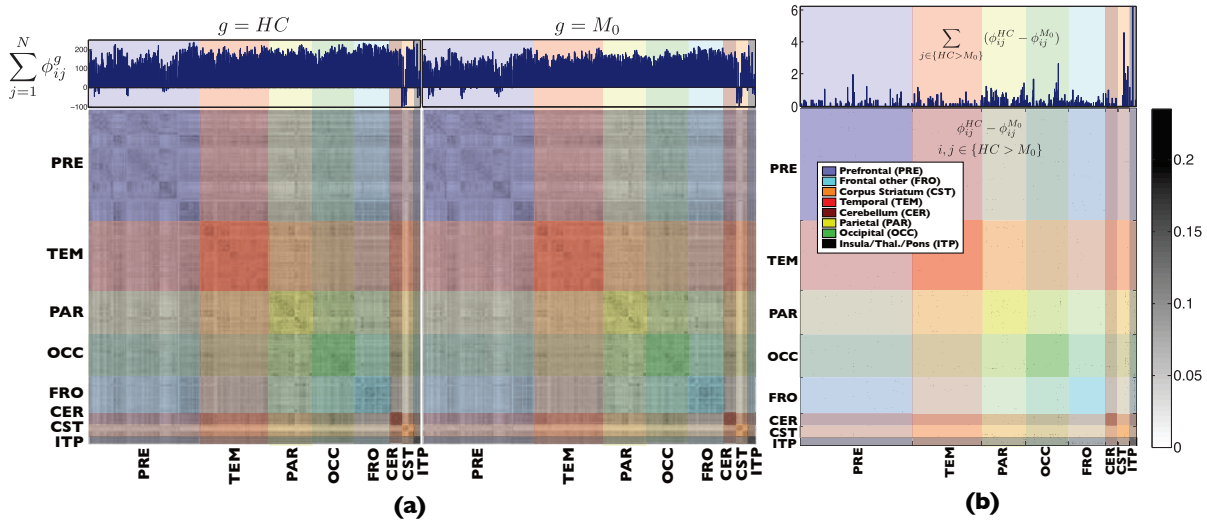

Figure 19: Group mean matrices for HC (top left) and M_0 (top right), where the bar graphs in the topmost part shows nodal strength (sum of matrix columns). The lower matrix (b) shows the significant FC difference and the overlying bar-plot the resulting strength difference. Although only a small fraction of links differ significantly, certain crucial regions appear with many connections forming dotted lines in the matrix (b) and leaving a clear imprint in the strength profile.

over FC to a subset of significantly different links, we get a much more useful quantity that can be used to assess the relative importance of regions. We define

$$\sigma_i^{g_1} = \sum_{j\in\{g_1\neq g_2\}} \phi_{ij}^{g_1} \tag{13}$$

as the mean strength of node i in group g_1 on the set of links that separate group g_1 from g_2. This set $\{g_1 \neq g_2\}$, comprises all links that show significantly greater/smaller FC difference between groups g_1 and g_2.

We further define a very useful measure: the difference in mean strength between the two groups g_1 and g_2 on the set $\{g_1 \neq g_2\}$,

$$\Delta\sigma_i\{g_1 \neq g_2\} = \sum_{j\in\{g_1\neq g_2\}} (\phi_{ij}^{g_1} - \phi_{ij}^{g_2}) \tag{14}$$

This magnitude in strength difference is a very informative measure that is also directly related to the statistical significance level. Fig. 19 (b) illustrates Eq. 14 for groups HC and M_0, i.e. $\Delta\sigma_i\{HC > M_0\}$. Here it can be clearly seen which nodes are greatly affected by reduced FC, and we can the identify the two greatest peaks as part of right thalamus and left putamen.

7.3 General features

We note some striking features in the general connectivity architecture, present irrespective of group affiliation. Generally within lobes, we find blocks of highly correlating nodes that have weaker or even negative correlations with most other nodes. These blocks are manifestations of modularized processing, integrated by long range connections with a tendency toward negative correlations.

For now, we illustrate the importance of this pattern with a simple example. Fig. 20 shows the HC average matrix, indicating two modules or highly connected blocks in the corpus striatum region. Remarkably, one part (comprising caudate nuclei) anti-correlates with the vast majority of nodes, whereas the other part (containing putamen) generally correlates with a roughly equal magnitude. The resulting modules and their associated negative and positive connections to cortex are shown in Fig. 20.

The caudate nuclei bear a striking negative correlation signature, highlighting its unique role as a hub and integrator of signals on a global scale, receiving information from the cerebral cortex and working in tandem with putamen. This remarkable topology leaves a powerful negative footprint in the strength profile [see Fig. 19 (a)]. As we shall see, these two structures are heavily implicated in the cognitive decline associated with pathological CSF biomarker levels.

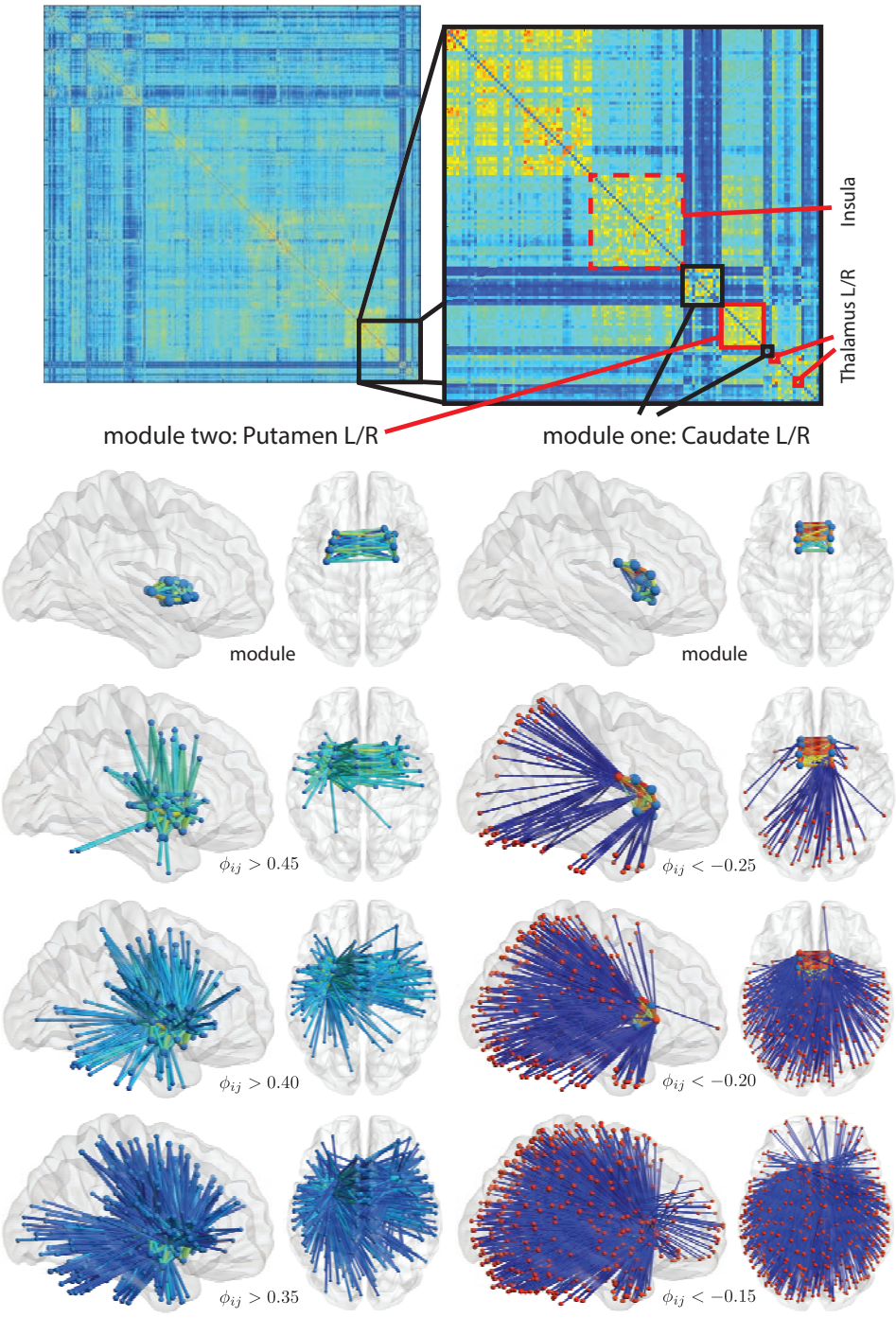

Figure 20: Illustration of two modules in corpus striatum. The right column shows the negative correlations with a module comprising the caudate nuclei with successive addition of lower-magnitude links by thresholding. Similarly, the left column shows the positive correlation with putamen (in actuality constituent of a module also comprising insula and thalamus).

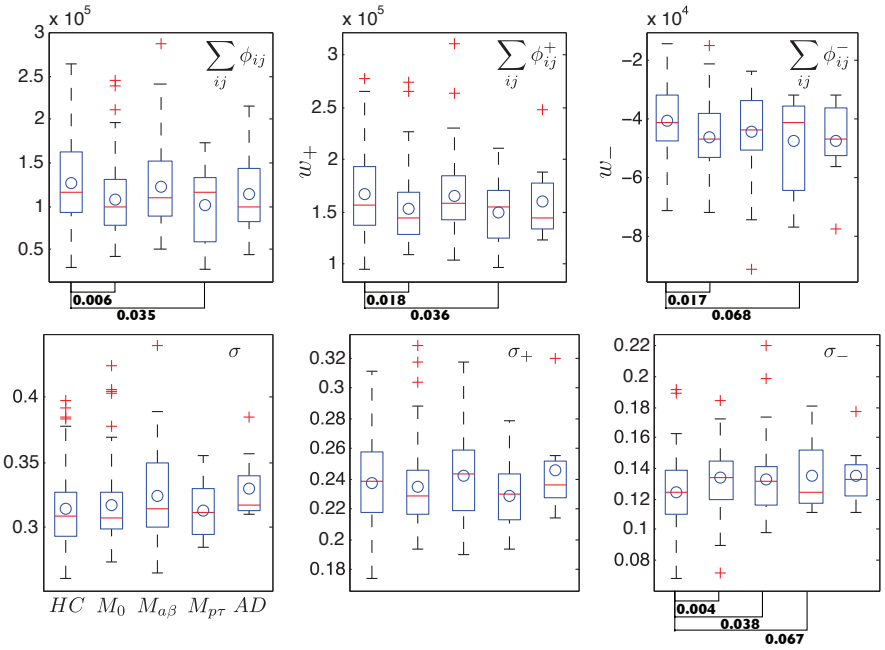

Figure 21: Box-plots of total FC and mean FC standard deviations (box legends are indicated in the lower right plot). The top row (from left to right) shows total strength: signed, positive and negative. The bottom row shows box plots of the corresponding standard deviation of mean FC values.

Fig. 21 shows box plots of the total signed, positive and negative functional connectivity, as well as the standard deviation of corresponding average FC values. The plots represent all 350 000 links in the $N = 840$ network, and we do not expect to see any features distinguishing groups using such crude measures (significant differences with respect to controls are marked with the p-value coming from two-sample t-tests with assumed unequal variance).

However, some interesting features emerge. The positive weights form a clear majority of all links, and statistics are very similar to that of the full, signed set of links. AD contains only 8 subjects and should be interpreted with great caution. Statistics are better for the other groups: $HC(126)$, $M_0(70)$, $M_{a\beta}(42)$ and $M_{p\tau}(18)$.

We note here again the pattern of compensatory[17] FC associated with a reduction in $a\beta$. Relative HC, there is a significant total connectivity reduction of M_0 and $M_{p\tau}$, but not $M_{a\beta}$. The pattern of significances carries through to the negative correlations, reinforcing the image of a general downshift in FC. The MCI with both pathological levels of $a\beta$ and $p\tau$ (i.e. $M_{p\tau}$) exhibit a very asymmetric distribution, stretching much farther into the negative range.

No significant differences in average variance are found for signed and positive connections, although qualitative trends carry over from the total FC plots. For the negative correlations, there appears to be a general increase in variance for all MCI relative HC, consistent with a pattern of reduced FC affecting the same general areas, but with a spread in severity, or even specific node-node connection.

7.4 HC versus MCI with non-pathological CSF

Group M_0 consists of 70 subjects with an MCI diagnosis, but with non-pathological levels of CSF biomarkers, i.e. $a\beta > 550$ ng/l and $p\tau < 80$ ng/l. Fig. 22 shows the links where univariate testing with controlled FDR reveals significantly reduced correlation in group M_0 relative controls, i.e. where $HC > M_0$. We refer to this set of links as $\{HC > M_0\}$.

In these link plots we have added a lot more information; link diameter is now proportional to the correlation magnitude and colored according to the signed value. In addition, the spheres marking node positions are now given a radius proportional to strength magnitude (not the degree as in Fig. 15), with blue color for positive strength and red color for negative strength. In the connectivity analysis we always

[17]It is indeed possible that there is compensatory increase in connectivity in response to oxidative stress and increased amyloid burden. It is also possible that what we are seeing is a consequence of the wide variety of MCI in M_0.

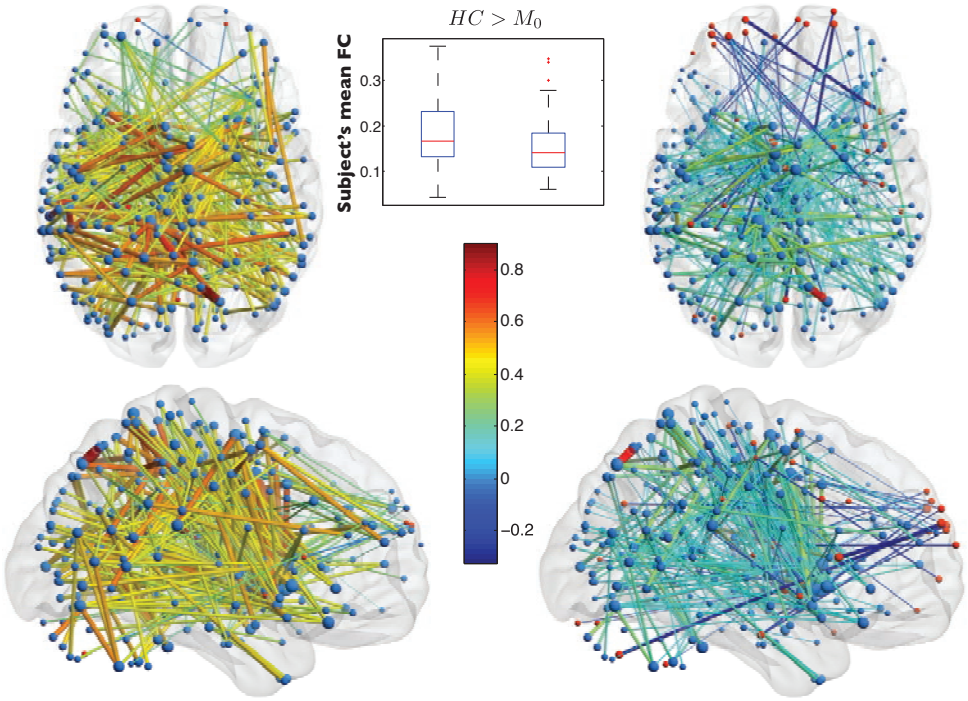

Figure 22: $HC > M_0$ link plots, which HC on the left and M_0 on the right. Links are colored by signed value of correlation (thermometer in center) and the diameter is proportional to absolute magnitude. In addition, the sphere radius signifies strength magnitude, with red color for negative and blue for positive strength.

use strength on the set of differing links to highlight relative importance of nodes, i.e. in Fig. 22 spheres represent $\Delta\sigma_i\{HC > M_0\}$ as defined in Eq. 14.

Although the difference in links appear to be somewhat omnipresent, it is important to note that only a tiny fraction of all possible links form the set $\{HC > M_0\}$ (roughly 0.1 permille). However difficult to make out in Fig. 22, there is a pattern that we will attempt to expose using thresholding techniques and maximal intensity projections of HC-MCI differences in strength. The strength difference is formed from by summing group mean connectivity matrix differences (see Eq. 14).

A few important features can be inferred already from Fig. 22. The inset box-plot shows subject's mean FC. Although a large number of links differ significantly (relative other HC-MCI comparisons), a clear majority of these links do not come with large differences in FC [this is also clear from Fig. 17 (a)]. We note in passing some similarity with Fig. 20 where the vital parts of corpus striatum link up with sensory/motor parts of cortex, but only very sparsely to the frontal lobe, already hinting at which central network parts are affected.

On closer inspection, we find a number of long distance links ($\gtrsim$ 8 cm), where the FC reduction of M_0 extends into the negative range [this is also clear from Fig. 17 (a)]. These negative correlations (dark blue links) are clearly visible as they lead to negative strength (red spheres) in isolated areas. The effect is strongest in the frontal superior parts, and in particular appears lateralized to the left hand side.

The majority of reduced FC links run between the parietal and corpus striatum region. Regional differences are easier to see if we focus on the difference in strength on the differing set of links, i.e. $\Delta\sigma_i\{HC > M_0\}$ defined in Eq. 14.

Fig. 24 (a) shows the result of thresholding $\Delta\sigma_i\{HC > M_0\}$ to retain the largest differences in strength and the connections from which they originate. Maximal intensity projections (MIPs) of $\Delta\sigma_i\{HC > M_0\}$ are shown in Fig. 23 (b). Fig. 24 is the result of applying a suprathreshold to $\Delta\sigma_i$ and then an anatomical labeling algorithm [31], that identifies the overlap of functionally relevant regions with members of a coarser 116 anatomical ROI set [21], and assigns multiple labels accordingly.

Referring to Fig. 24, both sides of thalamus have high strength differences, but the right part has twice as large difference, easily identifiable with numerous links in Fig. 23. Connectivity of putamen is bilaterally reduced, but includes a part of pallidum on the right. The negative nodes appearing in the front left part emerge with strong differences for parts of frontal mid/sup left. Cingulum posterior has differences of the mid-range magnitude, and forms part of a contiguous group extending bilaterally to

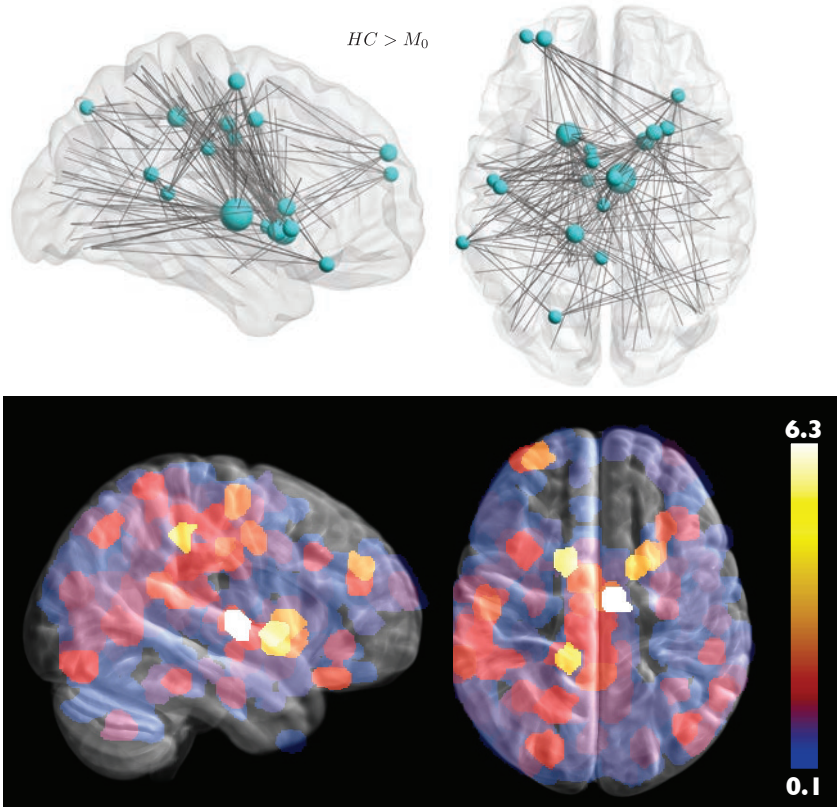

Figure 23: Strength differences for $\{HC > M_0\}$. (a) shows the effect of applying a suprathreshold to retain high strength difference regions and their connecting links (sphere size is proportional to strength difference). In (b), MIPs of all the strength difference of all regions is shown, revealing a maximum in thalamus R.

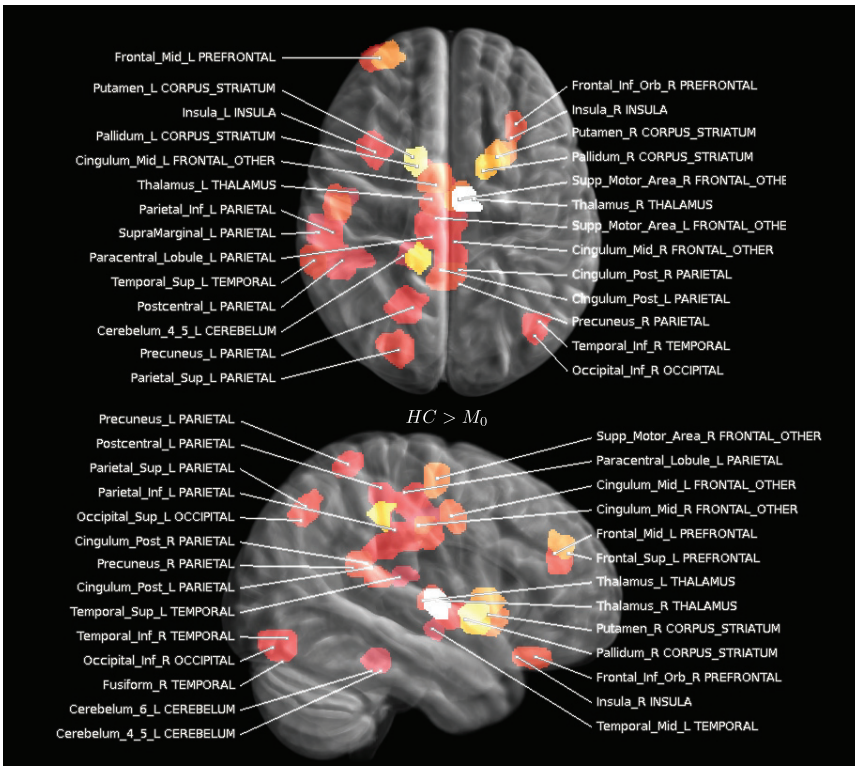

Figure 24: These MIPs are the result of applying a suprathreshold to the strength difference of $\{HC > M_0\}$ and then employing a labeling algorithm[31], which assigns multiple labels to functional regions according to overlap with region of anatomical ROI set (with 116 ROIs) [21].

precuneus, the middle part of cingulum, supplementary motor area and the paracentral lobule. There is also a group of nodes with higher strength difference centered in the parietal region of the left hemisphere containing parts of parietal inf L, postcentral L, precentral L, supramarginal L and temporal sup L.

We may refine our observations further, by looking at the connectivity of the 13 nodes of greatest strength difference, represented graphically in Fig. 25 and listed in table 6.

The table indicates total difference in strength $\Delta\sigma_i\{HC > M_0\}$ for node i, the associated mean FC difference $\Delta\sigma_i/n_i$ (standard deviation is approximately 0.02 in all cases) over the n_i links connected to node i and part of the set $\{HC > M_0\}$. Since the functional nodes can overlap several anatomical regions, they are denoted by regions of greatest and second greatest overlap (only overlap >25% is considered).

The last column of table 6 contains short list of the most salient connections grouped by proximity, as well as isolated links of interest. Connections are denoted by the anatomical regions having majority overlap with the functional centers of interest.

Thalamus R has an overwhelming number links with reduced FC and it is quite remarkable that such a small area has so many failing connections. In general, it can be seen from table 6 that different functional centers in close proximity or even with the same anatomical label (such as putamen R in entry 5 and 8) appear, pointing to the possibility of grouping these.

The underlying geometrical pattern is a central hub region involving thalamus and putamen (sometimes in proximity to or overlapping caudate nucleus and pallidum) connecting to several distinct clusters of nodes centered on: 1) postcentral L parietal region, 2) medial superior region involving precuneus, post/mid cingulum and supplemental motor area, 3) cuneus and occipital inf. There are also failing connections between the posterior L and medial superior centers, which both have reduced FC with the corpus striatum hub, hinting at a connected component.

Both thalamus R and putamen L connect to a region involving the postcentral L, and indeed thalamus R connects to a part of putamen L directly (this part of putamen L also has a small overlap with hippocampus L). Thalamus R has a large number of reduced FC links with the occipital lobe: to a central cluster around cuneus, and bilaterally involving occipital inf, overlapping with parts of the temporal lobe and cerebellum crus. A region close to the interface between cerebellum, occipital and temporal lobes appears affected, particularly on the right hand side.

Putamen L overlapping with pallidum, has only one link to each of the three occipital centers (occ inf L, cuneus, occ inf R) but a large number of links leading to the medial superior region involving precuneus, cingulum mid and the paracentral lobule.

Putamen R shows a connection pattern similar to its left hand counterpart, especially when pooling the two functional centers 5 and 8 in table 6.

The connections to the prefrontal cortex appear to be relatively few, but some important links between hippocampus R and frontal sup/mid L have attained negative FC. This area in the frontal lobe appears several times in the reduced correlation patterns.

Postcentral L is very frequent, connecting bilaterally to putamen and thalamus, as well as to cingulum mid/post and precuneus. Interestingly, cingulum post has reduced FC links to many functional centers of the left temporal lobe. Temporal sup/mid L has in turn reduced FC connections to the post/precentral R and hippocampus L.

There is a particularly interesting set of links running between hippocampus/parahippocampal R and several nodes in the frontal mid L area. These can be seen as a bundle of negative links (see Fig. 22 upper right panel) running diagonally from the right temporal lobe to the left frontal cluster of nodes. Comparing with HC, we see correlations of similar magnitude, but with positive sign. This change of sign is manifested in the nodal strength on the significantly differing set of links (causing them to change color from blue to red in Fig. 22).

Summarizing our findings, a corpus striatum hub region has reduced connectivity to three main centers; 1) the postcentral L region; 2) the cingulum mid region 3) occipital centers. The postcentral L region (1) also has reduced connectivity with the central region (2). Reduced FC is also found between the cingulum post and temporal sup/mid L. The right hippocampus has reduced connectivity with several nodes in the frontal left lobe.

The FDR controlled univariate testing hints at a network component with reduced FC, and one might therefore expect the NBS search algorithm to produce results. Using a suprathreshold of $t = 3.0$, we find an large component comprising 3680 links ($\approx 0.1\%$ of all links). The corresponding link plots are shown in Fig. 26 and strength MIPs in Figs. 27 and 28.

Comparing the box plots in Figs. 22 and 26 we see that the difference in subject's mean FC increases substantially for the large NBS component, originating in both a reduction in M_0 and an increase in HC connectivity, consistent with the algorithm's ability to locate weaker contrasts. The reduction in

node i	$\Delta\sigma_i$	n_i	$\Delta\sigma_i/n_i$	*connections [#] (fraction of $\Delta\sigma_i$)*
1. thalamus R	6.3	33	0.19	PAR [9]: postcentral L, parietal inf L (0.18) OCC [16]: occ. mid/sup/inf, cuneus, calcarine (0.50)
2. putamen L, pallidum L	4.6	26	0.18	postcentral R, precentral R, supp motor area R PAR [8]: postcentral L, precentral L (0.31) FRO/PAR [13]: supp motor area, cingulum mid L, paracentral lobule, precuneus (0.52) putamen L, postcentral R, occipital inf R, temporal inf R
3. cingulum mid L	2.6	15	0.18	PAR [9]: precuneus, parietal sup L,postcentral L (0.63) thalamus L, occipital inf R, temporal inf R, postcentral R
4. putamen R, pallidum R (hip caudate small overlap)	2.5	15	0.16	PAR [4]: postcentral L, parietal inf L (0.25) PAR [3]: postcentral R (0.20) FRO/PAR[4]: cingulum mid L, supp motor area L, paracentral lobule L (0.28) putamen L
5. putamen R	2.0	12	0.17	PAR[3]: supp motor area, paracentral lobule R (0.23) PAR[4]: postcentral L, parietal inf R (0.32) front mid L/sup L, post/precentral L, putamen L, temporal/occipital inf R
6. front sup L	2.0	11	0.18	TEM/CST [3]: hippocampus R, parahippocampal R, putamen R (0.25) FRO [4]: supp motor area, cingulum mid (0.37) putamen L, precuneus R
7. supp motor area	1.7	9	0.19	CST [5]: putamen, thalamus (0.58) supramarginal
8. putamen R	1.6	10	0.16	FRO [5]: cingulum mid, precuneus, supp motor area L (0.52) front mid L/sup L, postcentral L
9. postcentral L	1.5	9	0.16	CST[4]: putamen, thalamus (0.47) FRO/PAR [4]: cingulum mid R, cingulum post R, precuneus (0.44) supp motor area L
10. cingulum mid L	1.4	8	0.18	CST[2]: putamen, pallidum (0.25) INS[3]: insula (0.39) front mid L/sup L
11. cingulum post L	1.2	7	0.18	TEM[6]: temporal mid L, temporal sup L (0.87) postcentral L
12. frontal inf orb R	1.2	8	0.15	FRO/PAR [3]: cingulum mid, paracentral lobule L (0.37) TEM [2]: temporal mid L, temporal sup L (0.25)
13. temporal sup L, temporal mid L	1.2	7	0.17	PAR [3]: precentral R, postcentral R, supramarginal R (0.44) hippocampus L, precuneus R

Table 6: The 13 regions for $HC > M_0$ with greatest strength difference ($\Delta\sigma_i$), the number of links (n_i), and average FC difference ($\Delta\sigma_i/n_{|i}$). The last column shows gives a summary of connecting areas grouped by proximity, with more or less isolated links listed last.

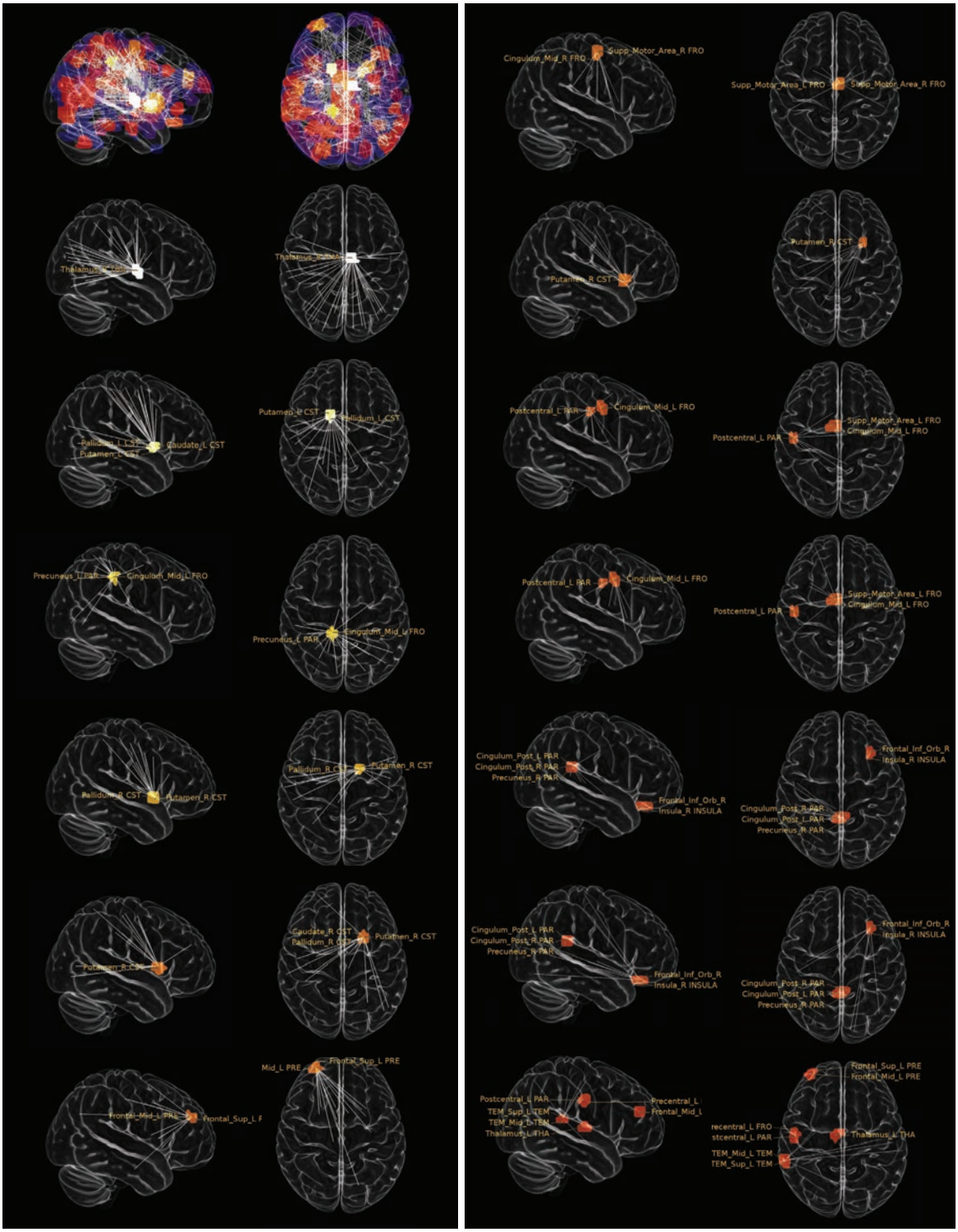

Figure 25: Connections of the thirteen regions with highest strength difference on the link set $\{HC > M_0\}$.

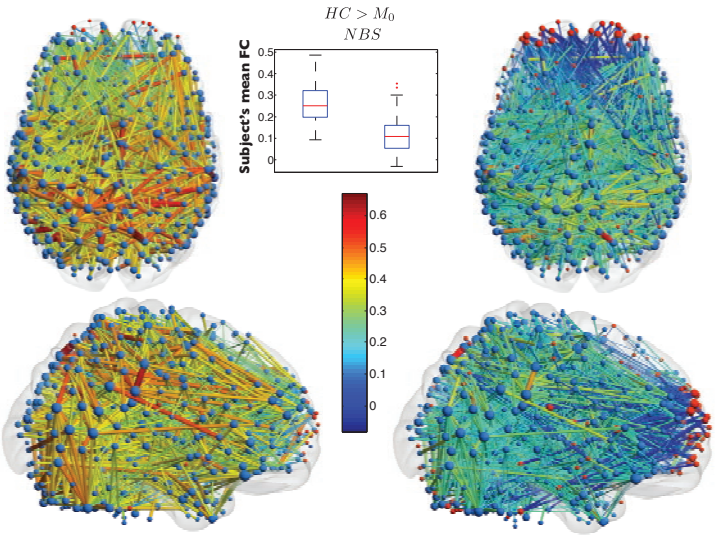

Figure 26: 3680 links form the connected network component with reduced FC in M_0 relative HC.

FC causing negative strength (red spheres) now extends to both sides of the anterior prefrontal cortex. Negative nodes of smaller magnitude can be found in the front-most part of HC, and comparing links with M_0 indicates that the majority of these are shifted down in FC by a characteristic amount.

Looking at the more revealing strength plots (see Figs. 27 and 28) it is clear that the connectivity difference pattern is very similar, although the maximum strength has quadrupled. However, some areas have increased their relative strength with the added power of NBS: frontal sup L, frontal inf orb R; putamen, caudate; hippocampi; cingulum mid and most notably: cingulum post.

7.5 HC versus MCI with pathological $a\beta$-levels

This MCI-group consists of 42 subjects with low levels of $a\beta$ in the CSF ($a\beta < 550$ ng/l), corresponding to a high amyloid burden, but $p\tau$ levels remain below 80 ng/l with lower levels of NFTs.

Figs. 29 and 30 show the correlation values of HC and $M_{a\beta}$ on the set of links defining reduced and compensatory FC, respectively (i.e. $\{HC > M_{a\beta}\}$ and $\{HC < M_{a\beta}\}$). Backtracking to the biomarker-FC road map in Fig. 15, it is clear that the most important trend is a large set of reduced FC links converging on a corpus striatum hub.

Comparing the box plots in Figs. 22 and 29, shows that the $M_{a\beta}$ subject's mean FC has not only decreased relative control, but virtually all individuals now lodge in the negative region. Again, we see low-correlation, longer links shifted to negative FC (this is also apparent from Fig. 17 (d)). Comparing Figs. 18 (a) and (e) we see that a greater proportion of longer links are now affected. The mean link length is similar to $HC > M_0$, but skewness has shifted sign (see table 4) as a result of long intermodular links of reduced FC. Negative strength appears in isolated HC nodes, but completely dominates the $M_{a\beta}$ link plot. Turning to $HC < M_{a\beta}$, it is clear that most compensatory links appear across hemispheres in the anterior part of prefrontal cortex (see Fig. 30).

MIPs of strength difference on the link sets are shown in Figs. 31 and 32 for $HC > M_{a\beta}$. The $\{HC > M_{a\beta}\}$ MIP (see Figs. 31 and 32) is completely overshadowed by the very large differences in the central corpus striatum hub, involving a maximum in caudate R with a difference in the adjoining putamen R. On the left hand side we also find large differences, but in a more widespread area extending to the superior part (caudate L) and in the inferior part (putamen L) of corpus striatum. We also find differences in familiar areas (see previous subsection): precuneus and the right hand side interface between temporal, occipital, and cerebellum.

Proceeding with the more detailed connectivity analysis, table 7 and Fig. 33 exposes the connectivity of the 13 areas with greatest strength difference on the set $\{HC > M_{a\beta}\}$. Comparing tables 6 and 7, we note that the mean FC difference on the subset of links from $\{HC > M_{a\beta}\}$ responsible for the nodal strength difference of $M_{a\beta}$ has increased relative M_0.

Caudate R has reduced correlation with a large number of nodes (37) - a remarkable figure for such a small region. Among these links we find distinct subsets grouped by proximity. One set of links leads to a central crest mainly comprising cingulum mid stretching from cingulum ant to post and overlapping

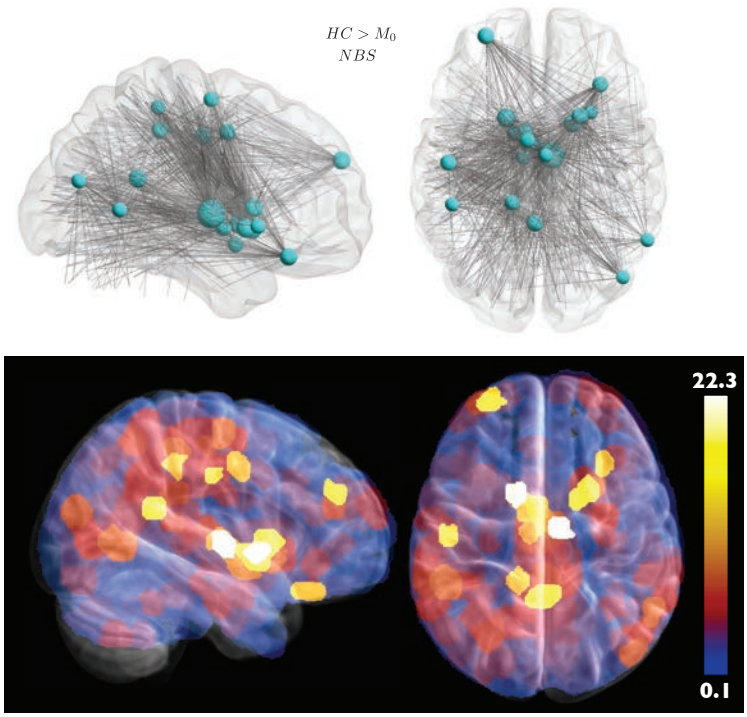

Figure 27: Two different suprathresholds applied to strength difference (a) and MIP of strength difference on $\{HC > M_0\}$ NBS component.

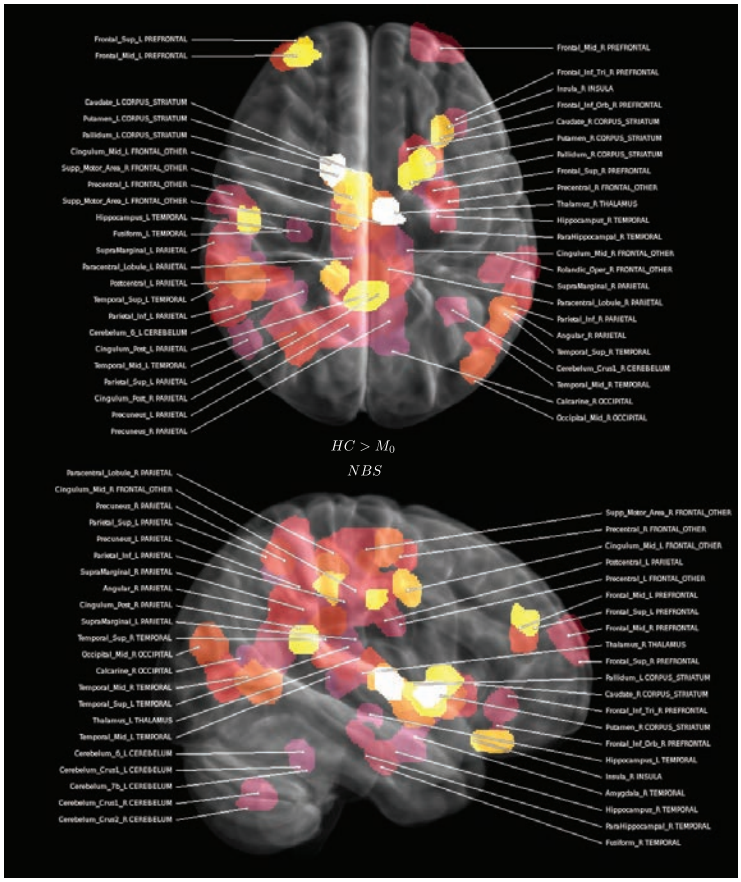

Figure 28: Suprathreshold and labeling algorithm applied to strength difference for NBS component of $HC > M_0$.

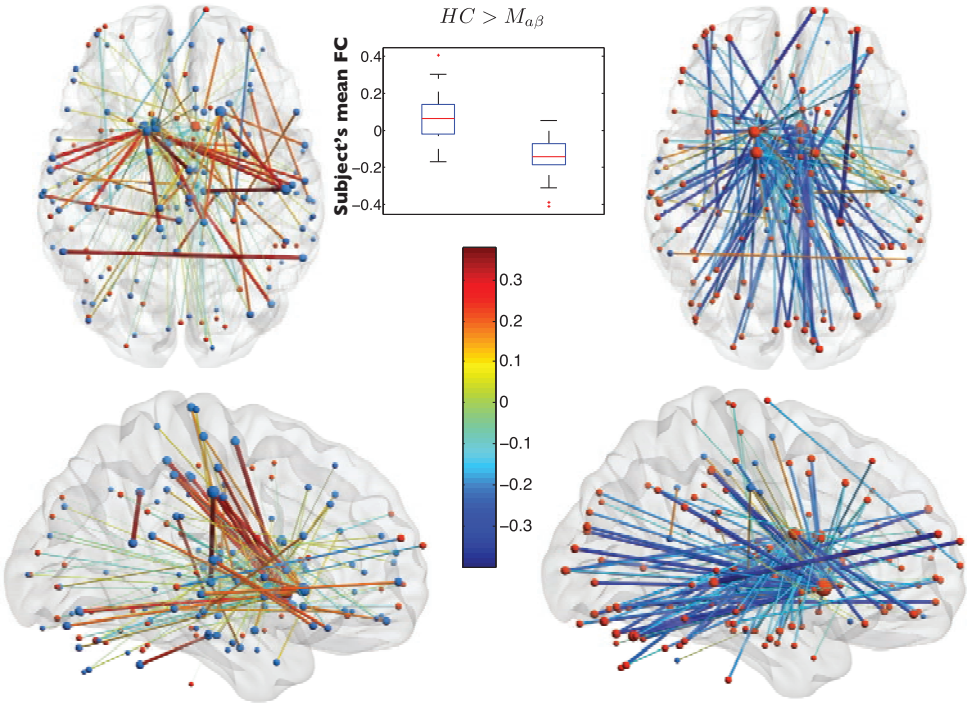

Figure 29: Group mean FC values for the link set $\{HC > M_{a\beta}\}$.

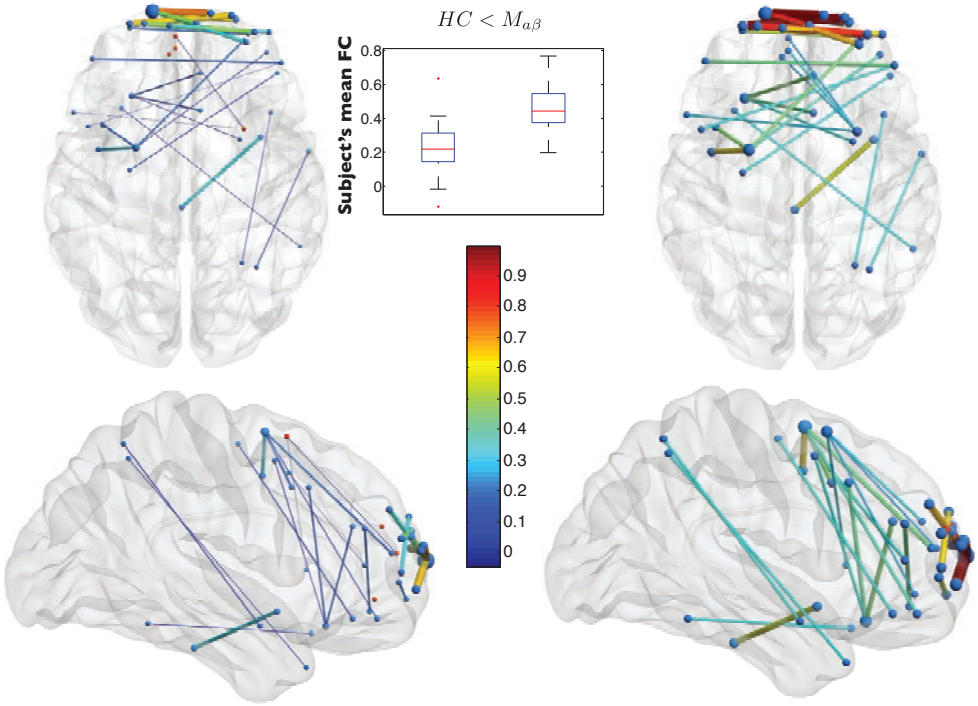

Figure 30: Group mean FC values for the link set $\{HC < M_{a\beta}\}$.

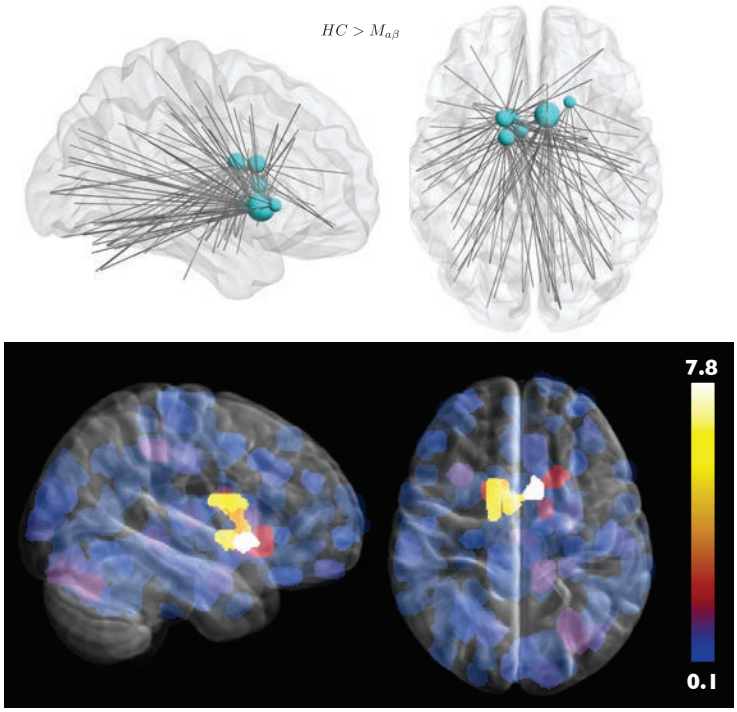

Figure 31: Applied suprathreshold to $\{HC > M_{a\beta}\}$ (a) and MIPs of strength difference (b).

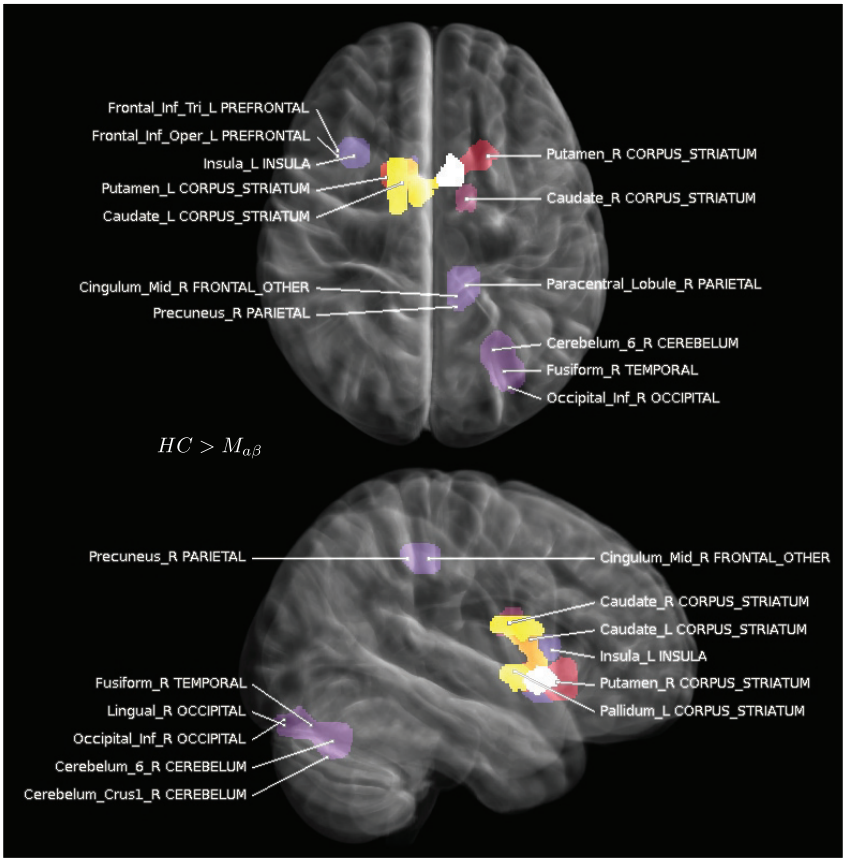

Figure 32: Applied suprathreshold and labeling to $\{HC > M_{a\beta}\}$ strength difference in Fig. 31.

node i	$\Delta\sigma_i$	n_i	$\Delta\sigma_i/n_i$	connections [#] (fraction of $\Delta\sigma_i$)
1. caudate R	7.8	37	0.21	FRO [8]: cingulum mid R, supp motor area (0.21)
				TEM/PAR [3]: temporal sup L, postcentral L, supramaginal L (0.08)
				OCC/CER [17]: cuneus, calcarine, lingual,
				fusiform, cerebelum crus, occipital inf, occipital mid L (0.48)
				insula L, putamen R, pallidum R; temporal mid/sup R, angular R
2. caudate L	3.7	18	0.21	OCC/CER [6]: calcarine R, lingual R (0.35), cerebellum crus
				parahippocampal, hippocampus; temporal mid L, temporal mid R;
				frontal sup med, cingulum ant L, front mid/sup orb R
3. caudate L	3.5	16	0.22	TEM [5]: hippocampus R, parahippocampal R, temporal mid R, putamen R, amygdala R (0.31)
				cingulum post L, cingulum mid L; front mid/sup orb R; putamen R, fusiform cerebellum crus
4. caudate L, pallidum L	3.2	16	0.20	TEM[2]: amygdala R, hippocampus R, putamen R (0.12)
				OCC/CER [5]: calcarine R, cuneus (0.31)
				cerebellum crus, fusiform R; temporal mid R, temporal sup R
5. caudate L	2.8	13	0.21	PRE [4]: frontal mid/inf orb L, frontal inf tri L, insula L (0.31)
				TEM [2]: amygdala R, hippocampus R, temporal mid/inf R (0.15)
				FRO [4]: cingulum mid R, supp motor area L, frontal sup med L (0.32)
6. putamen L	1.9	10	0.19	postcentral, temporal sup L; supp motor area R, cingulum mid R
7. putamen R	1.5	7	0.21	cerebellum crus; parietal sup L, postcentral L; supp motor area R, cingulum mid R
8. caudate R	1.2	6	0.19	parahippocampal R, fusiform R; frontal mid/inf/med R;temporal mid L
9. cerebellum R	0.9	4	0.23	caudate
10. cerebellum R	0.9	4	0.22	caudate, putamen R
11. cingulum mid R	0.8	4	0.21	caudate, putamen
12. insula L	0.8	4	0.20	caudate
13. caudate L, putamen L	0.8	4	0.2	links: insula L, cingulum mid R, hippocampus R, temporal sup R

Table 7: $\{HC > M_{a\beta}\}$ group mean strength differences, number of contributing links, and mean link FC. The last column summarizes connectivities behind the strength difference.

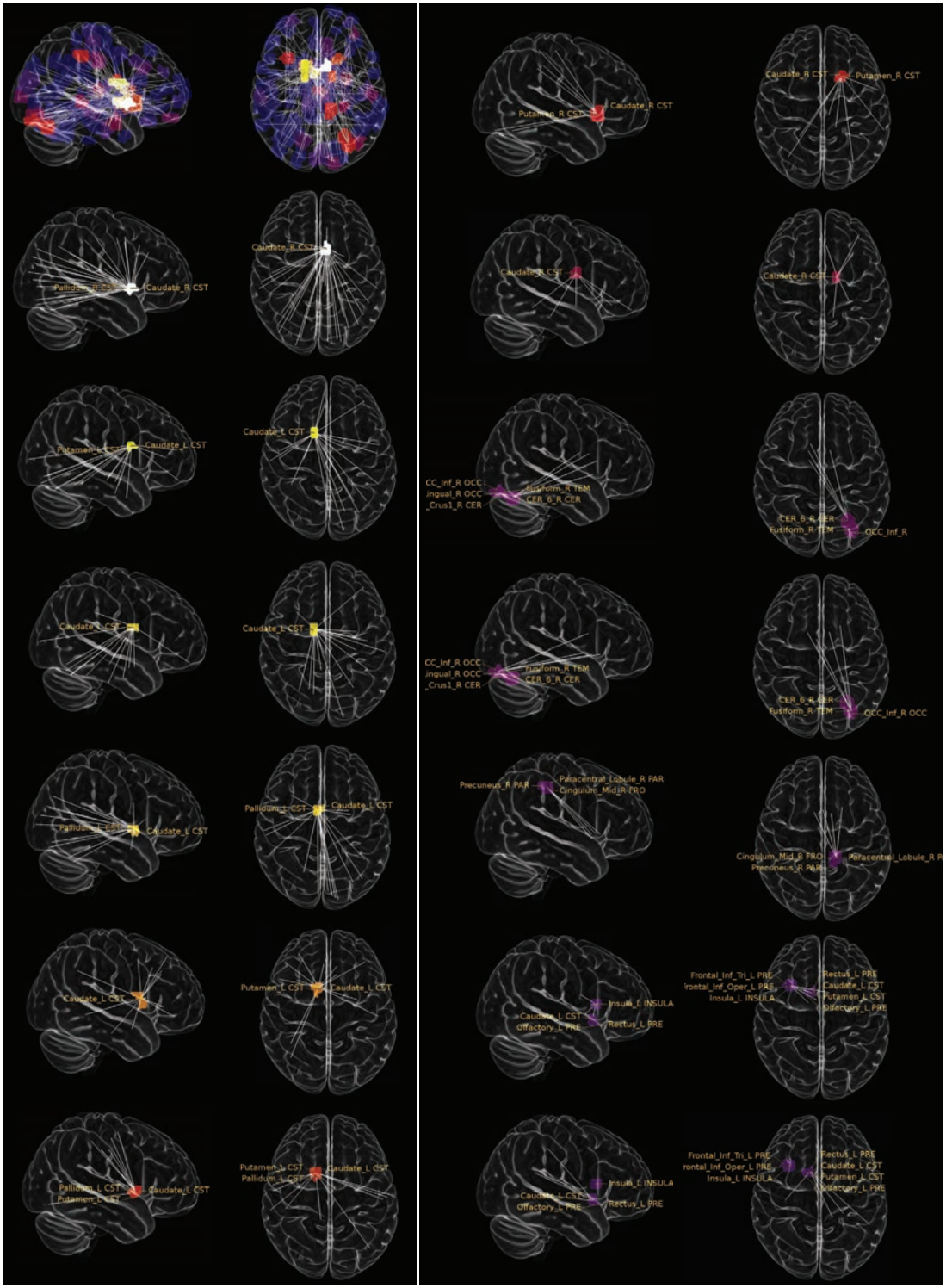

Figure 33: Connectivities of the 13 nodes with highest strength difference for $\{HC > M_{a\beta}\}$.

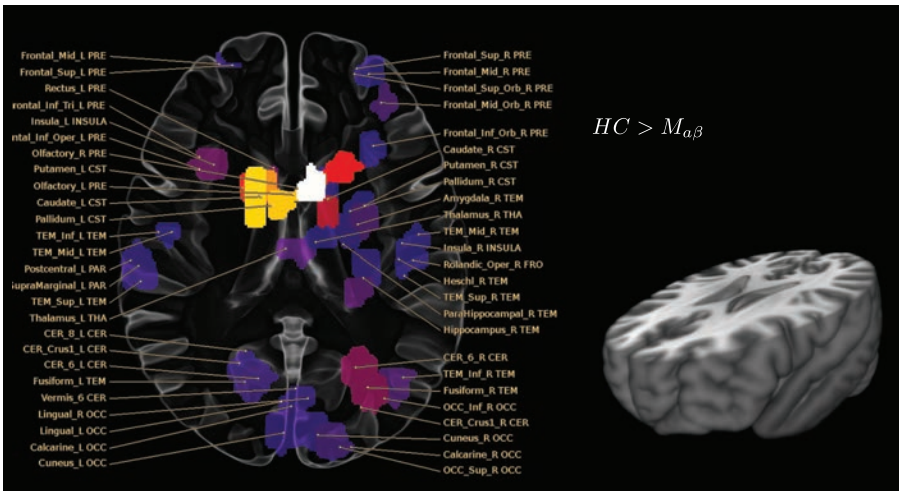

Figure 34: Cut with low strength difference threshold reveals a group of nodes including hippocampus R, parahippocampal R, amygdala R, and putamen R.

with these. Familiar nodes like supp motor area and some overlap with adjoining precuneus form part of this group. Caudate R also has reduced connections with the neighboring putamen R and pallidum R, and a cluster appears involving postcentral L and temporal sup L. Somewhat similar to thalamus R, the largest number of nodes showing reduced FC with caudate R form three occipital centers: two appear bilaterally at occipital inf near the cerebellum crus interface involving fusiform and one central area overlapping with occipital sup, cuneus and calcarine.

Turning to caudate L, we pool entry 2 and 3 in table 7 - these both lodge in the upper left part of corpus striatum. Whereas inferior caudate R has reduced FC with superior parts, upper caudate L mainly fails with inferior parts of the brain. Apart from connections to the bilateral occipital inf clusters, a strikingly large number of key regions linked with cognitive decline appear bilaterally: hippocampus, parahippocampal, temporal mid and cingulum post. The part of caudate L overlapping with pallidum L (entry 4 in table 7), has reduced FC with central superior occipital cluster, hippocampus R, amygdala R and several nodes in the left temporal lobe. The anterior part of caudate L (entry 5) also has reduced FC to hippocampus R, and a few nodes in prefrontal cortex.

Although the single region of caudate R exhibits the greatest reduction in connectivity, pooling the entries of caudate L (sometimes overlapping with putamen L) gives a much larger number of failing links. In addition, key regions form a part of this link set. A superior part of caudate R, has reduced FC to inferior parts, involving parahippocampal R with some hippocampus R overlap.

Putamen L, has similarities with caudate L and reduced FC to superior parts bilaterally to postcentral and to precuneus/cingulum mid, as well as the frequently occurring occipital inf R interface. Both caudate L and R has reduced FC to putamen R, which in turn has reduced FC to the cingulum mid and postcentral L regions (similarly to caudate R).

The remaining entries in table 7 are generally part of the larger caudate connectivities. Hippocampus figures more prominently in $M_{a\beta}$, mostly the right hand side as evidenced by node 14 and 15 in the sorted list of greatest strength difference (see appendix A). Fig. 34shows a cut of the inferior parts of the brain, with a low strength difference threshold to reveal a contiguous group of nodes including hippocampus R, parahippocampal R, amygdala R and putamen R (in proximity to caudate R).

By virtue of the highly connected hub region involving primarily caudate nuclei, a large connected component can be identified using the NBS method. As before, the NBS yields a component with an order of magnitude more links (see Fig. 35 for link plots and Figs. 36 and 32 for strength plots). Although the pattern from univariate testing is greatly reinforced with a large number of links of reduced FC with corpus striatum, there are also a large number of links appearing between parietal/occipital inf and prefrontal areas. These are already visible in the set resulting from univariate testing, but appear much more numerous in the NBS component. Those connecting the posterior-most parts to the prefrontal cortex are extremely long and some of them are already in the negative for controls - the same links then obtain minimal FC in $M_{a\beta}$.

Comparing the boxplots of Figs. 29 and 35 we see that (unlike M_0) the subject's mean FC is not greatly affected by the increase in links from NBS.

Apart from a maximum strength difference that is six times greater in NBS than in the FDR controlled

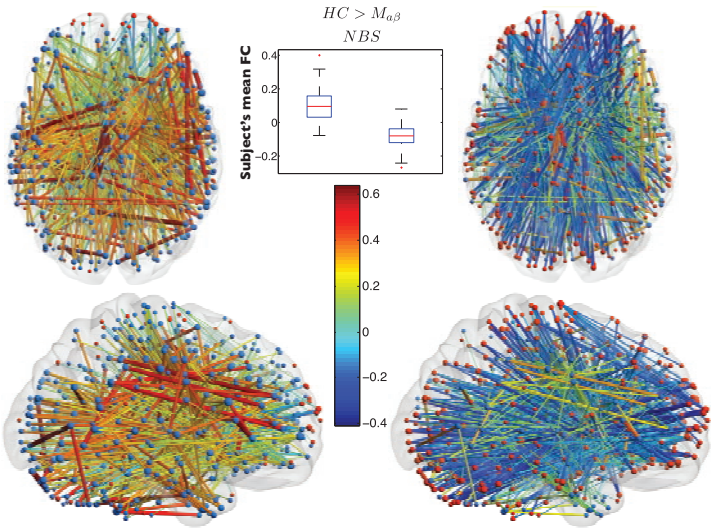

Figure 35: NBS component of $\{HC > M_{a\beta}\}$ yields an order of magnitude more links than univariate testing with FDR control.

set, it is hard to see any qualitative differences. Thresholding (see Fig. 37) reveals a set nodes with a difference in strength similar to the set identified in the detailed connectivity analysis, but anterior parahippocampal/hippocampus L appears much stronger in the NBS component[18].

[18] Although not shown here, choosing a lower threshold in Fig. 32 produces a similar image to the NBS MIP in Fig. 37, but hippocampus L has a much lower strength difference.

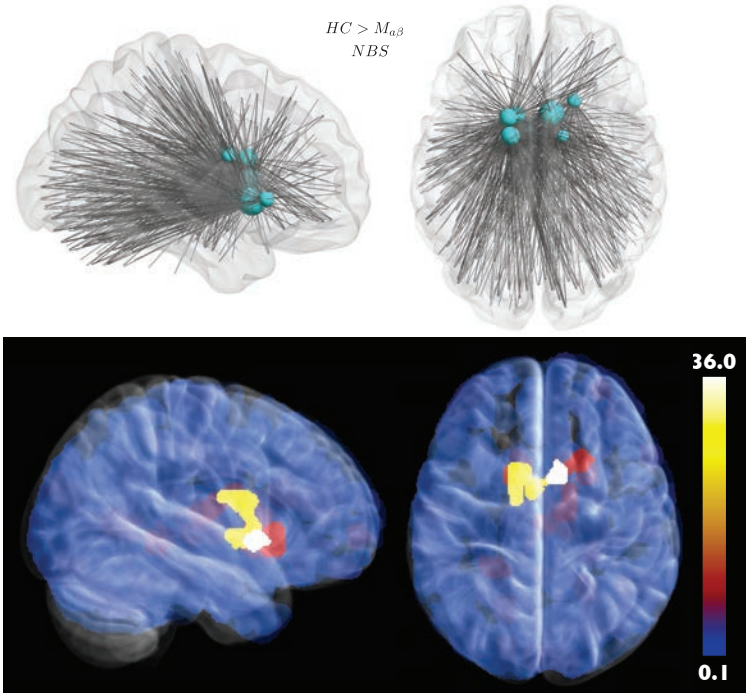

Figure 36: Threshold applied to strength difference (a), and MIP of strength difference (b) for NBS component $\{HC > M_{a\beta}\}$.

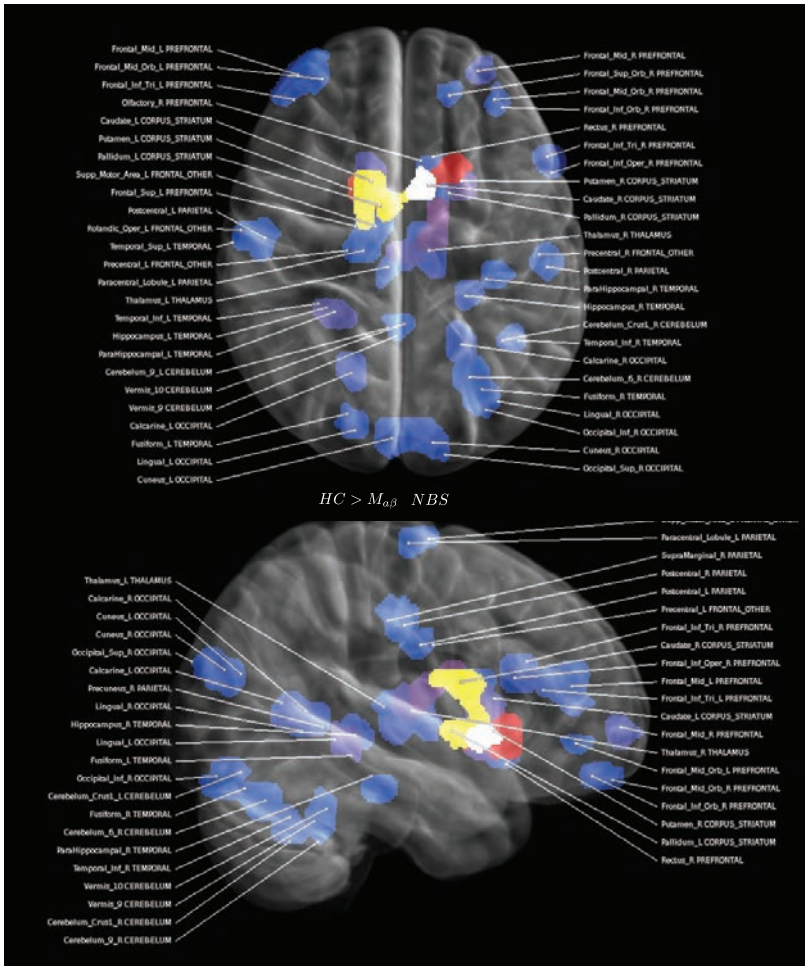

Figure 37: Threshold and labeling algorithm applied to strength difference of NBS component $\{HC > M_{a\beta}\}$.

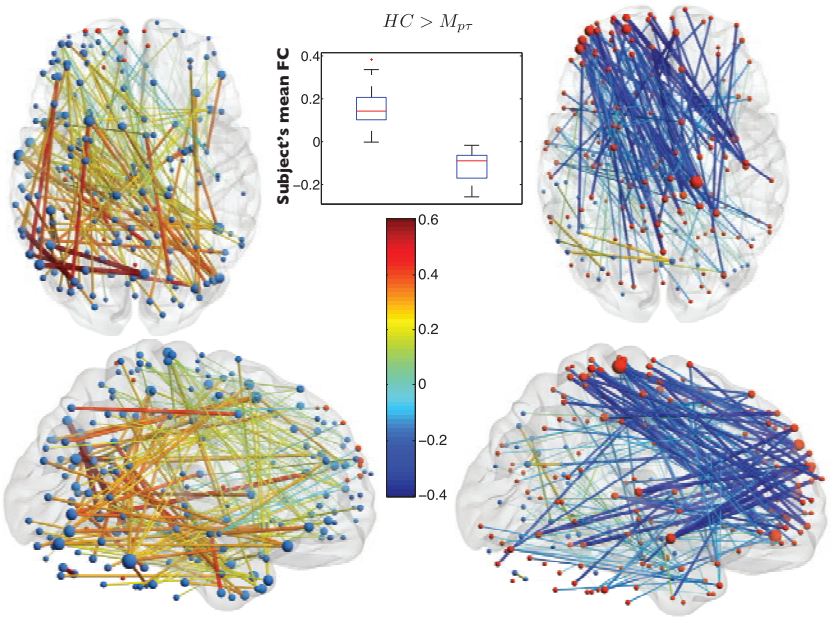

Figure 38: FC values on $\{HC > M_{p\tau}\}$.

7.6 HC versus MCI with pathological $a\beta$- and $p\tau$-levels

This MCI group consists of 18 subjects with both low levels of $a\beta$ and high levels of $p\tau$ (greater than 80 ng/l), corresponding to high levels of senile plaques and NFTs, respectively. These subjects are at very high risk of progressing to AD [4].

$M_{p\tau}$ has the highest difference relative controls in subject's mean FC on the set of links resulting from univariate testing (see box-plot in Fig. 38). Remarkably, all MCI subjects have negative and all HCs have positive mean FC on $\{HC > M_{p\tau}\}$. If the set of links $\{HC > M_{p\tau}\}$ could be used in a classification scheme (it cannot, since feature selection has been performed with all group subjects), then the relatively crude decision function $sgn(\sum_{i,j\in\{HC>M_{p\tau}\}} \phi_{ij})$ would suffice to classify all subjects.

We note a large set of links with negative correlations between the superior parietal region and left prefrontal cortex, which also has reduction into the negative with a set of nodes in the temporal lobe. We find links which in controls have large positive correlation connecting to the left posterior part, having been heavily reduced in the MCI group. Many links connecting diagonally across hemispheres with the posterior right, have switched sign relative HC.

The MIPs (see Figs. 39 and 40) reveal clusters of nodes with large strength differences in temporal mid left and frontal left parts, as well as parts of superior medial parietal with emphasis to the right. Both hippocampi appear with relatively large differences, but the value for the right one is twice as large.

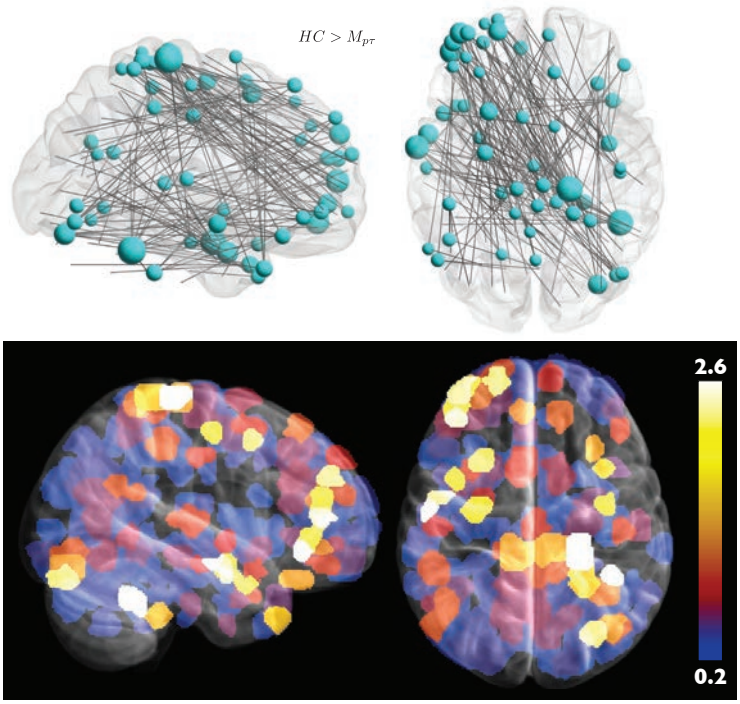

Figure 39: Threshold applied to strength difference (a) and MIP (b) of $\{HC > M_{p\tau}\}$.

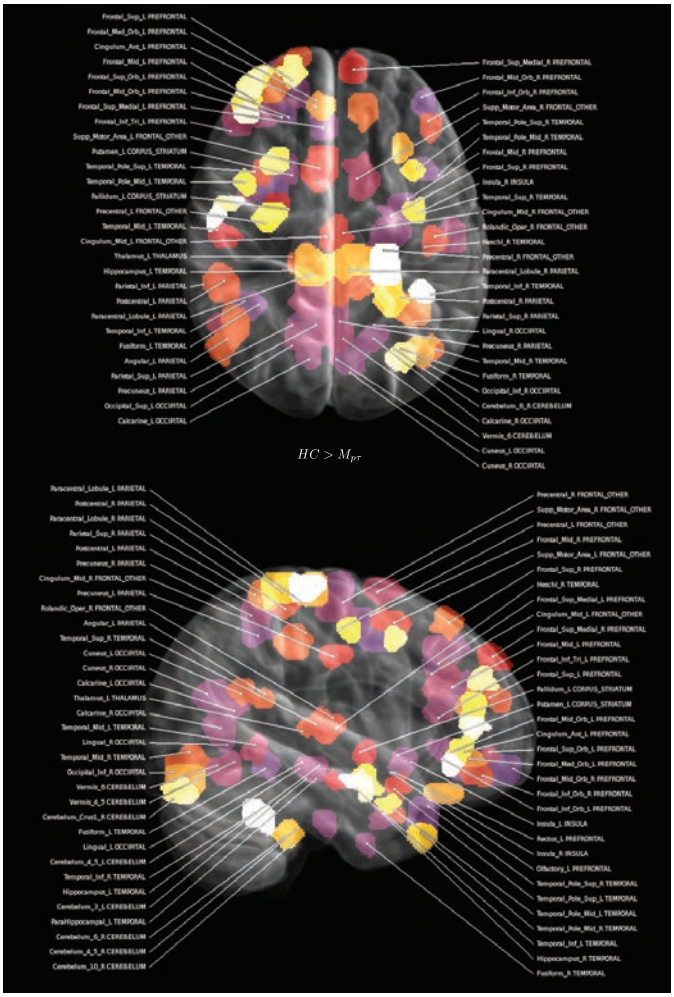

Figure 40: Threshold and labeling applied to strength difference MIP for $\{HC > M_{p\tau}\}$.

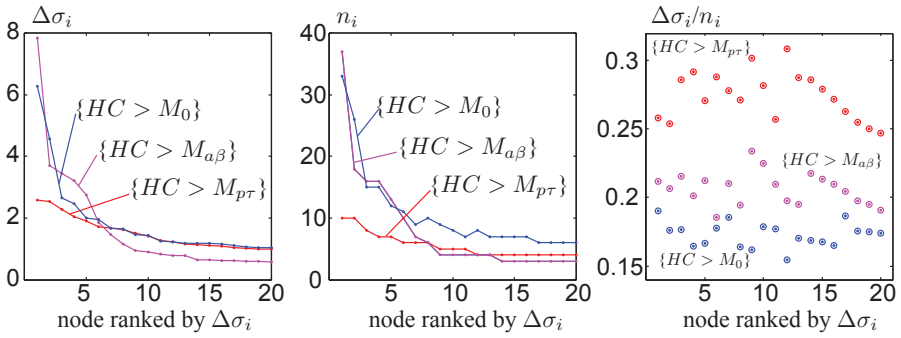

Figure 41: Difference in nodal strength ($\Delta\sigma_i$) on respective link set (left), the number of links (n_i) in strength values (center), and the mean FC difference ($\Delta\sigma_i$) on the subset of links contributing to the strength value (right). The x-axis corresponds to node number, ranked by $\Delta\sigma_i$ in the given link set.

We now proceed with the in-depth analysis of the connectivities of the nodes with greatest strength difference. The 13 nodes with greatest strength difference are listed in Table 8 and illustrated in Fig. 42.

Comparing table 8 with tables 6 and 7 we see that n_i for the nodes with very high $\Delta\sigma_i$ is generally greater in the latter two. This is reflected in the maximum strength differences: 6 with 10 links for $\{HC > M_{p\tau}\}$, 7.8 with 37 links for $\{HC > M_{p\tau}\}$, and 6.3 with 33 links for $\{HC > M_0\}$. However, the mean FC of the links forming the strength value has increased substantially in $\{HC > M_{p\tau}\}$.

Fig. 41 shows how the strength difference ($\Delta\sigma_i$), number of associated links (n_i) and mean FC difference ($\Delta\sigma_i/n_i$) varies for the sets $\{HC > M_{p\tau}\}$, $\{HC > M_{a\beta}\}$ and $\{HC > M_0\}$. Again, very little hard conclusions can be drawn regarding M_0. Naturally, the strength difference is related to the number of links involved and the differences are not as localized in $M_{p\tau}$ as in $M_{a\beta}$ with its corpus striatum hub. Initially larger, the $\{HC > M_{a\beta}\}$ link numbers drop from the nodes with the highest differences in strength (belonging to caudate), to coincide with the link numbers for $\{HC > M_{p\tau}\}$. Comparing the three plots of Fig. 41 shows that the origin of the greater $\Delta\sigma_i$ in $\{HC > M_{p\tau}\}$ relative $\{HC > M_{a\beta}\}$ is the link FC differences rather than their numbers.

The greatest strength difference $\Delta\sigma_i\{HC > M_{p\tau}\}$ occurs in a medial superior parietal part overlapping with both precentral R and postcentral R. Most of this difference originates in connections with prefrontal nodes, located in the frontal sup/med L and frontal mid/inf L parts. In addition two links in the left temporal lobe show reduced FC.

Next, temporal inf R has reduced FC to an area overlapping both amygdala R and hippocampus R, as well an area in overlapping amygdala L and putamen L. Interestingly, there is reduced FC to the symmetrically placed node of temporal inf R/cerebellum crus R in the left hemisphere. There is also a set of reduced FC links to the postcentral L area. Although $\Delta\sigma_i$ is large, it mainly comes from a reduction from high positive correlations in HC, to approximately zero correlation in $M_{p\tau}$, setting it apart from the majority of high $\Delta\sigma_i$ nodes which originate in negative correlations.

Temporal mid L (entry 3) has reduced connectivity to an area in temporal inf R, and more strikingly a cluster of nodes overlapping thalamus R, hippocampus R and parahippocampal R, and even a small part of thalamus L and hippocampus L. The strongest reduction in FC is to cingulum post L and we also find strongly reduced FC to the adjoining precuneus. Temporal mid L (entry 6 in table 8 neighboring entry 3) also has reduced FC to precuneus, and in addition cuneus/calcarine, and cerebellum crus R. This last part has in turn reduced FC with putamen L and several nodes in the left temporal lobe.

It is clear from the MIP of strength difference (see Fig. 40) that the left part of prefrontal cortex has several adjoining areas with reduced FC. One such area is in frontal inf orb L (entry 4 in table 8), which has its heaviest reduction in FC with an area overlapping thalamus L and hippocampus L, but also with a number of regions in the superior medial parietal area overlapping precuneus, paracentral lobule L and post/precentral. The nearby area, frontal mid L (entry 5), also has reduced FC with the superior parietal area, and additionally a single link to putamen R is affected.

Frontal mid/sup L occur frequently, most often failing with pre/postcentral - the superior medial parietal, preferentially on the right-hand side.

We note that front mid/inf orb L has reduced FC to thalamus L/hippocampus L (see entry 10 and 4). Hippocampus R, overlapping with putamen R and temporal sup R (entry 11), further reinforces the pattern of hippocampi-prefrontal disconnection, failing with both frontal inf/mid orb R and a cluster of

node i	$\Delta\sigma_i$	n_i	$\Delta\sigma_i/n_i$	connections [#] (fraction of $\Delta\sigma_i$)
1. precentral R, postcentral R	2.6	10	0.26	PRE [8]: frontal med/sup L, frontal mid/inf orb L, cingulum ant L (0.81)
				temporal pole sup L, temporal mid L
2. temporal inf R, cerebellum crus R	2.5	10	0.25	amygdala R, hippocampus R, putamen L; frontal inf oper/tri L; frontal mid L, precentral L
3. temporal mid L	2.3	8	0.29	PAR/OCC [4]: cingulum post L, precuneus, cuneus (0.51)
				hippocampus R, thalamus; temporal mid/inf R
4. frontal inf orb L	2.0	7	0.29	PAR [5]: precuneus, precentral R, postcentral R, paracentral lobule L, parietal sup L (0.71)
				thalamus L, hippocampus L, cerebellum R
5. frontal mid L	1.89	7	0.27	postcentral R, paracentral lobule L, parietal sup L; insula R, putamen R; cerebellum R
6. temporal mid L	1.7	6	0.29	cuneus L, precuneus L; calcarine R, lingual R, temporal mid R, cerebellum crus R
7. cerebellum crus R	1.7	6	0.28	TEM [3]: temporal mid L, temporal pole mid L (0.51)
				frontal inf orb R, frontal sup med R; insula L, putamen L
8. frontal sup L	1.6	6	0.27	PAR [4]: precentral R, postcentral R, supp motor area R, parietal sup R (0.67)
				temporal sup R, postcentral L
9. front mid/sup L	1.5	5	0.30	OCC [4]: occipital sup/mid L, occipital R (0.80)
				temporal pole mid R
10. front mid orb L	1.4	5	0.28	PAR [3]: precentral R, postcentral R, paracentral lobule R (0.60)
				thalamus L, hippocampus L; supramarginal R
11. putamen R, hippocampus R, temporal sup R	1.3	5	0.26	PRE [2]: frontal inf/mid orb R (0.36)
				PRE [3]: frontal sup/mid L, frontal sup med L (0.63)
12. precentral L, frontal sup L	1.2	4	0.30	frontal mid L; temporal mid R; cerebellum crus L
13. temporal pole mid L	1.2	4	0.28	cerebellum crus R, lingual R

Table 8: $\{HC > M_{p\tau}\}$ group mean strength differences, number of contributing links, and mean link FC. The last column summarizes connectivities behind the strength difference.

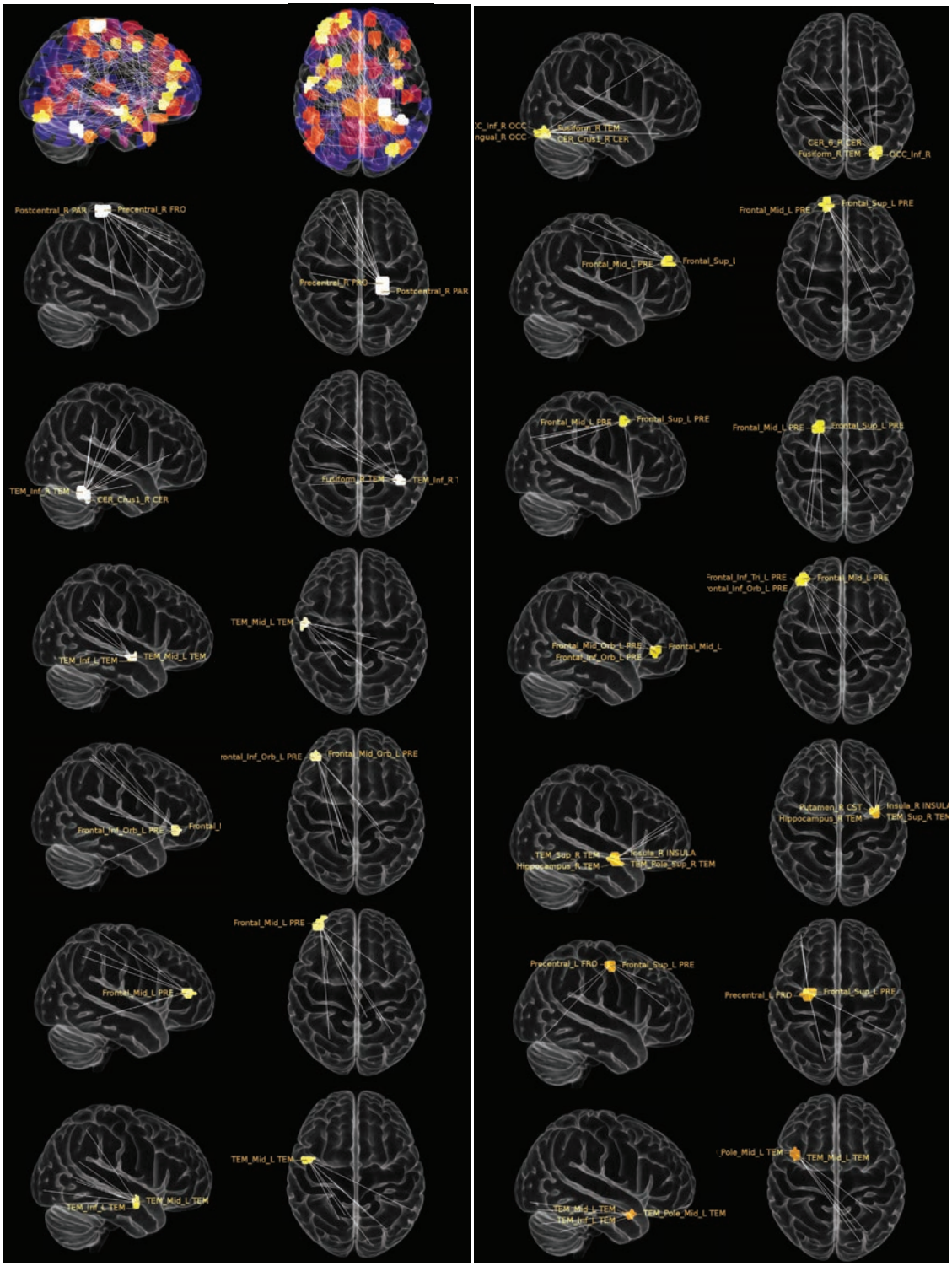

Figure 42: Connectivities of the 6 nodes with highest strength difference in table 8 for $\{HC > M_{p\tau}\}$.

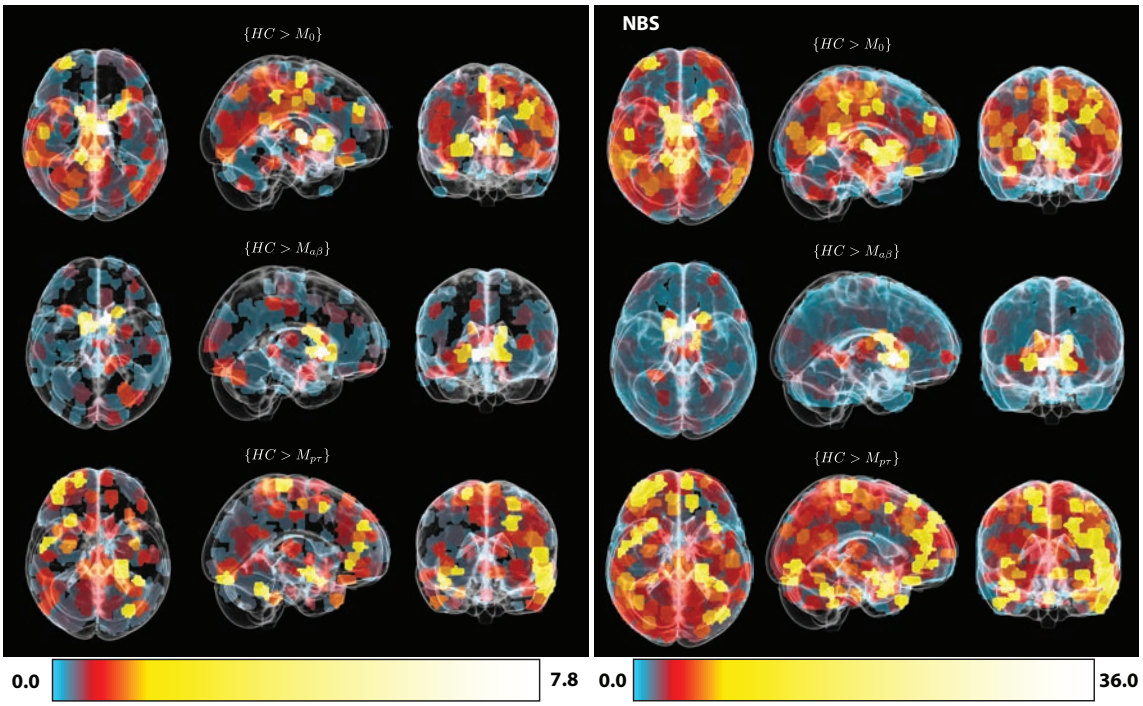

Figure 43: Strength differences of $\{HC > M_0\}$,$\{HC > M_{a\beta}\}$ and $\{HC > M_{p\tau}\}$ using a single common color-scale (FDR on left and NBS on right).

nodes in the left hemisphere: frontal sup/mid L and frontal sup med L.

The maximum strength difference in Fig. 39 is much lower than that of $\{HC > M_0\}$ and $\{HC > M_{a\beta}\}$ which can affect comparison with the two other sets. It is better to compare the strength differences across groups on a common scale and we choose the highest maximal strength difference over all group comparisons as a common maximum. Comparative plots with the same color-scale of strength differences for $\{HC > M_0\}$,$\{HC > M_{a\beta}\}$ and $\{HC > M_{p\tau}\}$ are shown in Fig. 43.

Although some similarities between the $\{HC > M_0\}$ and the other two groups can be found, comparison is always muddled by the heterogeneous character of M_0, and we focus our efforts on comparing $\{HC > M_{a\beta}\}$ and $\{HC > M_{p\tau}\}$. The similarity between $\{HC > M_0\}$ and $\{HC > M_{p\tau}\}$ is the corpus striatum hub, which in the former is located in thalamus and putamen rather than caudate.

There is an eyesore when comparing $\{HC > M_{a\beta}\}$ and $\{HC > M_{p\tau}\}$: the $\{HC > M_{a\beta}\}$ corpus striatum hub failure is not present or hardly visible in $\{HC > M_{p\tau}\}$. In fact, this pattern hints at a progression and we will address the possible reasons for the missing hub below, when summarizing of FC differences. For now we note that some areas, for example the left prefrontal lobe, medial parietal and left temporal areas, have weak pockets of strength differences that increase when going from $\{HC > M_{a\beta}\}$ to $\{HC > M_{p\tau}\}$.

Figs. 44, 45 and 46 show the link plots and strength difference for the NBS component $\{HC > M_{p\tau}\}$. In the link plot we see that the subject mean FC on the NBS component does not change significantly, and that the qualitative diagonal trend now extending to right anterior prefrontal cortex.

Thresholding the strength difference (see Fig. 45) produces a much more dense, but very similar pattern with lateralization to the left.

Comparing the MIPs, we see that the NBS strength difference maximum increases by a factor five, and the pattern spreads out, merging contiguous nodes. The added power of NBS reinforces the clusters comprising several nodes in the left temporal and prefrontal lobe. The prefrontal cluster expands to the superior, and the temporal cluster forms a contiguous chain of nodes stretching into the medial parts.

Also, cingulum posterior appears bilaterally with reduced connectivity to both hippocampi and parahippocampal parts, as well as frontal L and temporal L nodes (see Fig. 47 for cross sectional map). Hippocampus L and R appear with reduced strength, along with parahippocampal, putamen and amygdala. The difference in $\Delta\sigma_i$ between the right and left hippocampus is reduced in the NBS component.

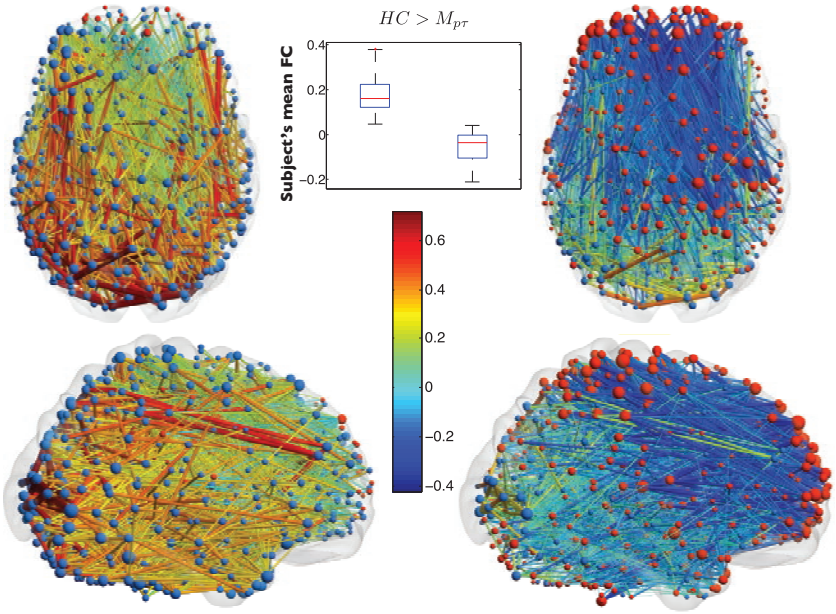

Figure 44: NBS component connectivity on $\{HC > M_{p\tau}\}$. HC on the left and $M_{p\tau}$ on the right.

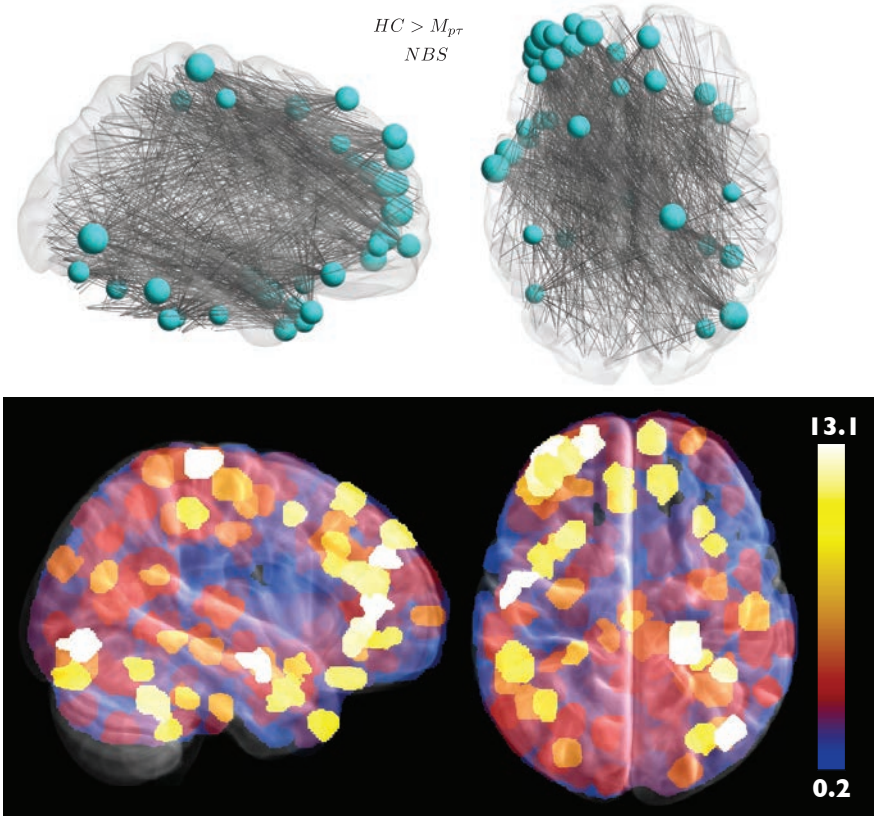

Figure 45: Strength difference for NBS component $\{HC > M_{p\tau}\}$.

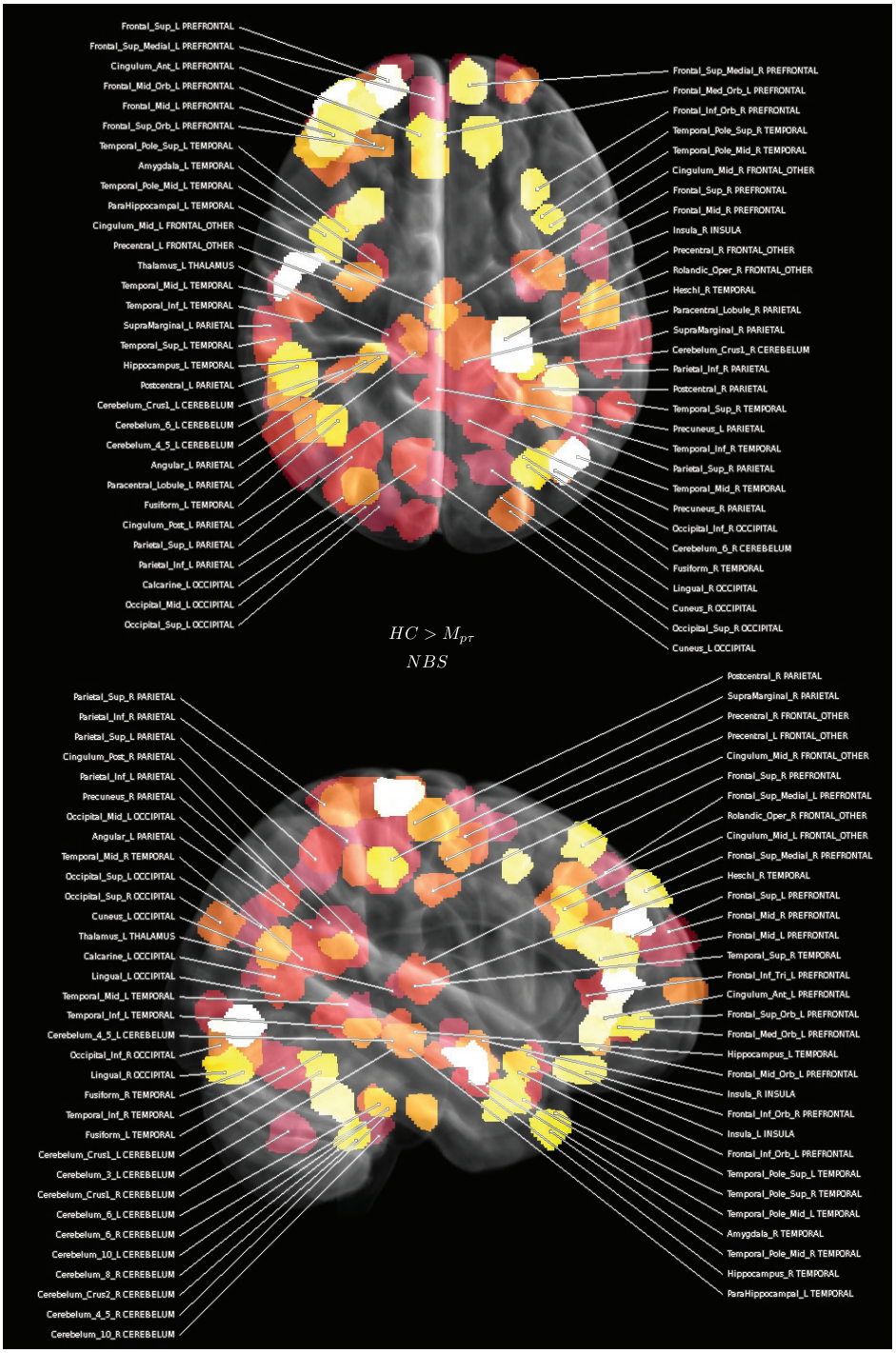

Figure 46: Suprathreshold and labeling algorithm applied to NBS component $\{HC > M_{p\tau}\}$.

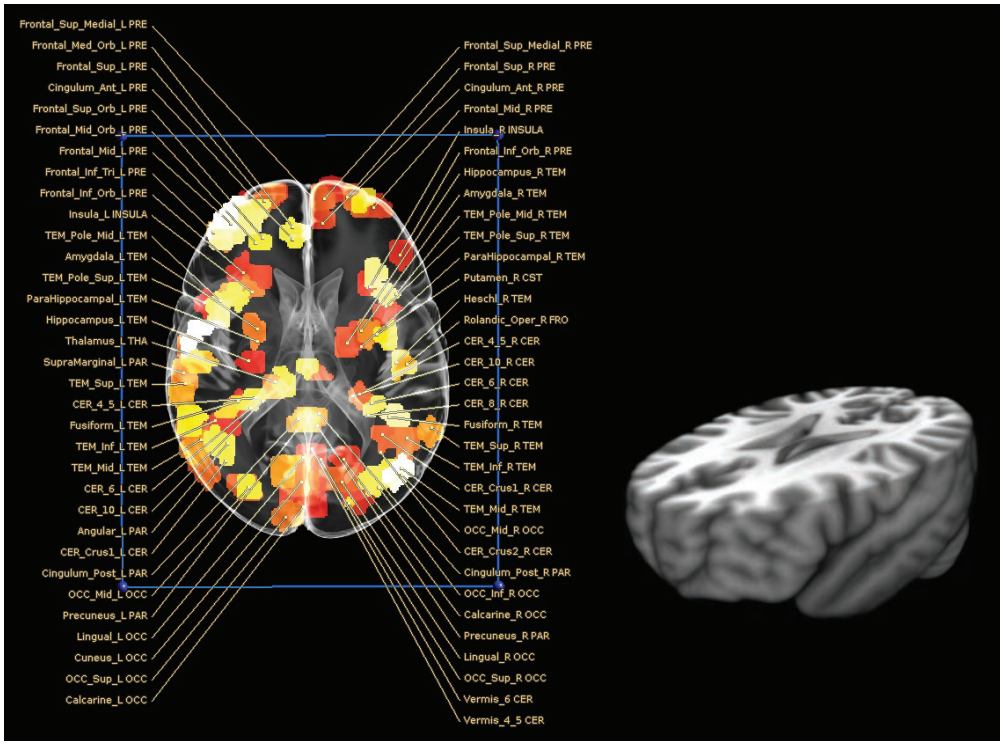

Figure 47: Cut revealing inferior regions (see right), to which suprathreshold and labeling algorithm has been applied to NBS component $\{HC > M_{p\tau}\}$, in order to expose hippocampus, parahippocampal areas, amygdala and cingulum posterior.

7.7 MCI with low vs high $a\beta$-levels

The NBS algorithm fails when it comes to MCI-MCI comparisons and we are left with results from univariate testing.

Although M_0 is difficult to compare with, we can draw some conclusions regarding its general position in the group landscape. Referring to the biomarker map in Fig. 15, we will now show results for panel (b), i.e. $M_0 \neq M_{a\beta}$. The link plots for $\{M_0 > M_{a\beta}\}$ and $\{M_0 < M_{a\beta}\}$ are shown in Figs. 48 and 49, MIPs of strength differences in Figs. 50 and 51.

$\{M_0 > M_{a\beta}\}$ involves a relatively small number of links on which M_0 subject's mean FC is centered on zero, and $M_{a\beta}$ has shifted to the negative side. Superior caudate L has reduced connectivity with symmetrically situated bilateral posterior temporal nodes, a few nodes in prefrontal L, and a contiguous set of nodes involving amygdala R, putamen R and hippocampus R. The latter also has reduced connectivity with frontal mid orb R.

Despite the smaller number of links in the set, some very interesting patterns emerge. The hippocampus/parahippocampal/amygdala R nodes connect mainly to different parts of caudate L, but there is also a link with a relatively large, negative weight to caudate R, despite the short distance between them.

There are similarities between $\{M_0 > M_{a\beta}\}$ and $\{HC > M_{a\beta}\}$ that imply a relative closeness of M_0 and HC. On the other hand, there are great differences manifested in $\{M_0 < M_{a\beta}\}$ with enhanced FC (see Fig. 49). Here we find links running mainly in the inferior-superior direction, scattered across the brain, with the single largest strength difference bilaterally in precuneus, and isolated pockets in post/precentral L and parahippocampal R. With the exception of these nodes, mostly isolated links between two otherwise unconnected nodes occur. The box-plot of the mean FC (see Fig. 49) indicates a smaller FC difference, something which can be clearly seen in Fig. 17 (c) and points to a pattern with a relatively poor separation. The distance distribution of links is fairly broad (see Fig. 18) and a positive skewness indicates a bias towards shorter links (see table 4).

Although we can certainly benchmark our MCI groups against HC, comparing the MCI-groups directly has one distinct advantage: the absence of biomarker data for HC circumvents the potential contamination with undiagnosed MCI. On the other hand, we are faced with a plethora of possible MCI conditions in M_0.

Turning now to the $f = 0.01 - 0.03$ Hz versions of $\{M_0 \neq M_{a\beta}\}$, link plots and MIPs are shown in

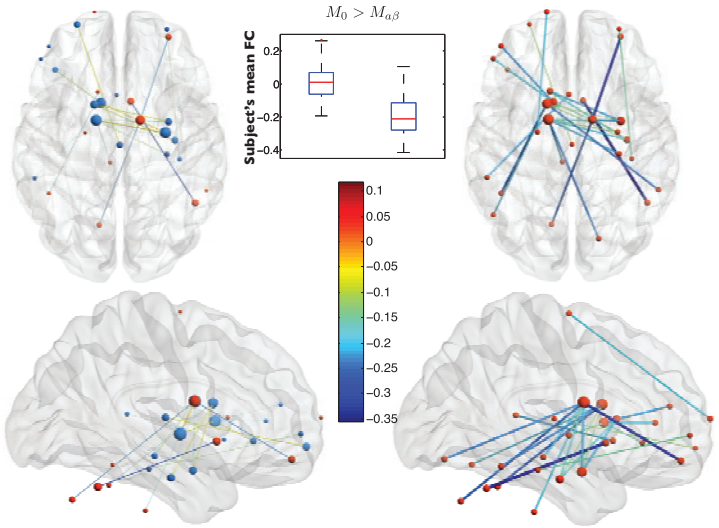

Figure 48: Connectivity of M_0 (left) and $M_{a\beta}$ (right) on the set $\{M_0 > M_{a\beta}\}$.

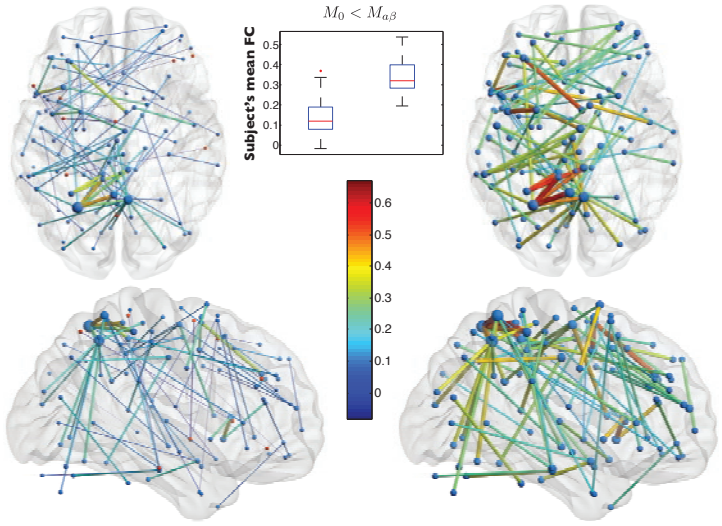

Figure 49: Connectivity of M_0 (left) and $M_{a\beta}$ (right) on the set $\{M_0 < M_{a\beta}\}$.

Figs. 52-55. The pattern in Fig. 52 also contain links with superior caudate L, but appears otherwise random with more isolated links. The distance distribution for the compensatory FC in $f = 0.01 - 0.03$ Hz is very similar to that of the adjacent band and we also find links running in inferior-superior direction. There are two interpretations of the 'spill-over' effect into the lower frequency band.

1. The slowing down of oscillations is something that could occur in the earlier phases of cognitive decline, causing the appearance of enhanced FC in the lower interval. This occurs with a geometrically similar, simultaneous compensatory enhancement of FC in $f = 0.03 - 0.06$ Hz.

2. The appearance of patterns in a lower frequency interval could be symptomatic of another affliction, connected with e.g. the structural changes in vascular dementia, that populates M_0. The fact that the major low frequency pattern appears when comparing with M_0 supports this hypothesis.

Again attributable to the diffuse character of M_0, interpretation number 2 appears most feasible - patterns of high discriminative power can lodge in different bands depending on affliction (for example schizophrenia [49]).

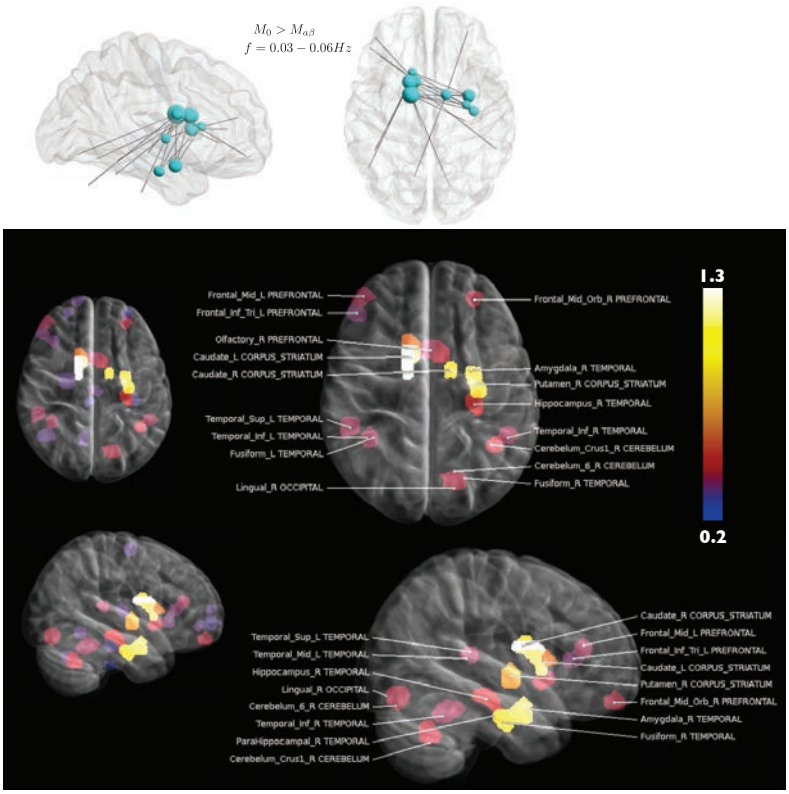

Figure 50: Threshold applied to strength difference (top row) for $\{M_0 > M_{a\beta}\}$, MIP of strength difference (center), and MIP with applied labeling algorithm (bottom).

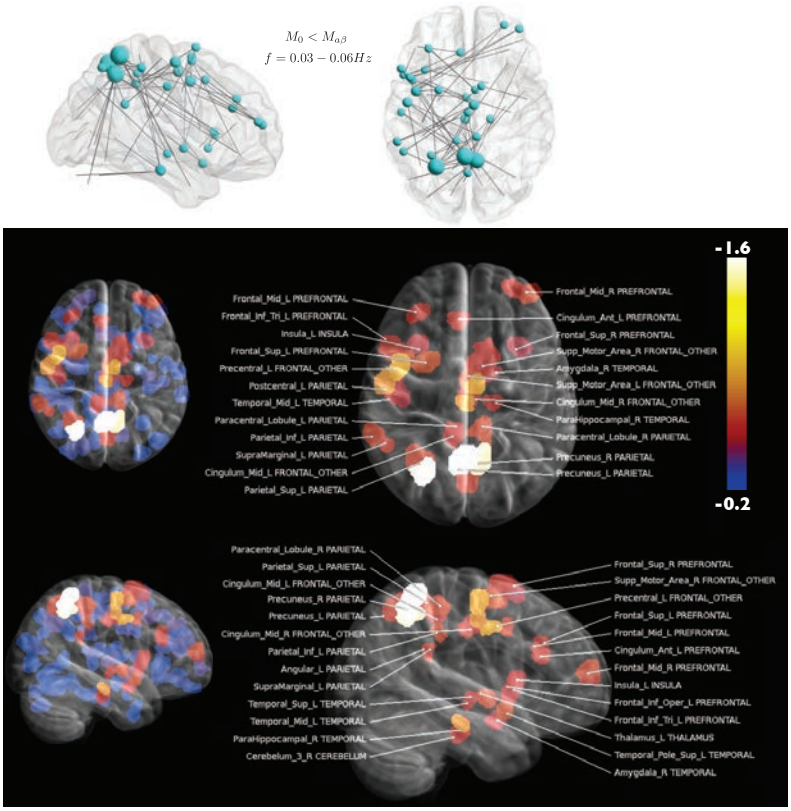

Figure 51: Threshold applied to strength difference (top row) for $\{M_0 < M_{a\beta}\}$, MIP of strength difference (center), and MIP with applied labeling algorithm (bottom).

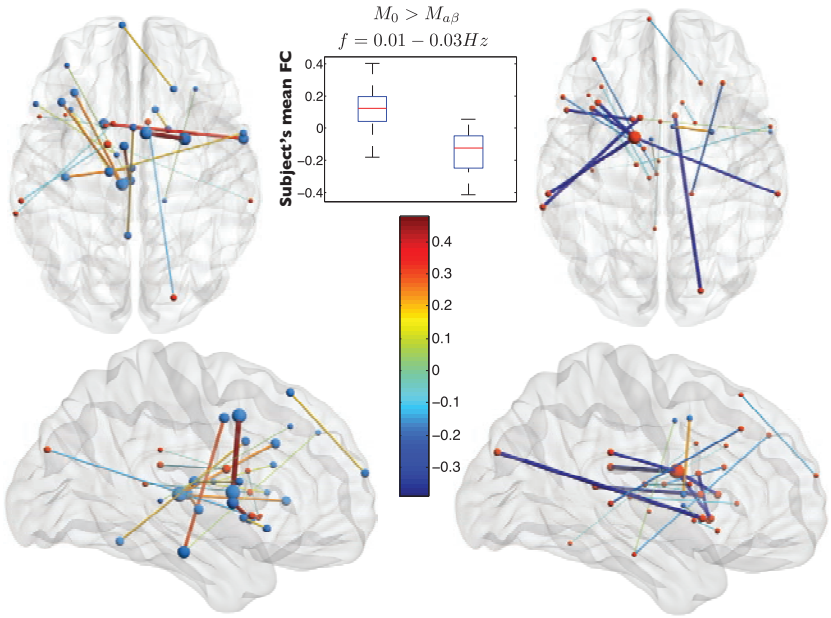

Figure 52: Connectivity in $f = 0.01 - 0.03$ Hz of M_0 (left) and $M_{a\beta}$ (right) on the set $\{M_0 > M_{a\beta}\}$.

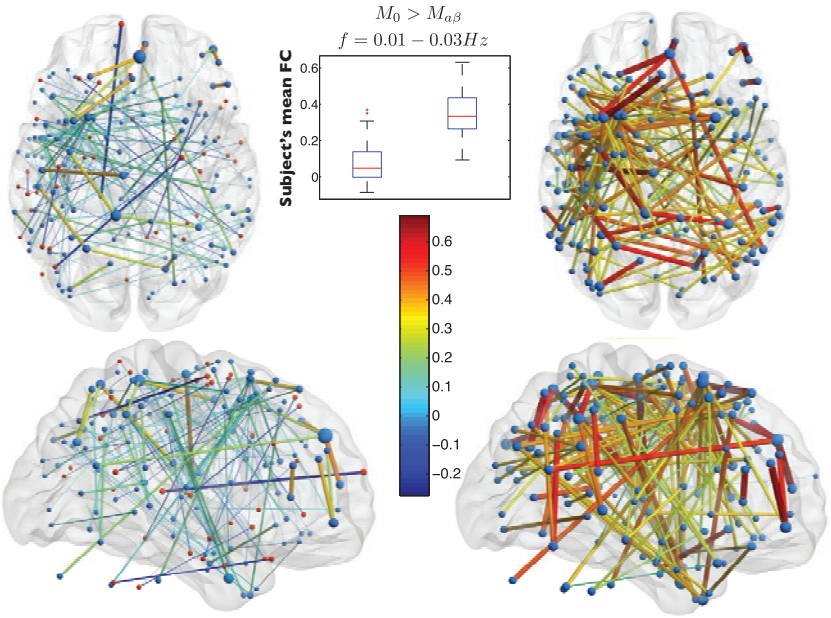

Figure 53: Connectivity in $f = 0.01 - 0.03$ Hz of M_0 (left) and $M_{a\beta}$ (right) on the set $\{M_0 < M_{a\beta}\}$.

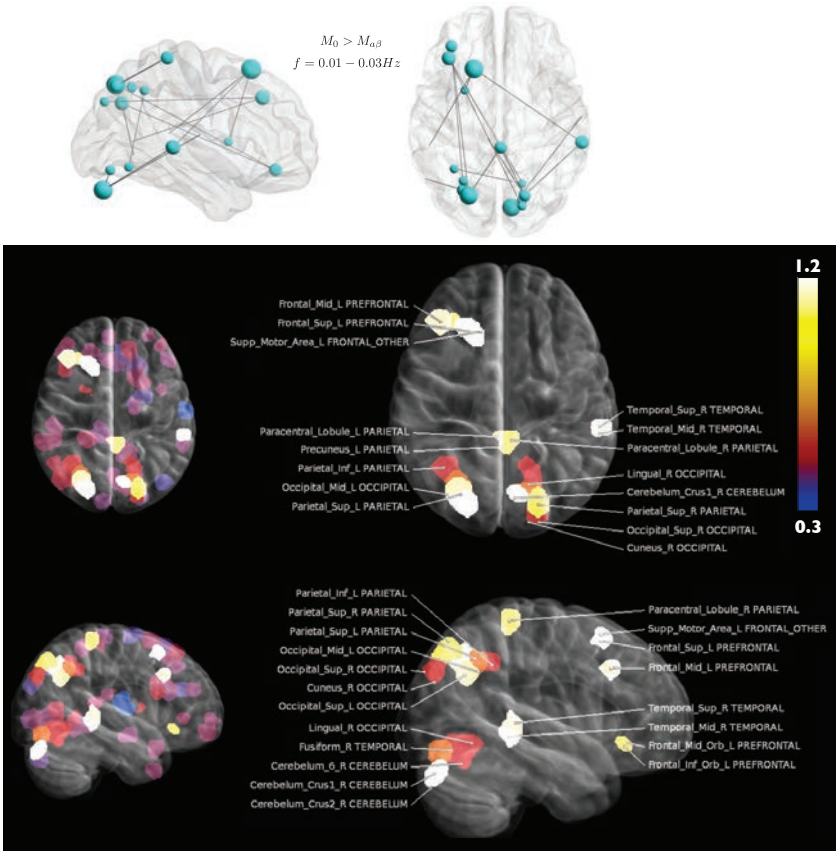

Figure 54: Threshold applied to strength difference (top row) for $\{M_0 > M_{a\beta}\}$ and $f = 0.01 - 0.03$ Hz, MIP of strength difference (center), and MIP with applied labeling algorithm (bottom).

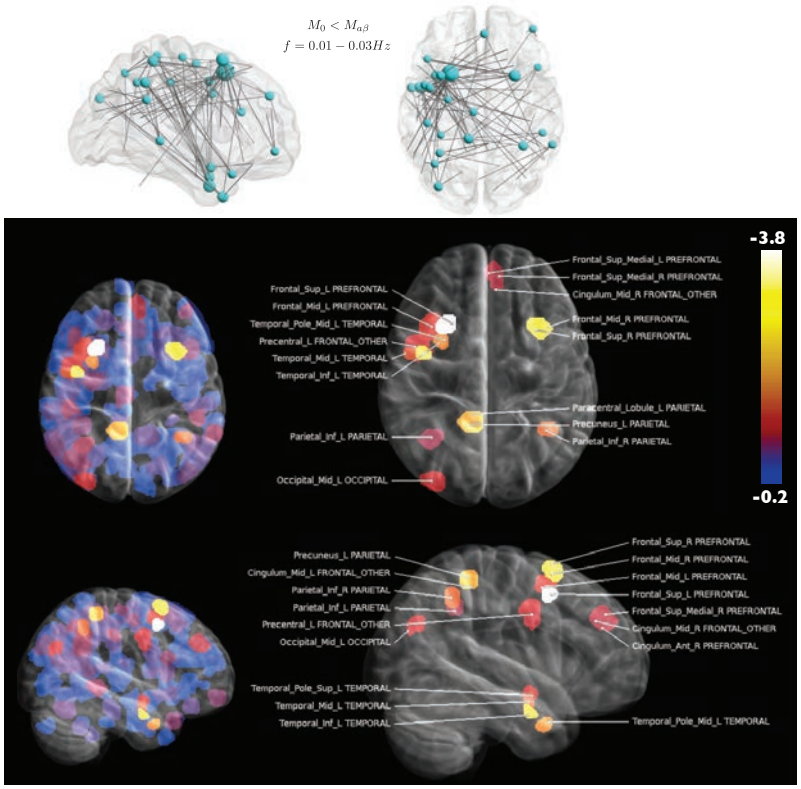

Figure 55: Threshold applied to strength difference (top row) for $\{M_0 < M_{a\beta}\}$ and $f = 0.01 - 0.03$ Hz, MIP of strength difference (center), and MIP with applied labeling algorithm (bottom).

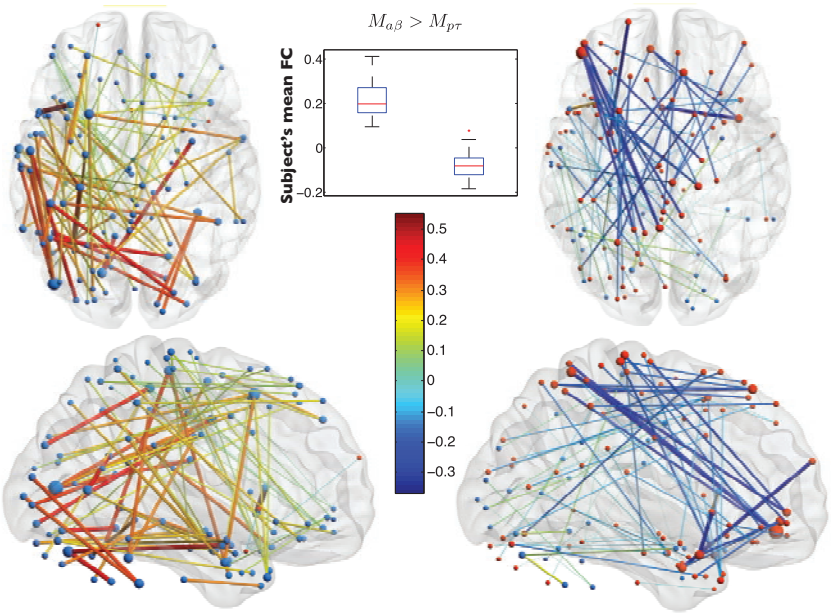

Figure 56: Connectivity of $M_{a\beta}$ (left) and $M_{p\tau}$ (right) on the set $\{M_{a\beta} > M_{p\tau}\}$.

7.8 MCI with low vs high $p\tau$-levels

Here we directly compare the two groups of MCI that have low levels of $a\beta$/high amyloid burden, one of which has high levels of $p\tau$ (more than 80 ng/l CSF) and NFTs. Whereas both groups suffer high risk of developing AD, the group with $p\tau > 80$ ng/l is presumably in the latter stages of progression.

Connectivities of $M_{a\beta}$ and $M_{p\tau}$ on the link sets $\{M_{a\beta} > M_{p\tau}\}$ and $\{M_{a\beta} < M_{p\tau}\}$ are shown in Figs. 56 and 57 and corresponding MIPs of strength differences in Figs. 58 and 59.

Comparing Figs. 38 and 56 we see a similar difference in mean FC in $\{HC > M_{a\beta}\}$ and $\{M_{a\beta} > M_{p\tau}\}$ and a qualitatively similar contrast, although certainly weaker and $\{HC > M_{a\beta}\}$ has many more parietal/temporal-prefrontal links.

$\{M_{a\beta} < M_{p\tau}\}$ displays some structure with nodes in the left temporal lobe connecting to caudate nuclei (and a single link between hippocampus R and caudate L). This structure contributes to a reduction in FC magnitude that leaves $\{HC > M_{p\tau}\}$ with a gaping hole replacing the failing central corpus striatum hub. Comparing the connectivity of hippocampus R and caudate L across $\{M_0 > M_{a\beta}\}$ and $\{M_{a\beta} < M_{p\tau}\}$, we note that the reduced FC value between $M_0 \to M_{a\beta}$ increases for $M_{a\beta} \to M_{p\tau}$. The increase in FC is however not as great as in the initial reduction. The reason for this seemingly paradoxal behavior, hints at a fundamental mechanism of connectivity evolution with progression, which we will attempt to clarify in the sections to come. For now, we note a crucial piece of information: almost all the links in $M_{a\beta} < pt$ swing from negative to values close to zero.

The MIPs (see Figs. 40 and 58) reinforce the image of a strong qualitative correspondence despite a weaker contrast.

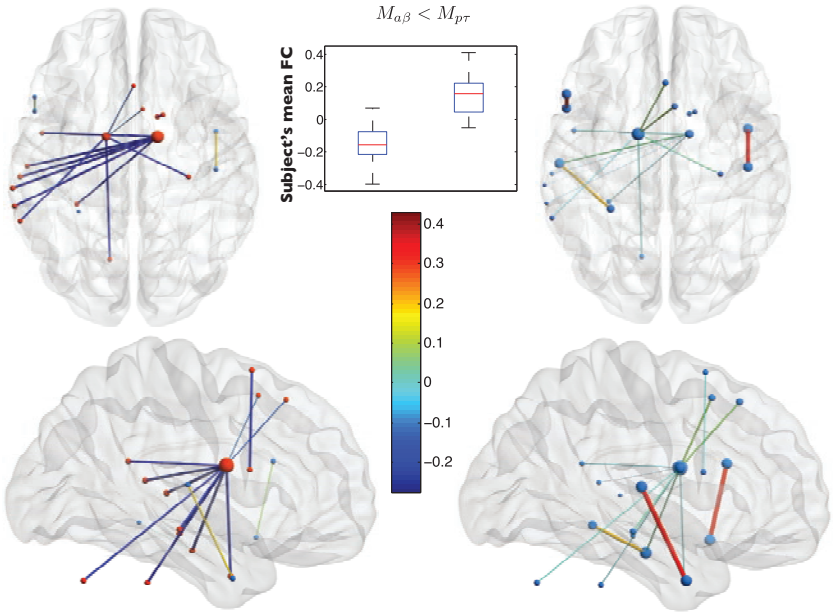

Figure 57: Connectivity of $M_{a\beta}$ (left) and $M_{p\tau}$ (right) on the set $\{M_{a\beta} < M_{p\tau}\}$.

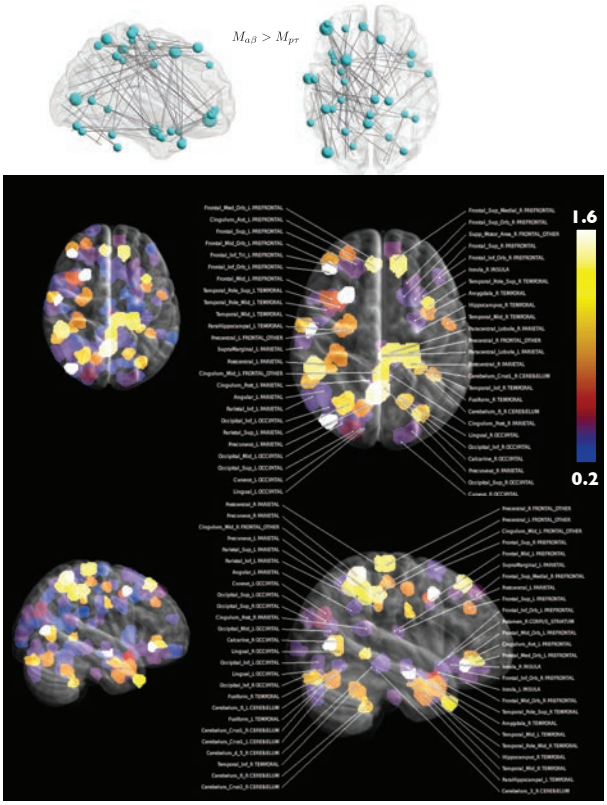

Figure 58: Threshold applied to strength differences on the set $\{M_{a\beta} > M_{p\tau}\}$ (a), MIPs of strength differences (b) and labeling algorithm and threshold applied to MIPs (c,d).

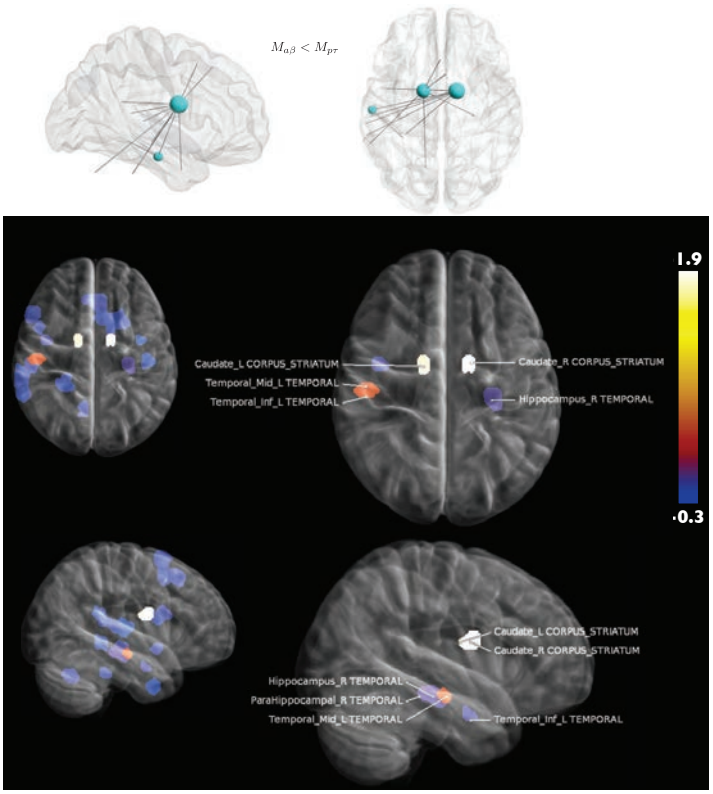

Figure 59: Threshold applied to strength differences on the set $\{M_{a\beta} < M_{p\tau}\}$ (a), MIPs of strength differences (b), and labeling algorithm/threshold applied to MIPs (c,d).

7.9 Controls versus AD

The confirmed AD group consists of 8 subjects (9 before applying QA) and the results should be interpreted with caution. The connectivity of $\{HC > AD\}$ is shown in Fig. 60 and corresponding strength differences in 61.

With the exception of one suspicious looking individual, all subjects have negative mean FC on $\{HC > AD\}$, whereas the HC are positive, neatly separating the groups by the sign of the summed connectivity.

As expected, we find similarities with the $\{HC > M_{p\tau}\}$, but also some striking differences. With the caveat of a low number of subjects, we note that although the diagonal pattern of long links across hemispheres appears to be present, there are holes in $\{HC > AD\}$ corresponding to clusters of nodes in $\{HC > M_{p\tau}\}$. For example the cluster in the prefrontal and the temporal left lobes are absent. Indeed, the nodes with high strength differences seem to have shifted to neighboring nodes. Bilateral parahippocampal areas flare up on the MIPs, as does hippocampus R and to a lesser extent hippocampus L. These nodes have predominantly reduced FC with frontal mid/sup areas.

The NBS component search fails to converge for the high-resolution ROI-set with 840 nodes, but does however converge for 392 ROIs. This is most likely due to the increased variability of functional connectivity breakdown in the confirmed AD state. Fig. 62 shows the 392-ROI component for $\{HC > AD\}$, where the absence of nodes in the left frontal and temporal lobes can be clearly seen. Comparing the MIPs for the $N = 392$ NBS components of $\{HC > p\tau\}$ and $\{HC > AD\}$ in Figs. 62 and 63, exposes the trend further.

In the next section we will summarize how functional connectivity changes with biomarker configuration, and attempt to interpret the results as an expression of disease progression, with valuable insight into the regional decline of functional networks with increasingly pathological levels of CSF biomarkers.

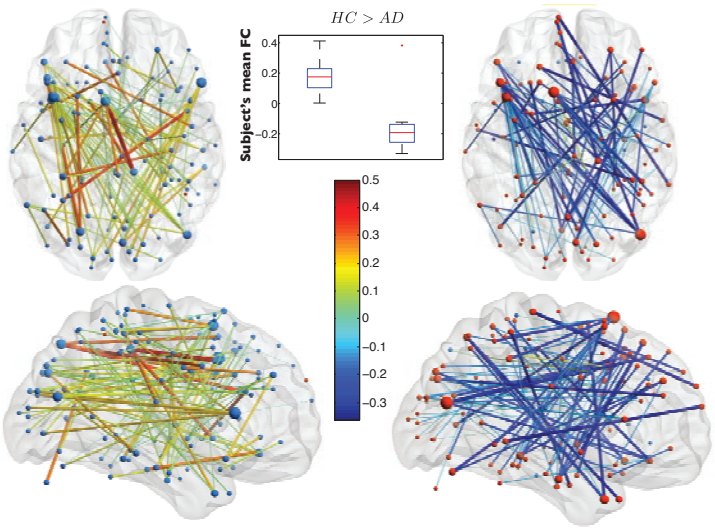

Figure 60: Connectivity on the set $\{HC > AD\}$.

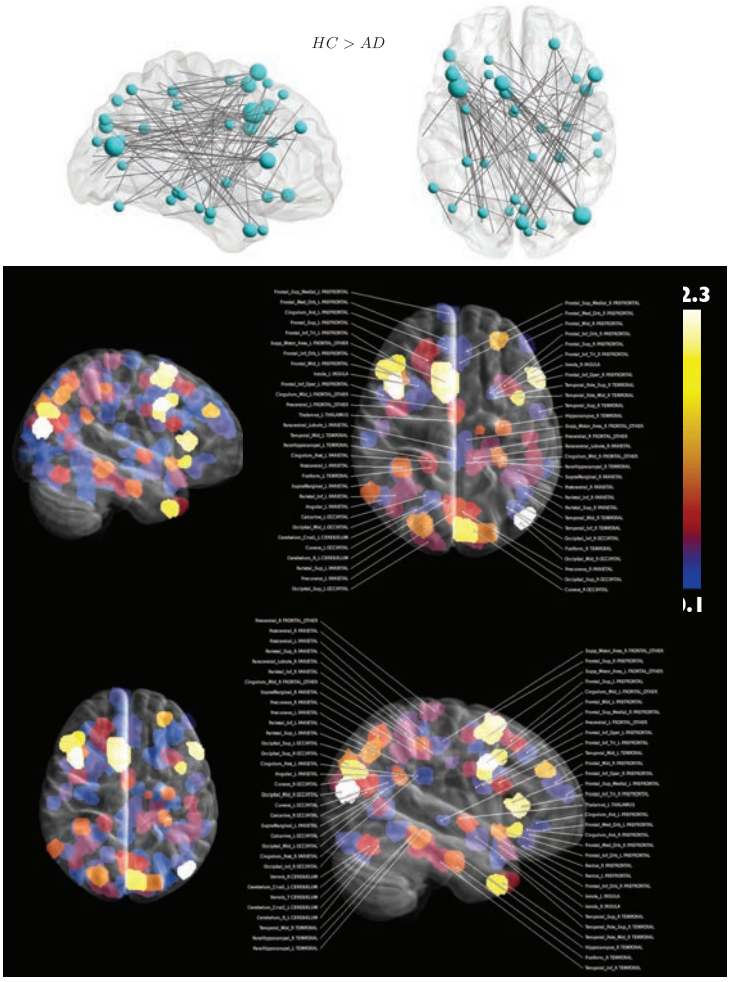

Figure 61: Threshold applied to $\{HC > AD\}$ strength difference (a) and MIPs of strength difference. max is 2.9, min 0.2

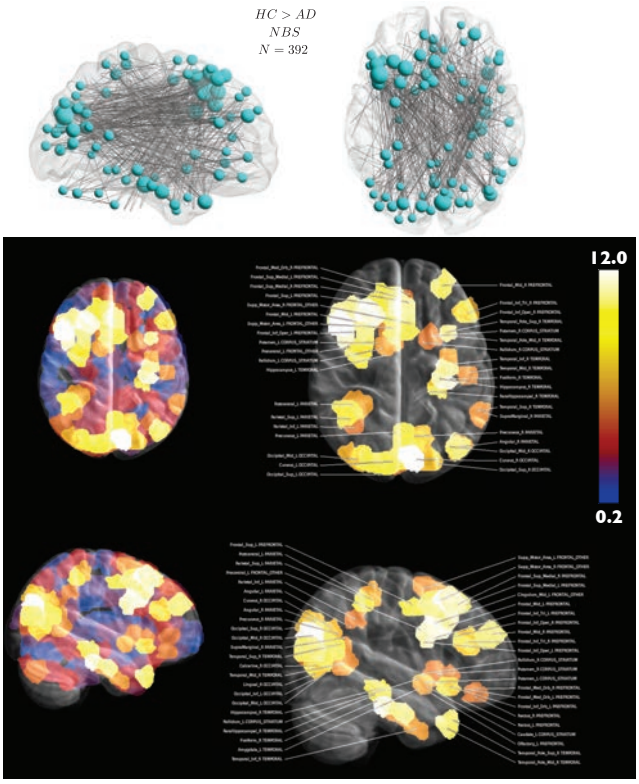

Figure 62: MIP of NBS component for $\{HC > AD\}$ using 392 ROIs.

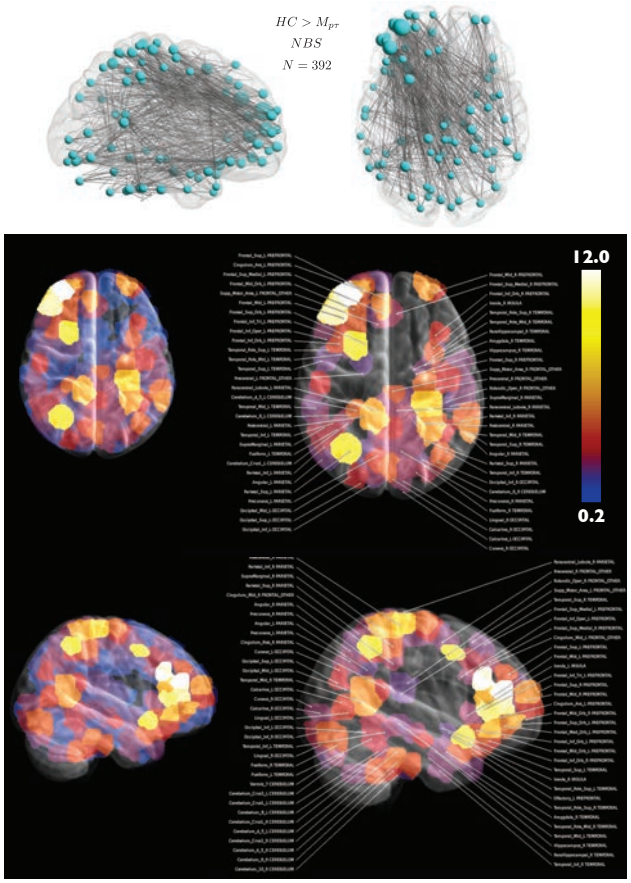

Figure 63: MIP of NBS component for $\{HC > M_{p\tau}\}$ using 392 ROIs.

8 Summary of connectivity in biomarker space

In this section we summarize the essential features of connectivity variation in biomarker space over all groups (following Fig. 15): $\{HC \neq M_0\}$, $\{M_0 \neq M_{a\beta}\}$, $\{HC \neq M_{p\tau}\}$, $\{M_{a\beta} \neq M_{p\tau}\}$, $\{HC \neq M_{p\tau}\}$, $\{HC \neq AD\}$.

1. $\{HC \neq M_0\}$. M_0 subjects have an MCI diagnosis, but non-pathological levels of both $a\beta$ and $p\tau$, possibly representing a plethora of conditions. This group has a widespread, diffuse and relatively weak FC reduction relative controls [see Figs. 15 (a) and 22]. Masked by this diffuse pattern, we see the emergence of large strength differences in a central hub region in the inferior corpus striatum area involving primarily putamen and thalamus (see Figs. 23 and 24). This hub has failing connections to a parietal region (involving postcentral L), medial superior region (involving precuneus, cingulum post/mid), occipital parts (involving cuneus and occipital inf). Cingulum post has reduced connectivity to the left temporal left lobe, which in turn has reduced FC to hippocampus L. Hippocampus R has reduced FC with nodes in right prefrontal cortex. Cingulum post, parahippocampal R, amygdala R and anterior parts of hippocampus appear with clearer strength differences in the NBS component. The relevance of these patterns for progression to AD is unclear due to the inhomogeneity of M_0. However, the subgroup of interest is contained therein and we can look for similarities with $\{HC > M_{a\beta}\}$ in an attempt to isolate relevant patterns. Subject's mean FC difference on $\{HC > M_0\}$ is the lowest of all HC-MCI comparisons.

2. $\{M_0 \neq M_{a\beta}\}$. Comparing M_0 directly to $M_{p\tau}$ gives us an idea of how the transition to pathological levels of $a\beta$ affects connectivity, keeping in mind that M_0 contains a wide variety of MCI. $\{M_0 > M_{a\beta}\}$ reveals larger areas of corpus striatum failing - for example a superior part of caudate L flickers out as $a\beta$ drops, with reduced FC to many temporal nodes, e.g. a cluster containing amygdala R, putamen R, and parahippocampal R/hippocampus R. $\{M_0 < M_{p\tau}\}$ contains mainly scattered links with few exceptions of several links connected to one node, e.g. precuneus. The connectivity of key areas linked with cognitive decline is reduced, i.e. caudate nucleus and hippocampus R, parahippocampal R and amygdala R. How the $\{M_0 < M_{p\tau}\}$ should be interpreted is related to the character of M_0 - a matter to which we will return below. Patterns in $f = 0.01 - 0.03$ Hz have similarities with the higher frequency interval, but contain a large, seemingly random component as evidenced by the number of isolated links. It may represent oscillation slowdown in initial stages of connectivity deterioration and/or an artifact of M_0 group inhomogeneity.

3. $\{HC \neq M_{a\beta}\}$. As $a\beta$ drops below 550 ng/l, the reduced FC pattern of $\{HC > M_{a\beta}\}$ has condensed to reveal a more sharply defined corpus striatum hub (see Fig. 15). The hub now primarily comprises caudate nuclei and putamen (see Figs. 39 and 40). Caudate R has a very large set of reduced FC links with qualitative similarities to the area with the greatest strength difference in $\{HC > M_0\}$: thalamus R, in close proximity. Caudate L extends over a greater volume and encompasses superior parts of corpus striatum, having reduced connectivity with several key areas: hippocampus, parahippocampal, temporal mid, cingulum post, as well as many occipital and prefrontal nodes. Both hippocampi figure more prominently in $M_{a\beta}$ and the right side is again more pronounced, forming part of a contiguous group containing parahippocampal R, amygdala R and putamen R, in proximity to (and with reduced FC to) caudate R. The NBS component has a stronger anterior parahippocampal/hippocampus L difference. Subject's mean FC relative HC on $\{HC > M_{a\beta}\}$ is greater than that of $\{HC > M_0\}$ and virtually all values for $M_{a\beta}$ are now in the negative.

4. $\{M_{p\tau} \neq M_{a\beta}\}$ offers insights regarding the transition from lower to higher $p\tau$-levels. $\{M_{a\beta} > M_{p\tau}\}$ is similar to $\{HC > M_{p\tau}\}$, albeit with a weaker contrast containing fewer parietal-prefrontal links. $\{M_{a\beta} < M_{p\tau}\}$ contains a very small set of links associated with caudate nuclei, shifted to from negative to values of small magnitude. Comparing $\{M_0 > M_{a\beta}\}$ and $\{M_{a\beta} < M_{p\tau}\}$ reveals a striking correspondence between the decrease in FC between the key areas of caudate and hippocampus for the transition $M_0 \rightarrow M_{a\beta}$ and the increase in FC between the same areas for $M_{a\beta} \rightarrow M_{p\tau}$. This observation hints at a fundamental pattern of cognitive decline profoundly related to physiological mechanisms at work.

5. $\{HC \neq M_{p\tau}\}$. When $p\tau$ increases above 80 ng/l we find a large set of links with heavy reduction in FC. Clusters of nodes with high $\{HC > M_{p\tau}\}$ strength difference appear primarily in temporal mid left lobe, prefrontal left lobe and a superior medial parietal region (with more weight on the right). There are many links with reduced FC between the superior parietal and prefrontal L regions. Temporal mid L has reduced FC with hippocampus, thalamus and cingulum post/precuneus.

Frontal nodes with reduced FC to the superior parietal region also have decreased correlation with hippocampus, putamen R and parts of the right temporal lobe. Very large strength differences are also found in temporal inf R having reduced FC to hippocampus/amygdala R and putamen/amygdala L. The general pattern can be summarized as primarily prefrontal L-superior parietal failure, but also prefrontal/temporal L-parahippocampal, temporal L-cingulum post/precuneus/cuneus reduced FC. Again, hippocampus R figures more prominently. The reduced FC corpus striatum hub previously observed shines with its absence. Subject's mean FC difference $\{HC > M_{p\tau}\}$ is the greatest of all HC-MCI, with positive values for HC and negative for $M_{p\tau}$.

6. $\{HC \neq AD\}$. Finally, we compared HC to AD, with the major caveat of having only 8 AD subjects. The $\{HC > AD\}$ pattern has both quantitative and qualitative similarities to $\{HC > M_{p\tau}\}$, but there are also some crucial differences. The HC-AD difference in subject's mean FC is slightly greater in $\{HC > AD\}$, as one would expect. On the other hand, there are fewer links which, although they follow a parietal-prefrontal connection pattern similar to $\{HC > M_{p\tau}\}$, clearly lack the clusters of nodes in left temporal and prefrontal lobes. Hippocampus, predominantly on the right side, exhibit reduced FC to frontal mid/sup. The NBS component search fails for $\{HC > AD\}$, which may be connected to increased variability and too few subjects.

9 Progression

In this section, we will attempt to connect the above outlined patterns and identify progression between them. This leads us to postulate an hypothesis related to the fundamental mechanisms at work. Finally, we will attempt to verify this hypothesis by a series of targeted tests.

To begin with, we will outline the quantitative trend in terms of the FC reduction magnitude, and then move on to evaluate pattern changes. Keeping in mind the similarities between $\{HC > M_{a\beta}\}$ and $\{M_{a\beta} > M_{p\tau}\}$, we have also seen similarities between $\{HC > M_{a\beta}\}$ and $\{M_0 > M_{a\beta}\}$. Considering $\{M_0 < M_{a\beta}\}$ largely as an artifact of M_0 inhomogeneity, we see that qualitatively, M_0 is more similar to HC than $M_{a\beta}$, which in turn is closer to HC than $M_{p\tau}$. These relations carry over to quantification in terms of distributions of subjects mean FC (comparing boxplots in corresponding link plots):

$$\delta(M_0) > \delta(M_{a\beta}) > \delta(M_{p\tau}), \tag{15}$$

where $\delta(G)$ is the difference between mean FC of MCI group G and HC on the link set $\{HC > G\}$,

$$\delta(G) \equiv \Phi(HC, \{HC > G\}) - \Phi(G, \{HC > G\}), \tag{16}$$

in which we have further defined $\Phi(G, \{S\})$ as the mean FC over N_S links in the set S and N_G subjects of group G,

$$\Phi(G, \{S\}) \equiv \frac{1}{N_G N_S} \sum_{s=1}^{N_G} \sum_{i,j \in S} \phi_{s,ij}. \tag{17}$$

To get an idea of the relative importance of the two biomarkers, we may drop the $a\beta$ condition altogether and simply compare MCI with $p\tau < 80$ to $p\tau > 80$. The results are shown in Fig. 64. Comparing with Fig. 15, we see that the $\{(p\tau < 80) < (p\tau > 80)\}$ pattern is very similar to $\{M_{a\beta} < M_{p\tau}\}$, reaffirming the relative strength of contrasts, with $p\tau > 80$ being the strongest.

We now proceed to look for a progression in patterns and seek to identify fronts and epicenters of functional connectivity degradation. All the while, we log essential nodes and earmark them for further investigation. Figs. 65 show strength differences of group means on $\{HC > M_0\}$, $\{HC > M_{a\beta}\}$ and $\{HC > M_{p\tau}\}$ on the same color-scale with applied suprathreshold and labeling algorithm. These images are useful when comparing ROIs across groups that have similar anatomical labels but actually correspond to different functional centers.

Let us begin by considering the actual group mean strength (rather than strength differences) of HC, $M_{a\beta}$, $M_{p\tau}$ and AD on the two link sets $\{HC > M_{a\beta}\}$ and $\{HC > M_{p\tau}\}$ shown in Fig. 66. The purpose of plotting strength on the wrong set of links is to highlight variations from the means of $M_{a\beta}$ and $M_{p\tau}$ with biomarker. We cannot expect a progression pattern to pop out, because we are simply

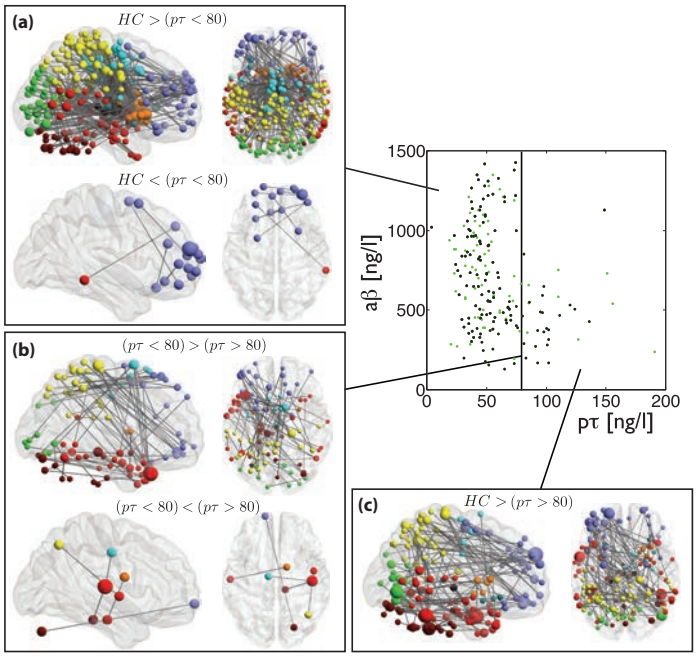

Figure 64: Results of dropping the $a\beta$ condition and simply comparing $p\tau > 80$ to $p\tau < 80$.

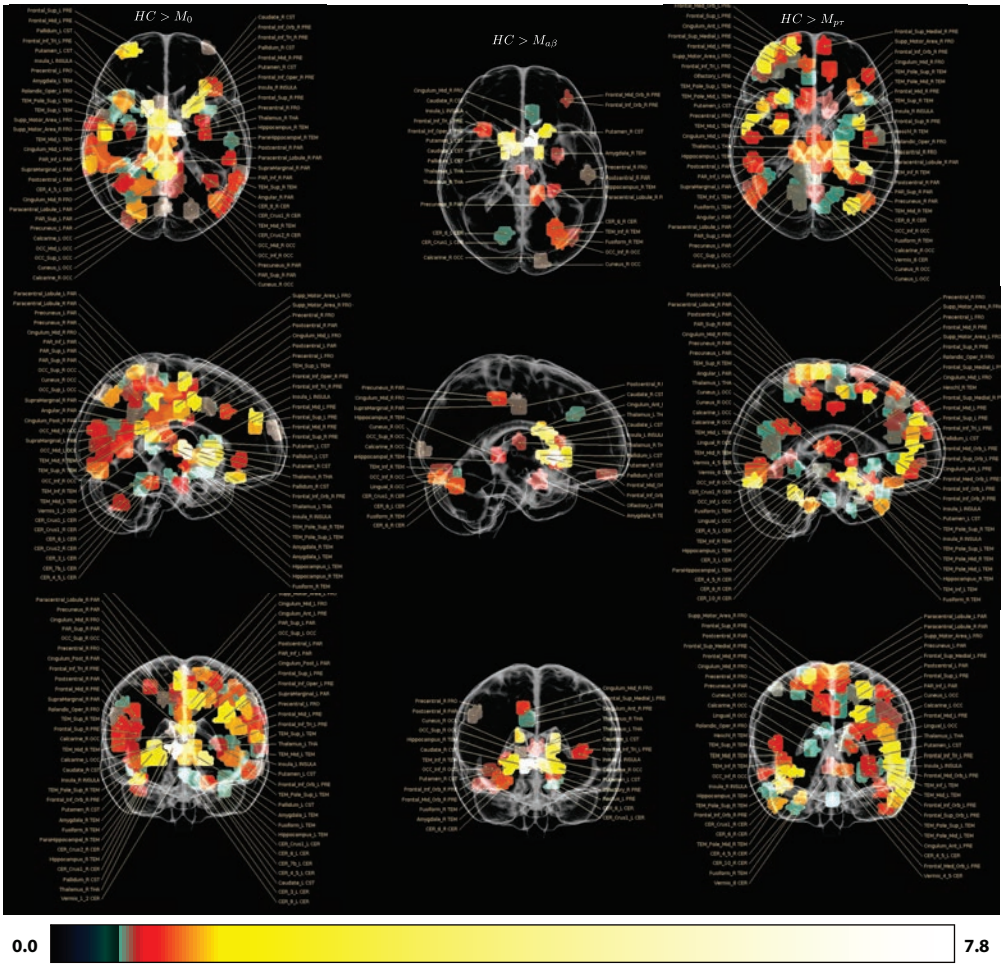

Figure 65: Strength difference of group means on$\{HC > MCI\}$ using same color-scale

transposing the FC values up and down in biomarker space on a set of links which distinguishes $M_{a\beta}$ or $M_{p\tau}$ from HC. Nevertheless, the procedure gives an idea of functional proximity of groups.

For $\{HC > M_{a\beta}\}$ we see very little negative strength HC except for weak negativity in caudate R. In $M_{a\beta}$, negative strength dominates with minimum in caudate R. The only node staying in the far positive over all groups is putamen L. $M_{p\tau}$ has mixed positive and negative strength of weak magnitude. In particular, superior caudate L vanishes and caudate R loses magnitude. The statistically poor AD group shows a similar pattern, somewhat weaker.

For $\{HC > M_{p\tau}\}$ (see Fig. 66) we find virtually no negative strength in HC, with the exception of weak negativity in the anterior-most part of the prefrontal cortex. This negative region expands to the left in $M_{a\beta}$ which also weakens in patches corresponding to $M_{p\tau}$ minima. Overall, the $M_{a\beta}$ pattern is more similar to HC than $M_{p\tau}$, which is completely dominated by negative strength. AD shows a patchy landscape of positive and negative, with small magnitudes overall.

The observed trends are quantified in Fig. 67, which shows the mean FC of group means on the two sets. We find decreasing values with progression dipping into a minimum for the group defining the link set (remember that the link set is extracted to maximally separate HC and the $M_{a\beta}$ or $M_{p\tau}$) and then increases to small magnitudes, closer to zero.

We did not include M_0 in the strength plots, because it contains large, diffuse patterns are obscuring the progression trends. Before proposing a progression hypothesis, we make a brief excursion to discuss the how M_0 should be interpreted.

If we accept the very plausible conjecture that M_0 contains many MCI subjects that are irrelevant (e.g. vascular dementia) to the type we are attempting to isolate (i.e. those likely to progress to AD), then the patterns observed across groups make more sense. Let us illustrate this notion by attempting to interpret table 5 in light of the heterogeneous character of M_0.

We obtain a very large number of links in the set $\{HC > M_0\}$, but as we have seen, the overall reduction in FC is relatively low compared to the other sets. The positive skewness indicates a shorter link bias. This widespread, weaker reduction in FC, is consistent with several phenotypes being mixed in the $\{HC > M_0\}$ group comparison. In other words, we are forced to look at M_0 as a group containing obfuscated features of the MCI group with incipient AD. As such, we can see some similarities with $M_{a\beta}$, i.e. the corpus striatum hub instead being shifted to putamen and thalamus. These similarities will be the starting point for our attempts at identifying progression.

$M_{a\beta}$ should contain a more homogeneous set of MCI, much more likely to be in an intermediate stage of incipient AD. Here we see a very clear $\{HC > M_{a\beta}\}$ pattern with a hub region involving less links than $\{HC > M_0\}$, but with a stronger reduction in FC. The skewness is small and positive, signifying a widening distribution where a subgroup of longer links has begun to grow (see Fig. 18).

When $p\tau$-levels rise above 80 ng/l, the striking hub region vanishes $\{HC > M_{p\tau}\}$. Instead we find a larger set of longer links with heavily reduced FC. Table 5 shows sizes of NBS components are consistent with the above reasoning and a have a skewness that reflects successively longer link failure.

Fig. 15 is very revealing and can be used as a starting point for deciphering potential progression patterns. Starting from panel (a), we have the widespread, diffuse low FC reduction of M_0. Panel (b) shows how the pattern in (a) is modified when $M_0 \to M_{a\beta}$, resulting in the upper part of panel (c). We see that if we take $\{HC > M_0\}$, remove $\{M_0 < M_{a\beta}\}$ and add $\{M_0 > M_{ab}\}$, we end up with something qualitatively more similar to $\{HC > M_{a\beta}\}$. The increase in FC going from M_0 to $M_{a\beta}$ causes both a part of the $\{HC > M_0\}$ pattern to fade, but partially overshoots the HC FC, resulting in the $\{HC < M_{a\beta}\}$ interhemispherical links in prefrontal cortex.

The observed patterns prompt the question: what does panel (b) represent? We are left different interpretations of $\{M_0 \neq M_{a\beta}\}$, depending on the unknown MCI mixture of M_0.

1. M_0 is very contaminated with MCI of a different origin/end point relative those progressing to AD. The widespread, diffuse character of $\{HC > M_0\}$ originates in a superposition of several phenotypes associated with the subgroups of M_0. Given the sharpness of the $\{HC > M_{a\beta}\}$ pattern, the diffuse character of $\{HC > M_0\}$ and $\{M_0 < M_{a\beta}\}$, and given that a progression towards AD should mainly involve a reduction in FC, we may discard $\{M_0 < M_{a\beta}\}$ as largely irrelevant to the progression pattern - an artifact of MCI subspecies contamination. Armed with this simplification, we seek a progression pattern observing that $\{M_0 > M_{a\beta}\}$ outlines central hub parts for $M_0 \to M_{a\beta}$, involving strength reduction in caudate sup/inf L, caudate R, putamen R, amygdala R and hippocampus R (see Fig. 50). Most strikingly, the caudate-hippocampus connectivity is reduced in the transition $M_0 \to M_{a\beta}$. As we have seen, the most prominent regions with the largest strength differences in $\{HC > M_0\}$ are putamen L/R, caudate R in close proximity to hippocampus R, and thalamus R (see Figs. 24 and 28) - nodes not as prominent, but also present in $\{HC > M_{a\beta}\}$ (see Figs. 32 and 37,

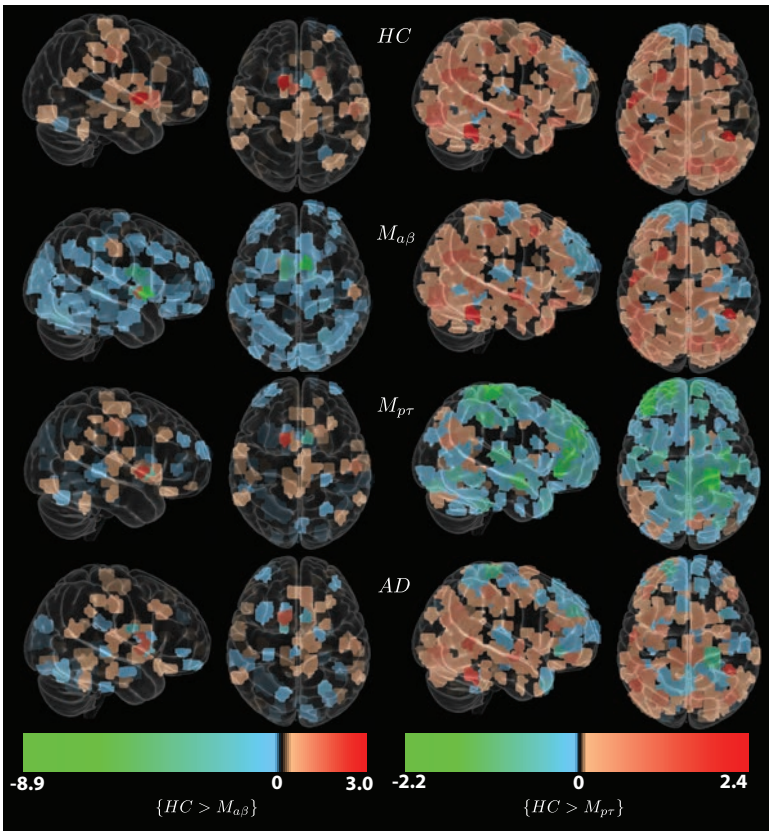

Figure 66: Strength of group means on$\{HC > M_{a\beta}\}$ and $\{HC > M_{p\tau}\}$.

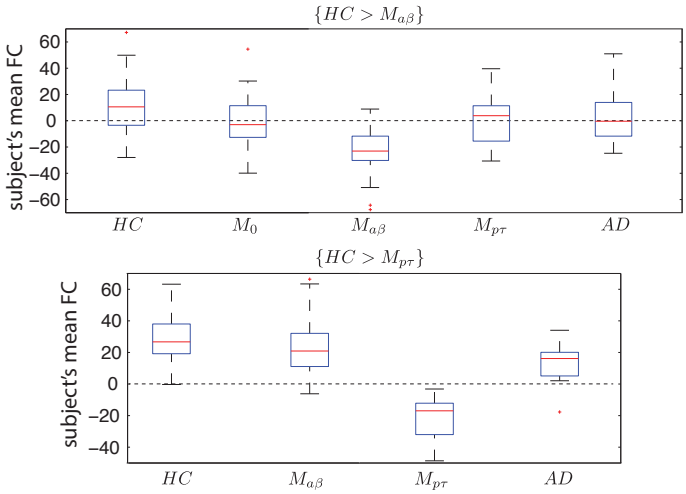

Figure 67: Mean FC on group mean matrices masked by the link sets $\{HC > M_{p\tau}\}$ and $\{HC > M_{a\beta}\}$.

set	nodes
$\{HC > M_0\}$	thalamus R [620], putamen/pallidum L [593] putamen R/pallidum R [605], putamen R [599, 602]
$\{HC > M_{a\beta}\}$	587_1 caudate R [587, 586], caudate L [579, 570, 580] caudate L/pallidum L [604], putamen R [598], putamen L [593], caudate L/putamen L [578]
$\{HC > M_{p\tau}\}$	pre/postcentral R [18], temporal mid L [672, 685], putamen/hippoc/temp sup R [263], frontal inf orb L [162], front sup L [34], frontal mid/sup L [76], frontal mid orb L [10]

Table 9: $\{HC > MCI\}$ nodes selected for progression tests (unique ROI identifiers in square brackets).

a slightly lower threshold gives two more nodes overlapping hippocampus R and parahippocampal R). Given the hypothesis of a contaminated M_0, we may therefore speculate that the following major progression pattern is present:

(a) For the $MCI \rightarrow AD$ subgroup in M_0 with non-pathological levels of $a\beta$: Initially, primarily connections with the inferior parts of corpus striatum are affected, involving putamen L/R, caudate R and thalamus R, with more weight to the right and weaker strength difference for hippocampus R and parahippocampal R. This being likely, follows from the proximity to the $\{HC > M_{a\beta}\}$ hub and the diffuse, spread out, weak FC character of $\{HC > M_{a\beta}\}$ and $\{M_0 < M_{a\beta}\}$.

(b) Pathological $a\beta$-levels in $M_{a\beta}$: The reduced FC hub expands to encompass both superior and inferior parts of caudate L. Amygdala R, putamen R and hippocampus R obtain greater strength difference. Hippocampus R also obtains stronger FC difference (with caudate and prefrontal) and expands to the posterior part. The NBS component reveals weaker strength difference in parahippocampal L and hippocampus L (see Fig. 37).

(c) A weak, compensatory effect occurs interhemispherically in the anterior parts of prefrontal cortex. This compensatory effect presents itself in response to oxidative stress, and is weak in the sense that it is only a small part of $\{M_0 > M_{a\beta}\}$, with the remainder being a strong part originating in confounding MCI subjects (similarly for the corresponding parts in $\{HC > M_0\}$).

2. M_0 is not greatly contaminated, and contains a majority of MCI that will progress to AD. The full pattern of enhanced FC in $\{M_0 > M_{a\beta}\}$ is a real and strong compensatory mechanism in response to increased oxidative stress. In this case the initial stages in M_0 are characterized by a diffuse set of relatively weak reduction in FC, that is counteracted by the strong compensatory effect [see Fig. 15 (b)] for $M_0 \rightarrow M_{a\beta}$. At the same time the corpus striatum hub of reduced FC is expanded as described in 1 (a) and (b).

3. We are seeing the combined effect of 1 and 2, at an unknown ratio.

Although an M_0 contaminated by confounding MCI appears to be a more likely scenario, the unknown mixture of M_0 opens up for different interpretations. Since the mechanisms cannot be untangled, it would perhaps be more prudent to adopt point 3.

For the purposes of continued exploration, we log the nodes of $\{HC > M_0\}$ that show great strength differences in proximity to the hub region, hypothesizing that these are the most likely early signatures of the $\{HC > M_{a\beta}\}$ pattern. We also add the nodes with the greatest strength difference in $\{HC > M_{a\beta}\}$, all belonging to the central corpus striatum region (see table 9).

Proceeding with $\{HC > M_{p\tau}\}$ we a larger population of longer links affected (primarily between superior parietal-temporal L/prefrontal L regions). The reduction in FC in single links is now much greater than for the other MCI groups. There are clear qualitative and quantitative similarities between $\{M_{a\beta} > M_{p\tau}\}$ and $\{HC > M_{p\tau}\}$, consistent with $M_{a\beta}$ being more similar to HC than $M_{p\tau}$.

The $M_{a\beta} \rightarrow M_{p\tau}$ transition clearly has a major impact on the functional connectivity with a very large set of links affected and we have added to our list of suspects parts of the clusters of nodes in temporal left, prefrontal left and parietal lobes (see table 10).

But what about the small, highly relevant set $\{M_{a\beta} < M_{p\tau}\}$? Also, in the $M_{a\beta} \rightarrow M_{p\tau}$ transition, we are faced with the gaping hole in $\{HC > M_{p\tau}\}$ where the corpus striatum hub should be. Indeed, how

set	nodes
$\{M_0 > M_{a\beta}\}$	caudate L [570, 579, 580, 575], amygdala/hippocampus R [346], caudate R [586, 587], putamen/pallidum R [600], hippocampus R [324], hippocampus/parahippocampal R [326]
$\{M_0 < M_{a\beta}\}$	precuneus L/R [540], parietal sup L [481], precuneus R [555]
$\{M_{a\beta} > M_{p\tau}\}$	frontal inf orb L [162], frontal mid/sup L [76], occipital mid L [397] temporal mid L [672], precuneus L/R [540], postcentral/parietal inf L [454] frontal sup med/frontal sup R [232], paracentral lobule R [568] frontal med orb L/cingulum ant L [243], precentral R/postcentral R [18]
$\{M_{a\beta} < M_{a\beta}\}$	caudate R [586], caudate L [570], temporal mid L [668], hippocampus R [324], temporal inf L [730], frontal sup medial L/R [223], frontal inf tri L [145] temporal pole sup L [656], cerebellum L [807], temporal mid L [680]

Table 10: $\{MCI \neq MCI\}$ nodes selected for progression tests (unique ROI identifiers in square brackets).

come the reduction in connectivity between key regions of $\{M_0 > M_{a\beta}\}$ increases in $\{M_{a\beta} < M_{p\tau}\}$? The caudate-hippocampus correlation decreases for $M_0 \rightarrow M_{a\beta}$ but increases again for $M_{a\beta} \rightarrow M_{p\tau}$. Further clues are provided in $\{M_{a\beta} < M_{p\tau}\}$ (see Fig. 57), where we note that most of the links connected to caudate, have gone from negative to small magnitude, with almost vanishing correlation.

To explain the vanishing hub and similar phenomena, we postulate a progression mechanism.

> *Nodes which are initially in phase, or separated by a phase factor related to their distance, become increasingly time-lagged due to failing connectivity, resulting in a correlation reduction. The increased phase factor and correlation reduction cannot continue indefinitely, and after a period of negative correlations, more or less random fluctuations occur, resulting in a correlation that approaches zero.*

It is important to note that we cannot rule out compensatory mechanisms and the remodel ling of functional architecture as contributing to an observed increase in connectivity with illness progression. The two mechanisms of 1) increasing phase factor/time-lag leading to random fluctuations and 2) compensatory response/functional remodel ling cannot be cleanly untangled, at least not using correlation as a measure of connectivity. Indeed, the two mechanisms may present themselves at the same time.

The progression hypothesis does however predict a pattern which is somewhat different from what one would expect from a purely compensatory mechanism. According to the hypothesis, a typical link that begins to deteriorate initially undergoes reduction in FC, corresponding an increasing time-lag between functional centers and their oxygenation time series. This can be viewed as an increase in the effective, functional distance between areas, possibly corresponding to an actual increase in wiring length.

At some point, even maintaining a lagged relation becomes untenable and the functional connection is lost, manifested as a relative increase in correlation magnitude that goes from negative to zero (or very small magnitude values). This progression pattern is elusive and would not be easily detected simply searching for strictly decreasing correlations with perceived progression.

Although compensatory effects cannot be cleanly untangled, it appears likely that they would result in boosting correlation into the positive range, or at the very least maintaining approximate variability in values across subjects. The progression hypothesis predicts a negative correlation, that swings back towards zero in discontinuous leap, marking the sudden loss of synchronicity with an inherent variability across group subjects. Such a pattern is already hinted in Fig. 67, which represents the relatively crude measure of subject mean FC.

Fig. 68 reveals a disturbing property of correlation as a functional connectivity measure. The sine function in panel (a) can be phase shifted by $\Delta\phi$ in order to emulate a communication delay in (b). Panel (d) shows the correlation coefficient between the sine function and the phase shifted version for shifts ranging from zero to 2π, i.e. a full cycle of the sine function. At $\Delta\phi = \pi/2$, the correlation vanishes as the cosine and sine functions are orthogonal. However, there is clearly a phase-locking between the two time-series. This situation is missed by the correlation as an FC measure. In fact, it is equated with the situation in panel (c), which is a random curve that has approximately zero correlation with the sine function. Increasing the shift further, the correlation becomes negative as we enter the region of anti-phase relationship between the curves. This situation can be recognized in the FC analysis and as we have seen often exists in a crossing of the origin as cognition deteriorates.

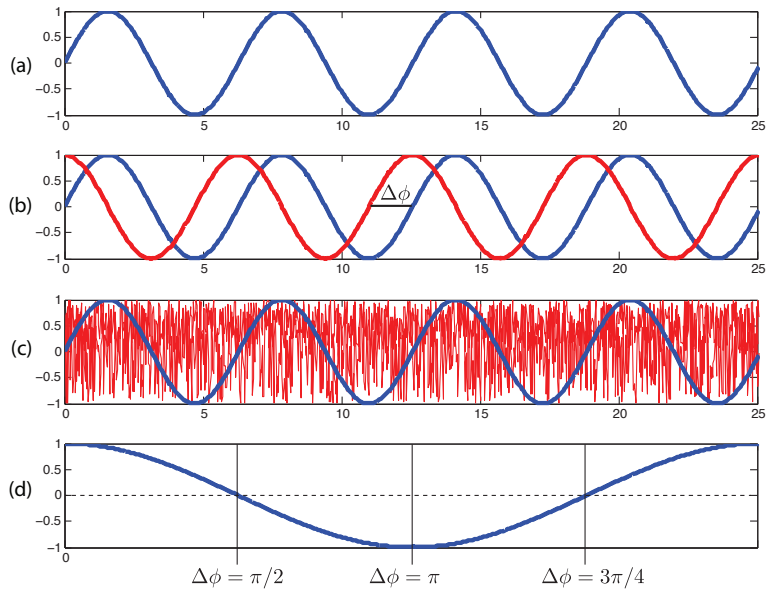

Figure 68: Correlation as an FC measure has a blind spot when two identical cyclic time-series are shifted by a quarter of the period. In this case correlation is zero even though phase-locking and synchronization is present. The situation in (b) is equated to (c), with a random series and no synchronization. The lower panel shows correlation between a sine curve and its phaseshifted counterpart for various phase-shifts $\Delta\phi$

We now look for the progression signature, keeping in mind the following caveats that will obscure such a pattern:

1. a compensatory mechanism may be present in parallel (probably resulting in positive FC if dominant),

2. limited subject numbers in combination with inherent variability in connectivity breakdown can make the progression hard to pinpoint,

3. due to the massive number of links present, we will look at strength differences on link sets across groups and not all constituent links may follow the same progression time line (but if they do, then the node in question is certainly highly relevant),

4. the biomarker limits defining our MCI subjects are somewhat arbitrary and may not correspond to an optimal progression time line, in the sense that the resulting groups are not defined before and after the most common breakdown points occur.

Maintaining perspective on the confounding effect of compensatory FC on the hypothesis of time lags, it is highly unlikely that the large corpus striatum hub structure could be amended by a compensatory increase in FC in such a far progressed group as $M_{p\tau}$, suffering from both high levels of senile plaques and NFTs.

In addition to the nodes from $\{HC > MCI\}$ selected for testing (see table 9), we choose the ten nodes with the greatest strength difference in $\{M_0 > M_{a\beta}\}$, $\{M_{p\tau} > M_{a\beta}\}$ and $\{M_{p\tau} < M_{a\beta}\}$, but only the three strongest in the diffuse set $\{M_0 < M_{a\beta}\}$ (hypothesized to be mainly an effect of M_0 MCI phenotype multiplicity). These nodes are enumerated in table 10.

Fig. 69 shows box plots of the total strength on the network (with out restricting to any link set) for the nodes of interest for $HC > MCI$ (see table 9) for all the subjects and groups.

We have now disregarded the link sets completely and calculated the more noisy, full network nodal strengths. For the nodes of interest emerging from $\{HC > M_0\}$ and $\{HC > M_{a\beta}\}$ we have included the M_0 subjects as these may contain a subset progressing to $M_{a\beta}$. M_0 has been excluded when looking at the nodes from $\{HC > M_{p\tau}\}$, since this group is far removed from the $p\tau$-pathology.

Despite the noisiness of the full strength, we see dips in the FC distributions for the groups corresponding to the MCI group in the nodes selected from looking at the $\{HC > MCI\}$ set.

The nodes from $\{HC > M_0\}$ are clearly different as they mainly lodge in the high positive strength range. That the full strength measure is less specific is seen for putamen/pallidum R, which has no

significant differences relative HC. None of the nodes follow the proposed progression pattern, which we could hardly expect for the M_0 group.

In the nodes from $\{HC > M_{a\beta}\}$, we see more of the expected pattern: an increasing bias towards the negative correlation that then shifts towards the zero. Mainly caudate, i.e. the nodes with the strongest differences, follow the progression pattern well. One exception is putamen L, which we have seen maintains a positive strength over all groups, even on the link subset where the most negative strength is expected (see Fig. 66)). We noted already in the introductory parts that whereas putamen is highly connected with positive correlations, caudate forms a hub region with many negative correlations (see Fig. 20). The diffuse character of full strength makes the inherent character of the nodes manifest itself with a great number of links not differing between groups.

In the same way, for the $\{HC > M_{p\tau}\}$ nodes we can see dips in the $M_{p\tau}$values sometimes followed by an increase in AD.

Fig. 70 shows the strengths now restricted to the indicated link sets for the nodes selected by inspection of the same sets. We remind the reader that these strengths, although more specific, still contains tens of links. The dip in M_0 strength on $\{HC > M_0\}$ is now more pronounced but (with the exception of putamen R) is not followed by a great increase. The fact that values generally don't approach zero after M_0 could stem from MCI homogeneity.

$\{HC > M_{a\beta}\}$ follows the pattern more clearly, in particular caudate. AD sometimes behaves strangely, but statistics is very poor, so this is to be expected. Putamen is again prone to staying in the positive, although the decrease in FC seems to proceed down the line, perhaps an indication of a slower decay.

For $\{HC > M_{p\tau}\}$ we now find great negative dips over $M_{p\tau}$. $M_{a\beta}$ does not show reduction relative HC at the $\alpha = 0.05$ level, with the exception of frontal mid/sup L, although there appears to be a trend in many cases.

We can also plot the strength on the $\{MCI \neq MCI\}$ set for the nodes with the greatest strength difference (see table 10). These are shown in Fig. 71 for $\{M_0 \neq M_{a\beta}\}$ and Fig. 72 for $\{M_{a\beta} \neq M_{p\tau}\}$. These sets contain fewer links and are directly relates MCI groups.

Comparing nodes between$\{M_0 > M_{a\beta}\}$ and $\{HC > M_{a\beta}\}$, shows the same progression pattern. The trends are remarkably similar, but M_0 appears to behave more like HC. This is not strange since $\{M_0 > M_{a\beta}\}$ is extracted by looking for maximal differences. It is interesting to note that several hippocampus nodes exhibit a progression trend.

$\{M_0 < M_{a\beta}\}$ is a result of interference from other MCI phenotypes, or a powerful compensatory mechanism in precuneus. Either way, we do not expect to see the progression pattern, but we may have a prototype for the compensatory effect.

Turning to $\{M_{a\beta} > M_{p\tau}\}$ (see Fig. 72) we find similar qualitative trends as in $\{HC > M_{p\tau}\}$, albeit with a boost of $M_{a\beta}$ values coming from the search for links of maximal difference between the two MCI groups. In $\{M_{a\beta} < M_{p\tau}\}$ most nodes follow a progression like trends, in particular the key nodes of hippocampus R and caudate R. Others show a signature more indicative of compensatory FC, but very few links are involved here.

We can quantify this behavior and calculate the correlation between strength and continuous biomarkers levels. Table 11 shows how the full strength of the nodes from $\{HC > MCI\}$ sets correlate with $a\beta$- and $p\tau$-levels across all MCI, as well as correlation with $a\beta$ across the union group $M_0 \cup M_{a\beta}$ and correlation with $p\tau$ across the union group $M_{a\beta} \cup M_{p\tau}$. Correlation values for $p < 0.05$ are reported and multiple comparison correction has not been applied, meaning that all results should be regarded as trends.

None of the nodes from $\{HC > M_0\}$ have a significant correlation with biomarkers, to be expected if multiple MCI are present. For $\{HC > M_{a\beta}\}$ the most interesting parts of the corpus striatum hub failure emerge, and exhibit reduced FC over all MCI with decreasing $a\beta$. When looking at all-MCI-correlation values, is important to remember that the to biomarkers correlate with each other - a lower $a\beta$ correlates with a higher $p\tau$ ($r = -0.34$, $p = 0.0001$). The caudate nuclei show reduced FC when $a\beta$ decreases in $M_0 \cup M_{a\beta}$, but show an even stronger increase with increasing $p\tau$. This is the progression mechanism by which the corpus striatum hub vanishes, and it is remarkably clear given the non-specific full strength measure.

$\{HC > M_{p\tau}\}$ cannot show the increase in strength following loss of synchronicity since the next step is AD, for which biomarker levels are presently unavailable. We do however see the clear reduction in FC with increasing $p\tau$, indicative of a node on its way to lose synchronization.

Table 12 shows the same correlation values as in table 11, but the strength is now calculated on the relevant set of links, rather than the whole network. Here, putamen R emerges as the only node for $\{HC > M_0\}$ with reduced strength for increased $p\tau$. For $\{HC > M_{a\beta}\}$ the other nodes in addition to

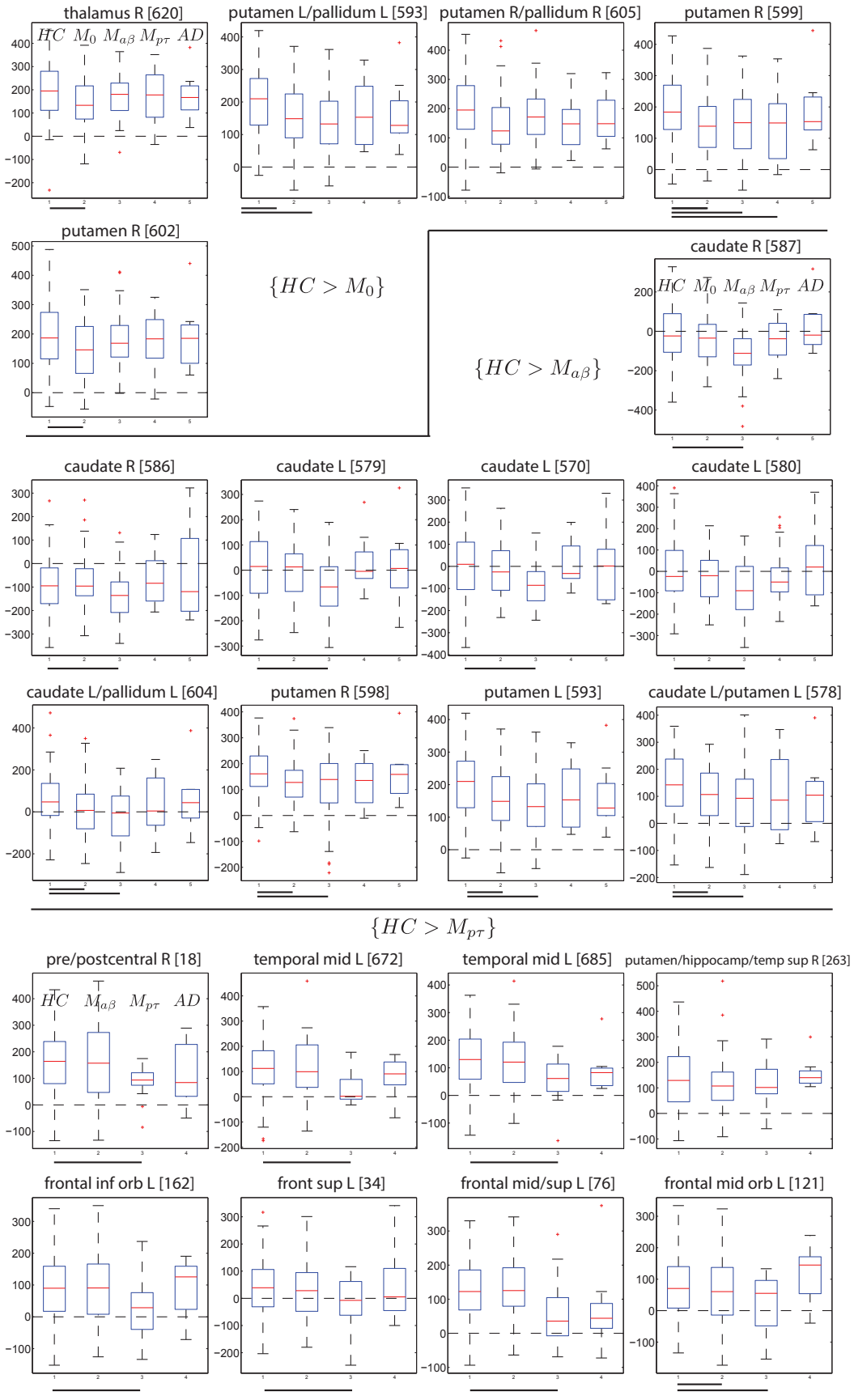

Figure 69: Total strength variation (without link subset restriction) across groups for the nodes of interest from $HC > MCI$. Lines at the bottom of each box plot denotes significant difference between indicated group and HC.

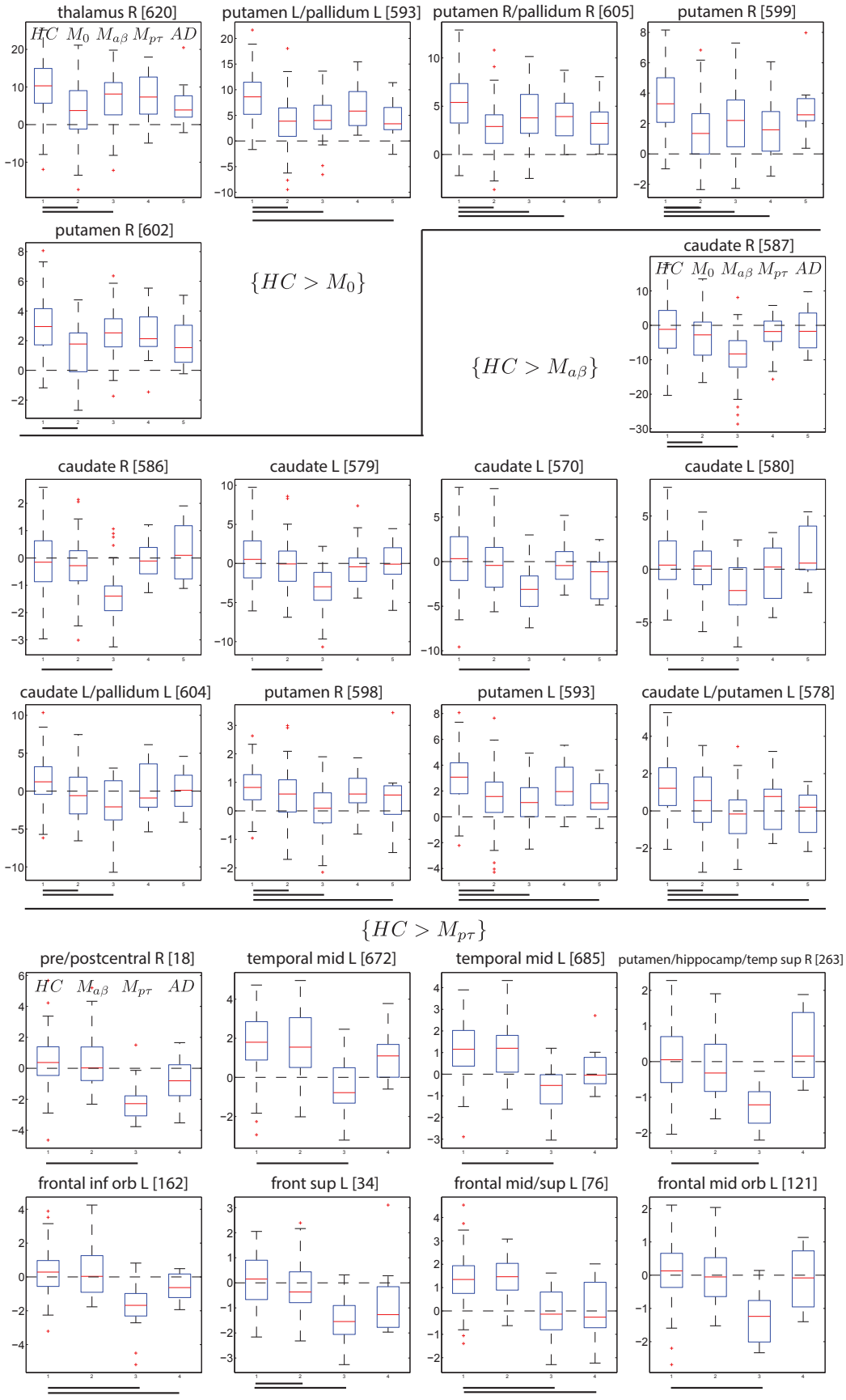

Figure 70: Strength variation on indicated set across groups for nodes selected by inspecting the same sets.

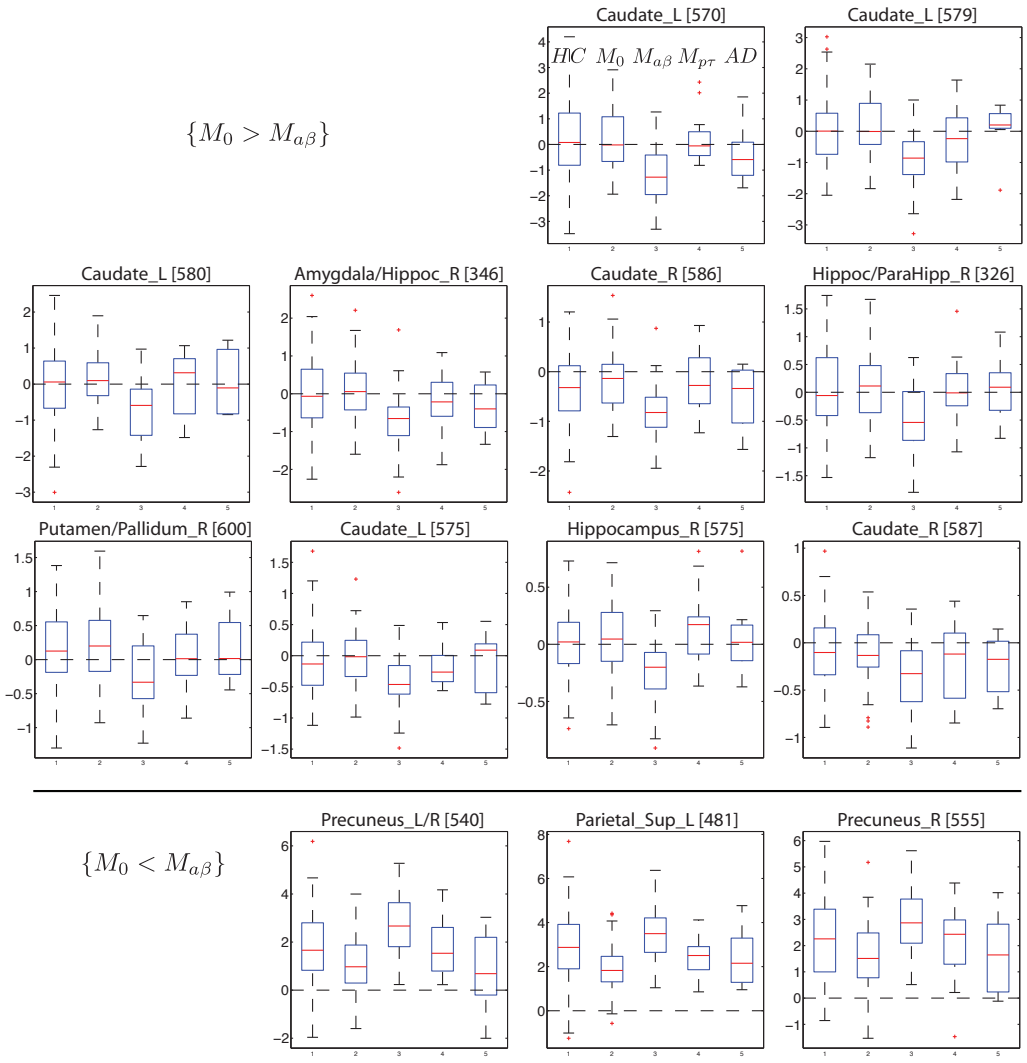

Figure 71: Strength on $M_0 \neq M_{a\beta}$ sets for selected nodes.

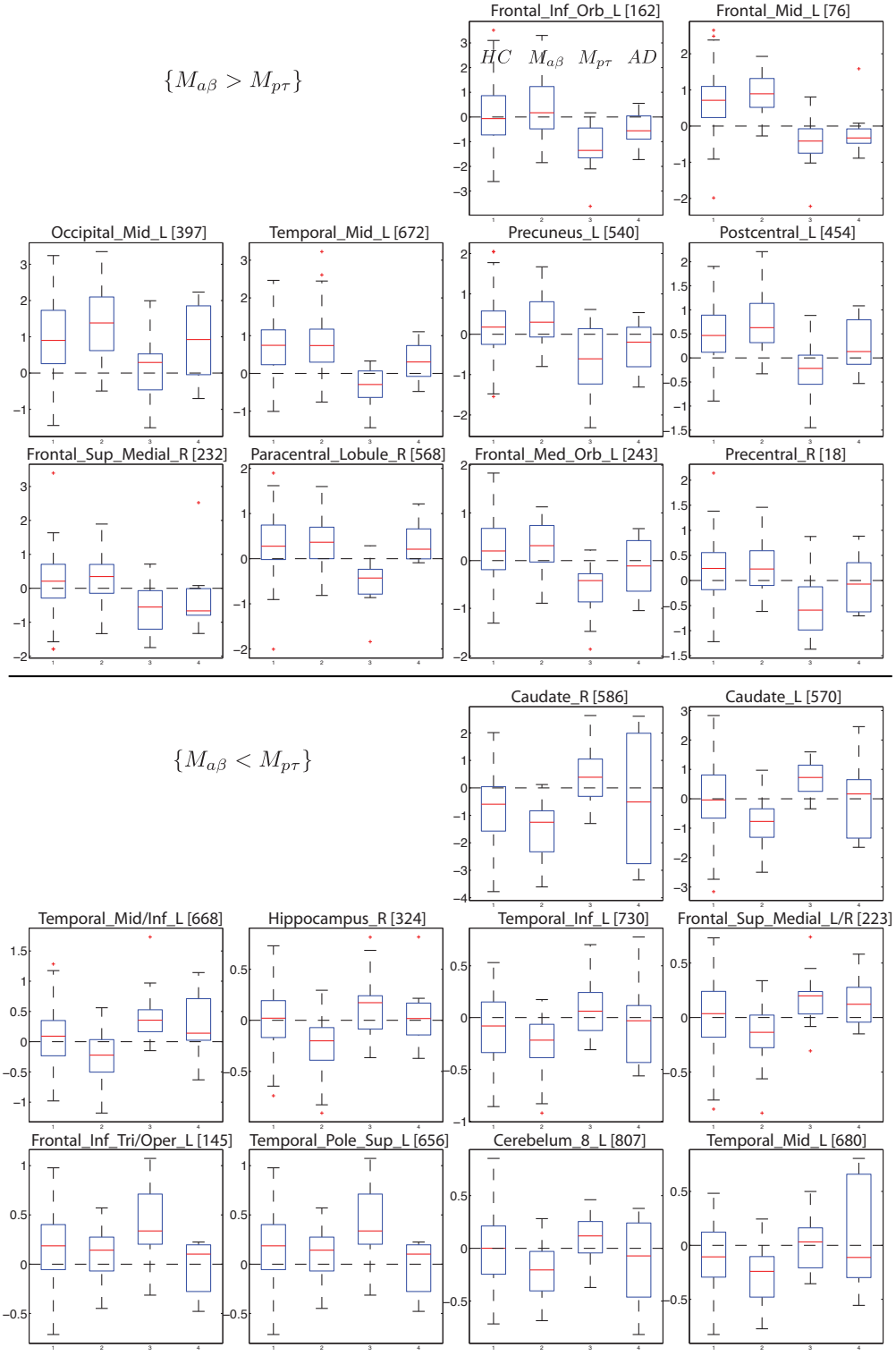

Figure 72: Strength on $M_{a\beta} \neq M_{p\tau}$ sets for selected nodes.

set	node	$r_{a\beta}$ all MCI	$r_{p\tau}$ all MCI	$r_{a\beta}$ $M_0 \cup M_{a\beta}$	$r_{p\tau}$ $M_{a\beta} \cup M_{p\tau}$
$\{HC > M_{a\beta}\}$	caudate R			0.19	0.34
	caudate R	0.29		0.38	0.34
	caudate L			0.22	0.38
	caudate L			0.23	0.45
	caudate L	0.18		0.27	0.35
$\{HC > M_{p\tau}\}$	temporal mid L		−0.18		−0.40
	temporal mid L				−0.39
	frontal inf orb L		−0.17		−0.32
	frontal sup L				−0.32
	frontal mid/sup L				−0.28
	frontal mid orb L				−0.26

Table 11: Correlation between biomarkers and full strength of nodes of interest from $\{HC > MCI\}$. Only correlation values for which $p < 0.05$ are shown (uncorrected). The 3rd column shows correlation between total strength on networks and $a\beta$ over all MCI subjects, the 4th column the same quantity for $p\tau$. The 5th column shows correlation between full nodal strength and $a\beta$ over pooled M_0 and $M_{a\beta}$ subjects, and the last column the same quantity for $p\tau$ over pooled $M_{a\beta}$ and $M_{p\tau}$ subjects.

caudate show weaker traces of the progression signature, mainly with reduction in strength with increased $p\tau$. Also $\{HC > M_{p\tau}\}$ shows more nodes with reduced strength with increasing $p\tau$ across all subjects and with a higher correlation magnitude when restricting to the union set $M_{a\beta} \cup M_{p\tau}$. A similar effect can be seen for $\{HC > M_{a\beta}\}$.

Table 13 shows the correlation between strength on indicated sets and biomarker levels for all MCI and the two union sets. $\{M_0 > M_{a\beta}\}$ shows clear evidence of the progression trend, and we see that $r_{a\beta}$ for the union set has been boosted by the direct MCI-MCI comparison. The compensatory effect in precuneus gives two correlation coefficients with negative sign, showing a reduction with increased $p\tau$ after an initial increase with dropping $a\beta$. $\{M_0 \neq M_{a\beta}\}$ shows that reduced strength follows decreasing $a\beta$ levels across all MCI.

Likewise, $\{M_{a\beta} > M_{p\tau}\}$ indicates reduced strength with increasing $p\tau$ across all subjects, and an even stronger effect in the $M_0 \cup M_{a\beta}$ union set.

Our hypotheses allows us to extrapolate the front of maximum lag and identify epicenters of functional connectivity breakdown. The major epicenters have already been identified: in the corpus striatum hub, putamen L/R expands to caudate L/R in the transition $M_0 \to M_{a\beta}$. In addition, nearby hippocampus R nodes begin to lag.

Then, for $M_{a\beta} \to M_{p\tau}$, the corpus striatum hub suffers total synchronicity break down, and a strong time lag occurs for longer interlobular links, primarily between parietal superior and prefrontal left, but also involving temporal left lobe. Hippocampus R loses synchronicity with caudate and connections with prefrontal nodes are lagged, as is hippocampus L-prefrontal.

Not only do we have very poor statistics for the AD group, but this group is also more prone to produce artifacts. There does however appear to be a indications of a breakdown in prefrontal L cluster (prominent in $\{HC > M_{p\tau}\}$), marked as an gaping hole in the AD $N_R = 392$ NBS component. Less obvious, the temporal L cluster of nodes also appears to have suffered synchronicity breakdown. The front of maximum time-lag is then shifted to adjoining areas.

Correlation is in fact not the only way to measure functional connectivity, there are many other information theoretic measures such as mutual information or Synchronization Likelihood (SL). The latter is often employed in EEG studies [36] and has even been applied to resting state fMRI [52]. Synchronization likelihood is perhaps better suited to monitor progression patterns, where our hypothesis would simply manifest itself as a successive reduction in this measure, making it easy to identify trends. Additionally, SL takes on values in $[0, 1]$, which makes it appropriate for a number of graph theoretical measures. Coherency is another measure that is based on separating the signal into several sub-bands and look for correlations in reciprocal space, at the same time extracting the phase lags [34]. Given the observed trends, correlation seems particularly ill equipped to study progression compared to SL and coherency these measures.

Graph theory is often applied to connectivity as measured by correlation and in doing so disregarding problematic negative values, or even applying an arbitrary threshold for binary connectivity matrices. Switching FC measure, not only seems appropriate given the observation of increasing lag and breakdown, it also resolves technical problems with applying group theoretical measures of network properties and

set	node	$r_{a\beta}$ all MCI	$r_{p\tau}$ all MCI	$r_{a\beta}$ $M_0 \cup M_{a\beta}$	$r_{p\tau}$ $M_{a\beta} \cup M_{p\tau}$
$\{HC > M_0\}$	putamen R		-0.20		-0.18
$\{HC > M_{a\beta}\}$	caudate R	0.18		0.26	0.37
	caudate R	0.33		0.46	0.51
	caudate L	0.20		0.30	0.42
	caudate L	0.26		0.37	0.49
	caudate L	0.29		0.36	0.42
	caudate L/pal L				0.28
	putamen R	0.20		0.27	0.35
	putamen L				0.30
	caudate L/put L			0.19	0.37
$\{HC > M_{pt}\}$	pre/postcentral R		-0.36	-0.20	-0.51
	temporal mid L		-0.36		-0.47
	temporal mid L	0.20	-0.35		-0.54
	put/hipp/t sup R		-0.31		-0.46
	frontal inf orb L		-0.43		-0.58
	front sup L		-0.31		-0.48
	frontal mid/sup L		-0.34		-0.53
	frontal mid orb L	0.20	-0.40		-0.52

Table 12: Correlation between biomarkers and strength of nodes on link sets of interest from $\{HC > MCI\}$. Only correlation values for which $p < 0.05$ are shown (uncorrected). The 3rd column shows correlation between strength on given link set (first column) and $a\beta$ over all MCI subjects, the 4th column the same quantity for $p\tau$. The 5th column shows correlation between nodal strength on the given set and $a\beta$ over pooled M_0 and $M_{a\beta}$ subjects, and the last column the same quantity for $p\tau$ over pooled $M_{a\beta}$ and $M_{p\tau}$ subjects.

topology.

In the sections to follow, we have chosen to apply graph theoretical measures such as strength and betweenness, that are relatively easily generalized from binary to weighted formalism, although interpretations may require some caution.

set	Nodes	$r_{a\beta}$ all MCI	$r_{p\tau}$all MCI	$r_{a\beta}$ $M_0 \cup M_{a\beta}$	$r_{p\tau}$ $M_{a\beta} \cup M_{p\tau}$
$\{M_0 > M_{a\beta}\}$	caudate L	0.34		0.43	0.57
	caudate L	0.29		0.33	0.33
	caudate L	0.34		0.42	0.41
	amyg/hipp R	0.36		0.43	0.34
	caudate R	0.34		0.44	0.28
	hipp/parah R	0.26		0.33	0.45
	put/pal R	0.25		0.30	0.36
	caudate L	0.31		0.35	0.32
	hipp R	0.25		0.38	0.49
	caudate R	0.22		0.26	0.23
$\{M_0 < M_{a\beta}\}$	precun L/R	-0.37		-0.40	-0.38
	par sup L	-0.35		-0.42	-0.32
	prec R	-0.35		-0.41	
$\{M_{a\beta} > M_{p\tau}\}$	frontal inf orb L		-0.33		-0.54
	frontal mid L		-0.37		-0.61
	occipital mid L		-0.22		-0.43
	temporal mid L		-0.36	-0.19	-0.62
	precun L/R		-0.30		-0.58
	postc L/par inf L		-0.24		-0.50
	f sup med/f sup R		-0.27	0.22	-0.52
	parac lob R		-0.38		-0.65
	f med orb/cing ant L		-0.28		-0.51
	prec/postc R		-0.31	-0.20	-0.53
$\{M_{a\beta} < M_{a\beta}\}$	caudate R		0.37	0.32	0.66
	caudate L	0.18	0.34	0.35	0.73
	t mid/inf L		0.36		0.64
	hipp R	0.25		0.38	0.49
	t inf L		0.27	0.25	0.54
	f sup med L/R		0.36	0.19	0.55
	f inf tri/oper L		0.30		0.35
	t pole sup L		0.30		0.35
	cerebellum		0.23	0.27	0.55
	t mid L		0.27		0.49

Table 13: Correlation between biomarkers and strength of nodes on link sets of interest from $\{HC > MCI\}$. The 3rd column shows correlation between strength on given link set (first column) and $a\beta$ over all MCI subjects, the 4th column the same quantity for $p\tau$. The 5th column shows correlation between nodal strength on the given set and $a\beta$ over pooled M_0 and $M_{a\beta}$ subjects, and the last column the same quantity for $p\tau$ over pooled $M_{a\beta}$ and $M_{p\tau}$ subjects.

10 Graph theoretical measures

In this section we will evaluate the performance of a few basic graph theoretical measures on our functional connectivity networks. We do this to simplify the horrendously complex networks of hundreds of thousands of links in an attempt to condense the information and highlight particularly interesting nodes. Here, we choose to focus on measures that yield properties of individual nodes. In doing so, we gain tractability, but suffer a major power loss, as the degrees of freedom are reduced from 350 000 links to 840 nodes.

There is a wide range of graph theoretical measures that can be used to characterize networks, offering potentially valuable information on how normal function is disrupted. Unfortunately, most of the fundamental nodal measures suffer from the loss of power that comes with a massive reduction in degrees of freedom, yielding weak contrasts with few or no significant differences.

Topological properties of networks are commonly evaluated by thresholding the networks into binary entities where all links above a more or less arbitrary threshold are set to unity and all those below are deleted. Some methods address this arbitrariness, by for example thresholding at maximal efficiency [53]. However, we are still removing ourselves from and severely marginalizing the original data cache, potentially introducing unknown artifacts.

The alternative is to remain within a fully weighted formalism, which is less tangible, less developed, mathematically and conceptually more difficult, not to mention computationally more demanding. For example, in order to pinpoint topological alterations of the binary networks, it is necessary to normalize some measures using a large number of random networks drawn from an ensemble with the same degree distribution as the networks under consideration. In the case of weighted networks, corresponding algorithms exist, approximately preserving strength and sign distributions of the weighted network [51]. The generation of these networks are computationally far more demanding relative their binary counterparts. Additionally, even though weighted null networks goes a long way towards generalizing many important binary measures, it does not resolve the more serious formalism breakdown due to the presence of negative links.

Indeed, what does it mean to assign negative weight between two regions? In our case it simply means that the two gray matter oxygenation curves are shifted towards an anti-phase relationship. In general network theory, there is little room for attaching such a meaning, where links should ideally reflect connection strength or probability, confining the weights to a mathematically well behaved normalized interval, e.g. [0,1].

Attempts have been made to deal with the troublesome negative weights, by interpreting it as a property of longer links that integrate modularized processing [51]. Rubinov and Sporns in Ref. [51] shift focus to partitions or modules of positively correlated regions integrated via negative intermodular correlations. Indeed, we have already noted the bias toward negative weight for longer links. Their approach attempts to split measures into a positive and negative part, with interpretations bordering the hypothetical, critically hinging on the interpretation of negative weights. To make matters worse, some authors regress out a global signal in the GLM, inducing large amounts of artifactual negative correlations void of physical meaning.[19] Currently, the debate regarding global signal removal has produced consensus that the regression produces artifacts. Whereas the hypothesis regarding the functional role of negative correlations, however hard to pinpoint, may hold some truth, the matter of how to deal it with and interpret results is far from resolved.

Given the observed trends in our biomarker cohorts, i.e. a general reduction in connectivity pushing into the negative for the individuals far progressed along the tentative biomarker time-line, it is clearly unsuitable to apply a binary threshold if one hopes to isolate and highlight these patterns. One could of course study different thresholds or even windows of thresholds. This approach results in a massive amount of data without hope of a clear interpretation.[20]

Separating into a positive and negative part is generally a bad idea for most measures, because such a sharp division does not capture the connectivity reduction across the origin very well. We have also seen that positive FC often swings over into the negative with roughly equal magnitude, indicating that one would be ill advised to take the absolute value, as one might when hypothesizing that negative weight has distinct functional origin rather than being a sign of pathology (when both may in fact be true at the same time).

[19] Unfortunately the tantalizing hypothesis of Ref. [51] is based on publicly available resting-state data, where the global signal has been regressed out. Their framework of splitting measures into a positive and a negative part fails due to small number of negative weights if global signal regression is omitted.

[20] The author is speaking from first-hand experience here.

No matter how one transforms the correlation, it is intrinsically and fundamentally unsuitable for a full graph theoretical analysis. In order to perform a complete analysis, one should ideally: 1) retain a weighted formalism in order to avoid marginalizing data and introducing artifacts, 2) avoid using a connectivity measure that produces values without a clear probabilistic meaning. Failure to fulfill this last point destroys one of the most desirable graph theoretical properties of a functional connectivity measure, which should reflect connection strength that can ultimately only be stated as a probability.

Synchronization Likelihood (SL) [52, 35], a form of generalized synchronization derived from signal theory, so far mostly applied to EEG/MEG data, does fulfill these requirements, providing a probability of synchronization. Although beyond the scope of this paper, SL appears to pave a feasible road to a complete graph theoretical analysis. Even then, one would be faced with the difficulties of a weighted formalism and a severe reduction in power using nodal measures[21], something which can perhaps be amended by increasing ROI-resolution further. The correlation analysis can as we have seen provide valuable insights on its own, but in conjunction with a fully weighted graph theory, calculations are cumbersome, the formalism tends to break down, results become are hard to interpret as negative weights are cut or some other trick is used to amend the failing formalism.[22]

In view of these difficulties, we focus here on a few simple measures that can be applied without null network normalization; nodal strength and betweenness and eigenvector centrality. In the case of the two centrality measures, we are forced to consider only positive weights, as these measures are ill defined for negative weights. Arguably the most fundamental measure of network differences, second to individual links, strength has already been employed in the previous section. Before, we merely used it as a tool to highlight relevant regions in the set of significantly different links. Below, we will explore the significant differences in strength, keeping the full network of links and additionally limiting calculations to connected network components.

The strength of a high resolution ROI-node is composed of 839 link values, reducing it's power relative link-testing, but at the same time mitigating multiple comparison problems. In this situation, we can attempt to boost power by looking for spatially contiguous ROIs.

As we have seen, characteristic hub regions with reduced FC is a recurring theme. The graph theoretical measures of eigenvector and betweenness centrality are designed to yield high values for regions that play a central role in the network. It is therefore reasonable to expect that the centrality measures can provide additional insights - an hypothesis which we will test below.

Comparing 840 nodes across groups, we still need to control the FDR, although the problem is much less severe than for 350 000 links. Again, we employ random permutations to construct a distribution of t-statistics for each nodal measure, which is then used to assign a p-value to the node in question. The number of permutations is chosen large enough to produce consistent FDR controlled p-values (in general 100000 permutations is sufficient [23])

We assign p-values by a two-tailed comparison, taking the absolute of the generated distribution of t-values and calculating the fraction of values greater than the t-statistic of biomarker groups. Once p-values have been assigned via the distribution from permutation testing, we perform Benjamini-Hochberg (BH) multiple comparison correction and threshold at $\alpha = 0.05$.

The FDR correction may be overly conservative, assuming that nodal tests are independent, although their proximity may play an important role, depending on the nodal measure in question. To enhance power, we can repeat the trick commonly used in statistical parametric mapping. As before, we first apply a t-statistic suprathreshold to uncorrected t-test values, qualifying the most important nodes for a subsequent component search. The connected component thus identified consists of a number of neighboring nodes with t-values exceeding the chosen suprathreshold.

To enumerate the neighbors of a given ROI we dilate it with a box kernel of dimensions chosen to reflect the spatial domain of influence, i.e. we define what constitutes a neighbor. Choosing kernel size too large will generate very large clusters and choosing it too small could cause the component search to miss important clusters. Fig. 73 shows how the matrix defining neighboring nodes varies for different kernel sizes. It is tempting to extend the range by choosing a larger kernel, but this will affect the null distribution of component sizes so that power is reduced. In general, the 3x3x3 kernel seems to have the greatest power and is employed in all component searches below.

The null size distribution is generated by pooling the two groups tested for nodal differences, and randomly partitioning into two new groups preserving old group sizes. Then, the suprathreshold is

[21] There are also measures that retain the connectivity space dimensionality, and that should therefore not suffer severe power loss.

[22] Again, speaking from first-hand experience here.

[23] This is only a small fraction of the complete distribution. For example, we would have to enumerate and test a staggering $(N_{g_1} + N_{g_2})!/(N_{g_1}!N_{g_2}!) = 168!/(126!42!) \approx 10^{40}$ partitions of HC pooled with $M_{a\beta}$.

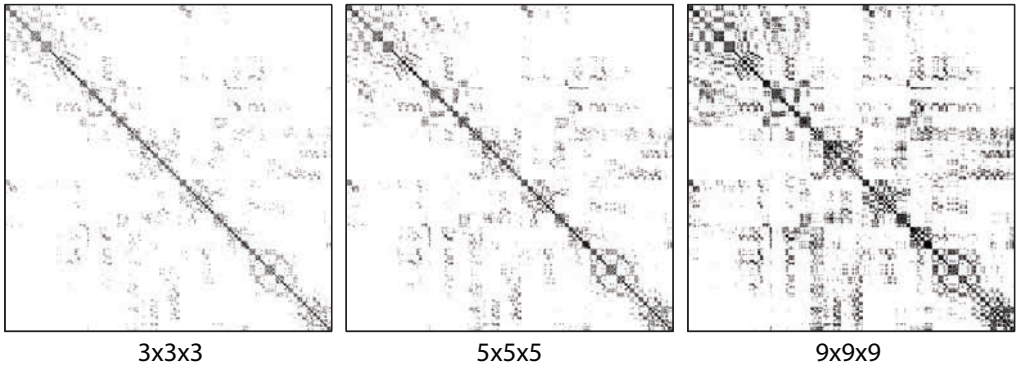

Figure 73: The neighbor matrices for different kernel sizes. A black dot indicates that the nodes (x and y-axis) are defined as neighbors.

applied and the size of the largest contiguous component found is logged in the size distribution. Any component found in our biomarker groups is declared significant its size is in the top 5% of the null distribution.

It is not evident how to define the size of a component. As for NBS, we may consider the number of constituent ROIs (these have roughly equal voxel numbers), i.e. the extent of the component. We may also choose to sum the t-values in the component and 'intensity' as our size. For the nodal measure, intensity appears to grant more power and has been employed in the results presented below. Note that we may have components comprising of a single node when we choose intensity as size-measure. A Benjamini-Hochberg correction is applied to the components found, but power is sustained relative the all node permutation since the components of significantly greater size comprise a small number.

There is no rule for selecting the supra-t value - it can be regarded as a parameter that allows us to probe the spatial extension of high-difference regions. In the end, results should be interpreted with knowledge of the brains functional architecture. As before, the component search should be seen as a complement to the FDR controlled results, providing auxiliary power. In the figures, the presence of a suprathreshold will indicate the use of component search, where components with $p < 0.05$ are after multiple comparison correction are kept.

Nodal measure analysis will be presented for the most important group comparisons, i.e. HC versus M_0, $M_{a\beta}$ and $M_{p\tau}$. All results are derived from permutation testing with 100 000 permutations where after p-values are corrected and differences declared significant at the significant at the $\alpha = 0.05$ level. When measures are calculated on connected components, the component used is always the one with the highest suprathreshold present for all $HC - MCI$ comparisons, i.e. the components found for $t = 3.5$ (any t-value in the figures, refers to the supra-t value used in searching for components of ROIs, not links).

10.1 Nodal strength

We now consider strength resulting from the full network of 350 000 links. We could also look at significant strength differences on the network components, but this will simply reproduce the previously presented MIPs of since all nodes are then flagged as significant. Fig. 74 (a) shows the results of component search for $HC > M_0$. Since we use intensity and not extent as a measure of size, single nodes can appear at a given suprathreshold, even though no significant results were found when permutation testing the individual node values. In that case, the FDR control becomes conservative for the 840 tests and eliminates all significances. FDR control is also applied to all the components found and single nodes may survive if their intensity is strong enough, but are more susceptible to discrimination than a contiguous set of nodes who are shielded by their total sum of t-values. The price of this shielding is of course that none of the constituent nodes can be flagged as individually significant (we plot all the components in one figure).

Remarkably, several key regions already highlighted in the connectivity analysis appear, despite the massive reduction in degrees of freedom. At $t = 3.5$, we find the nodes with the greatest group differences, recovering the familiar anterior nodes with putamen, pallidum and thalamus R, as well as the posterior center with parts of cingulum mid and precuneus. Lowering to $t = 3.0$, these extend focii to include cingulum post, putamen L, pallidum L, caudate L and R, as well as parts of Hippocampus L and R, parahippocampal and amygdala.

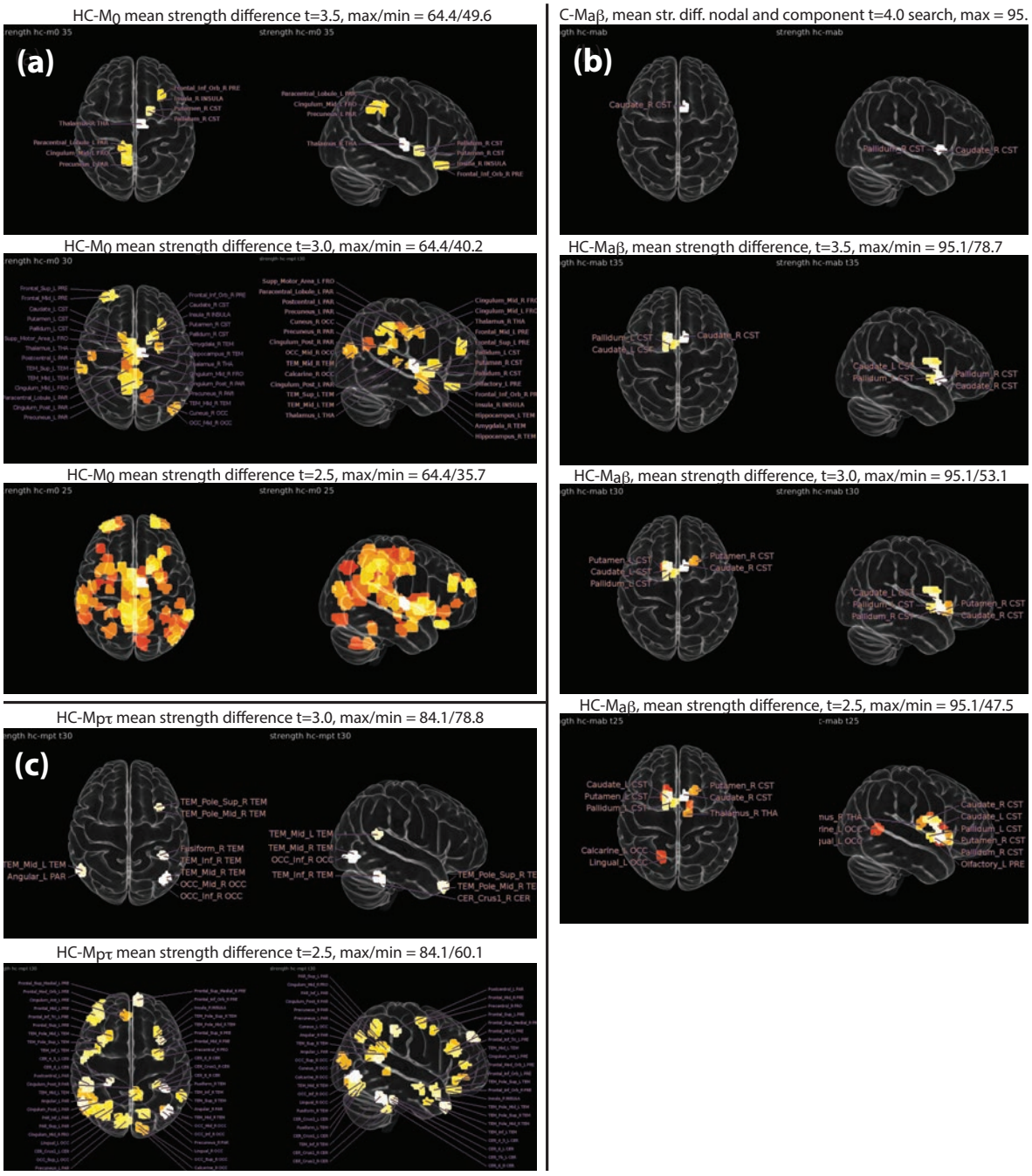

Figure 74: Areas where strength is significantly greater in HC relative M_0 (a), $M_{a\beta}$ (b), and $M_{p\tau}$ (c).

Going lower still to $t = 2.5$, we now see a remarkably symmetric image, with two clusters in front, both sides of corpus striatum extending to hippocampus, and two posterior clusters that are slightly misaligned.

Looking at Fig. 74 (b) and $HC > M_{a\beta}$, again only the nodal component search reveals results for the full network strength, with a single node component in caudate R at $t = 4.0$ that expands to involve putamen, pallidum and caudate L as the suprathreshold is lowered. At the lowest $t = 2.5$ thalamus R, familiar from $HC - M_0$, appears.

For $HC > M_{p\tau}$, fig. 74 (c) reveals isolated nodes in the component search at $t = 3.0$ and the more familiar pattern with a streak of nodes in temporal and frontal left appears only at the lower suprathreshold $t = 2.5$. Another feature catches the eye in the strength difference plot for $t = 2.5$ - cingulum posterior and precuneus now make an appearance.

This relatively weak strength contrast is unexpected, given the large FC reduction associated with the network components for this comparison. The fact that this is the smallest group with only 18 subjects may be a contributing factor. However, the weakness is consistent with the hypothesis of a progression that starts with an FC reduction, wanders into the negative and ends with a complete loss of synchronicity. As we have already noted in Sec. 9: *correlation as a connectivity measure has a blind spot when the phase lag between two times series is a quarter of a period.* Looking at Fig. 29, it is clear that HC has a large set of weak magnitude links that become negative for $M_{a\beta}$. It appears unlikely that the negative correlation with the corpus striatum would suddenly arise with a sudden increase in magnitude of functional connectivity. More likely, a rough quarter period phase shift is inherent in these connections in normally functioning brains, effectively rendering group differences for these links between $HC - M_{p\tau}$ invisible, even though they have suffered catastrophic connectivity failure and are fluctuating randomly and independently. This crucial inference on the evolution of FC with progression follows from Figs. 68, 29 and 38. The troublesome blind spot of correlation as FC measure also impacts compensatory effects, which may just be regions with an inherent and normal anti-phase relation for which correlation becomes zero when communication breaks down. Such long-distance, anti-phase relations are however rare.

10.2 Eigenvector centrality

This is a centrality measure related to Google's so-called PageRank score[54].

The basic idea of PageRank is that each page is assigned a score based on the number of external links leading to that page. This would just give us a version of degree or strength, but PageRank and eigenvector centrality impose yet another condition: the nodal score is boosted when linked up to other nodes that are also highly connected. In the same way, we can consider a node in our network to be extra important if it is connected to nodes, which are also highly connected.

Eigenvector centrality, also known as Gould's index of accessibility [55] embodies these ideas in a mathematically rigorous way. The calculation is simple enough: the elements of the eigenvector corresponding to the largest eigenvalue of the connectivity matrix gives the eigenvector centrality for all network nodes. We will now make a brief theoretical excursion to explain why this gives the desired measure.

One way to calculate the eigenvector with the largest eigenvalue is by power iteration[56]. This method is rather inefficient and may converge very slowly, but provides a useful intuitive picture of how the centrality measure is calculated. The power iteration starts from an approximation of the sought eigenvector $\mathbf{b}_0$, in which we may set all elements to unity. Convergence towards the dominant eigenvector is then assured by iterating a normalized product with the connectivity matrix Z,

$$\mathbf{b}_{k+1} = \frac{Z\mathbf{b}_k}{||Z\mathbf{b}_k||} \tag{18}$$

One may visualize this by first placing unity on each of our nodes in the network ($b_{0,i} = 1$ for all nodes $i = 1, ..., N$). Then, each unit is propagated to connected neighbors weighted by the associated link contained in Z. This corresponds to $Z\mathbf{b}_0$, which is normalized to unity before reiterating. Now each node contains a value different from unity and in the next iteration the new values are propagated with the same network weights, and so on until convergence is reached. Convergence is assured if there exists a single greatest non-degenerate eigenvalue and the initial vector has a non-zero component in the direction of the sought eigenvector.

In this way, iteration causes high values to accumulate at nodes with high connectivity to other nodes with high connectivity and the measure can therefore be categorized as self-referential. Clearly, it would be ill advised to use negative weights in this context, as interpretation is completely lost.

Negative links invalidate the premise of the Perron-Frobenius theorem [57], on which the measure is based. The theorem states that a non-negative primitive matrix has a non-degenerate largest eigenvalue that is positive, to which a unique eigenvector with positive entries is associated.

Non-negative simply means that all elements are positive definite and primitive means that the elements of Z^n ($n \in \mathbb{N}$) are non-negative. In fact, since we have no self-connections or directed links, matrix element ζ_{ij} of $\zeta = Z^n$ contains the multiplied link weights in crossing between node i and j in paths of n steps. Clearly, Z^n is primitive if Z is non-negative and real.

Let $\mathbf{v}_0$ be the eigenvector of the greatest eigenvalue λ_0, and let $\mathbf{b}_0$ be our initial guess in the power iteration,[24] which can always be written as a normalized linear combination of eigenvectors $\mathbf{v}_i$ with coefficients β_i such that

$$\mathbf{b}_0 = \sum \beta_i \mathbf{v}_i. \tag{19}$$

Repeated application of the connectivity matrix now yields,

$$Z^k \mathbf{b}_0 = \sum \lambda_i^k \beta_i \mathbf{v}_i. \tag{20}$$

Dividing by $\lambda_0 \beta_0$ and letting $k \to \infty$ we see that

$$\frac{Z^k \mathbf{b}_0}{\lambda_0 \beta_0} \to \mathbf{v}_0, \tag{21}$$

which follows since $\lambda_0 > \lambda_i$ causing $\left(\frac{\lambda_i}{\lambda_0}\right)^k \to 0$ as $k \to \infty$.

Eigenvector Centrality (EC) potentially offers greater sensitivity than strength, although results are hampered by the cutting of negative correlations. A more complete picture could be found by switching to a measure that does not suffer from the same limitations, such as synchronization likelihood. Nevertheless, we find many similarities between strength and eigenvector centrality, as seen by comparing Figs. 74 and 75. It is hard to assess the importance of negative links in this comparison, because eigenvector centrality is by its very nature more condensed, and highlights regions that are highly connected to other highly connected regions.

As for strength, we only find results for the component search. For $HC > M_0$ (see Fig. 75 (a)) Thalamus R and cingulum mid/precuneus appear to be the most significant hub regions with reduced centrality. These are further expanded to include putamen/pallidum R, cingulum mid R and supp motor area as t is lowered.

Comparing with strength (c.f. Figs. 74 (b) and 75 (b)) the greatest difference now occurs in caudate L rather than R. At $t = 3.5, 3.0$ EC and strength become identical, indicating that this region is very central indeed. $t = 2.5$ further exposes thalamus L, whereas the corresponding strength reveals thalamus R. We can presently only speculate that a positive definite FC measure would reveal a more symmetric EC.

Note that according to the progression hypothesis, some of these areas could very well be badly affected in $M_{p\tau}$ group also, suffering complete loss of synchronicity but rendered invisible to correlation by intrinsic quarter-period phase factors.

The same occipital/temporal med R shows up in strength and EC (Figs. 75 (c) and 74 (c)), further expanding first at $t = 2.5$ to include a similar part in the left hemisphere as well as a frontal mid in the left prefrontal lobe. The same sparsity as in the strength maps can be attributed to a corpus striatum hub with loss of synchronicity, rendered invisible by correlation artifacts.

10.3 Betweenness centrality

The measure in the previous subsection was designed by geographers, but betweenness centrality, like many practical graph measures, was born out of the analysis of social networks [58]. The calculation of betweenness centrality is resource demanding, although calculation times have been reduced with more efficient algorithms [59].

Betweenness centrality of node v is defined as[58, 59]:

$$B(v) = \sum_{s \neq t} \frac{\sigma_{st}(v)}{\sigma_{st}}, \tag{22}$$

[24] $\mathbf{b}_0$ must have some overlap with $\mathbf{v}_0$ for the power iteration to work.

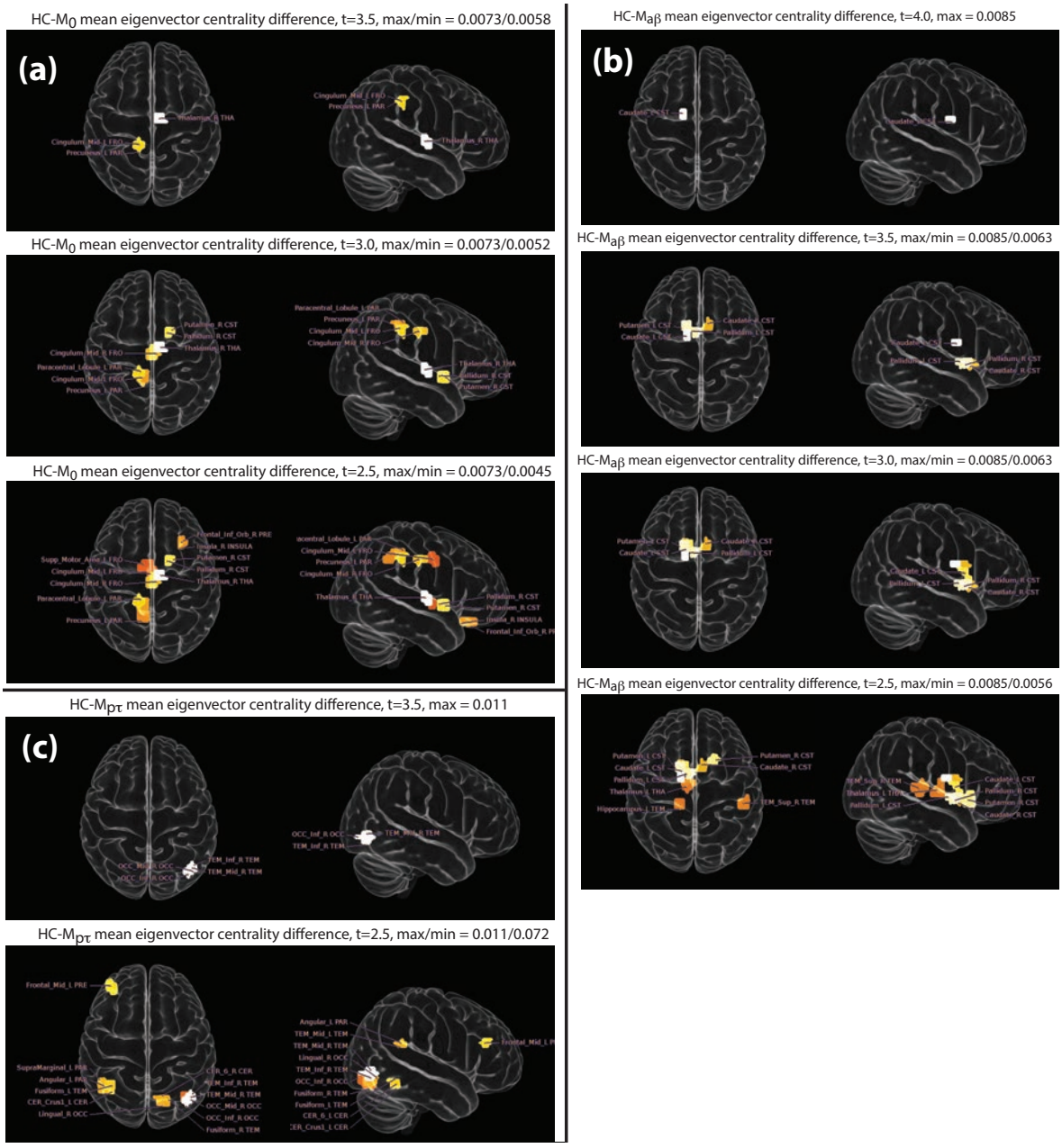

Figure 75: Areas where EC is significantly greater in HC relative M_0 (a), $M_{a\beta}$ (b), and $M_{p\tau}$ (c).

where none of the nodes summed over must be equal to v. σ_{st} is the number of shortest paths between node s and t ($\sigma_{ii} = 1$) and $\sigma_{st}(v)$ is the corresponding measure for paths running through node v. In words, betweenness centrality of node v is the fraction of all shortest paths that run through v. The denominator is generally unity for weighted networks, where the degeneracy of binary networks is virtually absent. So in the weighted formalism, we sum the number of shortest paths that cross the node of interest, meaning that hub regions should have high values.

We now have to define what constitutes a distance measure. Intuitively, the inverse of link weights fulfill the desired properties, approaching infinity when the link weight becomes very small and resulting in short distances for large weights. The inverse is commonly employed for weighted networks [60].

We are again struck by the difficulty with negative connection weights: from the basic connectivity analysis we know them to play a crucial role, however, there is no room for it in the graph theoretical formalism. Consider a small negative weight, that corresponds to a large negative distance. If we allow these, they will be ordered by virtue of their sign as being far closer (negatively so) and more important than links with high positive values, which on all accounts is wrong. One could take the inverse absolute value of the correlation as distance measure, but basic correlation analysis implies that one will then miss zero crossovers and the crucial latter stage pattern changes. We are left with the only option of cutting negative weights.[25] These problems are non-existent for measures like synchronization likelihood, phase coherence, coherency, representing a probability of functional connection.

The bottleneck in (22) is that of the shortest path calculation, a problem often attacked with variants of Dijkstra's algorithm [61], for which the prerequisite is non-negative weights.[26]

Dijkstra's algorithm can be used to calculate the shortest distance matrix for all nodes, which in turn can be combined with a measure known as the clustering coefficient, to produce another measure called 'small-worldness'. This measure attains a seemingly universal range of values in natural networks, characteristic of integrated modularized processing.[27]

Finding shortest paths is very central to graph theory and we give a brief description of Dijkstra's approach here [61]. For betweenness centrality, we need to find the shortest path between two given nodes u and v.

Let's say we start iterating from u looking for the shortest path $d_{u,v}$ to v. Each pair of nodes is connected with a path comprised of links with specified length (inverse positive correlation in our case). We traverse the network from the initial u, in each iteration sitting on current node c with neighbors c_n, looking for the target, v.

To begin with, all nodes are marked unvisited and assigned infinite tentative distance from the initial node (which itself has zero distance). Nodes are either marked as visited or unvisited. Once visited during iteration for $d_{u,v}$, the node will not be revisited.

At current node c, tentative distances d_{u,c_n} are calculated for all of its neighbors c_n (those marked unvisited) by adding the tentative distance $d_{u,c}$ to d_{c,c_n}. When all neighbors have been considered, c is marked as visited. If $c = v$, i.e. the current node happens to be the target node, we are done. Otherwise, we select the c_n with the smallest tentative distance as our current node c and repeat the procedure. Ultimately we will we reach v, or the smallest tentative distance is infinity (in which case there is no shortest path).

(22) was probably first designed with binary networks in mind, and we may speculate that better power to discriminate groups would result from summing the shortest path values traversing ν.

$$\beta(\nu) = \sum_{s \neq t} \frac{\gamma_{st}(v)}{\gamma_{st}}, \tag{23}$$

where γ_{st} is the shortest path length from s to t. The higher power is probable because we would boost the values of hub-regions that have strong weights (short link distances) converging on them. We have already seen the presence of high differences in hub regions using strength and eigenvector centrality - in particular for group $M_{a\beta}$.

[25] Omitting the Fisher Z transform, we can shift correlation values into the positive range by adding unity. Now we have lost the meaning of negative weights and would not consider their intrinsic functionality by demoting them to the lowest range of functional connectivity, when we know that high magnitude negative correlations exist and are important. On the other hand, we would perhaps capture the effect of a reduced connectivity from positive to negative, although the centrality values themselves would be incorrect.

[26] There are shortest path algorithms which under certain conditions allow negative weights (not distances), i.e. the Floyd-Warshall algorithm [62]. It would be fairly useless to us, since there is no still no physical meaning attached to paths derived from negative correlation values.

[27] The clustering coefficient becomes complex valued with negative links. Regardless, small-worldness calculation in weighted networks is marred by technical difficulties. Alternatively, somewhat arbitrary thresholding into binary networks allows one to proceed.

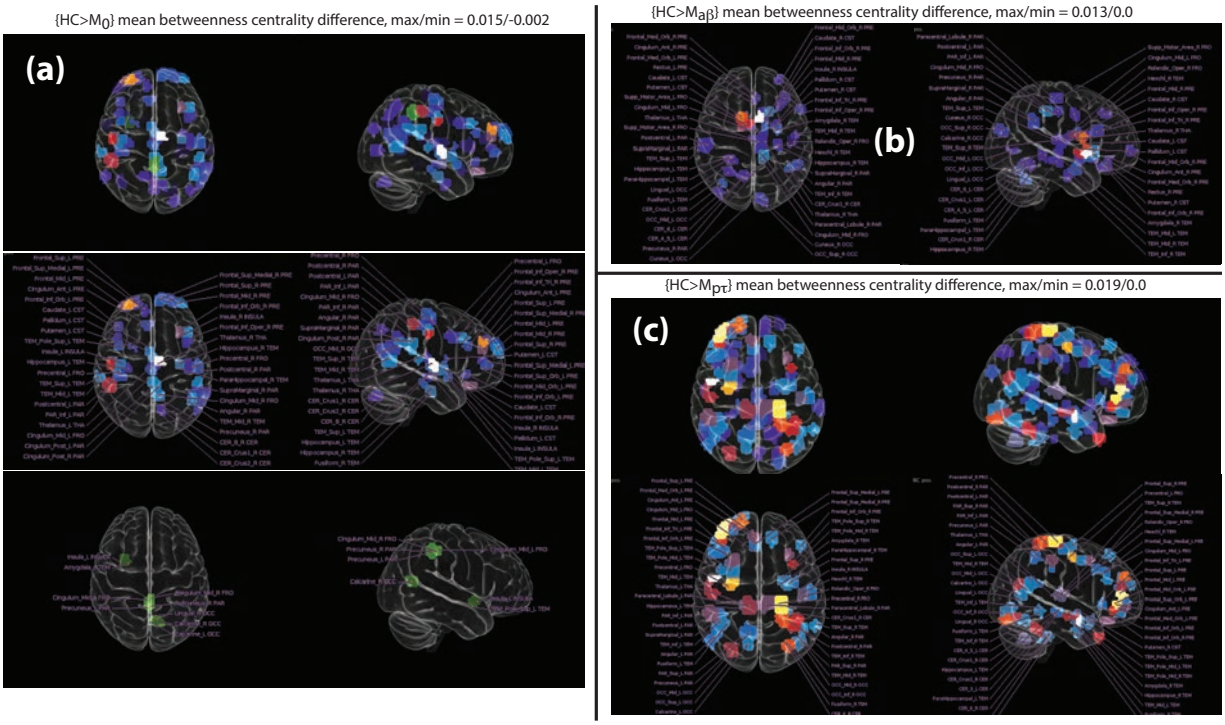

Figure 76: Panel (a) shows betweenness centrality differences calculated on the network component $HC > M_0$ ($t = 3.5$) using individual node permutation search. The center row is thesholded to positive differences (HC has larger BC than M_0). The bottom row shows areas where M_0 has higher BC than HC. Panel (b) and (c) show group mean BC differences where $HC > M_{a\beta}$ and $HC > M_{p\tau}$, respectively.

For betweenness centrality we only get results if we restrict the calculation to the differing network component (here we use the $t = 3.5$ NBS component). Then the contrast is strong enough that we do not need the nodal component search and Fig. 76 shows the results of permutation testing each node. As with the other measures, BC for M_0 shows a maximum for thalamus R (see Fig. 76 (a)), highlighting it as a key hub afflicted by functional connectivity breakdown. Again, cingulum mid appears stronger and we also find frontal mid L. Among others, both hippocampus and cingulum posterior appears in the mid-range of differences. Interestingly, a few regions appear with BC greater in MCI than HC, possibly signaling a compensatory mechanism (we use two-tailed t-test), which explains the proximity of one such region to cingulum mid/post. Turning to $HC - M_{a\beta}$ the familiar corpus striatum hub is highlighted as maximally different in Fig. 76 (b). This is no surprise as these central hub regions have been implicated many times before. Interestingly, hippocampus and thalamus are flagged bilaterally.

Finally, Fig. 76 (c) shows group mean BC difference for $HC > M_{p\tau}$. Here we get a much stronger contrast than for strength and EC, and we see echoes of the frontal/temporal left clusters previously identified, as well as precentral R and a mid-range difference in both hippocampi. The cerebellum/temporal/occipital interface on the right is also clearly visible. The corpus striatum hub shines with its absence, but again this probably has to do with the use of correlation as FC measure. Of course, calculating BC on a component of links (which is common practice) does tend to amplify the contrast. However, no such enhancement could be found when calculating EC on components.

11 SVM separation of groups

In this section we quantify how well separated the predefined MCI groups are in functional connectivity space. Any classification attempt is preceded by a feature selection - this is a difficult step, which some may argue largely constitutes the art of classification and machine learning.

Here we only assess the relative separation of groups using a mock-classification scheme, where we

allow so-called Support Vector Machines (SVMs)[63] to perform a pseudo-classification. It is not a real classification, because we supply the classifier with a feature selection filter or mask: the subset of links identified with group differences, as calculated by permutation testing. In a real classification, feature selection must be performed on a training set, held completely separate from the validation set. Nevertheless, supplying the feature filter will give us a very good idea of the relative degree of separation of the groups in FC space that these patterns represent. Part of the reason for doing this, is that the permutation testing is computationally far too costly to be employed in a rigorous classification scheme. This, would require an alternate strategy and represents a much more difficult challenge.

Although we will generate Receiver Operating Characteristic (ROC) curves, it is important to underline that these represent pseudo-classifications aimed only at mapping out the relative degree of separation of groups. Likewise, the pseudo-classification scores elucidate the separation implied by FC patterns.

We begin by providing a brief theoretical background of SVMs (for more details see Ref. [64]). The SVM is an algorithm that constructs optimal separation planes given two or more classes of data. The plane may not be linear and is generally a hyperplane separating data in higher dimensions. For example, two-dimensional data is separated by a line, three-dimensional points by a surface.

Originally proposed by Vapnik in 1995 [65], SVMs are now part of the standard arsenal with a good balance of speed and accuracy.

The basic idea is to construct the separating hyperplane out of linear combinations of the data points skirting class border (so-called support vectors). At the same time, the algorithm seeks to maximize the margin between the two groups, yielding the best separation plane for the given training data.

To get a feel for how this is done, consider looking for the optimal hyperplane separating a set of n-dimensional data points $\mathbf{x}_i \in \mathbb{R}^n$, with corresponding two-class labels $y_i = \{-1, 1\}$. The set is said to be linearly separable if there is a $\mathbf{w} \in \mathbb{R}^n$ and $b \in \mathbb{R}$ such that

$$y_i(\mathbf{w} \cdot \mathbf{x}_i + b) \geq 1, \tag{24}$$

for all points in the set. This equation is the result of combining the equations for the two class margins: $\mathbf{w} \cdot \mathbf{x} + b = \pm 1$. Between these margins, runs the optimal hyperplane, defined by setting the expression in parenthesis to zero, i.e. $\mathbf{w} \cdot \mathbf{x} + b = 0$. The distance of point $\mathbf{x}_i$ to the hyperplane is (with sign depending on which side of the plane we are)

$$d_i = \frac{\mathbf{w} \cdot \mathbf{x}_i + b}{w}, \tag{25}$$

where w is the length of vector $\mathbf{w}$. Rearranging (25) for $d_i w$ and substituting into (24) shows that $y_i d_i \geq 1/w$, i.e. the minimum distance of any data point to the hyperplane is $1/w$ (in the linearly separable system under consideration). Furthermore, hyperplane parameters can be rescaled into a canonical representation where the distance to the closest point is exactly $1/w'$, where w' is the rescaled parameter. Working in the canonical representation, the optimal hyperplane for a linearly separable set is now defined as the one which has maximal distance to the closest data point.

We now have a clear optimization problem where we attempt to maximize $1/w$, subject to the constraint $y_i(\mathbf{w} \cdot \mathbf{x}_i) \geq 1$ for all i in the set. In practice, it is easier to minimize $\mathbf{w} \cdot \mathbf{w}/2$, rather than maximizing $1/w$. The optimization problem can be solved by starting from the Lagrangian

$$L = \frac{1}{2}\mathbf{w} \cdot \mathbf{w} - \sum_i \alpha_i \left[y_i + i(\mathbf{w} \cdot \mathbf{x}_i - 1) \right] \tag{26}$$

and locating saddle points where L is minimized as a function of $\mathbf{w}, b$ and maximized as a function of the Lagrangian multipliers α_i. Seeking the minimum we get

$$\frac{\partial L}{\partial b} = \sum_i y_i \alpha_i = 0 \tag{27}$$

$$\frac{\partial L}{\partial \mathbf{w}} = \mathbf{w} - \sum_i \alpha_i y_i \mathbf{x}_i = 0 \tag{28}$$

which can be substituted into (26) to yield the dual form

$$\mathcal{L}(\alpha) = \sum_i \alpha_i - \frac{1}{2} \sum_{i,j} \alpha_i \alpha_j y_i u_j \mathbf{x}_i \mathbf{x}_j \tag{29}$$

to be maximized with positive definite Lagrangian parameters subject to the constraints $\sum y_i \alpha_i = 0$ and $\alpha_i \geq 0$.

The Karush-Kohn-Tucker (KKT) conditions generalize the Lagrangian multipliers by allowing inequalities as conditions. The KKT conditions for a stationary point x^*, arise in maximizing a function $f(x)$ subject to l inequality conditions $g_i(x)$ and m equality conditions $h_i(x)$. If the constraints are differentiable near a stationary point x^*, there exists KKT multipliers μ_i and λ_i analogous to Lagranges' multipliers. The conditions for stationarity can then be stated as

$$\nabla f(x) = \sum_{i=1}^{m} \mu_i \nabla g_i(x^*) + \sum_{i=1}^{l} \lambda_i \nabla h_i(x^*) \tag{30}$$

In maximizing (29) subject to the constraint $\sum_i y_i \alpha_i = 0$ and $\alpha_i \geq 0$ we obtain the KKT conditions

$$\bar{\alpha}_i \left[y_i(\bar{\mathbf{w}} \cdot \mathbf{x}_i + \bar{b}) - 1 \right] = 0 \tag{31}$$

We only have non-zero α_i for those points that satisfy the condition $y_i(\mathbf{w} \cdot \mathbf{x} + b) = 1$, meaning that the optimal hyperplane parameter calculated as

$$\bar{\mathbf{w}} = \sum_i \bar{\alpha}_i y_i \mathbf{x}_i, \tag{32}$$

is a linear combination of only a few $\mathbf{x}_i$, so-called support vectors. These points are nearest to, and define, the optimal hyperplane. Once the optimal hyperplane has been determined, the class of a given point $\mathbf{x}$ is simply determined by $sgn(\bar{\mathbf{w}} \cdot \mathbf{x} + \bar{b})$.

To deal with the situation when the points are not linearly separable, Vapnik proposed allowing a soft margin [65] that allows finding a solution with some misclassifications. Adding a regularization parameter C, we seek a solution to the same optimization problem in the dual form (29), but now subject to the condition $0 \leq \alpha \leq C$. The classification is no longer parameter free and the hardness of the margin is controlled by C, where a high C minimizes the number of misclassified points corresponding to a hard margin, but potentially over-fitting the hyperplane.

In addition, a linear separation may not always be sufficient and we can introduce a non-linear kernel function $k(\mathbf{x}_i, \mathbf{x}_j)$ into the dual form.

$$\mathcal{L}(\alpha) = \sum_i \alpha_i - \frac{1}{2} \sum_{i,j} \alpha_i \alpha_j y_i u_j k(\mathbf{x}_i \mathbf{x}_j) \tag{33}$$

This enables a more complex hyperplane which can better delineate the class border. With the non-linear kernel comes an obvious risk of over-fitting, which can be adjusted by modifying kernel function parameters. Below, we use a Radial Basis Function (RBF) kernel: $k(\mathbf{x}_i, \mathbf{x}_j) = e^{-\gamma \|\mathbf{x}_i - \mathbf{x}_j\|}$ and so we optimize SVMs with two parameters: the regularization parameter C and the range of the radial basis function via γ.

As a precursory step, the FC data is centered around its mean and rescaled to have unit standard deviation. This tends to improve classification accuracy.

Finally, more than one class can be separated at the same time via multiple hyperplanes and so-called multi-SVMs. Mostly commonly these consist of several binary classifiers working together in some scheme. Some algorithms solve the multiclass problem in a single optimization[66, 67]. This is particularly interesting, as it allows pitting all classes against each other at the same time. Below, we will make use of the single optimization approach to see how well HCs and the MCI groups can be simultaneously separated[66].

We begin with binary classifications of various groups and as a first step we perform an optimization of our SVMs with a grid search for RBF γ and regularization parameter C. Fig. 77 show the True Positive Rate (TPR), False Positive Rate (FPR), and Balanced ACcuracy (BAC) as a function of the two optimization parameters. The latter is an accuracy measure which reduces the effect of performance estimate boost due to difference in group numbers, defined as the average of sensitivity and specificity. The measures are evaluated by 100 training/validation sessions with 50% random, stratified hold-out. In choosing the optimal parameters, we prefer to let the TPR remain high at the expense of an increased FPR, all the while keeping an eye on the BAC. In Fig. 77 we see that whereas the TPR landscapes are relatively similar, the FPR is substantially reduced as we go from M_0 to $M_{a\beta}$ to $M_{p\tau}$, where the BAC peaks. Whereas the NBS components yield a surprisingly sharp threshold as γ is increased (reducing the range of the RBF) it is less so for the FDR controlled results. Here, the BAC also increases with perceived progression. We fix the parameters to values that work reasonably well for all group comparisons feature filtered by FDR - $\gamma = 30$ and $C = 1$, and similarly for the NBS filter, with a somewhat softer margin.

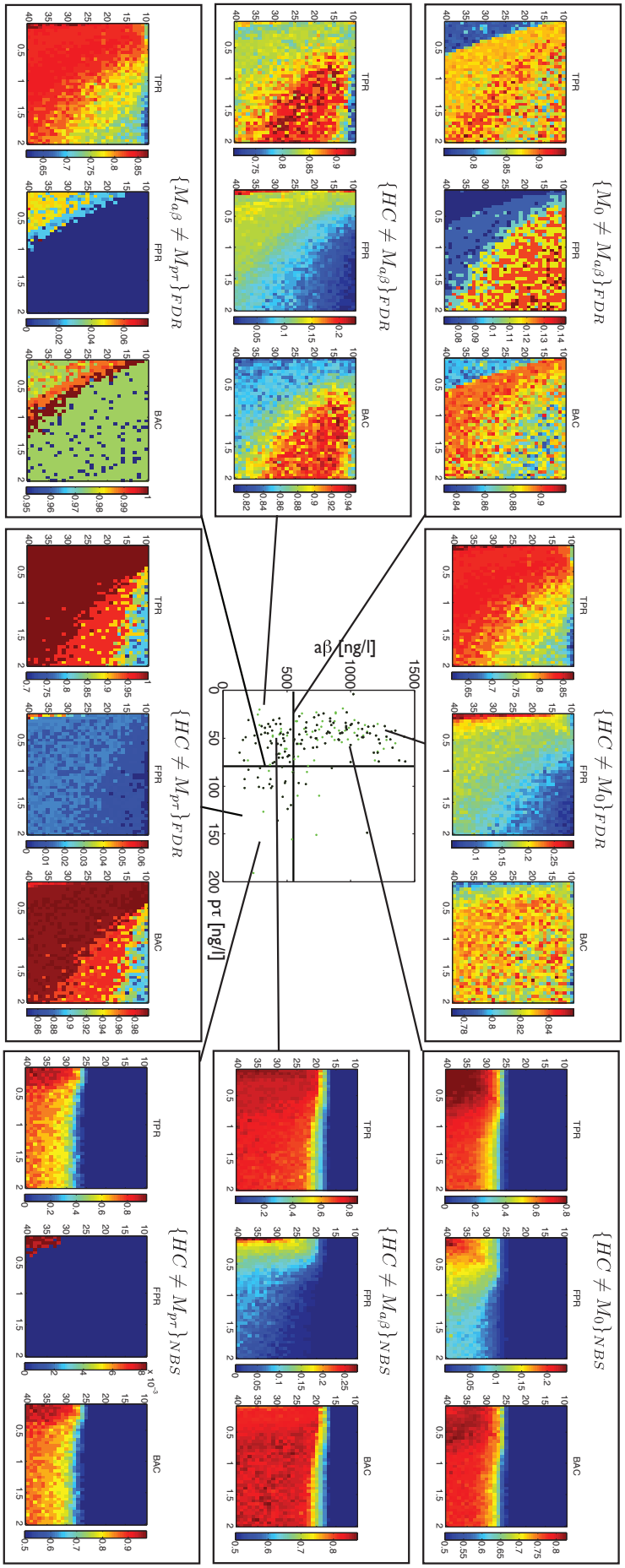

Figure 77: Grid search for optimal RBF γ and SVM regularization parameter C using the NBS components/FDR link sets as feature filter. The maps show how the true/false positive and balanced accuracy varies as a function of regularization parameter (y-axis) and radial basis function extension (x-axis).

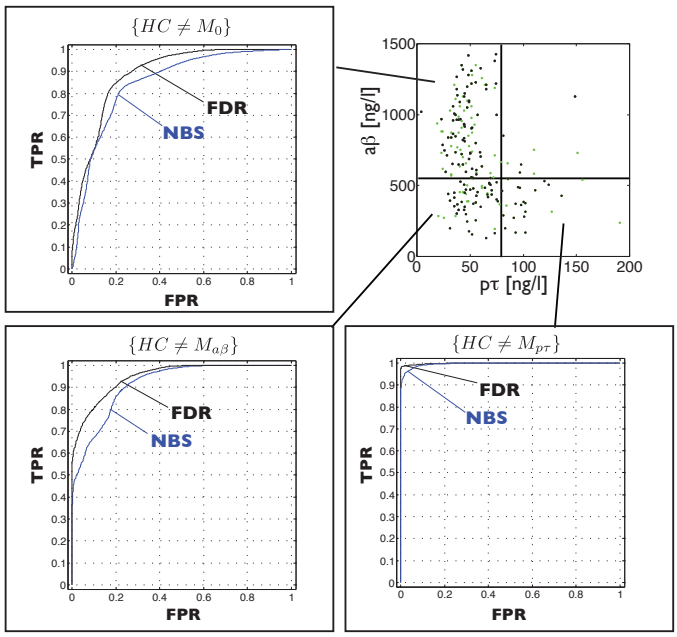

Figure 78: The averaged ROCs from 500 pseudo-classifications with optimal SVM parameters (separately determined for FDR and NBS filtered inputs) reveal a slightly better separation for the FDR filter. All curves are for the highest resolution ROI-set.

We can now compare the results of the pseudo-classifications using the NBS and FDR feature filter by 500 50% hold-out, stratified randomizations into training and validation sets. ROCs are constructed with the test scores in the form of distances from the optimal hyperplane, for which the FPR-TPR curve is generated by transposing the hyperplane from its optimal position. The final ROC is an average of the 500 ROC curves for each randomized pseudo-classification, shown in Fig. 78. Resulting confidence intervals would be too small to be visible in these plots. We see that the FDR filter gives a slightly better separation of the groups than the NBS filter. This is hardly surprising, as the many of the links present in the NBS component are not flagged as individually significantly different.

We now look at how the relative group separation depends on the ROI-resolution. After the initial optimization step using FDR controlled feature filters, we generate ROCs in an analogous fashion. The results are shown in Fig. 79.

There are a few important conclusion to be drawn from these ROCs. Classification accuracy is very poor for the low resolution sets, where the 90 AAL ROIs do not even produce any MCI-MCI differences. For higher resolutions, the MCI-MCI are well separated relative *MCI-HC* comparisons, possibly an effect of HC contamination. The groups become easier to separate with perceived progression along in biomarker space. For HC versus M_0, a high TPR can be obtained, but only at the cost of a relatively high FPR, thus reinforcing the relative closeness of the two groups. The best separations are obtained for the highest resolution and HC-$M_{p\tau}$ as well as $M_{a\beta}$-$M_{p\tau}$.

These results are reflected in the test scores shown in Fig. 80, where each subject has been tracked across training-validation randomizations and the test scores (hyperplane distances) recorded. Fig. 80 show the mean and standard deviations of the scores for each subject across 500 randomizations.

We can also perform a simultaneous separation of the groups using a multi-SVM, and again we optimizing parameters with respect to accuracy. Fig. 81 shows the test scores for the three decision functions associated with the separating hyperplanes, revealing that M_0 and $M_{a\beta}$ are relatively closer to each other than the distant $M_{p\tau}$ group. This is again showing that $p\tau$ overall has a larger impact on the functional connectivity.

The mean confusion matrix of 500 randomizations in Fig. 81 reports the average misclassifications of two groups. Each row in the confusion matrix shows what the corresponding group has been classified as on average. The so-called Matthews coefficients reported in the tables reflect the correctly classified fraction of each group, when seen as a binary one-against all classification.

Finally, we can also throw HC in the mix and let the multi SVM attempt separation by combining the group feature filters with each subjects FC. The results in Fig. 82 indicate that HC is closest to M_0,

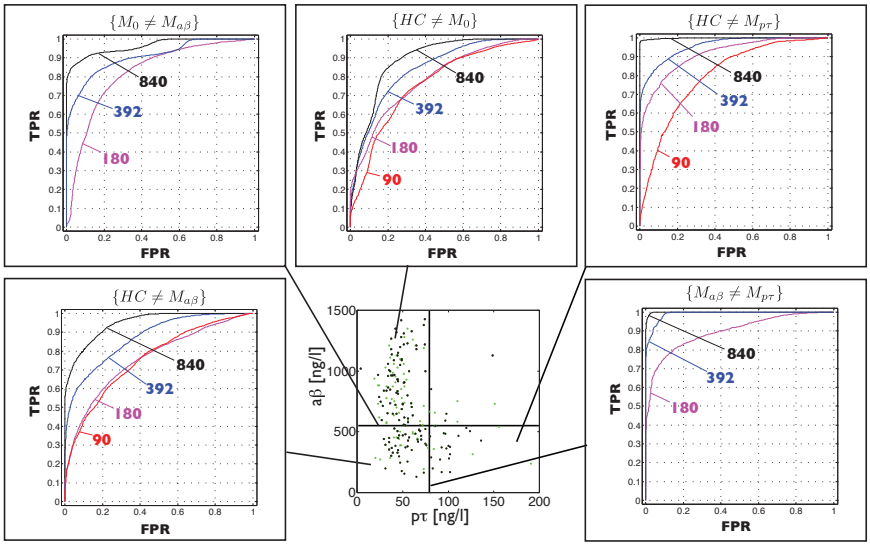

Figure 79: The ROCs for FDR controlled results and various resolutions.

which is closest to the MCI group $M_{a\beta}$. By the Matthews' coefficient $M_{p\tau}$ is the best separable group overall.

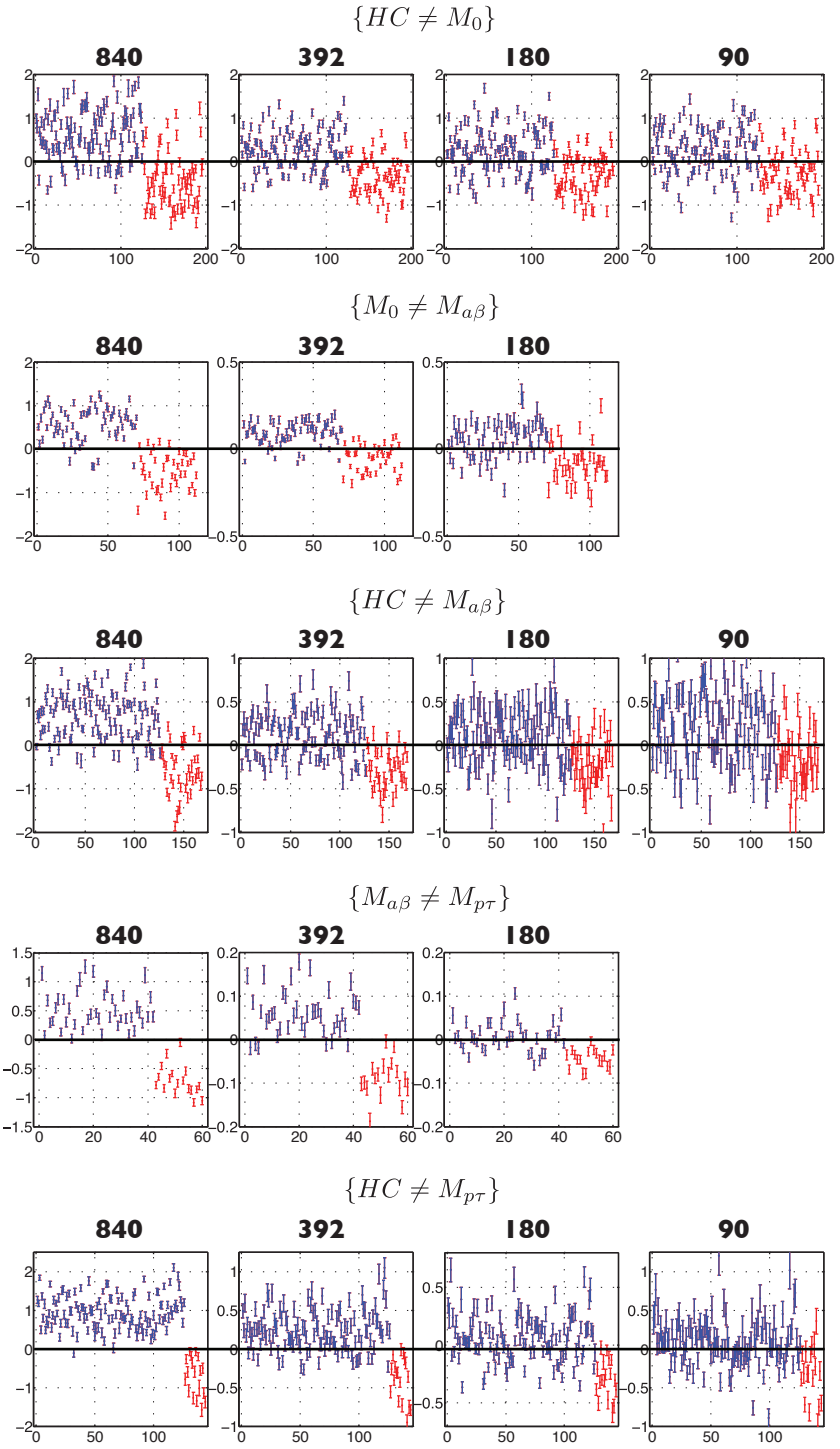

Figure 80: Subject test scores across 500 training-validation randomizations clearly show the importance of a high resolution ROI-set.

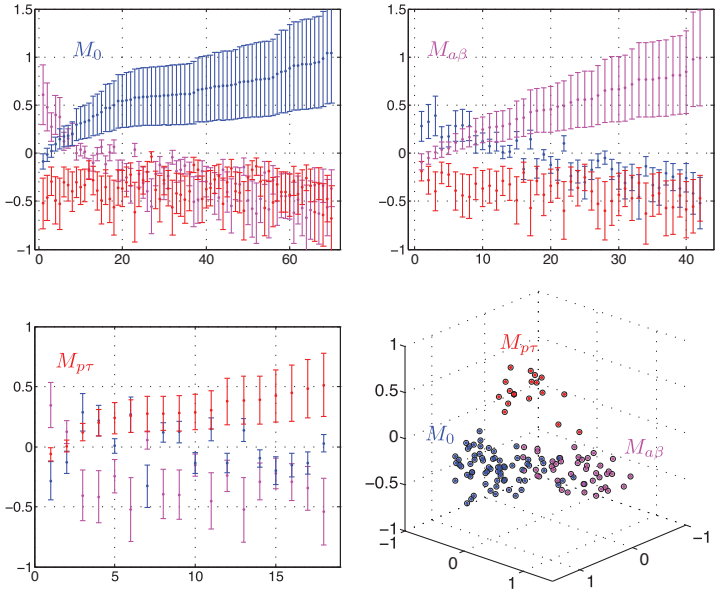

	M_0	$M_{a\beta}$	$M_{p\tau}$	HC
M_0	0.70	0.05	0.0	0.25
$M_{a\beta}$	0.13	0.63	0.0	0.24
$M_{p\tau}$	0.01	0.03	0.68	0.28
HC	0.06	0.01	0.0	0.93

	Matthews' coefficent
M_0	0.66
$M_{a\beta}$	0.68
$M_{p\tau}$	0.80
HC	0.69

Figure 81: Simultaneous separation of the three MCI groups. 2D plots indicates test score averages for the three decision functions associated with each hyperplane. The 3D plot shows the mean test scores for all decision functions at once (M_0=blue, $M_{a\beta}$=magenta, $M_{p\tau}$=red). The tables show the mean confusion matrix and Matthews' coefficients for the MSVM applied to the three MCI groups. Each row in the confusion matrix shows the average fraction of the row group as classified as the column group.

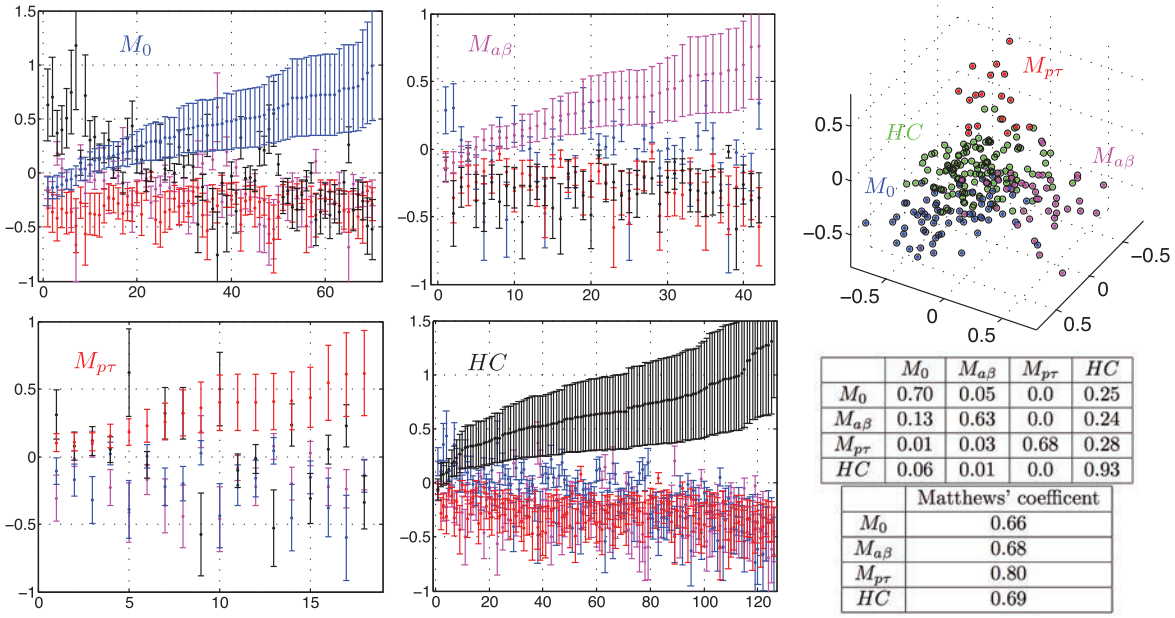

	M_0	$M_{a\beta}$	$M_{p\tau}$	HC
M_0	0.70	0.05	0.0	0.25
$M_{a\beta}$	0.13	0.63	0.0	0.24
$M_{p\tau}$	0.01	0.03	0.68	0.28
HC	0.06	0.01	0.0	0.93

	Matthews' coefficent
M_0	0.66
$M_{a\beta}$	0.68
$M_{p\tau}$	0.80
HC	0.69

Figure 82: Test scores for multi-SVM separation MCI and HC. The first four plots show the test scores for each decision function and the lower plots show difference perspectives of the mean test scores for three decision functions (green indicates HC). The mean confusion matrix and Matthews coefficients for the MSVM applied to all MCI groups and HC. Each row in the confusion matrix shows the average classification of the row group as the column group.

12 Comparison with literature

In conclusion, we have compared HC to MCI with non-pathological biomarker levels, those with pathological $a\beta$, and high levels of p_τ. Relative HC, the M_0 group exhibits a widespread pattern, perhaps containing the signature of several dementias. Key regions, such as thalamus, putamen and posterior cingulate cortex have reduced connectivity. This is the largest MCI group and most likely has the greatest overlap with MCIs studied in the literature.

In $M_{a\beta}$, a powerful signature appears with reduced FC converging on a corpus striatum hub, mainly comprising caudate, putamen, with radiating links to among others thalamus, amygdala R and hippocampus R among others.

Relative HC, $M_{a\beta}$ has a heavy FC reduction in a a large number of links involving frontal and sup parietal regions. This pattern has some similarities with $HC > AD$.

Additionally, we found that the connectivity patterns manifest themselves in the graph theoretical centrality measures. Noise levels are high enough to disrupt classification in a rigorous cross-validation scheme, although the groups are increasingly separable with higher resolution.

The difference in mean FC on the HC-MCI components gradually increases with perceived progression across M_0, $M_{a\beta}$ and $M_{p\tau}$, pushing into the negative correlations. This drift indicates an increasing time-lag between functional centers as the disease progresses, hinting at a progression pattern.

There appears to be some indication, although observations could be muddled by correlation blind spots, that a progression pattern is discernible. Loosely speaking, we find epicenters around putamen, caudate and thalamus, that spread with worsening biomarker levels to involve temporal, parietal and frontal areas. Further testing and calculations is needed before such claims can be substantiated and complementary FC measures such as coherency or synchronization likelihood are needed.

Relatively little work has been performed relating RS fMRI to CSF biomarker levels, and most studies stratify MCIs according to a battery of cognitive tests. A cautionary note on group sizes is also appropriate. Many of the references cited here have 10-20 individuals in their groups. This is nowhere near enough to claim the presence of a universal signal, and results must always be interpreted with some caution. With groups of these sizes, chances of spurious effects are high.

The reader should also note the we have chosen to do a whole-brain connectivity analysis, whereas many of the studies are based on ICA analysis which will identify salient networks, but smooths interactions. In addition, many authors focus on classical areas implicated in cognitive decline, ab initio. Studies that exclusively focus on single seeds and the associated connectivity introduce a bias in the literature, reinforcing images without a clear relation to the whole data set, without biased filtering.

It is certainly be true that the DMN is affected, for example the Posterior Cingulate Cortex (PCC) is commonly occurring in ICA studies. But when dealing with a larger material it is a fundamental mistake to focus on isolated regions ad hoc. Many other differences may be equally important, but are then disregarded as not being relevant to cognitive decline. Fair enough: there is a diverse and complex pattern present, and not all of it may be relevant to the postulated hypothesis. One should not forget that MCI are diagnosed as such because of a distinct set of symptoms. These symptoms may be less likely to appear if non-classical regions are afflicted, which does not mean that the neuropathology is absent.

Having said all that, the DMN is the dominant network in resting-state analysis and is also of particular interest as it overlaps with amyloid depositions. Furthermore, hippocampus and the medial temporal lobe are part of DMN [68], and these structures are associated with episodic memory loss, the first AD symptom.

One study of interest relates the quota of $a\beta$ to $p\tau$ to changes in DMN identified by ICA [69]. The groups consist of 21 AD, 36 MCI (lower MMSE score including memory score, i.e. amnestic MCI), Other Dementias (OD) and subjective cognitive impaired (SCI, presumed low MMSE but with not so low memory score, i.e. non-amnesic MCI[28])

The 36 MCI subjects in this study have a remarkably high level of $a\beta$ (842 ± 352 ng/l). In addition, the $p\tau$ levels are not particularly high (59 ± 24), such that their definition mostly overlaps with our group M_0, which we believe to be populated by a larger set of subspecies with less relevance to AD conversion. On the other hand, the authors of Ref. [69] even include OD, which contains a diffuse and wide variety of dementias, most of which seem irrelevant to the CSF biomarker pathway to AD. AD, OD, MCI and SCI subjects pooled show weak voxel-wise correlation between CSF quota and ICA DMN components in a very small cluster of 17 voxels located mostly in left cuneus (adjusted for age, gender and gray matter

[28]The SCI are only described as having subjective cognitive complaints but not failing objective cognitive tasks. However, comparing with MCI and the only cognitive test-scores available, there is not significant difference. Probably, the difference lies in memory tasks.

intensity). The authors of Ref. [69] proceed to analyze partial correlation between the very limited part of cuneus/precuneus and the CSF quota for various groups separately, finding only that the MCI group had moderate statistical significance. Their largest group (MCI) also has the largest spread in biomarkers levels. We also note that motion discrimination parameters are 3 mm, rather than our more conservative 1 mm. Unfortunately, using a more conservative QA protocol is no guarantee of artifact free material, and motion artifacts remain in the form of a global signal disruption even after regression, with a more or less heavy impact on contrasts [70, 71]. Motion thresholds are often set higher in cohorts of limited size. Relating these findings to our results does not lend itself easily, but their largest group (MCI) seems to resemble mostly our M_0 - precisely the group that gives most connectivity difference in PCC, relative controls (there is even larger differences on the left). One possibility is that the voxel mask they derived by ICA does not really reflect pathology to sufficient degree. This is could be the case because: 1) the mask is derived with a wide variety of dementias, many not relevant to AD at all, 2) their MCI group - the only isolated group correlating with CSF in the tiny mask - does not reflect pathological CSF, 3) the choice of CSF quota, when likely $p\tau$ has the heaviest impact on FC, 4) the high tolerance for motion in combination with small groups makes contrasts weak.

Another recent study of interest, focuses on the effect of biomarkers on connectivity [72]. This study is interesting, but unfortunately of very limited overlap with the groups in our study. The authors studied correlation between DMN functional connectivity and decrease/increase in $a\beta/p\tau$ levels in a large group of 207 subjects with *normal* cognitive functions. Targeting a population with normal cognition, the authors hypothesize that changes in CSF biomarker levels will still have a detectable impact on DMN function, thereby locating signatures potentially preceding the onset of cognitive decline. The cohort had normal Clinical Dementia Rating (CDR), and mean biomarker levels $a\beta = 624 \pm 254 ng/l$ and $p\tau = 61 \pm 31 ng/l$. The analysis directly focuses on posterior cingulate. A seed consisting of the voxels within a 6 mm radius placed on the MNI PCC center, where after correlation with all other voxels in the gray matter time series was calculated. This was done for all subjects in the subgroup with 8 AD and 8 controls. The seed-based correlation maps were then averaged over the 8 individuals in each subgroup. By simply taking the difference between the two group averaged maps, the authors concluded that there was a relative reduction in correlation between PCC and the other DMN nodes, which motivated them to use this seed for their subsequent analysis. This seems only to have served as a motivation for ROI creation, as it had no statistical power to speak of. Using this seed on the 207 subjects with normal cognitive function, correlation (Spearman rank partial correlation) between DMN connectivity and CSF biomarkers was examined. The biomarkers were treated as continuous variables, adjusting for variables such as age, PCC/MTL volume, and $a\beta$ when testing for $p\tau$. The authors employed limits for pathological CSF biomarker: $a\beta <>$ 500 ng/l and $p\tau <>$ 80 ng/l.

Decreased $a\beta$ was found to correlate with reduced PCC-MTL connectivity and increased $p\tau$ with reduced PCC-left MTL connectivity (only trend-level reduction in PCC-right MTL and PCC-medial prefrontal cortex). One should note however, that subjects termed $a\beta$ positive ($a\beta < 500$ ng/l), probably include many individuals with that are $p\tau$ positive. The fact that the $p\tau$ effect has been embedded in the $a\beta$ pathology in this way, means that the two effects have not really been untangled. The high degree of similarity between the $p\tau$ and $a\beta$ analysis is perhaps an indication of $p\tau$'s dominant role. This may seem counter-intuitive, because of the weaker correlation found for $p\tau$, but that is probably just an effect of the very small number of subjects remaining in the high $p\tau$-range. In addition, it is hard to believe that many cognitively normal subjects can be found with such high $p\tau$-levels. Comparison is also made harder because the authors have limited themselves to a connectivity with a 6 mm radius sphere located on PCC. Regarding our HC controls as having higher levels of $a\beta$ than M_0, posterior cingulate has reduced connectivity to left medial temporal parts. Other than that, it is difficult to compare and find any correspondence. Then again, all our MCI have been diagnosed as cognitively abnormal, whereas the cohort of Wang et al consists of cognitively normal subjects.

Many connectivity analyses have been performed on MCI material stratified by cognitive tests and criteria. Wang and co-workers investigated wavelet correlation differences (in intervals similar to ours) between 37 amnestic MCI (aMCI: i.e. with cognitive difficulties and memory problems, the most probable prodromal AD stage) and 47 controls [30]. The diagnosis was made with Petersen's criteria [73] and a battery of cognitive tests including MMSE, clock drawing test, Auditory Verbal Learning Test (AVLT) and Clinical Dementia Rating (CDR). This study is particularly interesting, since the imaging parameters used are almost identical to ours. This includes using a Siemens Trio 3T scanner, removal of five first volumes, SPM8 preprocessing, TR=2s and choosing to not remove the global signal (given the controversy, see Refs. [74, 75]). They have a longer total acquisition time than us (478 s rather than 350 s) which

should result in a better statistical basis for connectivity analysis[29]. Wang et al used 1024 random ROIs of roughly equal size and calculated Pearson correlation between wavelet coefficients from a maximal overlap discrete wavelet transform. The authors attempt a wide range of graph theoretical measures, but the main results stem from an NBS analysis [41]. Furthermore, the authors used linear regression to relate connectivity and cognitive test scores.

The basic analysis reveals that only in the frequency interval $f = 0.031 - 0.063$ Hz is there a significantly lower mean wavelet correlation and higher proportion of short range correlations for MCI. Looking at our results, we do not have the frequency information for high resolution ROIs, nor do we have them for HC. Since M_0 is closer to HC than the other groups we can only relate this to a trend-level reduction in FC between M_0 and $M_{a\beta}$, which we find to be greatest in the same frequency interval. The authors therefore focus on this particular interval in the remaining analysis.

The comprehensive graph theoretical analysis revealed small world network topology, but in terms of characterizing pathology only a significantly longer path length was found for MCI. This is a reflection of the observed reduction in correlation, as the distance measure is essentially just the inverse of the correlation [30].

The specificity/sensitivity of the component separating the groups was determined by ROC analysis to be around 85 %[31].

Analysis of the mean nodal strength, revealed 27 areas with reduced FC including bilateral frontal superior gyrus, precuneus and mid temporal gyrus, bilateral caudate and right putamen. These differences had $p < 0.01$, but were uncorrected for multiple comparison (which in all likelihood leaves nothing).

Comparing with our results from the graph theory section, we find good correspondence, with differences in frontal superior for $M_0 - HC$ (extending bilaterally for lower suprathresholds), putamen R at higher significance levels, both caudate, as well as precuneus, cuneus and posterior cingulate. In $HC - M_{a\beta}$, we find strong signatures in caudate and putamen R. The MCI group of Ref. [30] most likely reside in both M_0 and $M_{a\beta}$, as these constitute the most numerous population of MCI.

The component analysis reveals reduced FC on a network that mostly resembles $HC > M_0$, with many intermodular connections linking somatosensory, motor, visual processing. Since most MCI reside in M_0, the resemblance with M_0 is perhaps not surprising.

Regarding putamen and caudate, which figure largely in our analysis, these are identified as key nodes receiving input from cortex via thalamus. The authors note no specific deficiency in thalamus, but we do. These regions appear to be very central to the MCI pathology, shown to entail both gray matter atrophy in volumetric analysis [5] and metabolic disruption in PET studies [76].

In Ref. [5] Madsen et al choose to focus on caudate nucleus rather than the more commonly targeted medial temporal lobe and cortical structures. Memory function in hippocampus and the medial temporal lobe are known to be affected by both plaque and NFT pathology early on, whereas caudate atrophy has more often been associated with impaired motor skills and Parkinson's. However, both τ and amyloid aggregate in caudate which is also known to be involved in the formation of new and autobiographical memories.

Madsen et al used 3D surface mapping techniques to assess caudate atrophy in 100 AD, 200 MCI and 100 HC[32]. The caudate volumes were found to be significantly lower in MCI than in HC - by 2.5% on the left and 4.4% on the right. Controls were found to have the highest bilateral caudate nucleus volume, reduced in MCI and lowest in AD. Furthermore, this atrophy was associated with age and clinical dementia rating and other cognitive test scores. However, only the right-hand volume was associated with MCI-to-AD conversion and τ-levels. No association with CSF amyloid levels was found, but PET may provide better correspondence. There is also a natural asymmetry of the caudate in normally aging brains with caudate R approximately 4% larger than L. This asymmetry was found to vanish for the AD subjects, meaning that the right hand side atrophy is greater. In Ref. [5] right caudate atrophy was found to be associated with τ CSF levels. The hypothesis that goes along with the volumetric data analysis is that neuronal atrophy follows the amyloid and NFT pathology. The authors of [5] also point out that caudate atrophy may be secondary to loss of afferent connections to other regions, and that these may be more relevant to clinical differences between groups. The right hand caudate greatly overlaps with our ROI

[29] One the other hand, without global signal regression and no scrubbing or correction for global signal disruptions, as described in the last section of this thesis, longer times means greater chance of a severe global signal disruption manifesting itself in the correlation.

[30] Dijkstra's algorithm does identify shortest paths along several node jumps, but in general shortest path mainly consists of a direct link

[31] A matlab toolbox was cited in the ROC analysis, but no cross-validation scheme was mentioned in this context.

[32] The subject material is from the Alzheimer's Disease Neuroimaging Initiative (ADNI), accessible through www.loni.ucla.edu/ADNI/Data/

that has the single largest reduction in strength in $M_{a\beta}$ relative HC (see 33). The reduction in $a\beta$ going from M_0 to $M_{a\beta}$ does involve a simultaneous increase in $p\tau$, which is not surprising as the to markers are connected, and as we have noted $M_{p\tau}$ may suffer from a correlation-blind-spot (resulting in the corpus striatum hole in $HC - M_{p\tau}$). Comparing low and high $p\tau$ MCI groups directly for the highest resolution, reveals clear differences in both left and right caudate, with slightly higher relative FC reduction on the right.

The rare condition known as hyperthymesia involves a very detailed autobiographical memory seems to be connected with enlarged medial temporal lobe and caudate. We also note in passing that Deep Brain Stimulation of the fornix (a structure connecting hemispheres just underneath corpus striatum in close proximity to the caudate) in an attempt to treat morbid obesity, resulted in superior autobiographical memory as a surprising side-effect [77]. This hints at a possibly fruitful DBS target in treatments aimed at stemming the progression of cognitive decline. As Madsen notes, there is in fact an association between the Body-Mass-Index (BMI) and caudate atrophy.

The Caudate has also been histologically implicated with amyloid and τ aggregations [78]. It is the anterior part of caudate which displays most atrophy - and plays an important role in cognitive processing, by integrating information from the dorsolateral attention and planning orbitofrontal cortices [5].

We have also found reduced functional connectivity in other subcortical gray matter and basal ganglia, putamen and thalamus. These have reduced volume in AD, and the volume reduction correlates with cognitive decline [79].

We have previously noted a genetic component, that causes individuals with Down's syndrome to develop AD. This decline is associated with bilaterally reduced volume in hippocampus and caudate, as well as putamen R and amygdala R [80]. PET studies of dopamine receptors found a significant reduction in both caudate and putamen [81]. The corpus striatum is affected in other neuropathologies, such the autosomal disorder Huntington's disease.

In a similar 3d surface mapping volumetric study of hippocampus volume (again using the large ADNI material), the loss rates were found to be related to a worsening condition with 0.7%/year in HC, 3.1%/year in MCI and 5.6%/year in AD, correlating with cognitive test scores [82].

Choo et al studied atrophy in PCC and MTL, focusing in particular on the entorhinal complex and hippocampus [83]. Anatomical scans and diffusion tensor imaging was used to gauge atrophy and white matter damage. With cohorts of 19 MCI, 19 AD and 18 HC, it was found that both MCI and AD had reduced PCC volumes relative HC. The entorhinal complex also showed significant atrophy, but only AD showed significant volume change in hippocampus. MCI showed FA changes in parahippocampal cingulum, whereas AD was affected in both parahippocampal and posterior cingulum. The MTL volumes correlated with these FA values, and the authors conclude the presence of direct PCC atrophy and effects of fiber degeneration caused by MTL atrophy. Regarding our 8 AD, we find hippocampus R and PCC having significantly reduced FC, although they are not the strongest signatures. The MCI as stated many times, most likely reside in M_0, which has a clear posterior cingulum signature. Hippocampus appears more prominently in the high $p\tau$ group, which should be closest to AD. Both parahippocampal and hippocampus appear in the network component $HC > M_{a\beta}$, with failing connectivity to the corpus striatum hub region.

We have found that the strongest contrast is associated with levels of $p\tau$, this reflects the general findings of other groups. For example, using the ADNI data, it has been shown that τ concentrations progressively increase from controls to MCI to AD [84].

CSF levels of τ have been related to temporal lobe atrophy, but only at trend-level with hippocampus [85], which may explain why we don't see more of this central region in our data.

More work has been done comparing HC to AD, an easier target, arguably the starting point in understanding the pathology. Unfortunately the available number of AD in our analysis is limited to 8 subject, which is not enough to make statements with any statistical accuracy.

Li et al attempted an ambitious Bayesian network learning analysis to assess global connection differences (16 HC and 14 AD) in resting-state networks identified with ICA [86]. The Bayesian network approach allows extracting directionality of couplings, but these are not given much attention since the time resolution of RS fMRI is insufficient to claim such relations. The ICA network revealed a dominant DMN, but also other networks were found including lateral/medial visual, auditory, sensorimotor, self-referential, self-referential and dorsal/ventral attention networks. Many of the nodes we have identified belong to DMN such as PCC and parahippocampal complex, but key nodes such as caudate/putamen form part of the self-referential network. The networks identified by ICA were used to create network templates for subsequent Bayesian network analysis. Bayesian network analysis based on representing the system with a directed, acyclic graph [87]. The approach analyzes conditional dependencies, e.g. a

set of symptoms generated by a set of diseases with certain probability. Weak or no connection means that there is no conditional dependence. The authors note that previous studies have shown the DMN to be prone to accepting incoming connections from the other nets, which fits with picture of information integration and simulation being central functions. Led by this notion, the authors created an integration index quantifying the number of incoming DMN connections, regarding it as an accurate measure of cognitive function. This index was significantly reduced in AD. Despite our poor AD statistics, we note a large number of connections leading to DMN nodes as part of the reduced connectivity set. Li et al also show is that the connection between sensorimotor, self-referential and ventral attention network is heavily reduced in AD. This could correspond with our finding that connections between caudate/putamen and and nodes in the sensorimotor/attention network have significantly reduced correlation for both M_0 and $M_{a\beta}$. One drawback of global network communication is that detailed spatial information is lost, making comparison problematic. For the high $p\tau$ group we do not find these links, likely due to an intrinsic, approximate quarter period delay in these links. Hippocampus and other nodes of DMN such as cuneus/precuneus instead appear more strongly, as does connections between parietal superior (sensorimotor) and frontal left (parts of self-referential, attention). Looking our AD group it generally appears that DMN components are figuring largely, but the sensorimotor self-referential disconnection can also be seen. Since $M_{p\tau}$ resembles AD more than the other groups and should be closest by the progression hypothesis, it could also suffer from the quarter period correlation artifact.

Rambouts et al studied DMN, comparing 28 MCI, 18 AD and 41 HC [88]. This study did not target resting-state specifically, rather the deactivation of it during visual encoding tasks. The deactivation refers to decrease in brain activity and it was found that the deactivation of DMN became progressively less complete, going from HC to MCI to AD. Petrella et al follow a similar path as Rambouts and focusing only on the DMN during a face-name memory task, and concluded that the DMN integrity thus gauged, is capable of separating MCI that progress to AD from those that remain stable within a 2-3 year period [89]. Attempts have been made to create multivariate models predicting the endpoint of cognitive decline and assess the role of DMN in boosting power. One such study by Koch et al showed relatively low numbers for RS fMRI DMN, but the authors noted that larger samples would yield better results [90]. As noted in the last section of this thesis, there is good reason to expect reduced power unless extra care is taken dealing with motion artifacts related global signal anomalies. In addition, their TR=3s is a bit on the long side, possibly exacerbating the effect. Excellent classification results have been obtained combining functional and structural connectome data [91].

An interesting study [92], examined DMN with RS fMRI stratifying according to pathogenic presenilin-1/2 and amyloid precursor protein, thereby targeting known genetic components of AD. The authors found decreased FC in posterior cingulate/precuneus most severely in carriers with clinical dementia and to symptomatic carriers, which in regard to our results fit the M_0 group best, where MCI generally end up, by sheer probability of numbers. This study has a very conservative motion discrimination, recognizing the particularly sensitive motion dependence in RS fMRI [93]. Again, DMN studies focus on a limited (however very interesting) part of the connectome. Amyloid distribution overlaps with DMN, causing many to focus on this network. This is part of the reason why PCC is so frequently reported.

In a study by Sorg et al, resting-state network differences between 16 HC and 24 amnestic MCI was examined [94]. In addition a voxel-based morphometry analysis was performed. The authors interpret their results in the light of the two biomarkers, and begin by noting that tau pathology starts in MTL and correlates well with both cell loss and atrophy, whereas amyloid deposits in neocortex and less in MTL. Furthermore they note that MTL atrophy correlates with dementia and tempoparietal hypo-metabolism. Their main finding is that selected areas of DMN and executive attention network exhibited reduced network related activity. Note that the ICA RSN analysis in general does not consider interaction between the networks (exceptions exist, e.g. [87]), although ICA template correlations and anti-correlations measure the integrity of networks. We find similarities between our $HC > M_0$ differences and the DMN significant differences, both in the PCC and in the parietal superior regions. In the same data, we have reduced connectivity between temporal L and parietal/corpus striatum regions. Intriguingly, it seems that the $HC > M_0$ corresponds better with the areas of significant gray matter atrophy in the MTL.

Liu et al undertook a graph theoretical study of 16 MCI, 18 AD and HC. Among their findings were a decreased nodal centrality in the medial temporal lobe for the MCI relative HC. They further noted decreased centrality in the MTL, frontal gyrus and amygdala in MCI relative AD. However, the ROI-set had very a low resolution (90 regions [21]), although partial correlation is used[33] The results are hard

[33]Partial correlation is the correlation between residuals of two series after linear regression using all other timeseries. This procedures give correlation between the two time series, controlled for all other timeseries, and gives a more direct measure of functional connectivity.

to compare with, since a more or less arbitrary binarization threshold has been applied, tuning it for each subject to produce the same number of edges in each graph. Proceeding to compare our results, we should compare our weighted betweenness centrality to their binary version. Although we in general find reduced centrality in important hub regions, such as thalamus, putamen and caudate, we do indeed find some laterality with amygdala R and hippocampus R in $HC > M_{a\beta}, M_0$. Both hippocampus appear to have significantly reduced centrality in our case and we find many areas in the medial temporal lobe. Note that we have restricted our calculation to the network components, which produces more significances.

A famous graph theoretical analysis targeting nature's ubiquitous small-world property is performed by Supekar et al [48]. This is a purely binary formalism with arbitrary correlation thresholds (same degree thresholding - so not completely arbitrary). Furthermore, the resting state data predates the seminal papers demonstrating the severe impact of small, sudden movements on correlation analysis [93, 70, 71]. Note that in our analysis we suffer from the same effects, but we have attempted to mitigate their impact by applying strict QA limits, including a global signal variation threshold. Supekar et al perform a bandpass filtering into several bands, and then focus on a very low frequency interval 0.01-0.05 Hz, with the rationale that clustering coefficients are highest in this band, resulting in a small-world topology (path length did not vary between intervals). When comparing AD and HC, the group average correlations was controlled for by always selecting a threshold to obtain the same number of links, choosing to disregard the fact that correlations are in general lower in AD, with the rationale that this evokes topological differences. In this way, the authors determine a significantly lower correlation coefficient for the AD group, resulting in the loss of small-worldness. Later in the paper, the another analysis is preformed where correlation differences are examined. The regions are limited to 90 and differences very broadly described as reduced correlation within the temporal lobe, between thalamus and temporal/occipital/frontal lobe, between temporal lobe and corpus striatum. Another interesting find is that varying the threshold they find regions where the difference in local clustering coefficient are maximized in both hippocampus, with slightly larger differences on the right. Right hand laterality can also be found in our AD data. This kind of laterality may seem strange for homologous parts, but seemingly identical parts in the two hemispheres often have lateralized functionality.

13 How I learned to stop worrying and love resting-state fMRI

During the course of this work several mistakes have been made. Personally, I prefer to learn from my mistakes and not try to hide them. In this section, the shortcomings are highlighted and their logical conclusion and extension is revealed. On another personal note, I believe one should never stop asking questions. If, heaven forbid, you suffer from pathological performance anxiety and find yourself in deep waters where the pressure of generating results is getting to you: stop and think. Ask yourself what you are doing, what know and what you can prove. That is how good science is made.

If you have made it this far, you may very well have asked the question: 'Why so damn long? What's this guys problem?' The problem is precisely: to find the truth. Such an ambition can easily turn into obsession, even though the whole enterprise may fall short due to a kink somewhere in the long data processing chain, common in fMRI. Unfortunately for the disinterested reader, this obsessive behavior involves running through data at its deepest level before drawing conclusions.

The link permutation tests in this work are limited to 10000 permutations, which in all honesty is not enough to claim precise statistical significance. After this work was completed, additional computational resources became available, which in combination with highly effective parallel codes revealed that some groups may in fact require millions of permutations to converge completely (to be fair, the majority of links converge much quicker than this). The tails of the null-distributions in the Monte Carlo simulation are just too elusive by their improbable nature.

Apart from the importance of computational resources and the power of brute force, I learned that although the link distributions are not always normally distributed (rather the whole set of links is a mix of distributions), a simple t-test with multiple comparison correction can quickly gauge contrast strength. If you find significant differences in sufficient numbers, you may proceed with a few million permutations in the hope that these will not vanish. The situation is not as serious as it may seem - the component searches confirm that the contrasts located by link permutation search are valid. The component search is much better at locating weak contrasts and deals with the multiple comparison problem in a smart way, generally converging reliably within 10000 permutations. The less conservative nature of component

search is confirmed by the similarity with link testing using a low number of permutations, corresponding to a higher alpha and lower significance.

The frequency interval on which the main focus of this work is centered ($f = 0.03-0.06$ Hz), is perhaps not ideal. However, the best selection was made with available frequency data at the time (intermediate resolution with 392 ROIs, MCI data) according to sound selection criteria. Since then, calculation of an enlarged cohort of subjects (and with modified QA criteria) in all frequency intervals for both HC and MCI has revealed strong HC-MCI contrast is in $f = 0.01 - 0.1$ Hz. This is not as bad as it seems either, because analysis of the same data reveals that the intermediate interval has very similar contrasts to that of the encompassing, with preserved laterality and trends, albeit with a somewhat weaker contrast. This is a finding in itself: $f = 0.03 - 0.06$ Hz lodges most of the contrast. In addition, the larger frequency interval contains more noise, and may be more heavily impacted by motion and physiological signals.

On the bleeding edge, resting state imaging has proven far more challenging than first anticipated. Scrupulously eyeballing time-series data and associated correlation matrices, has since the time of writing revealed a very disturbing pattern. The pattern is revealed when plotting all matrices on the same color-scale and consists of certain subjects with large global signal changes, and overall higher correlation than the others. Turning to the literature, recent research shows that motion artifacts caused by sudden head movements as small as 0.5 mm is enough to cause a global signal peak [71, 70]. One may attempt (as we since have done) to reduce this effect by excluding subjects with large variations in global signal. Neither conservative motion limits, nor motion regression, eliminate the artifact in derived connectivity measures. The pseudo-motion parameters of the bulk motion correction are not the real ones, but those of a mathematical transform that mimics the real movement. As such, their correspondence with motion induced global signal changes can be quite poor.

Correlation is badly affected by global signal changes, that falsely enhances global correlation between all areas. Again, things are not as bad as they seem. We have focused on the HC-MCI patterns, which in general contain enough subjects that the effects of random motion are averaged out and there are no detectable differences in group motion profiles. The noise probably weakens our contrasts considerably, and may very well explain the miserable failure that results when attempting a correctly cross-validated classification.

The motion-to-global-signal-effect can be eliminated by global signal regression, but this is a desperate move that induces artifactual anti-correlations. An aggressive and effective approach is so-called scrubbing, in which frames with sudden motion are completely removed [70]. This approach can be combined with strategies to reduce global signal disruption by the so-called median angle approach [95]. In addition, one may include the movement in neighboring frames, adding many more motion regressors to tackle the effect [96]. In our case, scrubbing leads to heavily decimated data and the pseudo-motion is not accurate enough to eliminate the global signal change. Adding more motion regressors suffers from the same problem. A more fruitful approach is perhaps to target the handful of frames that are outliers in the signal variation curve, and eliminate them in the nuisance regression step.

Like I said, the important thing is to learn from your mistakes.

References

[1] R. Brookmeyer, E. Johnson, K. Ziegler-Graham, and M. H. Arrighi. Forecasting the global burden of alzheimer's disease. *Alzheimer's and Dementia*, 3(3):186–191, 2007.

[2] K. Ritchie. The dementias. *Lancet*, 360:1759–1766, 2002.

[3] L. L. Barclay, A. Zemcov, J. P. Blass, and J. Sansone. Survival in alzheimer's disease and vascular dementia. *Neurology*, 35:834–840, 1985.

[4] O.Hansson, H.Zetterberg, P.Buchhave, E.Londos, K.Blennow, and L.Minthon. Association between csf biomarkers and incipient alzheimer's disease in patients with mild cognitive impairment: a follow-up study. *Lancet Neurol.*, 5:228–234, 2006.

[5] S K Madsen, a J Ho, X Hua, P S Saharan, a W Toga, C R Jack, M W Weiner, and P M Thompson. 3D maps localize caudate nucleus atrophy in 400 Alzheimer's disease, mild cognitive impairment, and healthy elderly subjects. *Neurobiology of aging*, 31(8):1312–1325, August 2010.

[6] J. Skinner, J.O. Carvalho, G.G. Potter, A. Thames, E. Zelinski, P.K. Crane, and L.E. Gibbons. The Alzheimer's Disease Assessment Scale-Cognitive-Plus (ADAS-Cog-Plus): an expansion of the

ADAS-Cog to improve responsiveness in MCI. *Brain imaging and behavior*, 6(4):489–501, December 2012.

[7] Lewy body dementia association. `http://www.lbda.org`, December 2013.

[8] A. Anoop, P. K. Singh, R. S. Jacob, and S. K. Maji. Csf biomarkers for alzheimer's disease diagnosis. *Int J Alzheimer Dis*, 2010:606802, 2010.

[9] M. Hiltunen M, T. van Groen, and J. Jolkkonen. Functional roles of amyloid-beta protein precursor and amyloid-beta peptides: evidence from experimental studies. *J. Alzheimers Dis*, 18(2):401âĂŞ412, 2009.

[10] R. Capone, F.G. Quiroz, P. Prangkio, I. Saluja, A.M. Sauer, M.R. Bautista MR, R.S. Turner, J. Yang, and M. Mayer. Amyloid-beta-induced ion flux in artificial lipid bilayers and neuronal cells: resolving a controversy. *Neurotox Res*, 16(1):1–13, 2009.

[11] I. Grundke-Iqbal, K. Iqbal, and M. Quinlan. Microtubule associated protein tau. a component of alzheimer paired helical filaments. *J Biol Chem*, 261(13):6084–6089, 1986.

[12] I. T. Lott and E. Head. Alzheimer disease and down syndrome: Factors in pathogenesis. *Neurobiol Aging*, 26(3):383–389, 2005.

[13] T. Polvikoski. Apolipoprotein e, dementia, and cortical deposition of beta-amyloid protein. *N Engl J Med*, 333(19):1242–1247, 1995.

[14] W. Chun and G. V. Johnson. The role of tau phosphorylation and cleavage in neuronal cell death. *Front Biosci*, 12:733–756, 2007.

[15] Randy L Buckner, Abraham Z Snyder, Benjamin J Shannon, Gina LaRossa, Rimmon Sachs, Anthony F Fotenos, Yvette I Sheline, William E Klunk, Chester A Mathis, John C Morris, and Mark A Mintun. Molecular, structural, and functional characterization of Alzheimer's disease: evidence for a relationship between default activity, amyloid, and memory. *The Journal of neuroscience : the official journal of the Society for Neuroscience*, 25:7709–7717, 2005.

[16] H Braak and E Braak. Neuropathological stageing of Alzheimer-related changes. *Acta neuropathologica*, 82:239–259, 1991.

[17] J. C. Morris and J. L. Price. Pathologic correlates of nondemented aging, mild cognitive impairment and early-stage alzheimer's disease. *J Mol Neurosci*, 17(2):101–118, 2001.

[18] R.A. Poldrack, J.A. Mumford, and Thomas E. Nichols. *Handbook of fMRI data analysis*. Cambridge university press, New York, 2011.

[19] Randy L Buckner, Jessica R Andrews-Hanna, and Daniel L Schacter. The brain's default network: anatomy, function, and relevance to disease. *Annals of the New York Academy of Sciences*, 1124:1–38, March 2008.

[20] R.C. Craddock, G.A. James, P.E. Holtzheimer, X.P. Hu, and H.S. Mayberg. A whole brain fmri atlas generated via spatially constrained spectral clustering. *Hum. Brain Mapp.*, 33(8):1914–28, 2012.

[21] N. Tzourio-Mazoyer, B. Landeau, D. Papathanassiou, F. Crivello, O. Etard, N. Delcroix, B. Mazoyer, and M. Joliot. Automated anatomical labeling of activations in spm usin a macroscopic anatomical parcellation of the mni mri single-subject brain. *Neuroimage*, 15:273–289, 2002.

[22] Michael D Fox, Abraham Z Snyder, Justin L Vincent, Maurizio Corbetta, David C Van Essen, and Marcus E Raichle. The human brain is intrinsically organized into dynamic, anticorrelated functional networks. *Proceedings of the National Academy of Sciences of the United States of America*, 102(27):9673–8, July 2005.

[23] Zhijiang Wang, Jiming Liu, Ning Zhong, Yulin Qin, Haiyan Zhou, and Kuncheng Li. Changes in the brain intrinsic organization in both on-task state and post-task resting state. *NeuroImage*, 62(1):394–407, August 2012.

[24] Rémi Patriat, Erin K. Molloy, Timothy B. Meier, Gregory R. Kirk, Veena A. Nair, Mary E. Meyerand, Vivek Prabhakaran, and Rasmus M. Birn. The effect of resting condition on resting-state fMRI reliability and consistency: A comparison between resting with eyes open, closed, and fixated. *NeuroImage*, 78:463–473, 2013.

[25] S Moeller, E Auerbach, P van de Moortele, G Adriany, and K Ugurbil. fMRI with 16 fold reduction using multibanded Multislice sampling. In *Proceedings 16th Scientific Meeting, International Society for Magnetic Resonance in Medicine*, volume Toronto, page 2366, 2008.

[26] N Weiskopf, C Hutton, O Josephs, and R Deichmann. Optimal epi parameters for reduction of susceptibility-induced bold sensitivity losses: A whole-brain analysis at 3 t and 1.5 t. *NeuroImage*, 33:493–504, 2006.

[27] A C Evans, D L Collins, and B Milner. An mri-based stereotactic atlas from 250 young normal subjects. *Journal Soc Neurosci Abstr*, 18:408, 1992.

[28] Susan Whitfield-Gabrieli and Alfonso Nieto-Castanon. : A Functional Connectivity Toolbox for Correlated and Anticorrelated Brain Networks. *Brain Connectivity*, 2(3):125–141, January 2012.

[29] J. Malik. Normalized cuts and image segmentation. *IEEE Transactions on Pattern Analysis and Machine Intelligence*, 22(8):888–905, 2000.

[30] J. Wang, X. Zuo, Z. Dai, M. Xia, Z. Zhao, X. Zhao, J. Jia, Y. Han, and Y. He. Disrupted functional brain connectome in individuals at risk of alzheimer's disease. *Biol. Psychiat.*, 73(5):472–481, 2012.

[31] Timo Ropinski, Jörg-Stefan PraÃ§ni, Jan Roters, and Klaus Hinrichs. Internal Labels as Shape Cues for Medical Illustration. In *Vision, Modeling, and Visualization*, pages 203–212, 2007.

[32] Catie Chang and Gary H Glover. Effects of model-based physiological noise correction on default mode network anti-correlations and correlations. *NeuroImage*, 47(4):1448–1459, October 2009.

[33] Simo Särkkä, Arno Solin, Aapo Nummenmaa, Aki Vehtari, Toni Auranen, Simo Vanni, and Fa-Hsuan Lin. Dynamic retrospective filtering of physiological noise in BOLD fMRI: DRIFTER. *NeuroImage*, 60(2):1517–1527, April 2012.

[34] Felice T Sun, Lee M Miller, and Mark D'Esposito. Measuring temporal dynamics of functional networks using phase spectrum of fMRI data. *NeuroImage*, 28(1):227–37, October 2005.

[35] C.J. Stam and B.W. van Dijk. Synchronization likelihood: an unbiased measure of generalized synchronization in multivariate data sets. *Physica D: Nonlinear Phenomena*, 163(3-4):236–251, March 2002.

[36] T Montez, K Linkenkaer-Hansen, B W van Dijk, and C J Stam. Synchronization likelihood with explicit time-frequency priors. *NeuroImage*, 33(4):1117–1125, December 2006.

[37] F. Takens. Detecting strange attractors in turbulence. *Lecture Notes Math.*, 898, 1981.

[38] Florian Mormann, Klaus Lehnertz, Peter David, and Christian E. Elger. Mean phase coherence as a measure for phase synchronization and its application to the EEG of epilepsy patients. *Physica D: Nonlinear Phenomena*, 144(3-4):358–369, October 2000.

[39] Y Benjamini and Y Hochberg. Controlling the false discovery rate: a practical and powerful approach to multiple testing. *J R Stat Soc B*, 57:289–300, 1995.

[40] Thomas E Nichols and Andrew P Holmes. Nonparametric Permutation Tests For Functional Neuroimaging : A Primer with Examples. *Hun Brain Map*, 15:1–25, 2001.

[41] A. Zlesky, A. Fornito, and E.T. Bullmore. Network-based statistic: Identifying differences in brain networks. *Neuroimage*, 53:1197–1207, 2010.

[42] A P Holmes, R C Blair, and J D G Watson. Non-parametric analysis of statistic images from functional mapping experiments. *J Cereb Blood Flow Metab*, 16:7–22, 1996.

[43] C.R. Genovese, N.A. Lazar, and T. Nichols. Thresholding of statistical maps in functional neuroimaging using the false discovery rate. *Neuroimage*, 15:870–878, 2002.

[44] Markku Penttonen and György Buzsáki. Natural logarithmic relationship between brain oscillators. *Thalamus and Related Systems*, 2(02):145, April 2003.

[45] K. Shmueli, P. Gelderen, J.A. Zwart, S.G. Horovitz, M. Fukunaga, J.M. Jansma, and J.H. Duyn. Low frequency fluctuations in the cardiac rate as a source of variance in the resting-state fmri bold signal. *Neuroimage*, 38(2):306–320, 2007.

[46] S. Särkkä, A. Solin, A. Nummenmaa, A. Vehtari, T. Auranen, S. Vanni, and F. Lin. Dynamic retrospective filtering of physiological noise in bold fmri: Drifter. *Neuroimage*, 60:1517–1527, 2012.

[47] C.E. Davey, D.B. Grayden, G.F. Egan, and L.A. Johnston. Filtering induces correlation in fmri resting state data. *Neuroimage*, 64:728–740, 2012.

[48] K. Supekar, V. Menon, D. Rubin, M. Musen, and M.D. Greicius. Network analysis of intrinsic functional brain connectivity in alzheimers's disease. *PLOS Comput. Biol.*, 4(6):e1000100, 2008.

[49] D.S. Basset, B.G. Nelson, B.A. Mueller, J. Camchong, and K.O. Lim. Altered resting state complexity in schizophrenia. *Neuroimage*, 59:2196–2207, 2012.

[50] M.E. Lynnall, D.S. Basset, K.R. McKenna, M. Kitzbichler, U. Muller, and E. Bullmore. Functional connectivity and brain networks in schizophrenia. *J. Neurosci.*, 30(28):9477–9487, 2010.

[51] M.Rubinov and O.Sporns. Weight-conserving characterization of complex functional brain networks. *Neuroimage*, 56:2068, 2011.

[52] E J Sanz-Arigita, M M Schoonheim, J S Damoiseaux, S a Rombouts, E Maris, F Barkhof, P Scheltens, and C J Stam. Loss of 'small-world' networks in Alzheimer's disease: graph analysis of FMRI resting-state functional connectivity. *PLoS ONE*, 5(11):e13788, January 2010.

[53] Danielle S Bassett, Edward T Bullmore, Andreas Meyer-Lindenberg, José a Apud, Daniel R Weinberger, and Richard Coppola. Cognitive fitness of cost-efficient brain functional networks. *Proceedings of the National Academy of Sciences of the United States of America*, 106(28):11747–11752, 2009.

[54] S. Brin and L. Page. The pagerank citation ranking: Bringing order to the web. *Stanford InfoLab*, 1998.

[55] P. R. Gould. On the geographical interpretation of eigenvalues. *Transactions of the Institute of British Geographers*, 42:53–86, 1967.

[56] R. von Mises and H. Pollaczek-Geiringer. Praktische verfahren der gleichungsauflosung. *ZAMM - Zeitschrift fur Angewandte Mathematik und Mechanik*, 9:152–164, 1929.

[57] C. Meyer. *Matrix analysis and applied linear algebra*. SIAM, 2000.

[58] L. Freeman. A set of measures of centrality based on betweenness. *Sociometry*, 40:35âĂŞ41, 1977.

[59] U. Brandes. A faster algorithm for betweenness centrality. *J Math Sociol*, 25(2):163–177, 2001.

[60] Mikail Rubinov and Olaf Sporns. Complex network measures of brain connectivity: uses and interpretations. *NeuroImage*, 52(3):1059–1069, September 2010.

[61] E. W. Dijkstra. A note on two problems in connexion with graphs. *Numerische Mathematik*, 1:269–271, 1959.

[62] R. W. Floyd. Algorithm 97: Shortest path. *commun ACM*, 5(6):345, 1962.

[63] N. Cristiani and J. Shawe-Taylor. *An introduction to support vector machines and other kernel-based learning methods*. Cambridge university press, 2000.

[64] M. Pontil and A. Verri. Support vector machines for 3d object recognition. *IEEE pattern anal*, 20(6), 1998.

[65] V. N. Vapnik. *The nature of statistical learning theory*. Springer-Verlag, New York, 1995.

[66] F. Lauer and Y. Guermeur. MSVMpack: a multi-class support vector machine package. *J Mach Learn Res*, 12:2293–2296, 2011. `http://www.loria.fr/~lauer/MSVMpack`.

[67] K. Crammer and Y. Singer. On the algorithmic implementation of multiclass kernel-based vector machines. *J Mach Learn Res*, 2:265–292, 2001.

[68] Michael D Greicius, Gaurav Srivastava, Allan L Reiss, and Vinod Menon. Default-mode network activity distinguishes Alzheimer's disease from healthy aging: evidence from functional MRI. *Proceedings of the National Academy of Sciences of the United States of America*, 101(13):4637–42, March 2004.

[69] Xiaozhen Li, Tie-Qiang Li, Niels Andreasen, Maria Kristoffersen Wiberg, Eric Westman, and Lars-Olof Wahlund. Ratio of Aβ42/P-tau181p in CSF is associated with aberrant default mode network in AD. *Scientific reports*, 3:1339, January 2013.

[70] Jonathan D Power, Kelly a Barnes, Abraham Z Snyder, Bradley L Schlaggar, and Steven E Petersen. Spurious but systematic correlations in functional connectivity MRI networks arise from subject motion. *NeuroImage*, 59(3):2142–54, February 2012.

[71] Jonathan D Power, Anish Mitra, Timothy O Laumann, Abraham Z Snyder, Bradley L Schlaggar, and Steven E Petersen. Methods to detect, characterize, and remove motion artifact in resting state fMRI. *NeuroImage*, 84:320–41, January 2014.

[72] Liang Wang, Matthew R Brier, Abraham Z Snyder, Jewell B Thomas, Anne M Fagan, Chengjie Xiong, Tammie L Benzinger, David M Holtzman, John C Morris, and Beau M Ances. Cerebrospinal Fluid Aβ42, Phosphorylated Tau181, and Resting-State Functional Connectivity. *JAMA neurology*, pages 1–7, August 2013.

[73] R C Petersen, G E Smith, S C Waring, R J Ivnik, E G Tangalos, and E Kokmen. Mild cognitive impairment: clinical characterization and outcome. *Archives of neurology*, 56:303–308, 1999.

[74] Michael D Fox, Dongyang Zhang, Abraham Z Snyder, and Marcus E Raichle. The global signal and observed anticorrelated resting state brain networks. *Journal of neurophysiology*, 101:3270–3283, 2009.

[75] Kevin Murphy, Rasmus M. Birn, Daniel A. Handwerker, Tyler B. Jones, and Peter A. Bandettini. The impact of global signal regression on resting state correlations: Are anti-correlated networks introduced? *NeuroImage*, 44:893–905, 2009.

[76] J Koivunen, N Scheinin, J R Virta, S Aalto, T Vahlberg, K Nå gren, S Helin, R Parkkola, M Viitanen, and J O Rinne. Amyloid PET imaging in patients with mild cognitive impairment: a 2-year follow-up study. *Neurology*, 76:1085–1090, 2011.

[77] C Hamani, M P McAndrews, M Cohn, M Oh, D Zumsteg, C M Shapiro, R A Wennberg, and A M Lozano. Memory enhancement induced by hypothalamic/fornix deep brain stimulation. *Ann Neurol*, 63:119–23, 2008.

[78] H Braak and E Braak. Alzheimer's disease, striatal amyloid deposits and neurofibrillary tangles. *J Neuropathol Exp Neurol*, 49:215–224, 1990.

[79] L W de Jong, K van der Hiele, I M Veer, J J Houwing, R G Westendorp, E L Bollen, P W de Bruin, H A Middelkoop, M A van Buchem, and J van der Grond. Strongly reduced volumes of putamen and thalamus in alzheimerâĂŹs disease, an mri study. *Brain*, 131:3277–3285, 2008.

[80] F Beacher, E Daly, A Simmons, V Prasher, R Morris, C Robinson, S Lovestone, K Murphy, and D G Murphy. AlzheimerâĂŹs disease and downâĂŹs syndrome, an in vivo mri study. *Psychol Med*, 39:675âĂŞ684, 2009.

[81] N Kemppainen, H Ruottinen, and Rinn NaÌĆgren, and. Pet shows that striatal dopamine d1 and d2 receptors are differentially affected in ad. *Neurology*, 55:205âĂŞ209, 2000.

[82] Jonathan H Morra, Zhuowen Tu, Liana G Apostolova, Amity E Green, Christina Avedissian, Sarah K Madsen, Neelroop Parikshak, Arthur W Toga, Clifford R Jack, Norbert Schuff, Michael W Weiner, and Paul M Thompson. Automated mapping of hippocampal atrophy in 1-year repeat MRI data from 490 subjects with Alzheimer's disease, mild cognitive impairment, and elderly controls. *NeuroImage*, 45(1 Suppl):S3–15, March 2009.

[83] Il Han Choo, Dong Young Lee, Jungsu S Oh, Jae Sung Lee, Dong Soo Lee, In Chan Song, Jong Choul Youn, Shin Gyeom Kim, Ki Woong Kim, Jin Hyeong Jhoo, and Jong Inn Woo. Posterior cingulate cortex atrophy and regional cingulum disruption in mild cognitive impairment and Alzheimer's disease. *Neurobiology of aging*, 31(5):772–9, May 2010.

[84] Leslie M Shaw, Hugo Vanderstichele, Malgorzata Knapik-Czajka, Christopher M Clark, Paul S Aisen, Ronald C Petersen, Kaj Blennow, Holly Soares, Adam Simon, Piotr Lewczuk, Robert Dean, Eric Siemers, William Potter, Virginia M-Y Lee, and John Q Trojanowski. Cerebrospinal fluid biomarker signature in Alzheimer's disease neuroimaging initiative subjects. *Annals of neurology*, 65:403–413, 2009.

[85] A D Leow, I Yanovsky, N Parikshark, X Hua, S Lee, A W Toga, C R Jack, M A Bernstein, P J Britson, J L Gunter, C P Ward, B Borowski, L M Shaw, J Q Trojanowski, A S Fleisner, D Harvey, J Kornak, N Schuff, G E Alexander, M W Weiner, and P M Thompson. the alzheimerâĂŹs disease neuroimaging initiative: A 1-year follow up study using tensor-based morphometry correlating degenerative rates, biomarkers, and cognition. *Neuroimage*, 45:645âĂŞ655, 2009.

[86] R. Li, X. Wu, K. Chen, A. S. Fleisher, E. M. Reiman, and L. Yao. Alterations of Directional Connectivity among Resting-State Networks in Alzheimer Disease, 2012.

[87] Xia Wu, Rui Li, Adam S Fleisher, Eric M Reiman, Xiaoting Guan, Yumei Zhang, Kewei Chen, and Li Yao. Altered default mode network connectivity in Alzheimer's disease–a resting functional MRI and Bayesian network study. *Human brain mapping*, 32:1868–81, 2011.

[88] Serge a R B Rombouts, Frederik Barkhof, Rutger Goekoop, Cornelis J Stam, and Philip Scheltens. Altered resting state networks in mild cognitive impairment and mild Alzheimer's disease: an fMRI study. *Human brain mapping*, 26(4):231–9, December 2005.

[89] J R Petrella, F C Sheldon, S E Prince, V D Calhoun, and P M Doraiswamy. Default mode network connectivity in stable vs progressive mild cognitive impairment. *Neurology*, 76:511–517, 2011.

[90] Walter Koch, Stephan Teipel, Sophia Mueller, Jens Benninghoff, Maxmilian Wagner, Arun L W Bokde, Harald Hampel, Ute Coates, Maximilian Reiser, and Thomas Meindl. Diagnostic power of default mode network resting state fMRI in the detection of Alzheimer's disease. *Neurobiology of Aging*, 33:466–478, 2012.

[91] Chong Yaw Wee, Pew Thian Yap, Daoqiang Zhang, Kevin Denny, Jeffrey N. Browndyke, Guy G. Potter, Kathleen A. Welsh-Bohmer, Lihong Wang, and Dinggang Shen. Identification of MCI individuals using structural and functional connectivity networks. *NeuroImage*, 59:2045–2056, 2012.

[92] Jasmeer P Chhatwal, Aaron P Schultz, Keith Johnson, Tammie L S Benzinger, Clifford Jack, Beau M Ances, Caroline a Sullivan, Stephen P Salloway, John M Ringman, Robert a Koeppe, Daniel S Marcus, Paul Thompson, Andrew J Saykin, Stephen Correia, Peter R Schofield, Christopher C Rowe, Nick C Fox, Adam M Brickman, Richard Mayeux, Eric McDade, Randall Bateman, Anne M Fagan, Allison M Goate, Chengjie Xiong, Virginia D Buckles, John C Morris, and Reisa a Sperling. Impaired default network functional connectivity in autosomal dominant Alzheimer disease. *Neurology*, 81:736–44, 2013.

[93] Koene R A van Dijk, Mert R. Sabuncu, and Randy L. Buckner. The influence of head motion on intrinsic functional connectivity MRI. *NeuroImage*, 59:431–438, 2012.

[94] Christian Sorg, Valentin Riedl, Mark Mühlau, Vince D Calhoun, Tom Eichele, Leonhard Läer, Alexander Drzezga, Hans Förstl, Alexander Kurz, Claus Zimmer, and Afra M Wohlschläger. Selective changes of resting-state networks in individuals at risk for Alzheimer's disease. *Proceedings of the National Academy of Sciences of the United States of America*, 104(47):18760–18765, 2007.

[95] Hongjian He and Thomas T. Liu. A geometric view of global signal confounds in resting-state functional MRI. *NeuroImage*, 59:2339–2348, 2012.

[96] K J Friston, S Williams, R Howard, R S Frackowiak, and R Turner. Movement-related effects in fMRI time-series. *Magnetic resonance in medicine : official journal of the Society of Magnetic Resonance in Medicine / Society of Magnetic Resonance in Medicine*, 35:346–355, 1996.